NASA Contractor Report 172315

Inlet Flowfield Investigation Part II–Computation of the Flow About a Supercruise Forebody at Supersonic Speeds

G. C. Paynter
V. Salemann
E. E. I. Strom

Boeing Military Airplane Company
Seattle, Washington 98124

Contract NAS1-16612
April 1984

National Aeronautics and
Space Administration

Langley Research Center
Hampton, Virginia 23665

NASA Contractor Report 172315

Inlet Flowfield Investigation Part II—Computation of the Flow About a Supercruise Forebody at Supersonic Speeds

submitted to
National Aeronautics and
Space Administration
Langley Research Center
Hampton, Virginia 23665

in response to
NASA Contract NAS1-16612

April 1984

Boeing Military Airplane Company
Seattle, Washington 98124

TABLE OF CONTENTS

LIST OF TABLES

LIST OF FIGURES

LIST OF FIGURES

LIST OF FIGURES

LIST OF FIGURES

LIST OF FIGURES

1.0 SUMMARY

A joint program was carried out between the Boeing Military Airplane Company and the NASA Langley Propulsion Aerodynamics Branch to develop improved flow analysis methods useful in the design of supersonic fighter forebody geometries. A primary purpose of these methods was an improved definition of the flow field at potential inlet locations.

The joint Boeing/NASA program included both experimental and analytical studies. An advanced tactical supercruise fighter configuration was selected as a baseline model. This model was tested extensively for both its aerodynamic performance and propulsion/airframe interaction. Available data include wing/body static pressure and boundary layer total pressure distributions.

An existing flow analysis which numerically solves the parabolized Navier-Stokes (PNS) equations on a general curvilinear coordinate system for forebody geometries of arbitrary shape was used to predict the flow about the baseline model geometry. The objective of this study was to explore the use of such methods for configuration design. Flow calculations were completed at Mach numbers of 1.5 , 2.0, and 2.5 and at angles-of-attack of 0, 4, and 8 degrees. The purpose of this report is to present the results of these calculations and some comparisons between computed results and wind tunnel data. Conclusions are drawn as to the current status of the analysis and desirable improvements to the analysis are suggested.

The computer code was found useful for predicting inviscid flow properties at flight conditions where the shed vortex from the wing leading edge was not a dominant flow phenomenon. These inviscid properties were obtained by using a coarse mesh to minimize the computational cost and a laminar viscosity to minimize computed viscous effects. The code was found to be too costly and prone to numerical difficulties when run with sufficient mesh and a turbulence model necessary to resolve the wing and body boundary layers. A number of possible improvements to the current code are suggested to remove these difficulties.

2.0 INTRODUCTION

New and sometimes radically different inlet concepts are continually being proposed for advanced tactical airplanes. The great number of concepts, with numerous perturbations, makes concept evaluation through wind tunnel testing very time consuming as well as expensive. A great effort is being expended throughout the industry to develop new and improved analytical methods to analyze the inlet-forebody problem. With these analytical tools a great number of inlet concepts can be evaluated quickly with wind tunnel testing reserved for only the most likely candidates. To support future code development and validation, a comprehensive data base for the inlet flow field characteristics of an advanced tactical configuration is required.

The Boeing Military Airplane Company (BMAC) and the NASA-Langley Propulsion Aerodynmics Branch have undertaken a multi-task program (Contract NAS1-16612) directed at this problem. Program objectives are:

- Identify inlet concepts and locations which have potential for application on tactical supersonic cruise airplanes

- Determine, through wind tunnel testing, wing/body flow field characteristics at the representative inlet locations established in Task I.

- Apply existing codes to compute flow field characteristics measured in the wind tunnel.

All design work, test data analysis, and supersonic flow calculations were performed by BMAC. The wind tunnel testing and transonic flow computations were conducted by the Propulsion Aerodynamics Branch of NASA Langley.

A conceptual study was conducted in which several inlet concepts were defined for an Advanced Tactical Supercruiser. The baseline configuration (Figure 1) had an underwing half-axisymmetric inlet with a short diffuser. Alternate concepts included body mounted inlets ahead of the wing root and wing upper surface mounted inlets.

These inlet concepts established the flow field areas depicted in Figure 2. Areas 1 and 2 correspond to the lower and upper wing mounted inlet locations and area 3 is a representative of the body mounted inlet locations. Transonic flow field surveys and wing static pressure measurements over the forward portion of the wing were conducted and are reported in Ref. 1. Wing and body static pressure measurements were made during a further test of this model at supersonic Mach numbers, Ref. 2. These data are compared to theoretical predictions in this report. Locations of body and wing static pressures are shown in Figures 3 and 4 and are tabulated in Tables I and II.

An existing flow analysis, Ref. 3, was used to predict the flow about the baseline forebody geometry, Figure 1, at Mach numbers of 1.5, 2.0, and 2.5 and at angles-of-attack of 0^{o}, 4^{o}, and 8^{o}. The objective of these calculations was to explore the use of PNS methods for supersonic cruise forebody configuration design. The purpose of this report is to present these computed results and some comparisons with wind tunnel test data. Conclusions are drawn as to the current status of the analysis. Desirable improvements to the analysis are suggested.

3.0 FLOW ANALYSIS

The flow about a fighter forebody geometry at supersonic speeds is described by the Reynolds averaged Navier-Stokes equations. While solution of such flows has been demonstrated by time relaxation methods, these solutions have proven to be too expensive for design application because a full 3-D storage of the solution is required at each time step, and a large number of time steps is required if a grid fine enough to resolve the boundary layers is employed. In the absence of separation, such flows are known to exhibit very little upstream influence and are called "parabolic." Numerical marching procedures have been developed which take advantage of this feature of the flow. In these methods, a predominant flow direction is selected as one of the coordinate directions, and diffusion terms relative to this direction are deleted from the equations. The equations are set up in finite difference form such that only information from an initial plane of data and boundary conditions perpendicular to the predominant flow direction are required to solve for the flow properties in a plane parallel and downstream of the initial plane. The solution procedure can thus be "marched" through the flow domain of interest.

The great advantage of the marching or PNS procedures is that a full flow field solution is obtained in the equivalent of one to ten global iterations of a time relaxation method, which would typically require ten thousand or more global iterations on the same grid. There is, however, a reduction in the range of flow conditions which can be analyzed. Because of the assumption of a predominant flow direction and the neglect of certain terms to achieve a marching procedure, the degree of grid skewness which can be analyzed without violating a program assumption is reduced. Spurious solutions can be generated by too small or too large a step size, too high an angle-of-attack, mainstream flow separation, or a poor numerical treatment of the equations to be solved.

A PNS procedure was selected for application to a supercruise forebody at supersonic speeds to explore the usefulness of such methods for configuration design. A detailed description of the PNS procedure is given in Reference (3). The numerical procedure solves the parabolized Navier-Stokes equations

on a general curvilinear coordinate system for arbitrary forebody geometries. For turbulent flows a two-equation turbulence model is incorporated. An elliptic relation is used to calculate pressure and satisfy local continuity at each computational plane. Several smoothing routines are used to control computational noise and strong perturbations resulting from inconsistent initial conditions and discontinuities in the wall slopes. An iterative alternating direction implicit (ADI) marching solution procedure is used to advance the flow solution along the forebody. An initial set of data is required to start the solution. The bow shock is captured as part of the overall flow simulation.

The BMAC procedure has been applied to a number of different flows to evaluate the accuracy of the procedure. The code was applied to the flat plate boundary layer flow of Mabey et al[4] at M = 2.5, the axisymmetric waisted body flow of Winter, Smith and Rotta[5] at M = 2.8, and the cone at angle-of-attack flow of Tracey [6] at M = 8.

3.1 Sublayer Approximation

In the subsonic portion of the boundary layer the governing flow equations have a fundamentally different character than in the supersonic regions. When the pressure gradient P_σ (σ is in the axial or stream direction; ξ and η are cross-stream directions) is unknown in the subsonic layer (sublayer), the equations are elliptic in pressure, meaning that pressure waves should be able to propagate upstream. This presents a significant problem for a parabolic marching algorithm. The numerical solutions to the flow equations become unstable in the sublayer and generate departure solutions in which the pressure diverges wildly. One solution to the instability problem is to neglect the stream pressure gradient. The effect of neglecting P_σ causes an error of approximately 5-15% in the predicted wall pressure, but stable solutions are possible. Previous work in the development of viscous supersonic codes has highlighted the stability problem of unknown gradients, P_σ, in the sublayer.

In the present forebody analysis, P_σ is evaluated at a point outside of the sublayer, which is determined by a specified Mach number, and is imposed on the sublayer mesh points in the w-momentum equation. The Mach number that defines the sublayer edge has been studied only briefly, However, even

subsonic values seem to be acceptable. The pressure at the outside point is also used in the calculation of density in the sublayer. To account for the forebody geometry perturbations, the P_ξ and P_η gradients are not set to zero in the sublayer. They are calculated from the pressures generated by the pressure-continuity scheme. In practice the normal gradients are small except at the geometry perturbations when the boundary layer is disturbed.

3.2 The Computational Mesh

An algebraic mesh generation procedure by Kowalski[7] was used to define the computational meshes for the calculations performed herein. The computational domain is the region between the body surface and a cone which encompasses the bow shock. The mesh was constructed in a given plane perpendicular to the axis of the forebody, by connecting points on the body surface and on the outer cone with cubic connecting functions. The coefficients of these polynomials are functions of the boundary coordinates and the slopes of the mesh lines at the boundaries. Stretching functions are used to distribute a given number of points, n, around the outer cone and around the body. The cubic function is used to connect points of the same number starting from a given circumferential location on the cone and on the body.

On a given line between the body surface and the outer conical surface, stretching functions are used to distribute a given number of points, m, between the body and the cone. Moving in the circumferential direction, a line is assumed to connect points of the same number (counting outward from the body) on each radial line. This forms an nxm mesh in the plane perpendicular to the body surface.

If the same number of points is used to form an nxm mesh in a series of "K" planes distributed along the body, a three-dimensional nxmxk mesh is formed by sequentially connecting corresponding points moving in a direction along the body axis. This mesh establishes the transformation between the physical domain and the computational domain.

4.0 DISCUSSION OF COMPUTED RESULTS

The original plan was to complete a coarse mesh analysis of the configuration without a canard at (3) Mach numbers (between 1.5 and 2.5) and at (4) angles-of-attack (between 2^{o} and 12^{o}) at each Mach number. The coarse mesh analysis was then to be repeated for the same configuration with a canard at the same Mach numbers and angles-of-attack as for the configuration without a canard. Then six cases were to be computed with a refined mesh. The above cases were to be computed assuming that the boundary layer flow was turbulent. It was noted in the proposed work statement for this task that the computer code was in development and that mesh refinement to adequately resolve the boundary layers on such configurations and analysis of configurations with a canard had not been attempted.

Table III lists the configurations and flow conditions for which flow predictions were made. The first (20) cases listed in Table III were computed toward completion of the original plan. Several laminar flow cases among these were included to investigate the influence of viscosity on the computed results.

Computed results from the first (20) cases inferred that further code development was needed to compute turbulent flow phenomena, vortex flows, or flows with complex geometry features such as a canard. The code did, however, appear to compute the inviscid flow properties accurately for cases without a strong shed vortex from the wing when a laminar viscosity was specified.

As a result of conclusions made from completion of the first (20) cases, the work plan was revised to take advantage of the code capability to compute inviscid flow properties for the configuration without a canard at angles-of-attack and Mach numbers where shed leading edge vortices would not significantly alter the inviscid flow properties. A coarse mesh was used and a laminar viscosity was specified to minimize viscous effects. The Mach numbers and angles-of-attack cases selected for the revised plan were Mach 1.5, 2.0, and 2.5 and angles of 0^{o}, 4^{o}, and 8^{o}. These are cases 21-29 listed in Table III.

Refined mesh runs were to be attempted at the higher angles-of-attack where the coarse mesh failed to produce a leading edge vortex. Desirable code improvements to allow calculation of turbulent flows, shed leading edge vortices, and configurations with a canard were to be identified.

The turbulent computed results (Cases 1-20), laminar computed results (Cases 21-29), difficulties encountered, desirable code improvmenets, and conclusions drawn from the present study follow below.

4.1 Turbulent Computed Results

The coarse mesh used for the turbulent flow cases computed had 40 radial and 56 circumferential points in each cross-plane. An example mesh is shown in Figure 5 at the upstream rake survey station. The estimated boundary layer thickness at that station is also shown.

Figures 6 and 7 are an example of the coarse mesh results which were obtained when a turbulent viscosity was specified. These results are for the configuration without canard at $M = 1.5$ and $\alpha = 0$ (Case 1, Table III). The flow conditions specified for the calculation corresponded to a model in the wind tunnel. Figure 6 is a map of computed constant Mach number contours at the axial station of the forward survey plane. Figure 7 is a map of computed constant total pressure contours at the same station. The boundary layer thickness at this station estimated from a correlation for the boundary layer development on a flat plate is shown in Figure 7.

As expected, the computed defect in total pressure extends far beyond the estimated boundary layer thickness. The computer code uses a law-of-the-wall function to minimize the mesh required to resolve the boundary layer. The near wall point is assumed to be in the law-of-the-wall region when the boundary layer is computed. This region is typically between $0.01\,\delta$ to $.2\,\delta$ in a direction normal to he wall. If, as in the coarse mesh turbulent cases computed, the near wall point is too far from the wall, an unrealistically thick boundary layer results. Similar results were obtained at higher angles-of-attack and at higher Mach numbers.

Some calculations were completed with a denser mesh near the body surface. The computed boundary layer thickness did decrease with increasing mesh density. The computational cost and the difficulty in obtaining solution

convergence, however, increased with increasing mesh density. The denser mesh distribution and the computed contour map of total pressure are shown in Figures 8 and 9. Note that the computed total pressure defect is closer to that expected from flat plate boundary layer theory.

For the configuration with a canard, the mesh generator program was found to be inadequate. Before the calculation, cross plane meshes are generated at an arbitrary number of axial stations. The program automatically connects the nth points of each cross-plane when it analyzes the flow field. Near the nose, the body cross section is circular and the mesh is uniform in the circumferential direction. As the canard grows, the mesh generator redistributes the spacing between the points to cover the canard, but does not keep the same (Nth) point at the tip of the canard. The program connects corresponding circumferential points of the mesh at each cross plane to generate a three-dimensional mesh. It therefore connects the tip of the canard at the second section through the canard to a point above or below the tip of the canard on the first section through the canard. This results in a canard that is analytically described as very thick near the intersection of the canard leading edge and the body. This inaccurate analytic description of the body geometry causes either large errors in the computed flow properties or program failure.

4.2 Laminar Computed Results

By specifying a laminar rather than a turbulent viscosity level to minimize viscous effects, it was possible to obtain a reasonable prediction of the inviscid flow properties with a coarse mesh. Cases 21-29, Table III, were computed with a coarse mesh and a laminar viscosity for the configuration without a canard. Cases were computed at Mach numbers of 1.5, 2.0, and 2.5 and at angles-of-attack of 0^{o}, 4^{o} and 8^{o} at each Mach number. The objective of these calculations was to obtain a good estimate of the inviscid flow properties through minimizing computed viscous effects by specifying a laminar rather than a turbulent viscosity. Computed viscous effects for these cases are not accurate because the mesh is too coarse and because the flow is expected to be turbulent in the Reynolds number range considered.

Plots of computed results are presented on Figures 10 to 27 for each case at the forward and aft survey stations. These plots include contour maps of Mach

number, total pressure, upwash angle, sidewash angle and the cross plane vector velocity. Table IV lists the plots presented herein for each case.

Qualitatively, the calculation procedure predicts the correct trends. At the 8^0 angle-of-attack, even with a laminar viscosity, a substantial boundary layer thickness is predicted at the top of the body which undoubtedly contaminates the inviscid solutions to some extent because of displacement thickness effects. No wing leading edge vortex was predicted, although a body vortex was predicted in the vicinity of the wing-body junction.

4.3 Comparisons With Test Data

For the wing-body configuration without a canard, comparisons are made between computed and measured body surface static pressures at Mach 2.0 and at angles-of-attack of 0^0 and 8^0. The test data are from a supersonic wind tunnel test at NASA Lewis Reference 2. The computed results were obtained with the PNS code described herein using a coarse mesh and with a laminar viscosity specified to minimize viscous effects.

Figure 28 is a comparison between computed and measured body pressure coefficient distributions at Station 49.5. Station 49.5 is just upstream of the wing leading edge and slightly aft of the crest of the canopy. Experimental data were available on the side and undersurface of the body. Computed pressure coefficients (Cp's) were slightly higher than those measured. This may have been due to inaccurate calculation of the boundary layer because a coarse mesh and a laminar viscosity were used in the calculation. Qualitatively, the analysis appears to predict the correct behavior.

Figure 29 is a comparison between computed and measured body pressure coefficient distributions at Station 69.6. Station 69.6 is well aft on the body about midway along the wing. On the lower surface, agreement between computed and measured Cp's is good at both $\alpha = 0^0$ and $\alpha = 8^0$. On the upper surface, quantitative agreement between computed and measured Cp's is not as good although the trends are qualitatively correct. Near the wing tip, the measured Cp's fall well below the computed values at both 0^0 and 8^0 (data for $\alpha = 2^0$, 4^0, and 6^0 are also shown). This suggests that the vortex lift develops continuously and increases in strength with

angle-of-attack. The PNS code apparently does not pedict this effect. Whether this is due to the use of an inadequate mesh or an inability of the PNS approximation to predict this phenomenon is unknown at this time.

Figures 30a and 30b are comparisons between computed and measured body pressure coefficient distributions along water line 10.5 and along the bottom symmetry plane at $\alpha = 0^{o}$ and 8^{o} respectively. Quantitative agreement is generally good. Once again the measured Cp's fall slightly below the computed values.

Rake measurements obtained at Mach 2.0 and 2.5 were analyzed for comparison to predictions. As-measured total pressure recovery for rakes near the two body stations is shown on Figures 31 to 34. These data include the normal shock loss in front of each probe. Some of the rake data were further reduced to obtain boundary layer total pressure recovery ahead of the normal shock, which corresponds to the analytical recovery predictions. This calculation requires the stream static pressure ahead of each probe. The nearest available wall static was used. For rakes at body station 50.5, the wall statics at B.S. 49.5 were used. Rakes at the downstream station were installed at B.S. 72.5, whereas the closest statics are at B.S. 69.5, 3 inches ahead of the rakes. This difference and normal pressure gradients probably contribute to errors in the normal shock correction resulting in recoveries above unity, particularly above the wing. See Figure 35 and 36, rake 6, where the wing vortex induces high velocities and normal pressure gradients resulting in large, inexact corrections based on upstream wall statics.

Only rake 12 at B.S. 50.5 and rakes 1, 2, and 6 at B.S. 72.5 had working body statics ahead of the rakes. The static pressure taps to be used with the other rakes were either plugged or open in the body cavity during the supersonic test. Thus, most of the rake data could not be corrected for the normal shock. It is shown as-measured for comparison with future analytical predictions which could be made to include the normal shock using analytically predicted static pressure.

Measured boundary layer thicknesses were close to flat plate predictions at $\alpha = 0$. The boundary layer thickens at $\alpha = 8^{o}$ below the wing and on top of the fuselage, but thins down where lift is developed. The shape at B.S.

50.5 behind the canopy indicates incipient separation at M = 2.5, probably due to recompression of the flow over the canopy.

4.4 Difficulties Encountered

The difficulties encountered in the present study can be attributed to one of the following causes: (1) a violation of the underlying PNS assumptions, (2) poor application of the code due to its early stage of development, or (3) inadequate modeling.

As noted in Section 3.0, Flow Analysis, PNS methods offer great cost savings relative to time relaxation methods. The use of a marching procedure, however, implies a reduction in the range of flows and geometries which can be computed. The flow external to the boundary layer must be everywhere supersonic. If a combination of a low free stream Mach number, high angle-of-attack, and a rapid change in the local slope of the body results in a local subsonic pocket (usually downstream of a local strong oblique shock), the solution cannot proceed. If a rapid change in surface slope results in a high local adverse pressure gradient and streamwise separation, the solution cannot proceed. If the local longitudinal surface slope varies substantially from the marching direction, terms which are neglected in the equations solved become large and large solution errors can result.

Available PNS codes to model supersonic 3-D visouc flows are typically in a research stage of development as is the code used in the present study. While, as noted in Section 3.0, the code has been successfully applied to several 2-D and 3-D turbulent flows, the flows considered herein are much more complex than those attempted before with the analysis. Several problems uncovered in the course of this study are briefly discussed below.

Many of these problems were associated with inadequate guidelines for the mesh required to resolve the critical regions such as the boundary layer, wing leading edges, and abrupt changes in body geometry. Another problem was the interpolation of the mesh and the geometry between pre-generated mesh planes, as described in Section 4.1. Another problem was the lack of logic to control solution iteration between planes. During the present contract, it was found that an under-relaxation process was desirable in this iteration. It was not possible, however, to automate this iteration process or to optimize the under-relaxation of the various variables.

Numerical solution of partial differential educations generates "noise" (disturbances) which can grow in amplitude and destroy the solution process unless these are damped with artificial viscosity terms. The amount of artificial viscosity required to control noise is a property of a particular algorithm. The smoothing requirements of the present algorithm are not yet well understood. This typically resulted in either poor convergence and errors due to excessive smoothing or errors due to excessive noise buildup because the smoothing was insufficient.

A marching solution procedure requires specification of an initial plane of data to initiate the solution. In the calculations performed for the present study, the initial plane was assumed to be at the tip of the body and the properties were assumed equal to free stream conditions. The body surface at this initial plane was assumed to be a small cylinder aligned with the free stream. In many cases, especially at angle-of-attack, this starting process caused problems because of the strong oblique shock immediately encountered as the solution attempted to advance to the second plane. Whether these were due to a poor mesh and geometry representation (due to a poor interpolation) or a violation of the underlying PNS assumptions is unknown.

Although the results presented were not definitive in uncovering deficiencies in the physical modeling, some of the problems encountered may have been due to either a violation of the parabolic assumptions or the handling of the sublayer. Further work will be required with the code to investigate these. Elimination of the usage problems noted above and the analysis of initially simple configurations followed by increasingly complex configurations should result in a clearer picture of the adequacy of the modeling.

4.5 Desirable Code Improvements

To overcome the difficulties observed in applying the current code to fighter forebody flow field prediction, various modifications to the code are briefly enumerated below. In addition to resolving the usage problems described in Section 4.4 (by further benchmark applications of the code), the suggested modifications would result in a code that could be more fully evaluated for defining the extent or boundaries to which PNS codes can be utilized for design applications.

The first modification recommended is to incorporate a routine for more accurately defining the initial conditions at the starting plane. This should eliminate many of the problems associated with initial transients.

The pressure continuity scheme currently adjusts pressure, density, and cross-flow velocity components. This procedure can be extended to include all velocity components as well as temperature. It is expected that such an extension would improve convergence rate and reduce the number of interplane iterations required. This may be particularly important with high angles of attack.

The smoothing procedures have not been studied in sufficient detail. Global damping schemes as well as local wavelength filtering should be studied to obtain a more effective damping scheme.

Interplane convergence rate is generally too slow, and frequently the solution diverges. Under-relaxation was used to improve the convergence properties of the algorithm. A study should be made to achieve a more optimum scheme.

The mesh generation procedure, which is a separate set of programs, should be modified such that the circumferential spacing around the body will produce a better representation of the geometry in wing-body or canard-body transition regions.

In many cases, it is desirable to compute just the inviscid flow properties with a coarse mesh. At present a no slip boundary condition must be used at the wall. For cases where just inviscid properties are wanted, modification of the code to allow a slip wall boundary condition is desirable, and would eliminate the need to run laminar flow cases, as was done in cases 21-29, to obtain inviscid flow predictions.

5.0 CONCLUSIONS

Following a revised work plan, the inviscid flow properties about a wing body configuration were computed at Mach numbers of 1.5, 2.0, and 2.5 and at angles-of-attack of 0^{o}, 4^{o} and 8^{o} using a laminar viscosity and a coarse mesh to minimize both viscous effects and computational cost. The computed inviscid flow properties were found to be qualitatively correct. Predictions of supersonic cruise forebody flows, where a wing leading edge vortex or streamwise separation are not present, can thus be effectively done for fighter design applications.

The present work uncovered a number of areas in the computer code used, which need to be improved. Desirable modifications to the present code are suggested. A detailed evaluation of the usefulness of a PNS code to predict viscous flow properties can be done when these modifications are accomplished.

6.0 REFERENCES

1. Yetter, J. A., Salemann, V., and Sussman, M. B., "Inlet Flowfield Investigation Part I - Transonic Flowfield Survey," NASA CR-172239, November 1983.

2. Hutchison, R. A., "Supersonic Wind Tunnel Test Results for a Tactical Supercruiser," Boeing Document D180-27925-1, 1984.

3. Roberts, D. W. and Forester, C. K., "Three-Dimensional Viscous Supersonic Forebody Analysis," AFWAL-TR-81-3137, December 1981.

4. Mabey, D. G., Meier, H. V. and Sawyer, W. G., "Experimental and Theoretical Studies of the Boundary Layer on a Flat Plate at Mach Numbers from 2.5 to 4.5," RAE TR 74127, 1974.

5. Winter, R. G., Smith, K. G., and Rotta, J. C., "Studies of the Turbulent Boundary Layer on a Waisted Body of Revolution in Subsonic and Supersonic Flow," Ministry of Technology, Aero Research Council and Memo R&M No. 3633, August 1968.

6. Tracey, R. R., "Hypersonic Flow over a Yawed Circular Cone," Ph.D. Thesis, CALTECH, August 1963.

7. Kowalski, E. J., "Boundary Fitted Coordinate Systems for Arbitrary Computational Regions," Workshop on Grid Generation, NASA Langley Research Center, October 1980.

Table I. Fuselage Static Taps (Right-Hand Side Only)

Tap number	M.S.	W.L.	B.L.	Comment
CPB 1	19.5	–	0	Bottom
2		9.9	–	
3		10.5	–	
4		–	0	Top
CPB 5	29.5	–	0	Bottom
6		9.9	–	
7		10.5	–	
8		11.7	–	
9		13.5	–	
10		–	0	Top
CPB 11	39.5	–	0	Bottom
12		9.9	–	
13		10.5	–	
14		11.7	–	
15		13.5	–	
16		15.3	–	
17		–	0	Top
CPB 18	49.5	–	0	Bottom
19		9.9	–	
20		10.5	–	
21		11.7	–	
22		13.5	–	
23		15.3	–	
24		–	0	Top
CPB 25	59.5	–	0	Bottom
26		9.9	–	
27		12.6	–	
28		14.0	–	
29		15.3	–	
30		–	0	Top
CPB 31	69.5	–	0	Bottom
32		12.6	–	
33		14.0	–	
34		–	0	Top

Table II. Wing Static Taps (Right Wing Only)

Tap number	Surface	W.S.[a]	B.L.	Comment
	Upper	11.784	3.997[b]	Existing
		12.850	3.997[b]	
CPUS 1		17.609	3.997[b]	
2			4.800	
3			6.100	
4			6.581	
5			6.937	
CPUS 6		24.906	3.997	
7			6.600	
8			7.295	
9			7.900	
10			9.308	
11			9.811	
CPLS 1	Lower	17.609	3.997	New
2			4.800	
3			6.100	
CPLS 4		24.906	3.997	
5			6.600	
6			7.900	
7			9.308	Existing
8			9.811	Existing

[a]W.S. = M.S. - 44.68
[b]Not available

Table III. Computed Flow Cases

CASE #	M	α	SCALE	P_∞	T_T	MESH	CANARD	REMARKS
1	1.5	0	Model	190.5	545	Coarse	W/O	Turbulent Flow
2	1.5	4	Model	190.5	545	Coarse	W/O	Turbulent Flow
3	1.5	8	Model	190.5	545	Coarse	W/O	Turbulent Flow
4	1.5	12	Model	190.5	545	Coarse	W/O	Turbulent Flow
5	2.0	0	Model	107.2	545	Coarse	W/O	Turbulent Flow
6	2.0	4	Model	107.2	545	Coarse	W/O	Turbulent Flow
7	2.0	8	Model	107.2	545	Coarse	W/O	Turbulent Flow
8	2.0	12	Model	107.2	545	Coarse	W/O	Turbulent Flow
9	2.5	0	Model	68.6	545	Coarse	W/O	Turbulent Flow
10	2.5	4	Model	68.6	545	Coarse	W/O	Turbulent Flow
11	2.5	8	Model	68.6	545	Coarse	W/O	Turbulent Flow
12	2.5	12	Model	68.6	545	Coarse	W/O	Turbulent Flow
13	2.5	0	Full	151	877.5	Coarse	W/O	Turb. Fl., One Sta.
14	2.5	12	Full	151	877.5	Coarse	W/O	Laminar Flow
15	1.5	0	Full	151	565.5	Coarse	W/O	Turbulent Flow
16	1.5	12	Full	151	565.5	Coarse	W/O	Laminar Flow
17	1.5	0	Full	2116	754	Coarse	W/O	Turbulent Flow
18	1.5	12	Full	2116	754	Coarse	W/O	Turbulent Flow
19	1.5	0	Model	190.5	545	Refined	W/O	Turb. Fl., One Sta.
20	2.5	0	Model	68.6	545	Coarse	W/O	Turb. Fl., One Sta.
21	1.5	0	Model	190.5	545	Coarse	W/O	Laminar Flow
22	1.5	4	Model	190.5	545	Coarse	W/O	Laminar Flow
23	1.5	8	Model	190.5	545	Coarse	W/O	Laminar Flow
24	2.0	0	Model	107.2	545	Coarse	W/O	Laminar Flow
25	2.0	4	Model	107.2	545	Coarse	W/O	Laminar Flow
26	2.0	8	Model	107.2	545	Coarse	W/O	Laminar Flow
27	2.5	0	Model	68.6	545	Coarse	W/O	Laminar Flow
28	2.5	4	Model	68.6	545	Coarse	W/O	Laminar Flow
29	2.5	8	Model	68.6	545	Coarse	W/O	Laminar Flow

Table IV. Contour Plots of Computed Properties

FIGURE NO.	M	α, DEG.	STATION	PROPERTY
10-a	1.5	0	50.5	Mach number
10-b	1.5	0	50.5	Total pressure
10-c	1.5	0	50.5	Upwash angle
10-d	1.5	0	50.5	Sidewash angle
10-e	1.5	0	50.5	Cross-plane velocity
11-a	1.5	0	70.5	Mach number
11-b	1.5	0	70.5	Total pressure
11-c	1.5	0	70.5	Upwash angle
11-d	1.5	0	70.5	Sidewash angle
11-e	1.5	0	70.5	Cross-plane velocity
12-a	1.5	4	50.5	Mach number
12-b	1.5	4	50.5	Total pressure
12-c	1.5	4	50.5	Upwash angle
12-d	1.5	4	50.5	Sidewash angle
12-e	1.5	4	50.5	Cross-plane velocity
13-a	1.5	4	70.5	Mach number
13-b	1.5	4	70.5	Total pressure
13-c	1.5	4	70.5	Upwash angle
13-d	1.5	4	70.5	Sidewash angle
13-e	1.5	4	70.5	Cross-plane velocity
14-a	1.5	8	50.5	Mach number
14-b	1.5	8	50.5	Total pressure
14-c	1.5	8	50.5	Upwash angle
14-d	1.5	8	50.5	Sidewash angle
14-e	1.5	8	50.5	Cross-plane velocity
15-a	1.5	8	70.5	Mach number
15-b	1.5	8	70.5	Total pressure
15-c	1.5	8	70.5	Upwash angle
15-d	1.5	8	70.5	Sidewash angle
15-e	1.5	8	70.5	Cross-plane velocity

Table IV. Contour Plots of Computed Properties (Continued)

FIGURE NO.	M	α, DEG.	STATION	PROPERTY
16-a	2.0	0	50.5	Mach number
16-b	2.0	0	50.5	Total pressure
16-c	2.0	0	50.5	Upwash angle
16-d	2.0	0	50.5	Sidewash angle
16-e	2.0	0	50.5	Cross-plane velocity
17-a	2.0	0	70.5	Mach number
17-b	2.0	0	70.5	Total pressure
17-c	2.0	0	70.5	Upwash angle
17-d	2.0	0	70.5	Sidewash angle
17-e	2.0	0	70.5	Cross-plane velocity
18-a	2.0	4	50.5	Mach number
18-b	2.0	4	50.5	Total pressure
18-c	2.0	4	50.5	Upwash angle
18-d	2.0	4	50.5	Sidewash angle
18-e	2.0	4	50.5	Cross-plane velocity
19-a	2.0	4	70.5	Mach number
19-b	2.0	4	70.5	Total pressure
19-c	2.0	4	70.5	Upwash angle
19-d	2.0	4	70.5	Sidewash angle
19-e	2.0	4	70.5	Cross-plane velocity
20-a	2.0	8	50.5	Mach number
20-b	2.0	8	50.5	Total pressure
20-c	2.0	8	50.5	Upwash angle
20-d	2.0	8	50.5	Sidewash angle
20-e	2.0	8	50.5	Cross-plane velocity
21-a	2.0	8	70.5	Mach number
21-b	2.0	8	70.5	Total pressure
21-c	2.0	8	70.5	Upwash angle
21-d	2.0	8	70.5	Sidewash angle
21-e	2.0	8	70.5	Cross-plane velocity

Table IV. Contour Plots of Computed Properties (Concluded)

FIGURE NO.	M	α, DEG.	STATION	PROPERTY
22-a	2.5	0	50.5	Mach number
22-b	2.5	0	50.5	Total pressure
22-c	2.5	0	50.5	Upwash angle
22-d	2.5	0	50.5	Sidewash angle
22-e	2.5	0	50.5	Cross-plane velocity
23-a	2.5	0	70.5	Mach number
23-b	2.5	0	70.5	Total pressure
23-c	2.5	0	70.5	Upwash angle
23-d	2.5	0	70.5	Sidewash angle
23-e	2.5	0	70.5	Cross-plane velocity
24-a	2.5	4	50.5	Mach number
24-b	2.5	4	50.5	Total pressure
24-c	2.5	4	50.5	Upwash angle
24-d	2.5	4	50.5	Sidewash angle
24-e	2.5	4	50.5	Cross-plane velocity
25-a	2.5	4	70.5	Mach number
25-b	2.5	4	70.5	Total pressure
25-c	2.5	4	70.5	Upwash angle
25-d	2.5	4	70.5	Sidewash angle
25-e	2.5	4	70.5	Cross-plane velocity
26-a	2.5	8	50.5	Mach number
26-b	2.5	8	50.5	Total pressure
26-c	2.5	8	50.5	Upwash angle
26-d	2.5	8	50.5	Sidewash angle
26-e	2.5	8	50.5	Cross-plane velocity
27-a	2.5	8	70.5	Mach number
27-b	2.5	8	70.5	Total pressure
27-c	2.5	8	70.5	Upwash angle
27-d	2.5	8	70.5	Sidewash angle
27-e	2.5	8	70.5	Cross-plane velocity

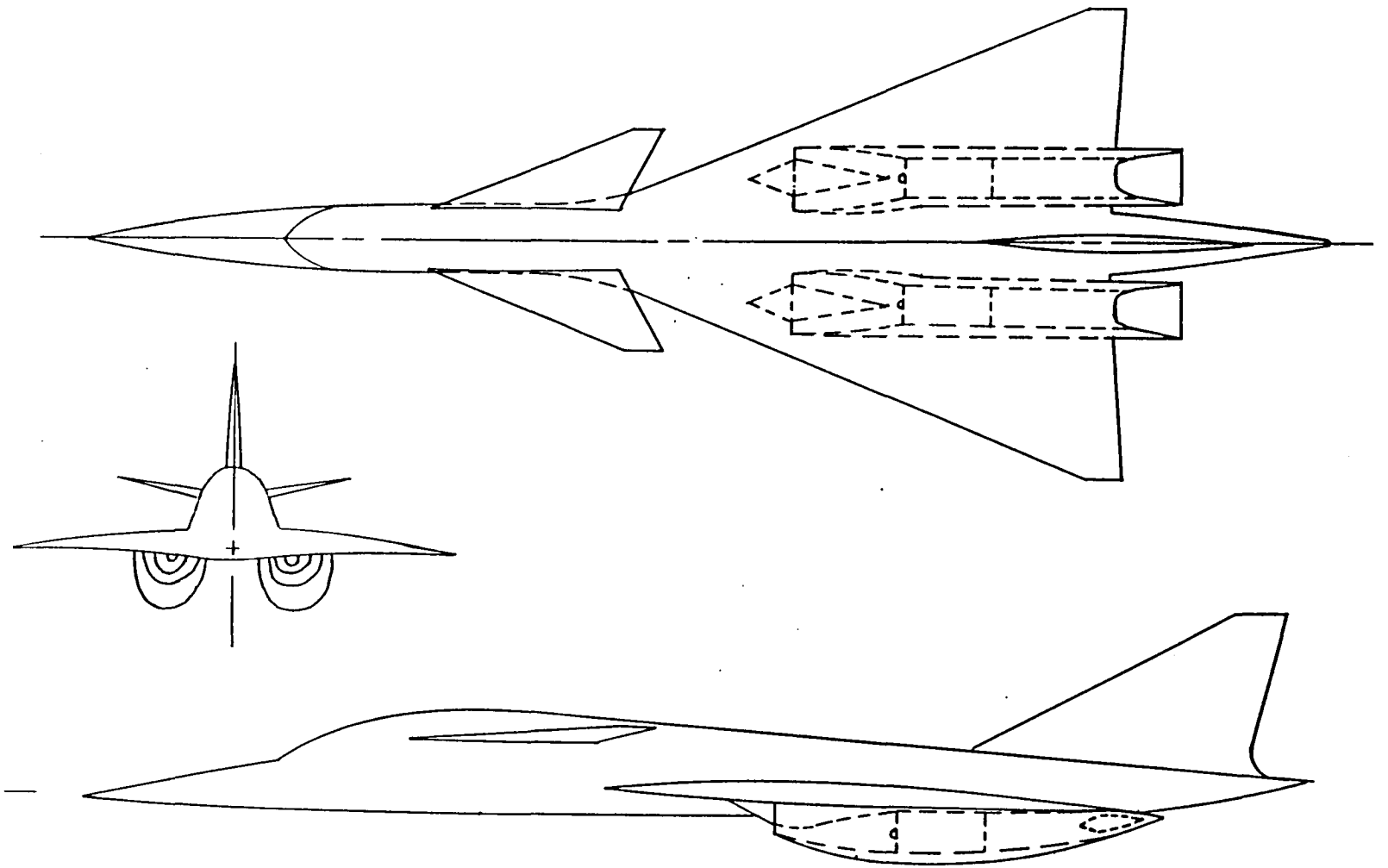

Figure 1. Boeing Advanced Tactical Supercruiser—ATS-350

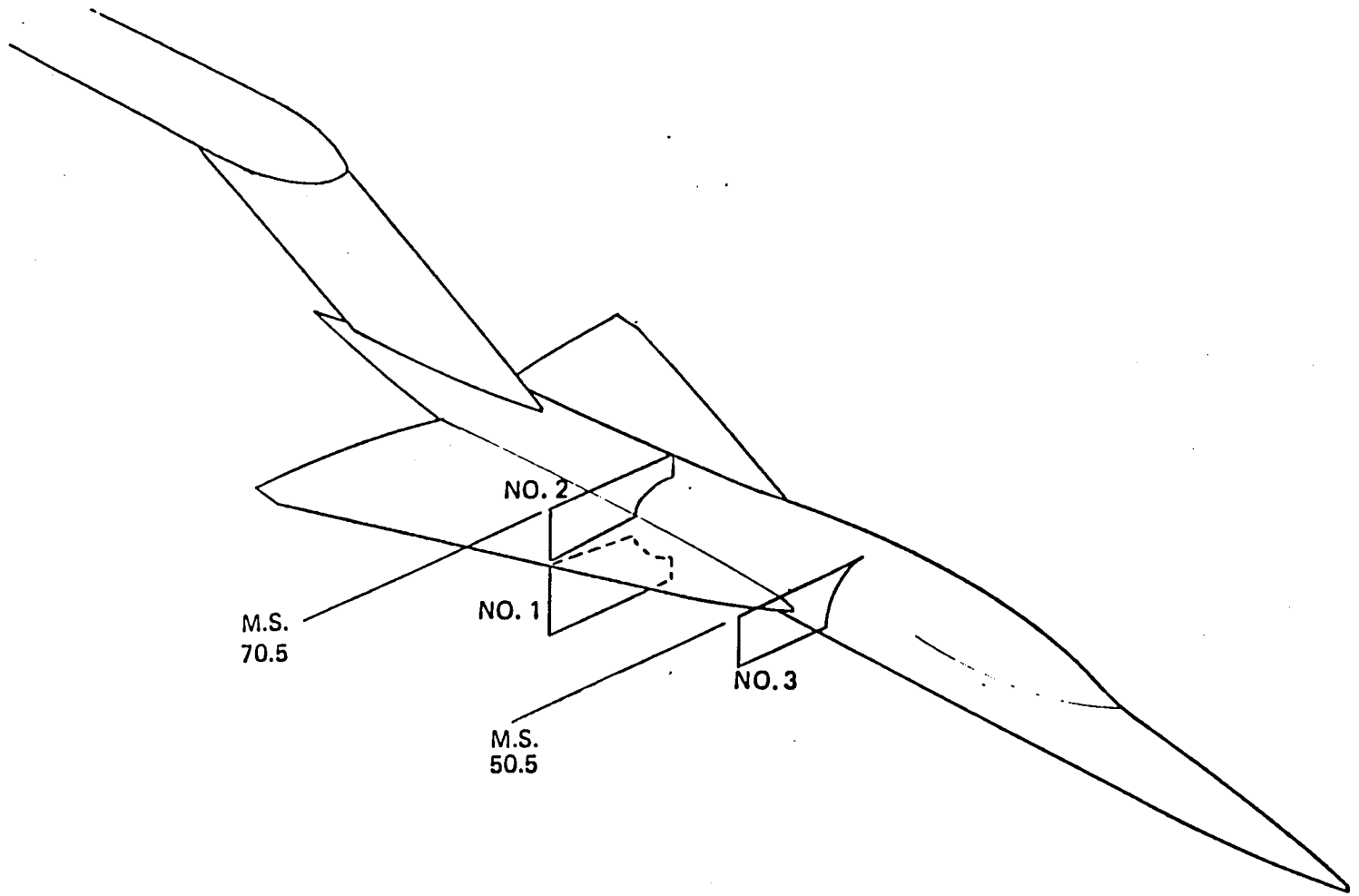

Figure 2. Inlet Flowfield Survey Areas

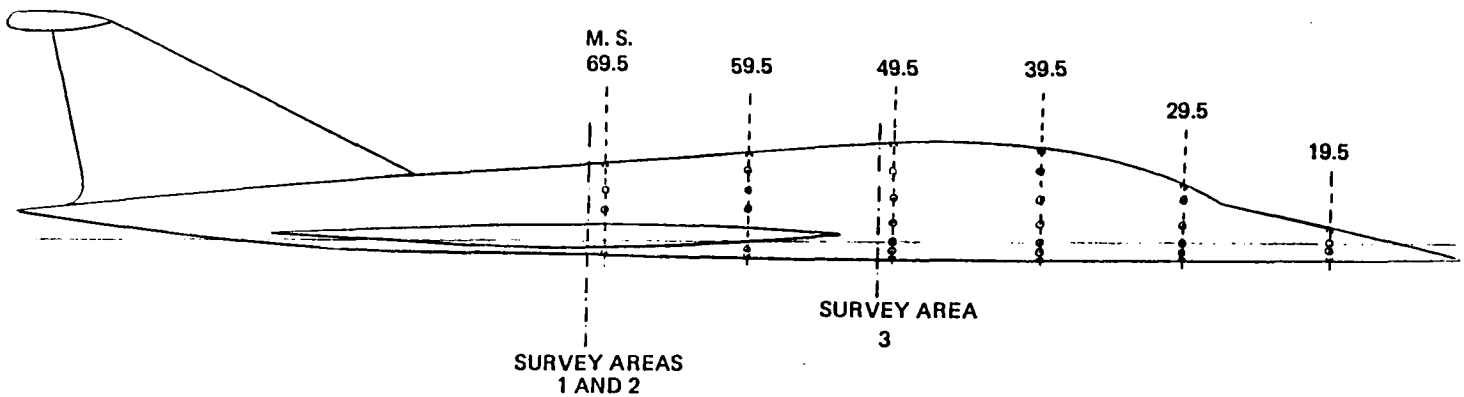

Figure 3. Fuselage Static Taps

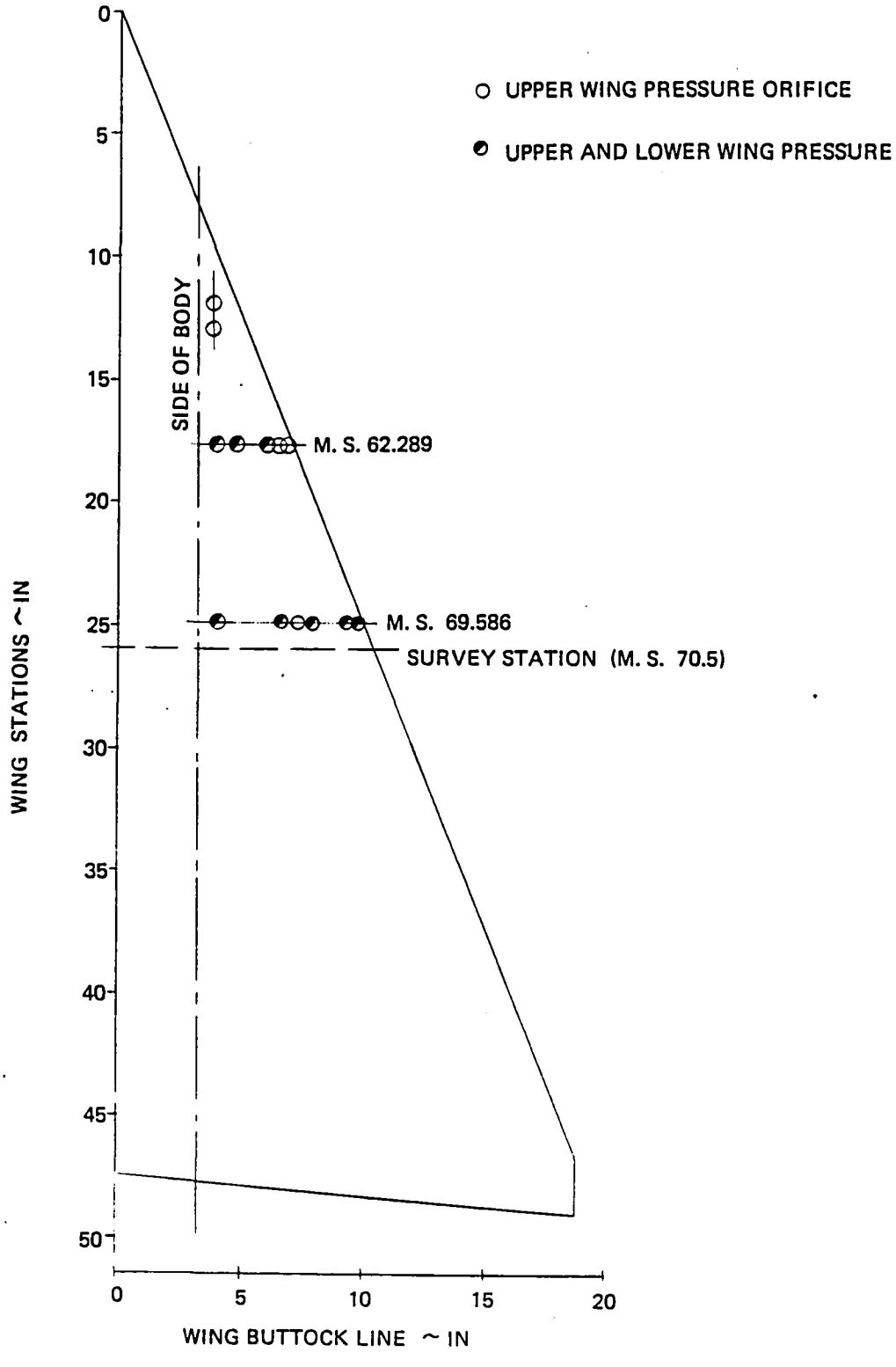

Figure 4. Wing Static Taps

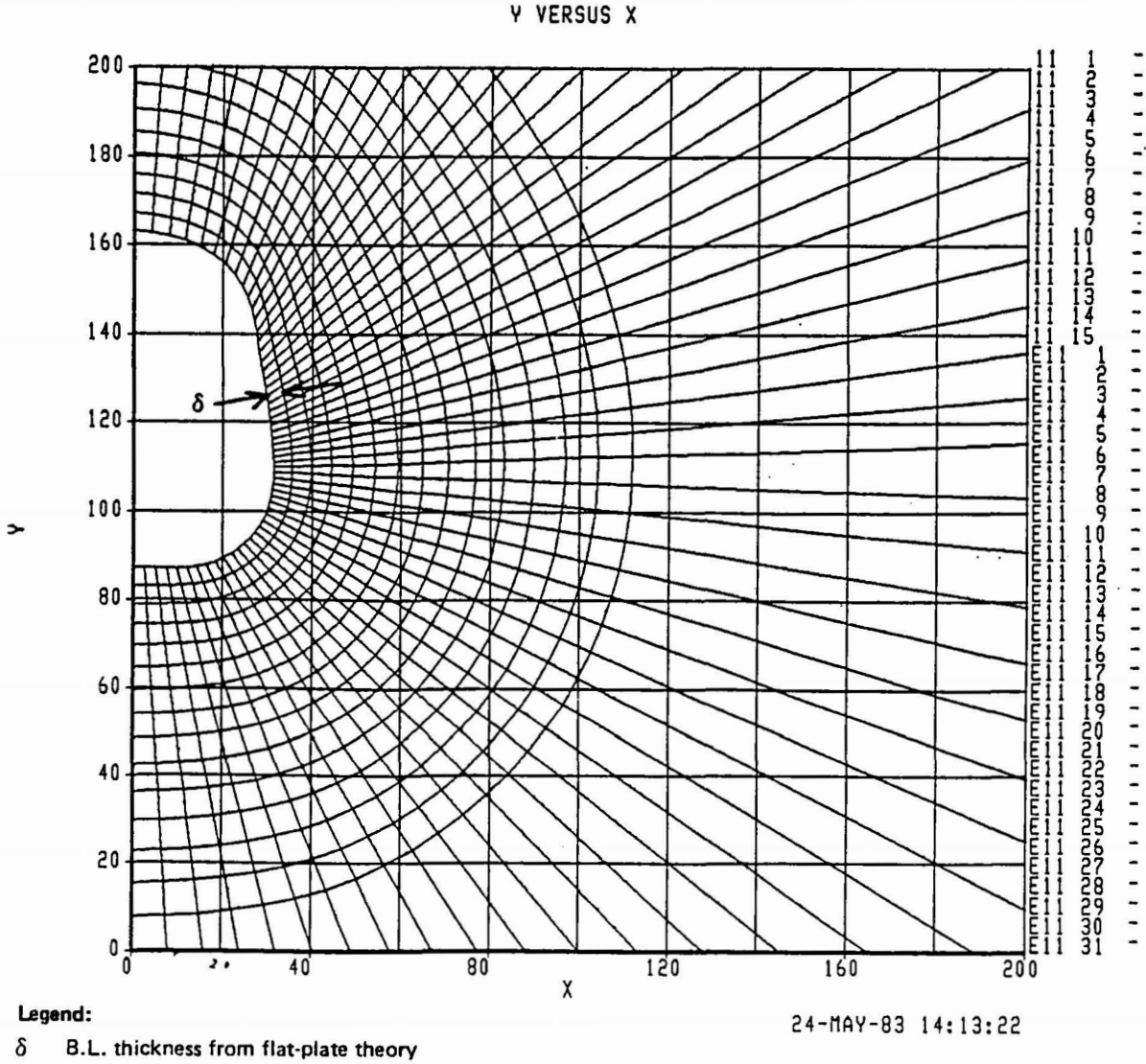

Legend:

δ B.L. thickness from flat-plate theory

Figure 5. Coarse Computational Mesh Forward Survey Station

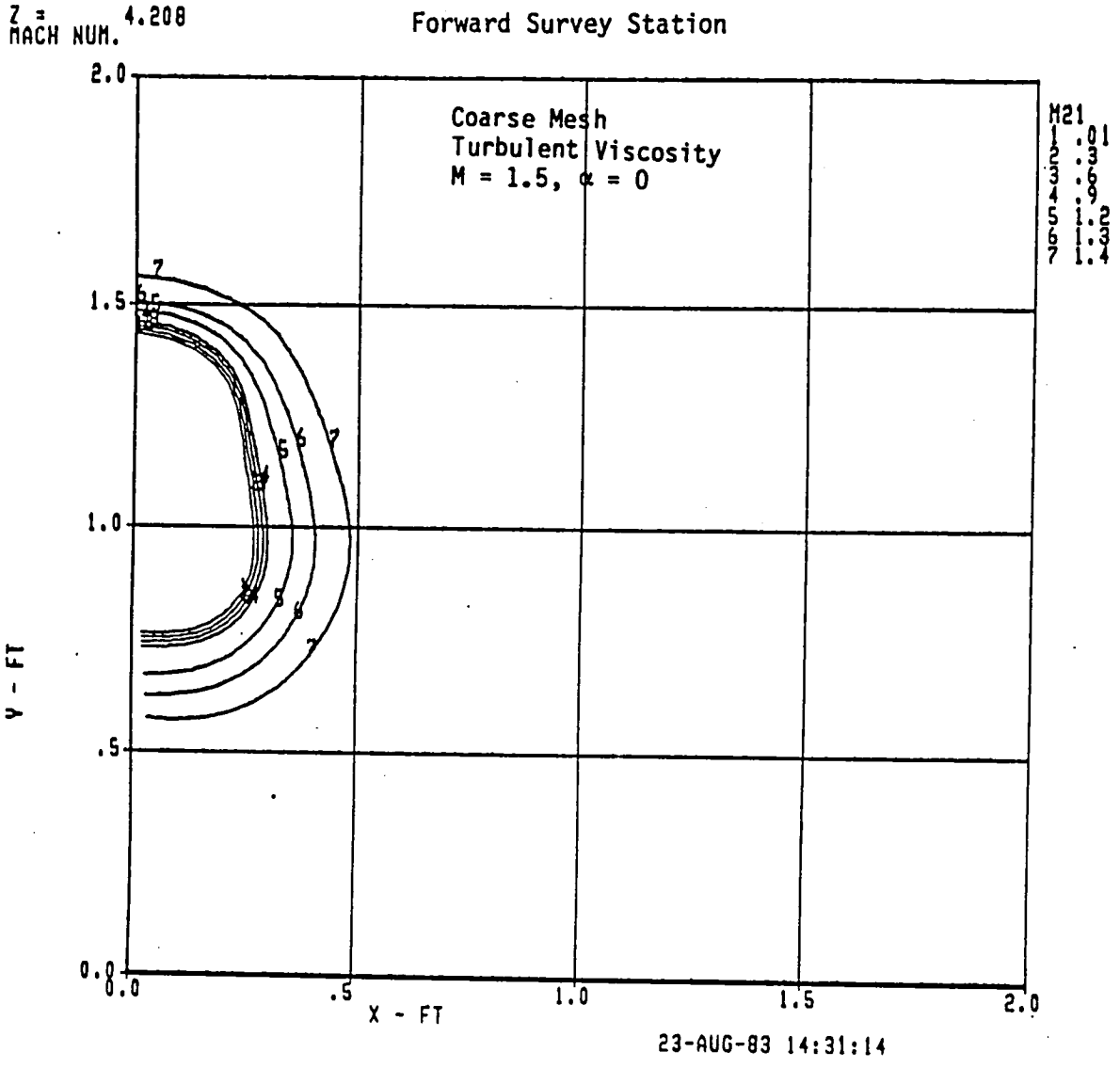

Figure 6. Mach Number Distribution

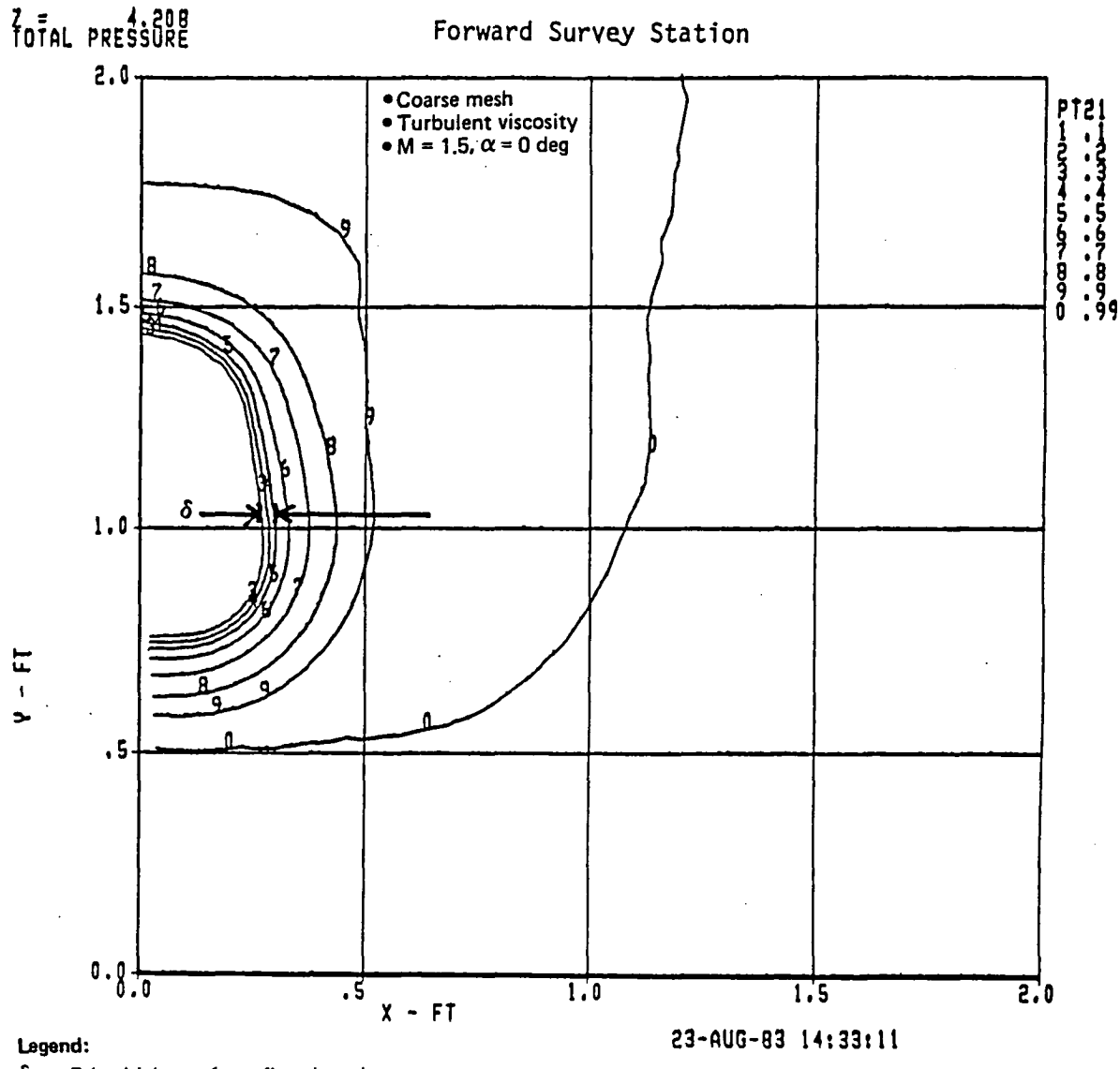

Legend:

δ B.L. thickness from flat-plate theory

Figure 7. Total Pressure Distribution

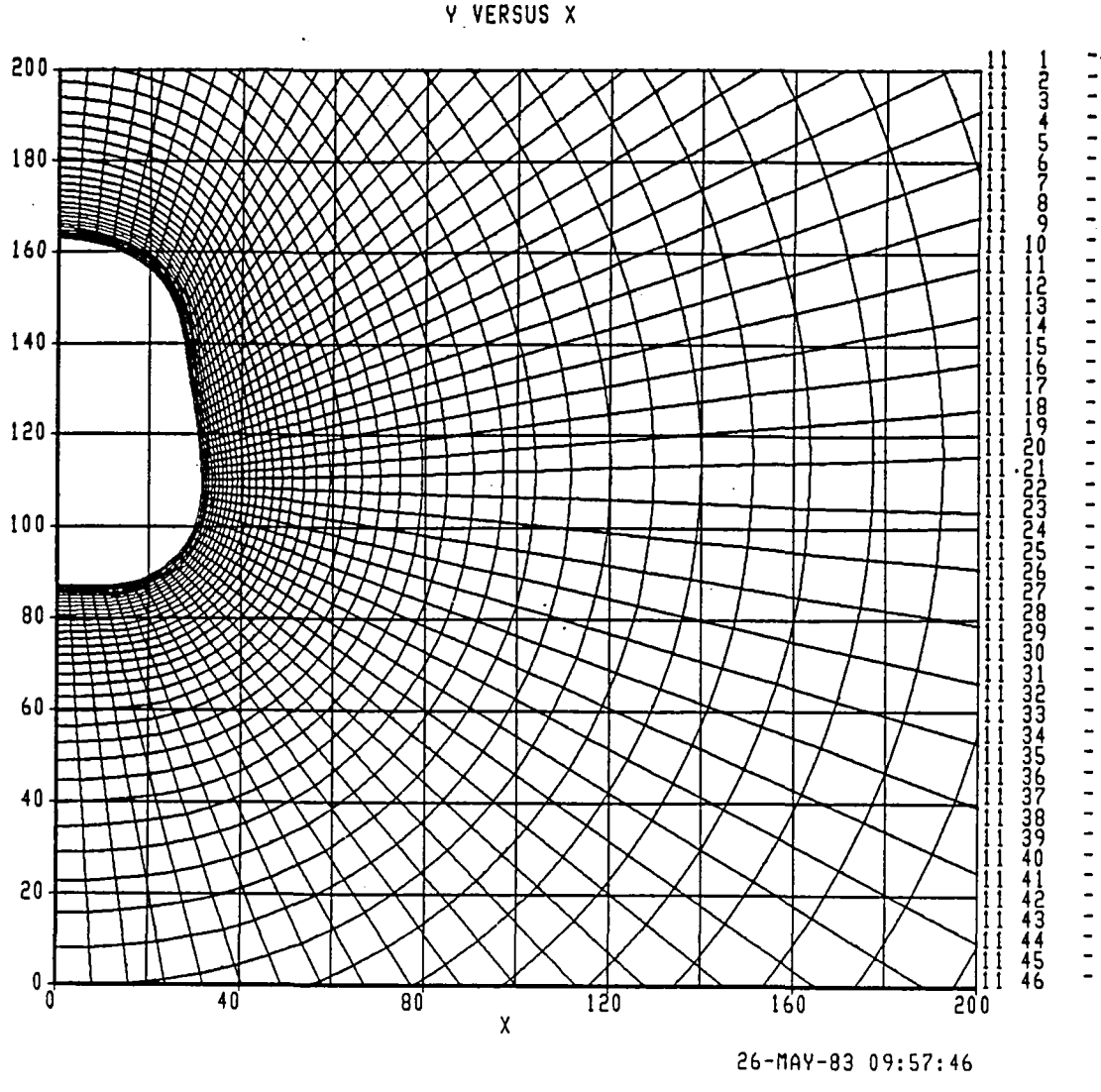

Figure 8. Fine Computational Mesh, Forward Survey Station

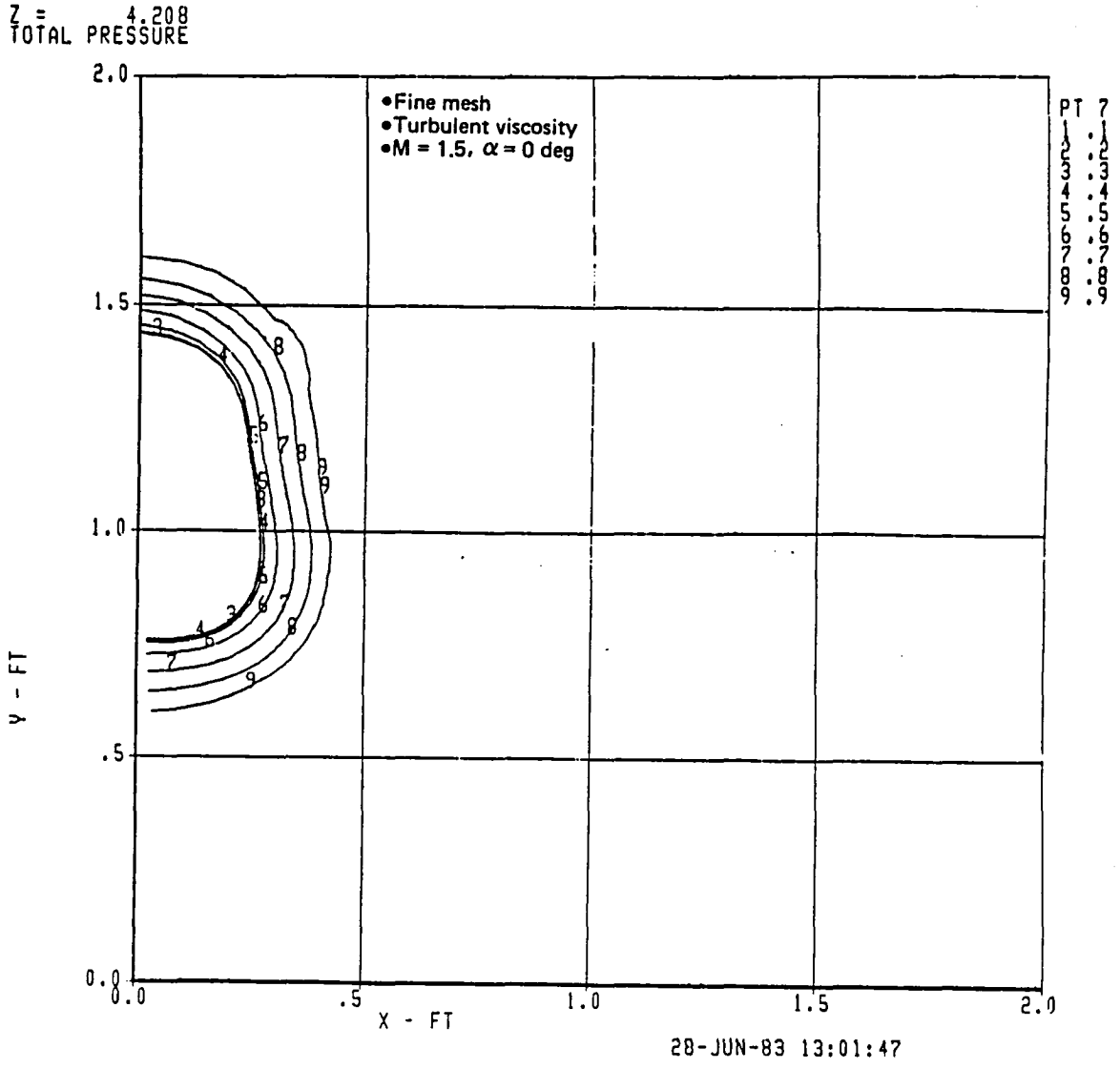

Figure 9. Total Pressure Distribution, Using Fine Computational Mesh

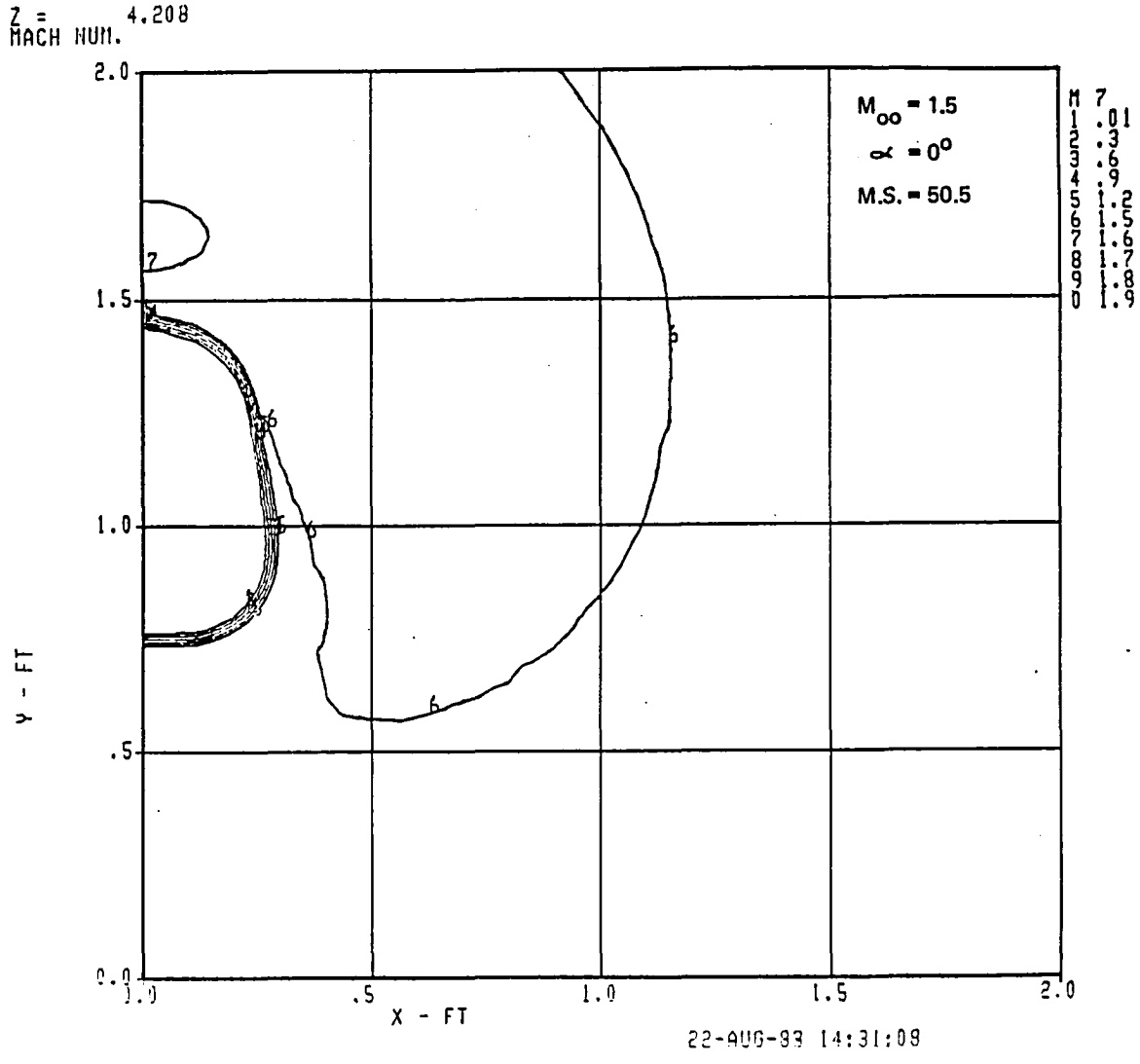

Figure 10(a). Mach Contours

Figure 10. Computed Results for Model Station 50.5, Mach 1.5, at 0-deg Angle of Attack

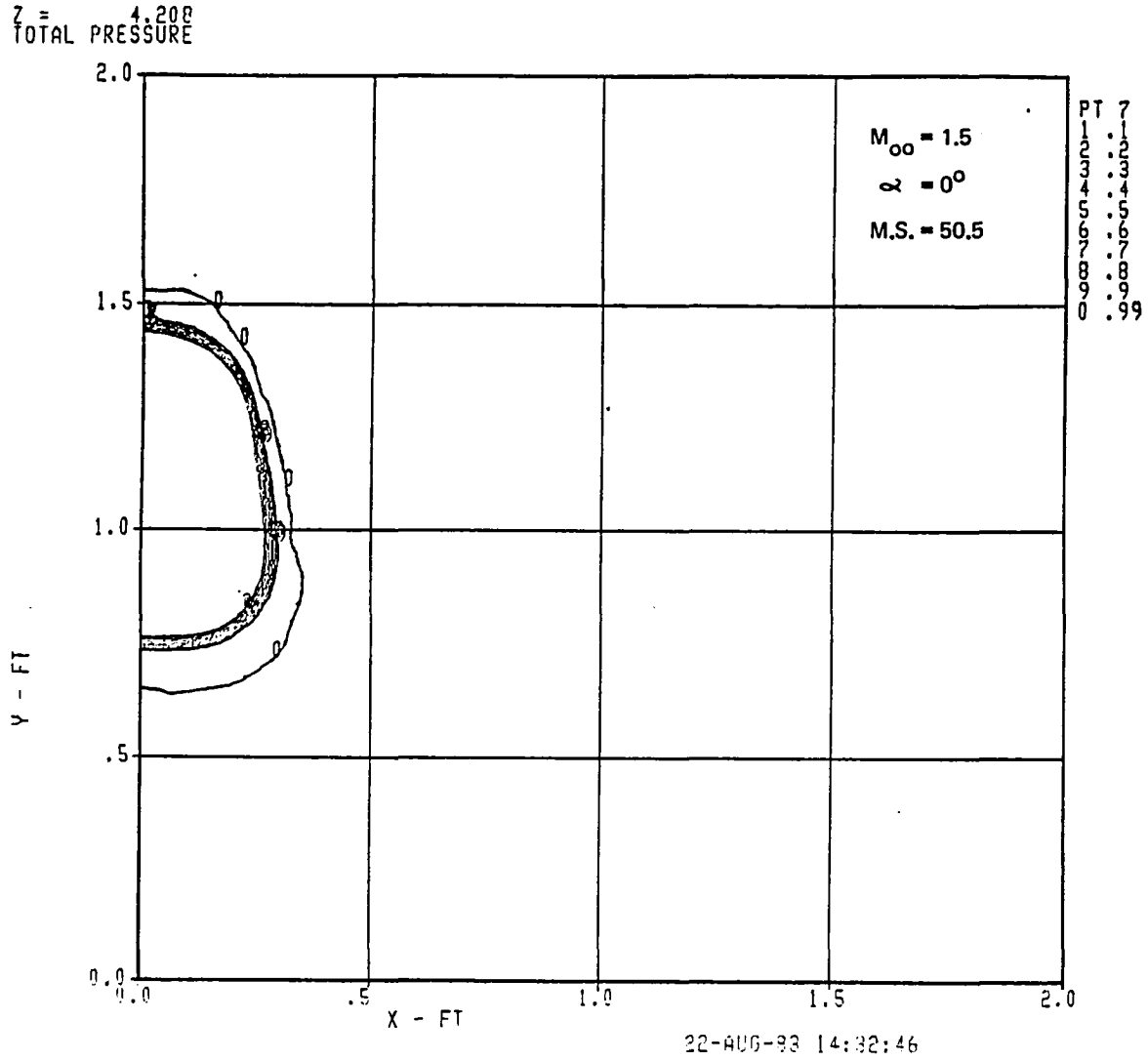

Figure 10(b). Total Pressure Contours

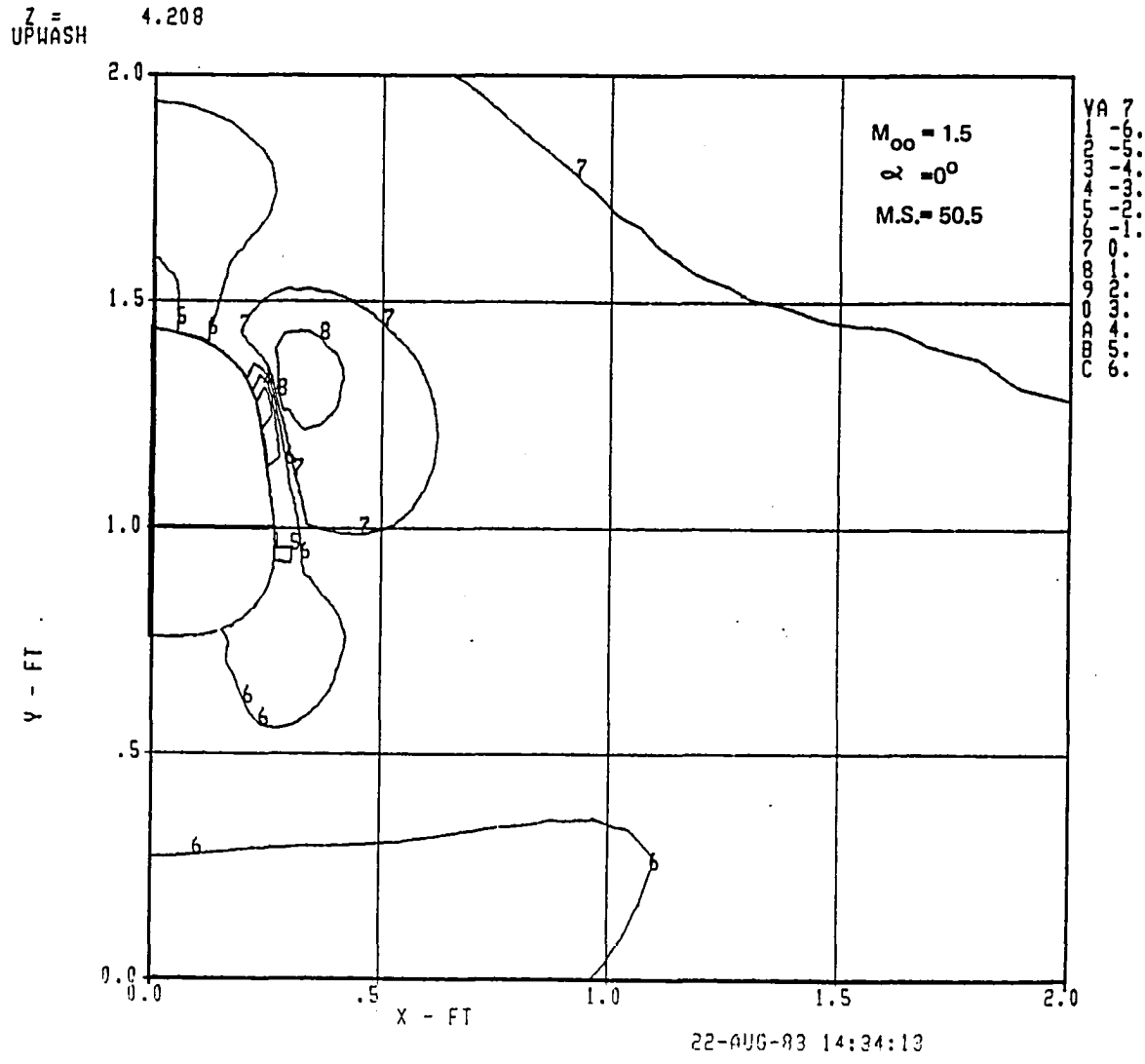

Figure 10(c). Upwash Angle Contours

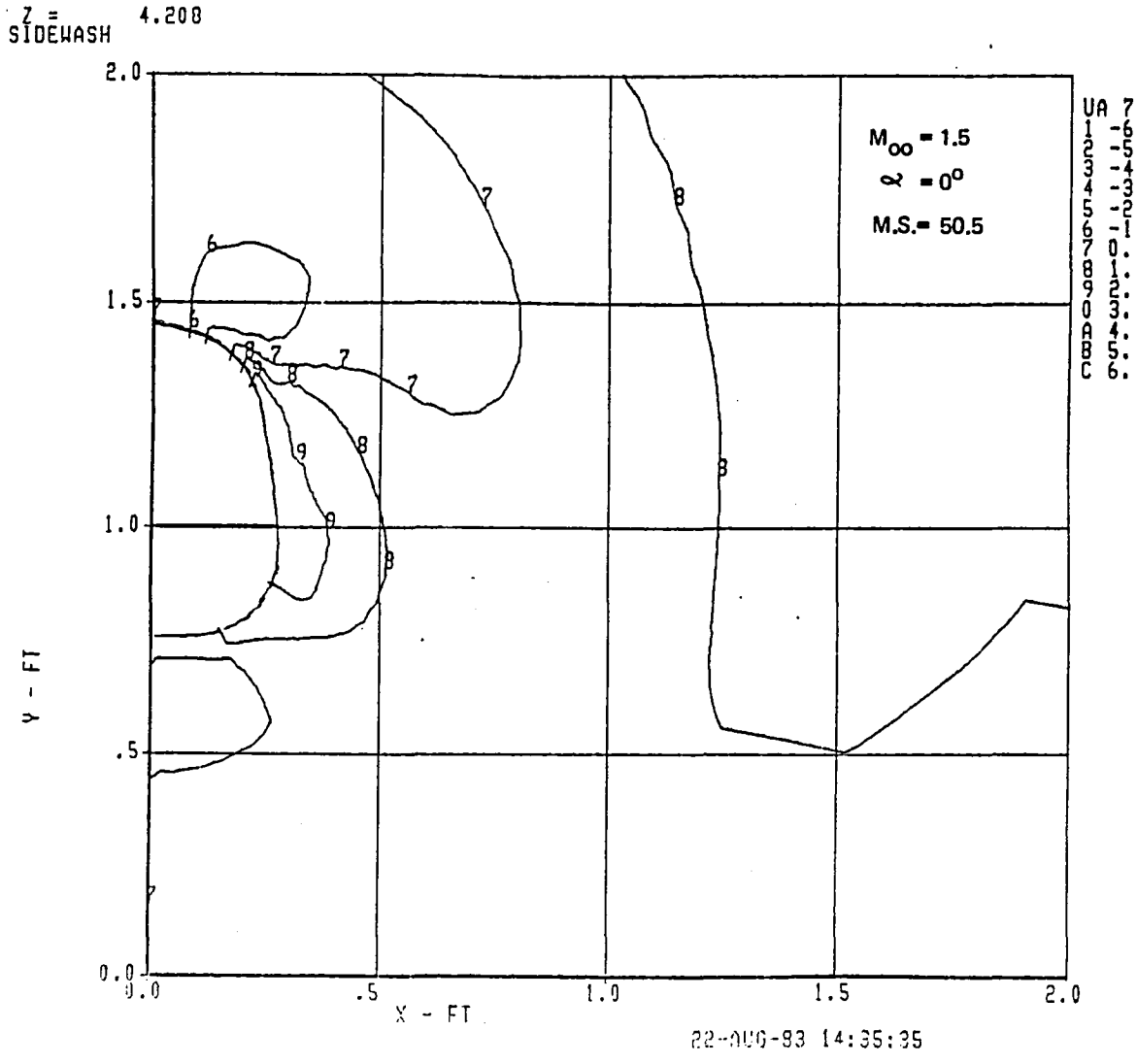

Figure 10(d). Sidewash Angle Contours

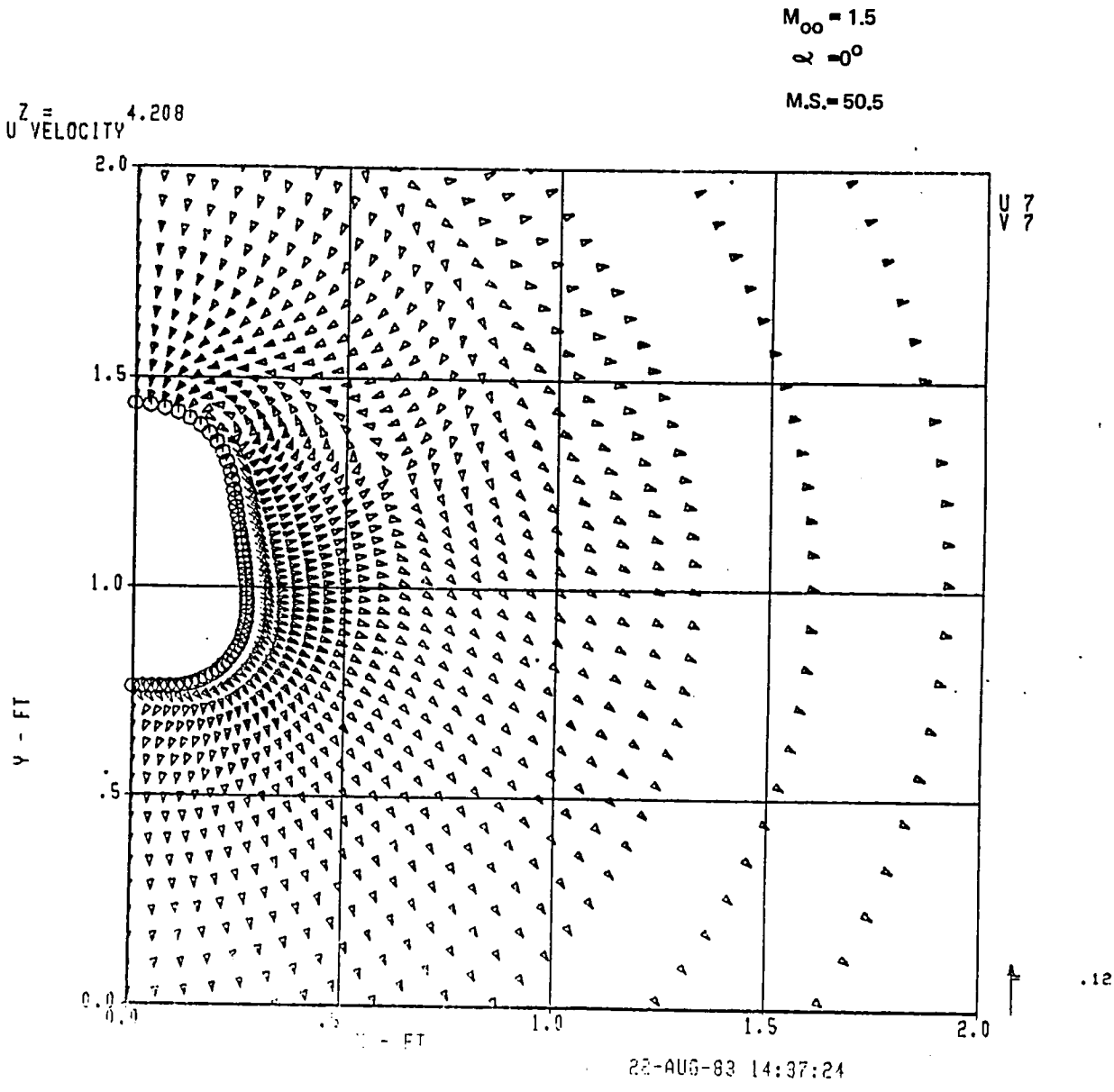

Figure 10(e). Cross-Plane Velocity

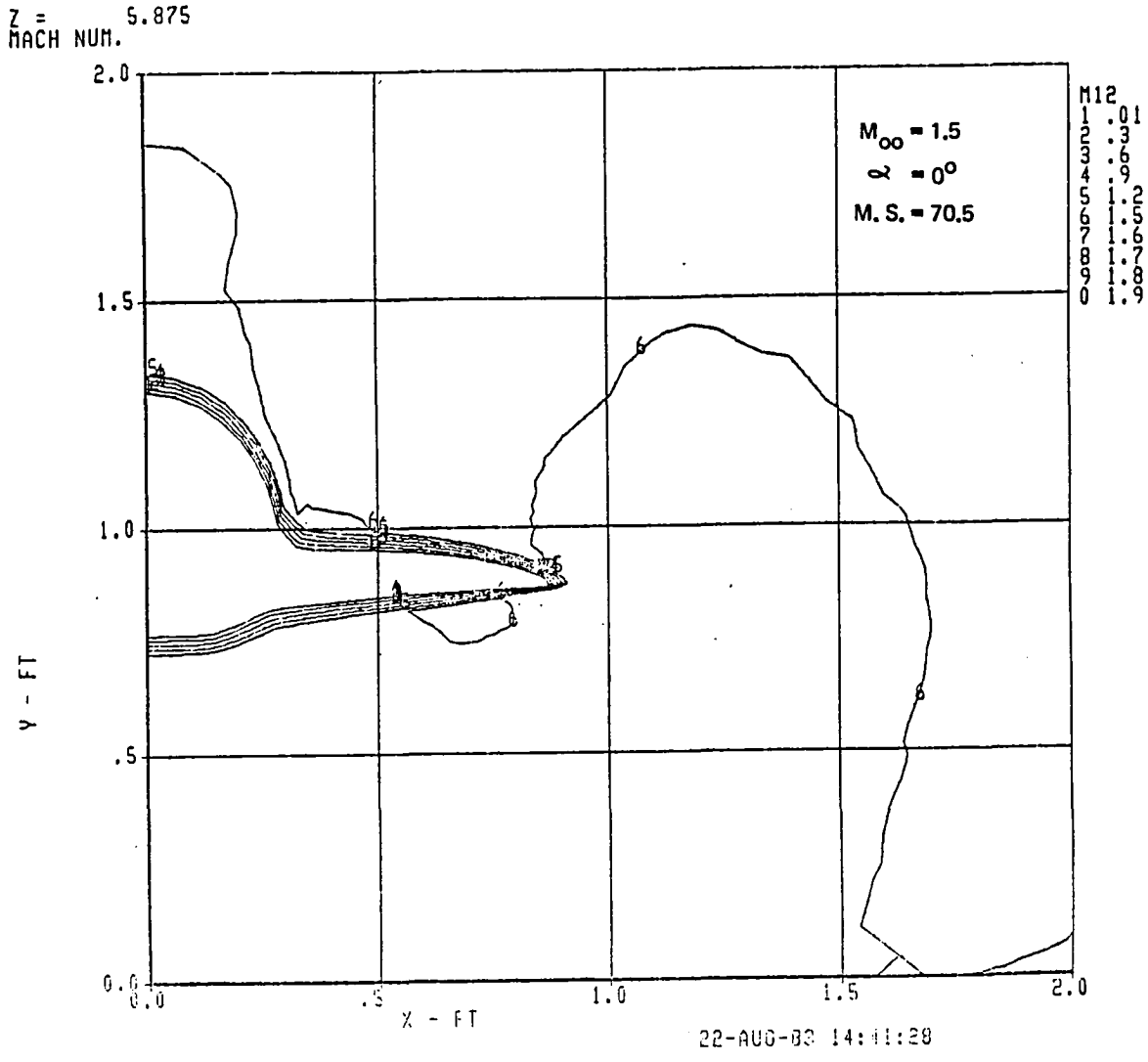

Figure 11(a). Mach Contours

Figure 11. Computed Results for Model Station 70.5, Mach 1.5, at 0-deg Angle of Attack

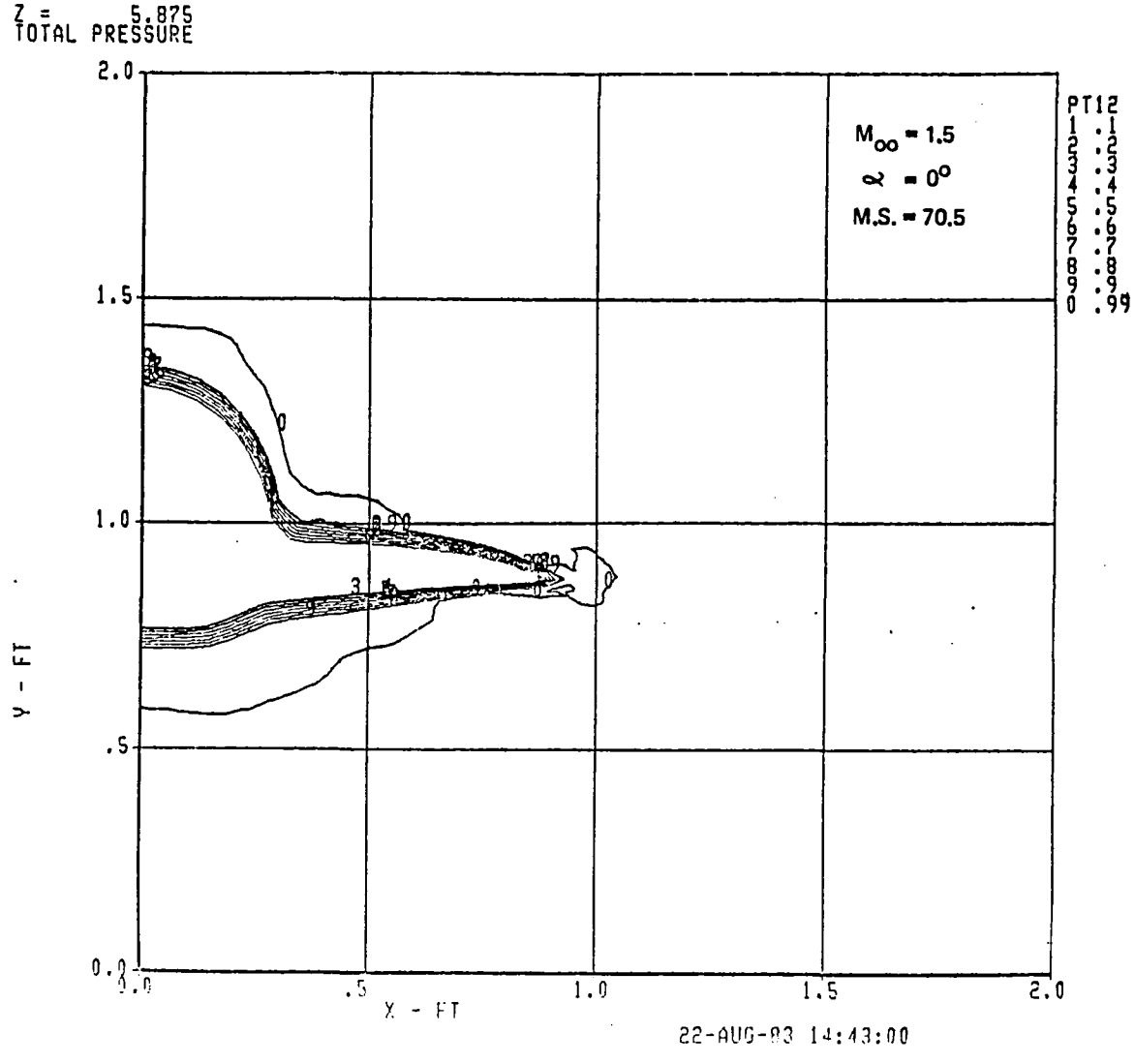

Figure 11(b). Total Pressure Contours

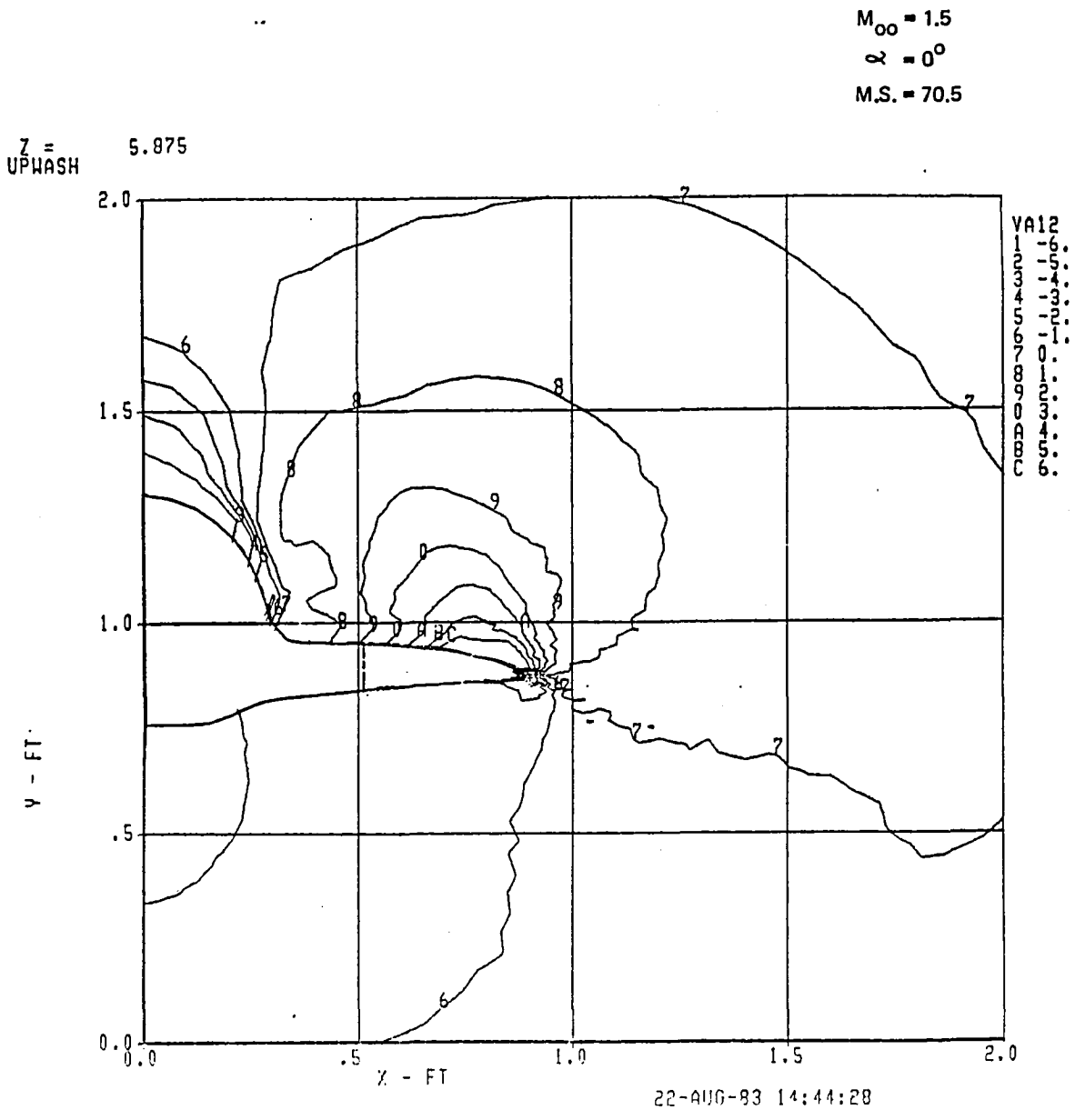

Figure 11(c). Upwash Angle Contours

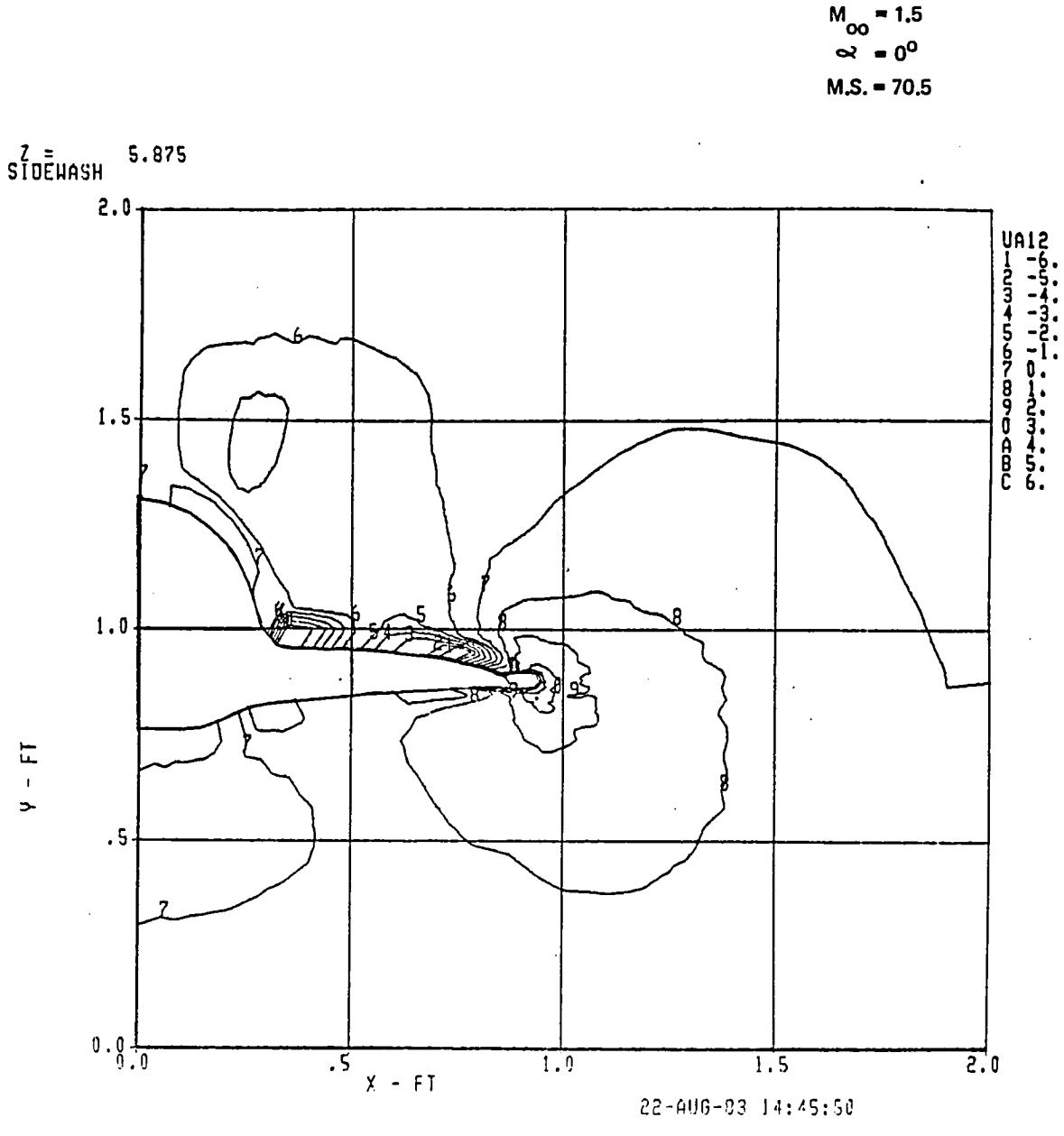

Figure 11(d). Sidewash Angle Contours

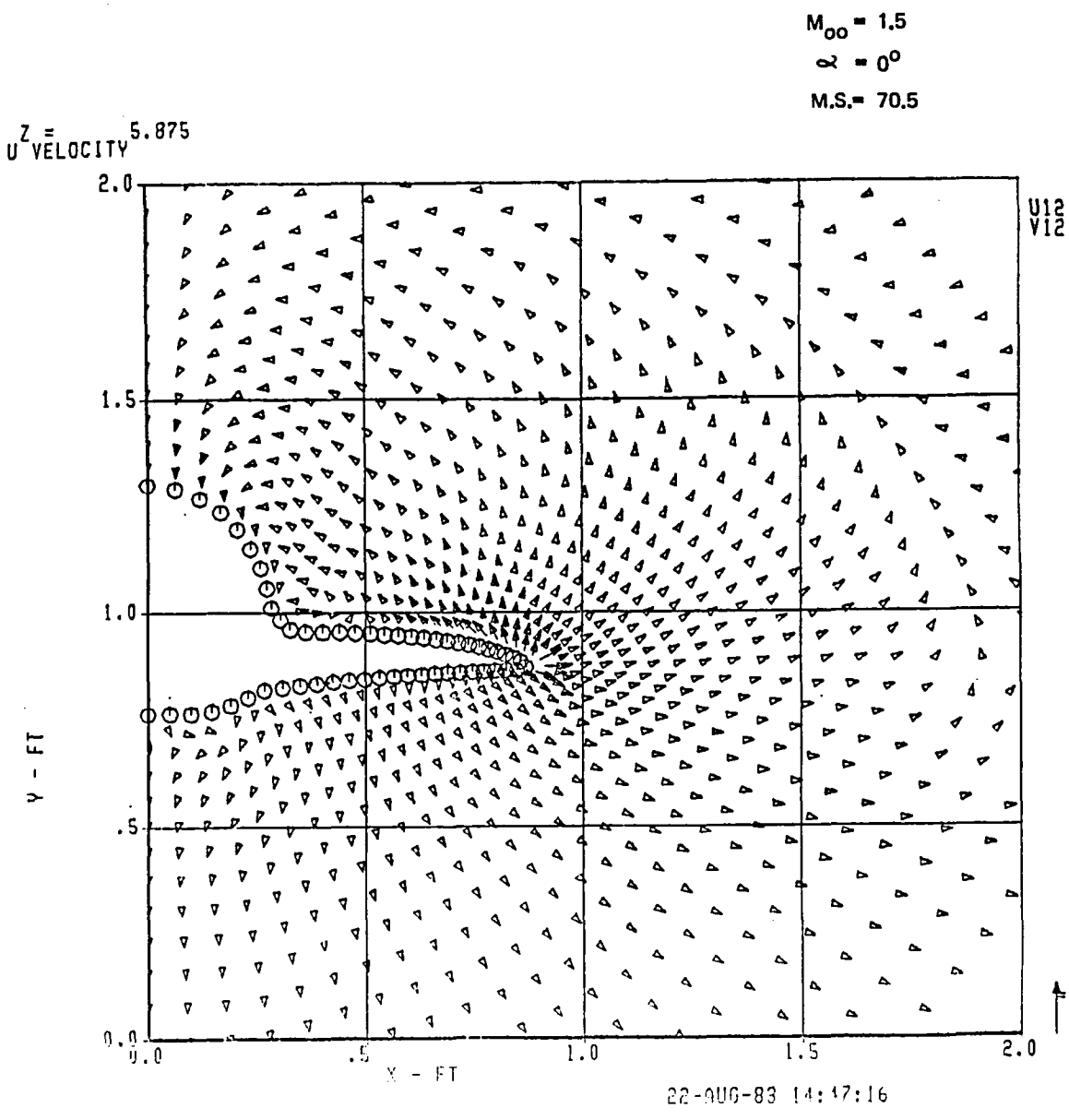

Figure 11(e). Cross-Plane Velocity

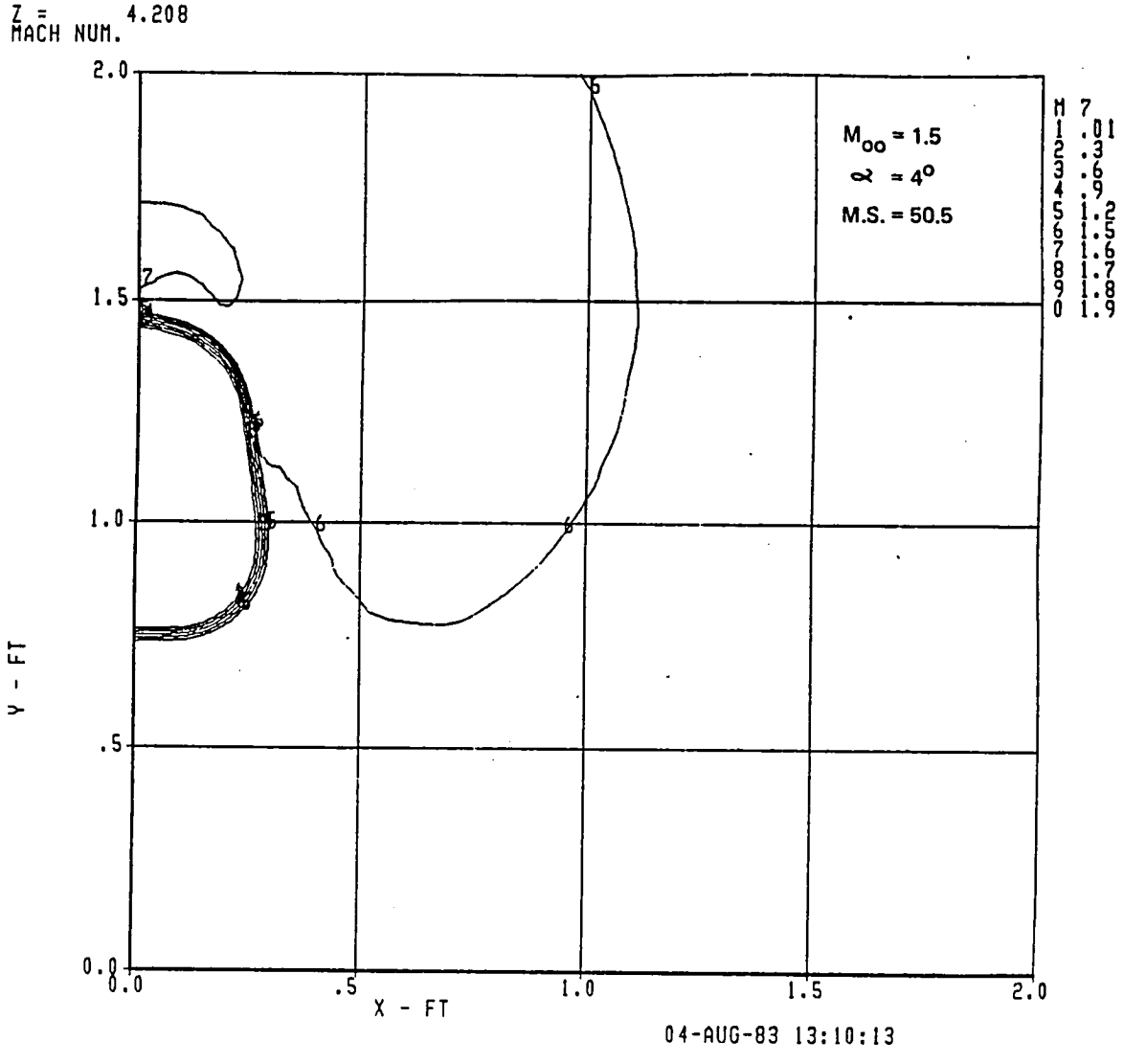

Figure 12(a). Mach Contours

Figure 12. Computed Results for Model Station 50.5, Mach 1.5, at 4-deg Angle of Attack

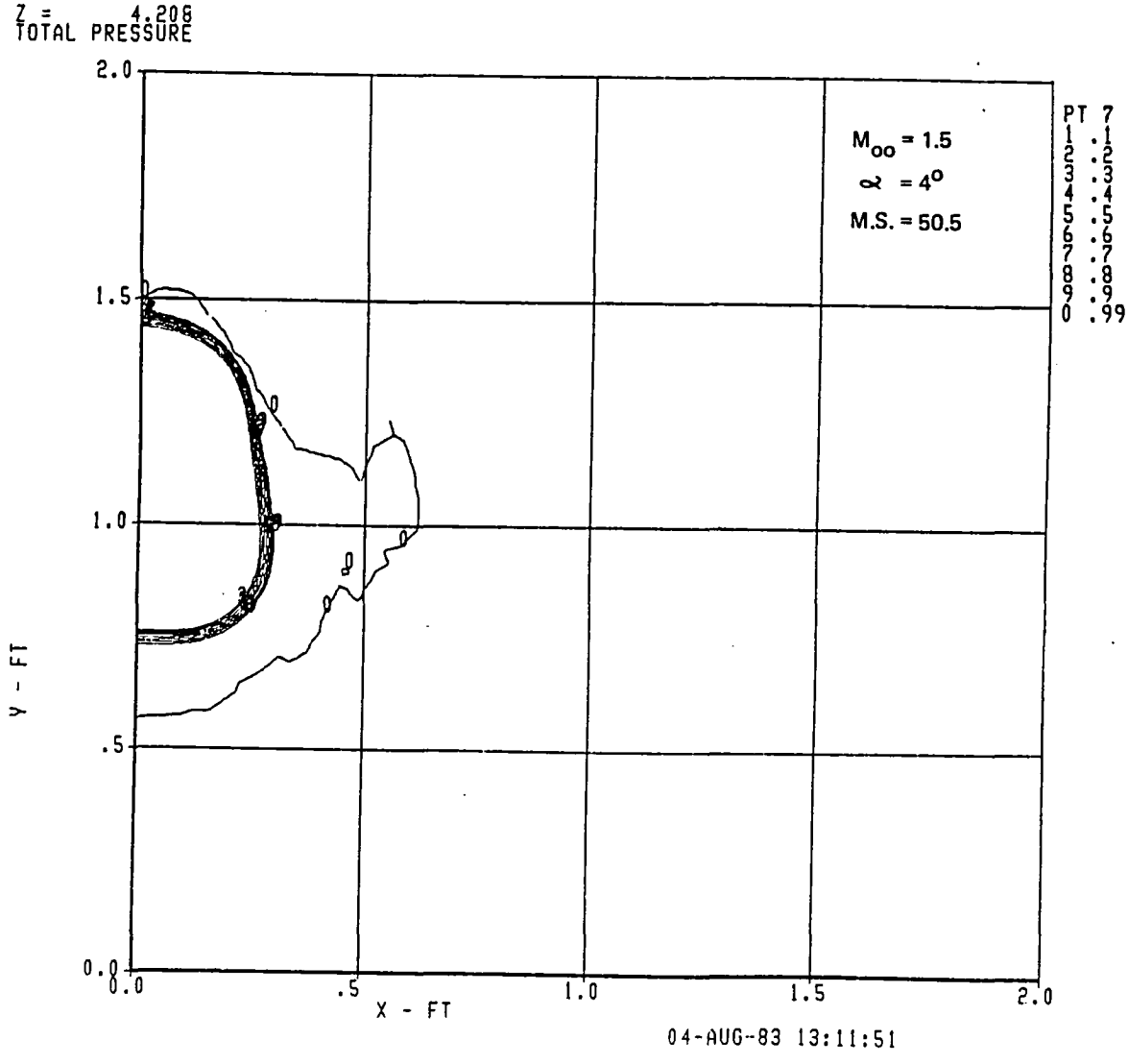

Figure 12(b). Total Pressure Contours

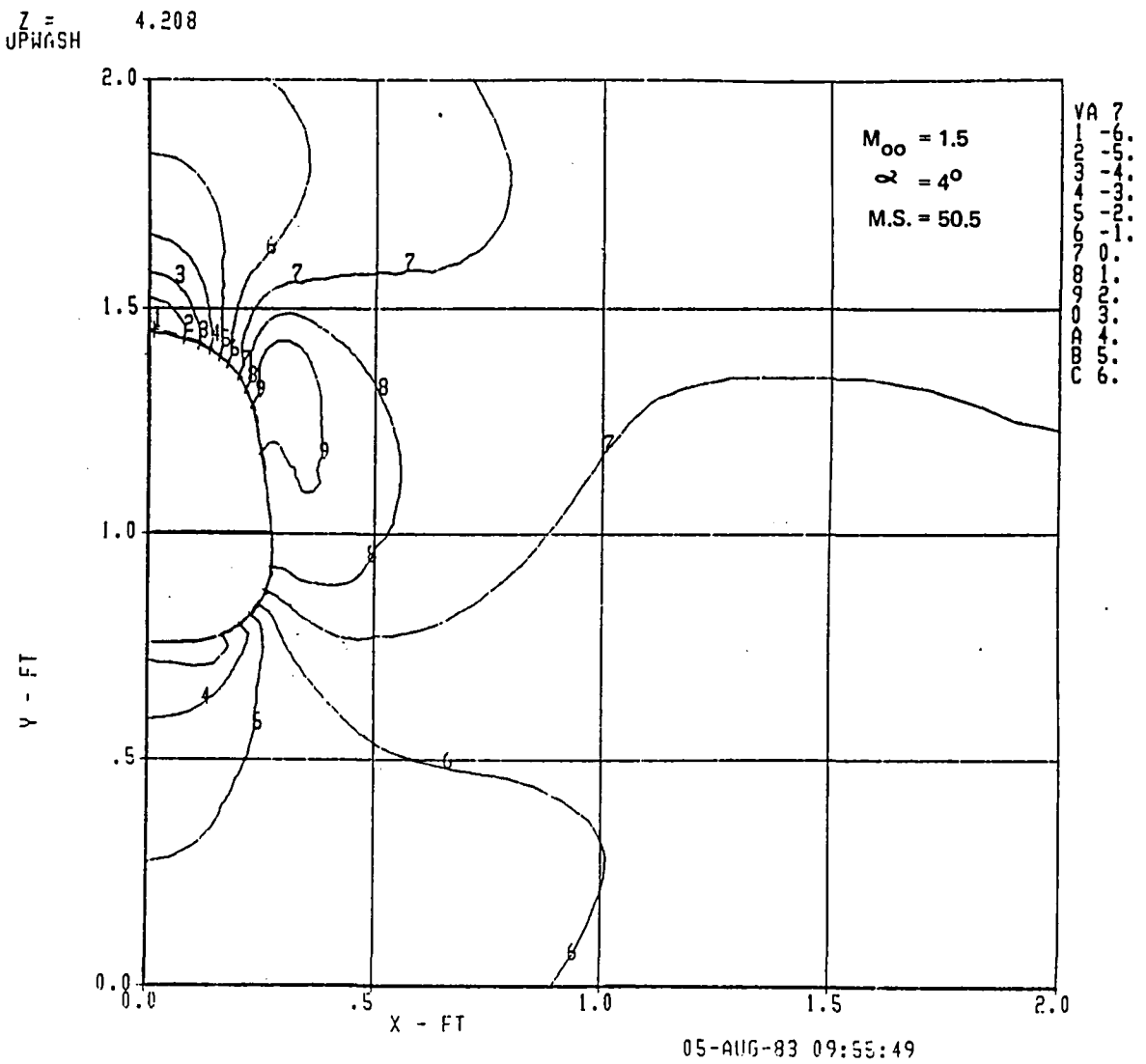

Figure 12(c). Upwash Angle Contours

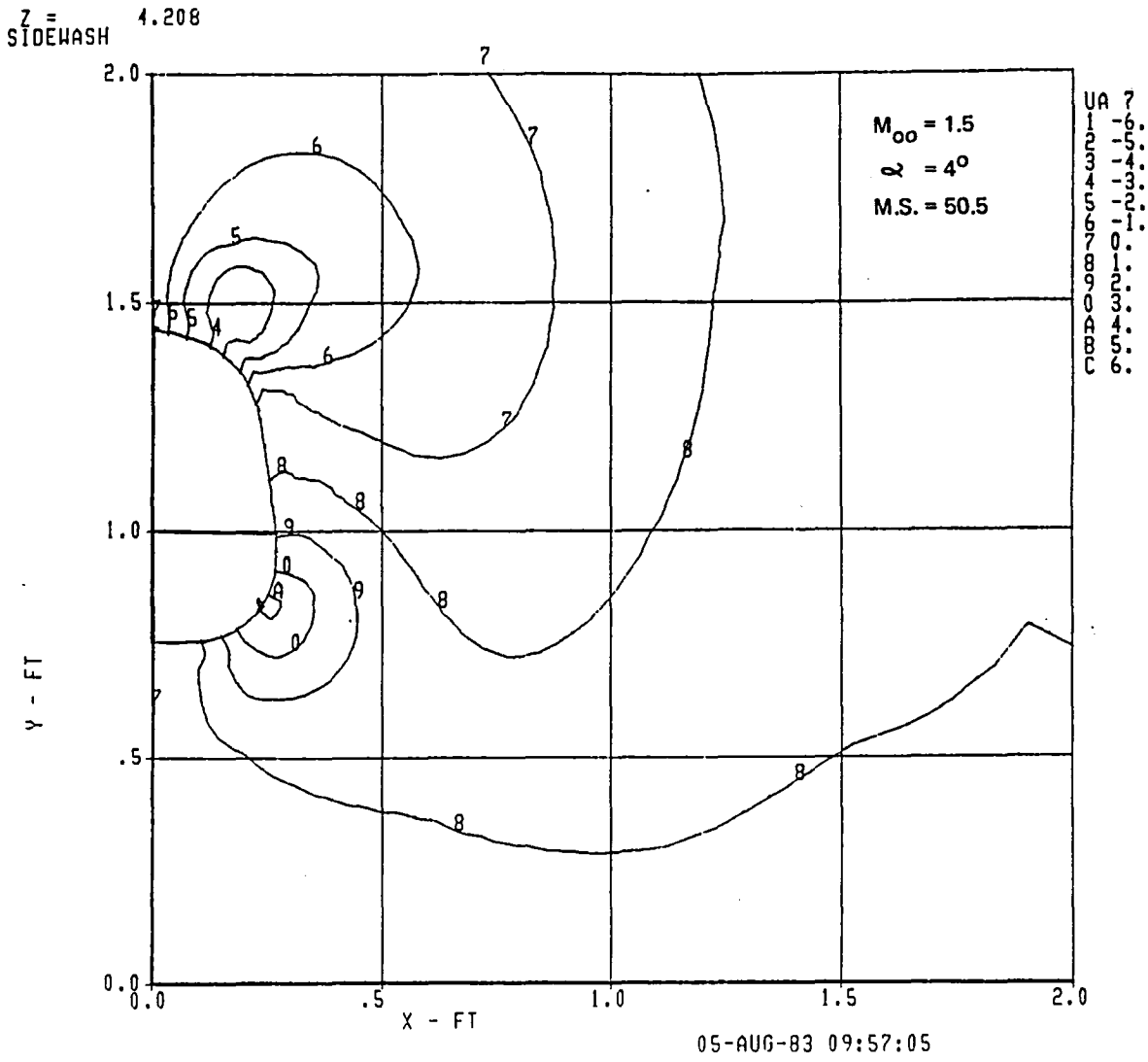

Figure 12(d). Sidewash Angle Contours

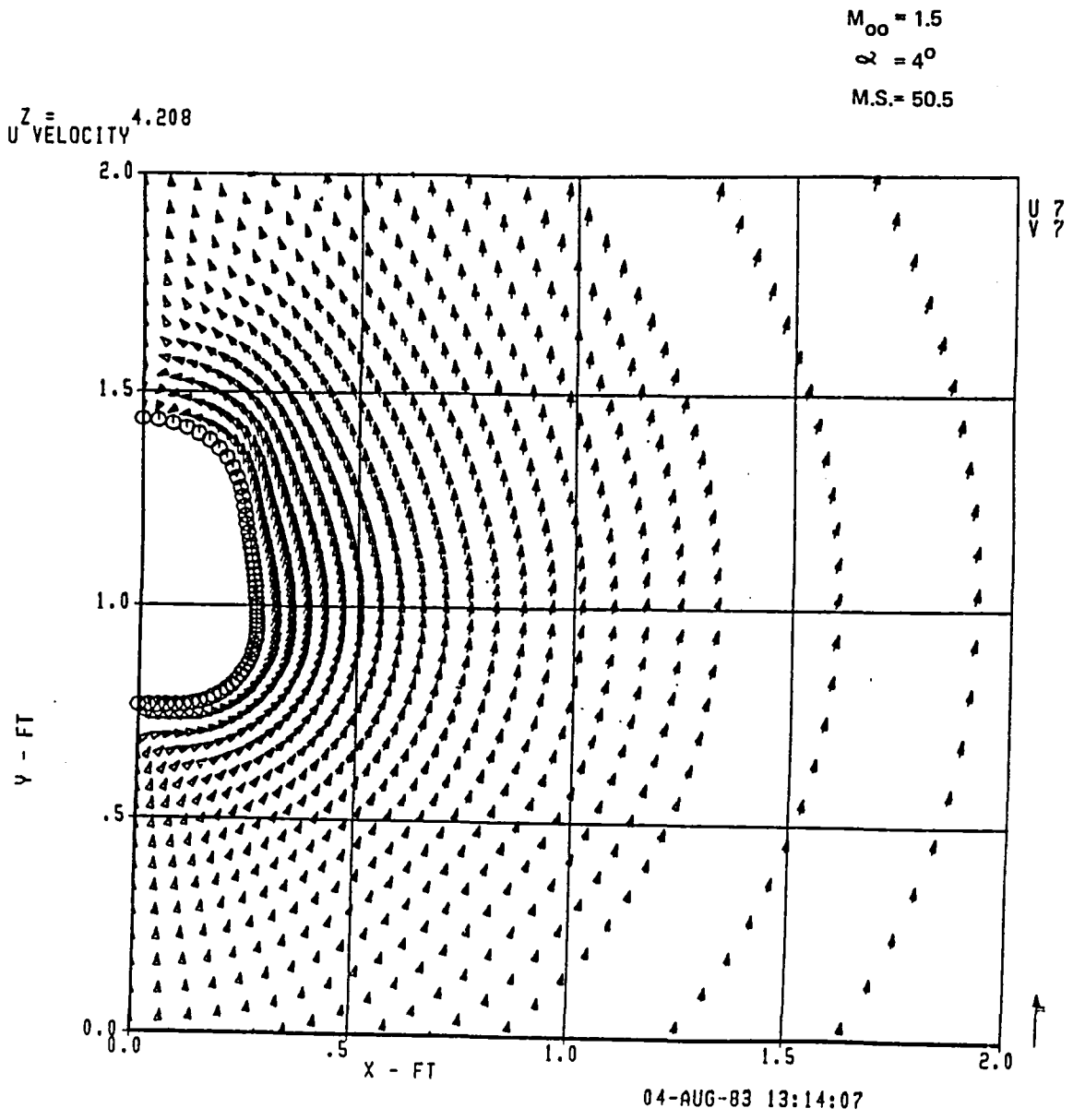

Figure 12(e). Cross-Plane Velocity

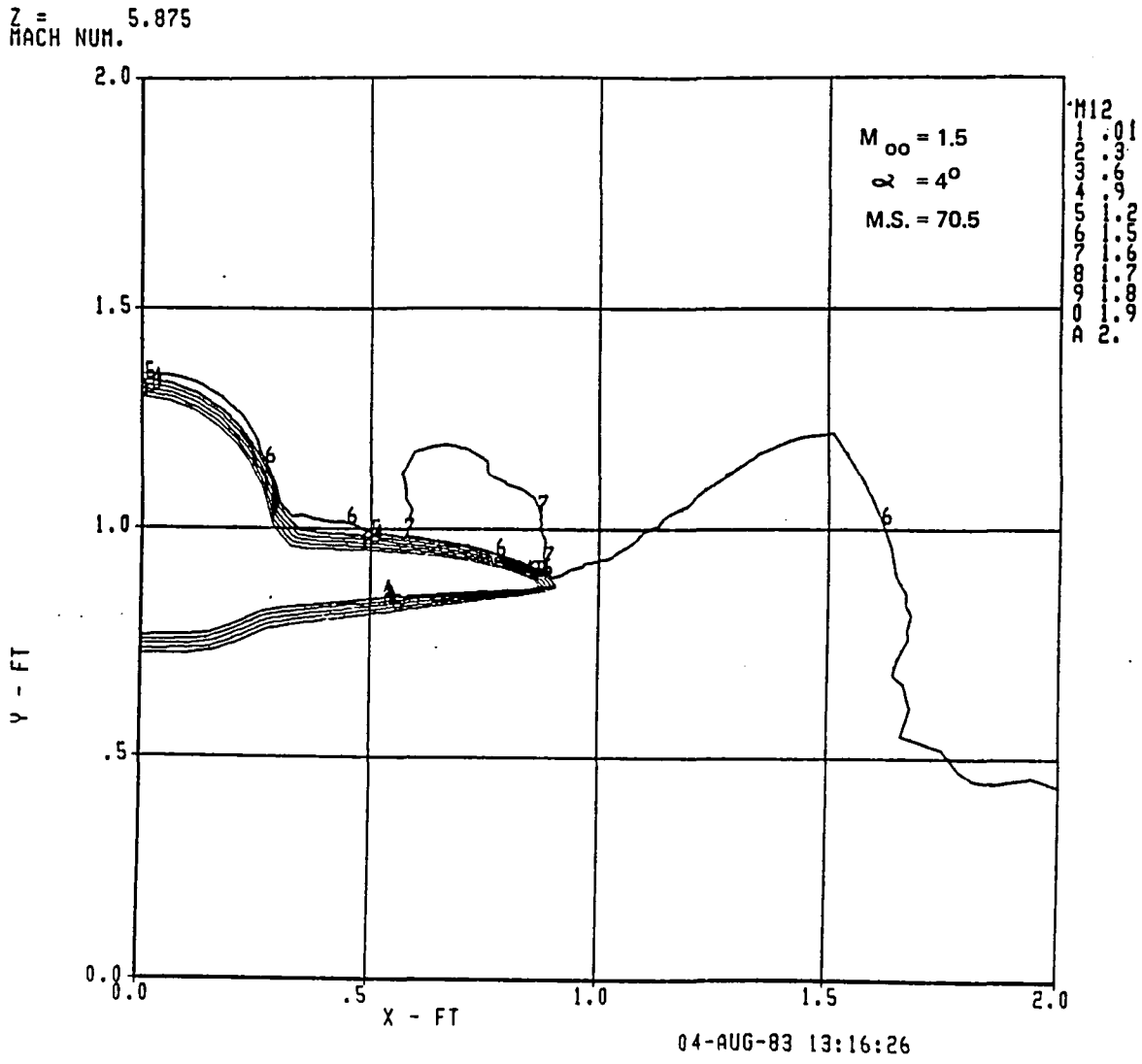

Figure 13(a). Mach Contours

Figure 13. Computed Results for Model Station 70.5, Mach 1.5, at 4-deg Angle of Attack

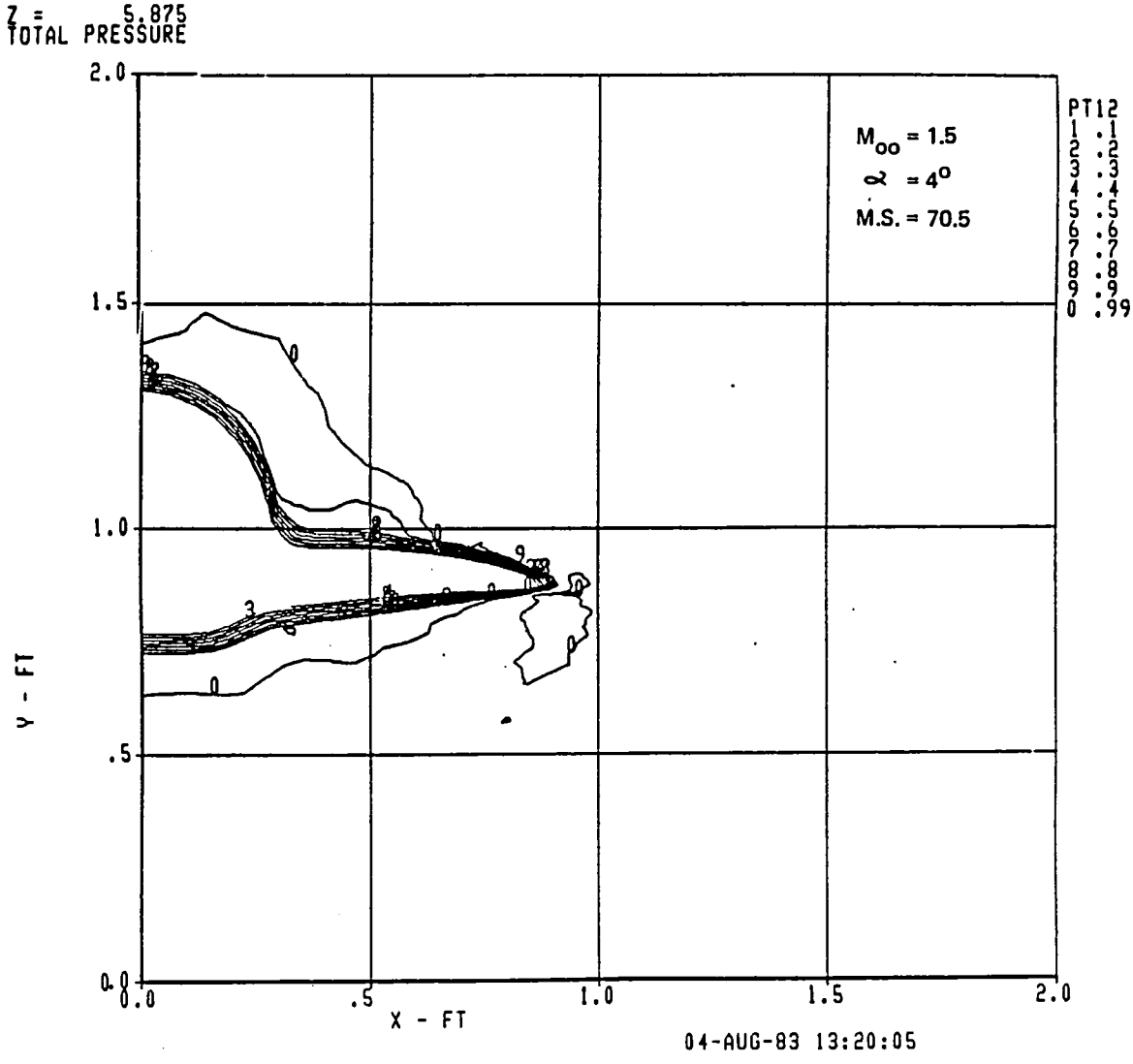

Figure 13(b). Total Pressure Contours

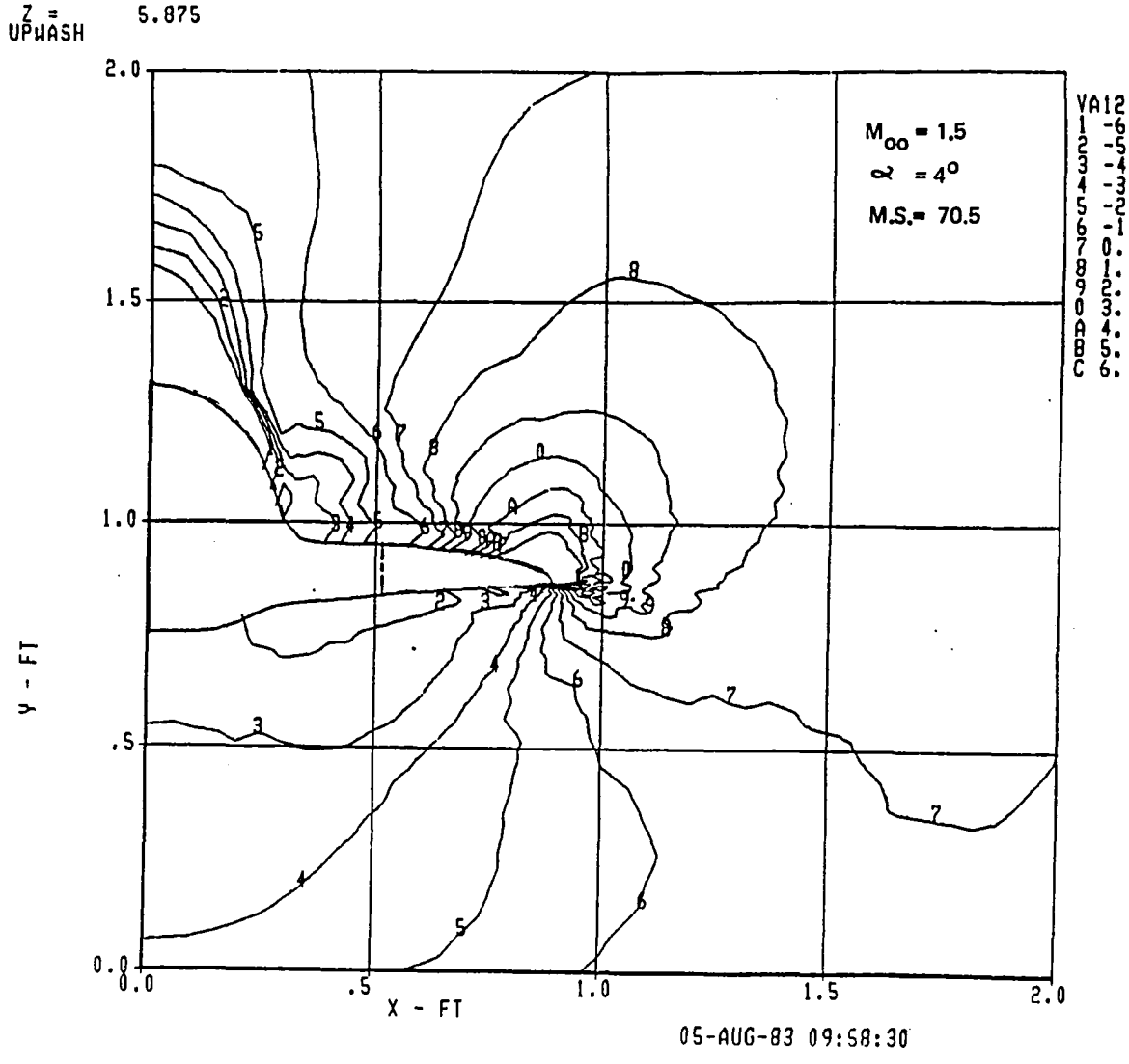

Figure 13(c). Upwash Angle Contours

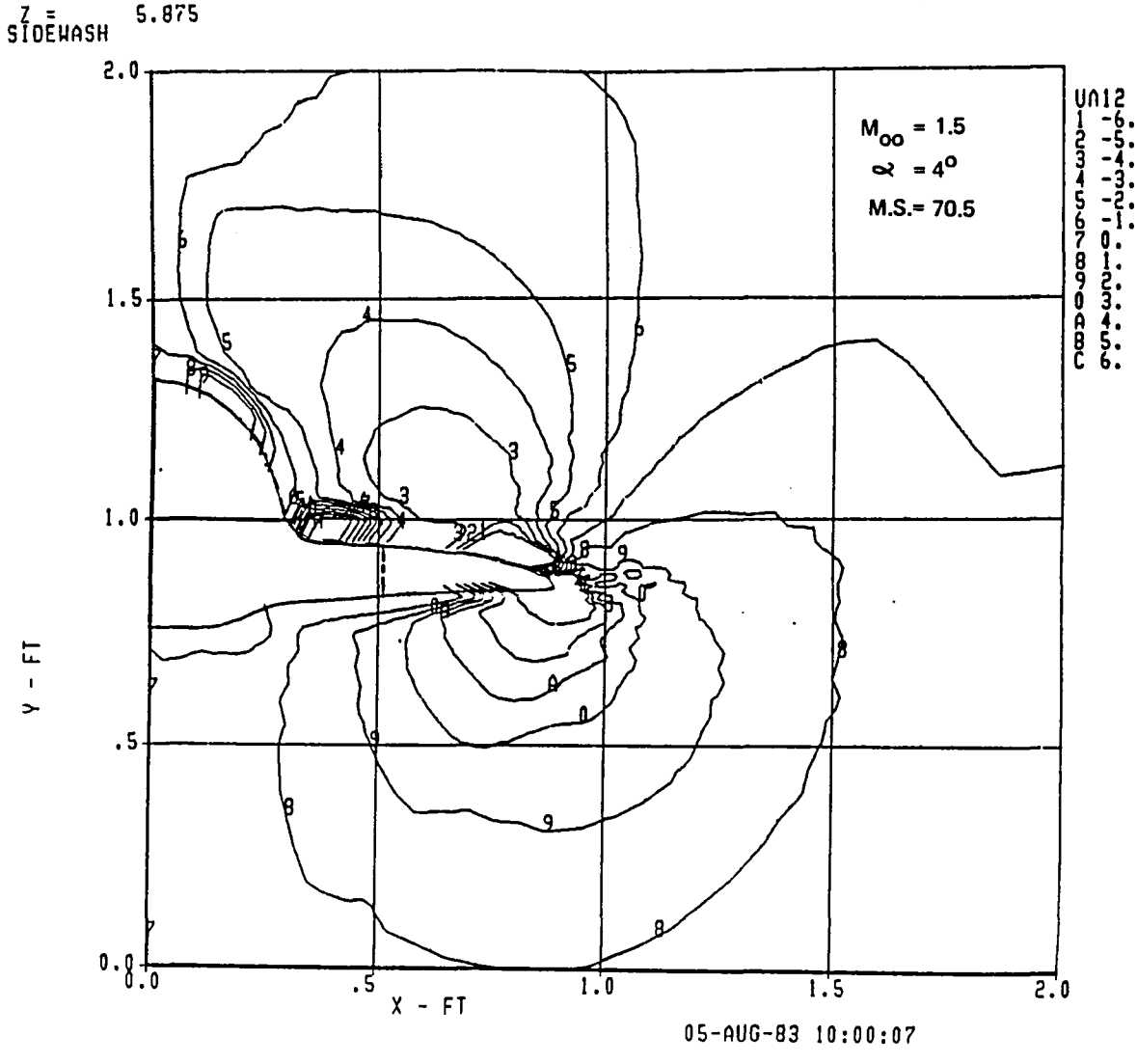

Figure 13(d). Sidewash Angle Contours

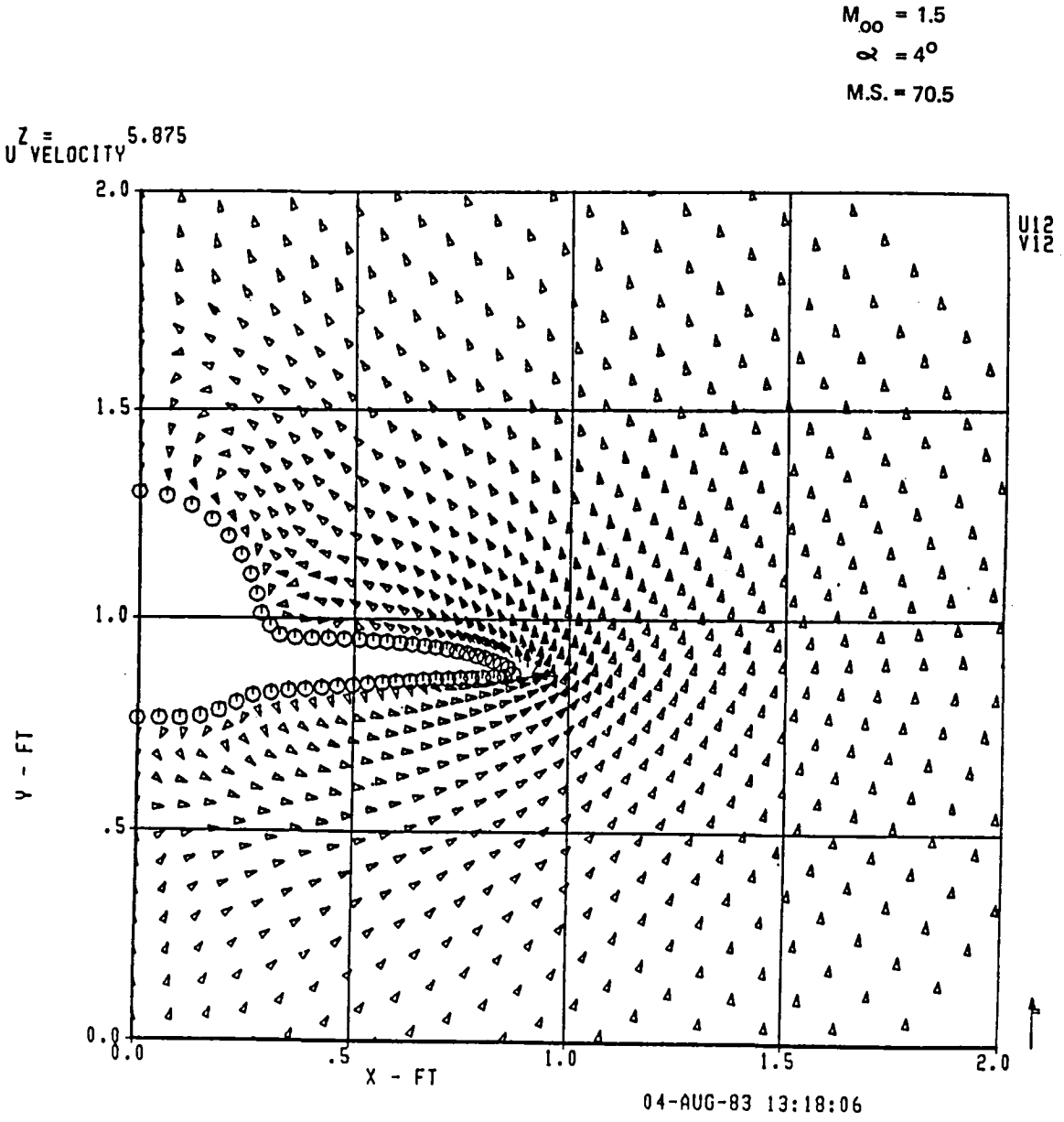

Figure 13(e). Cross-Plane Velocity

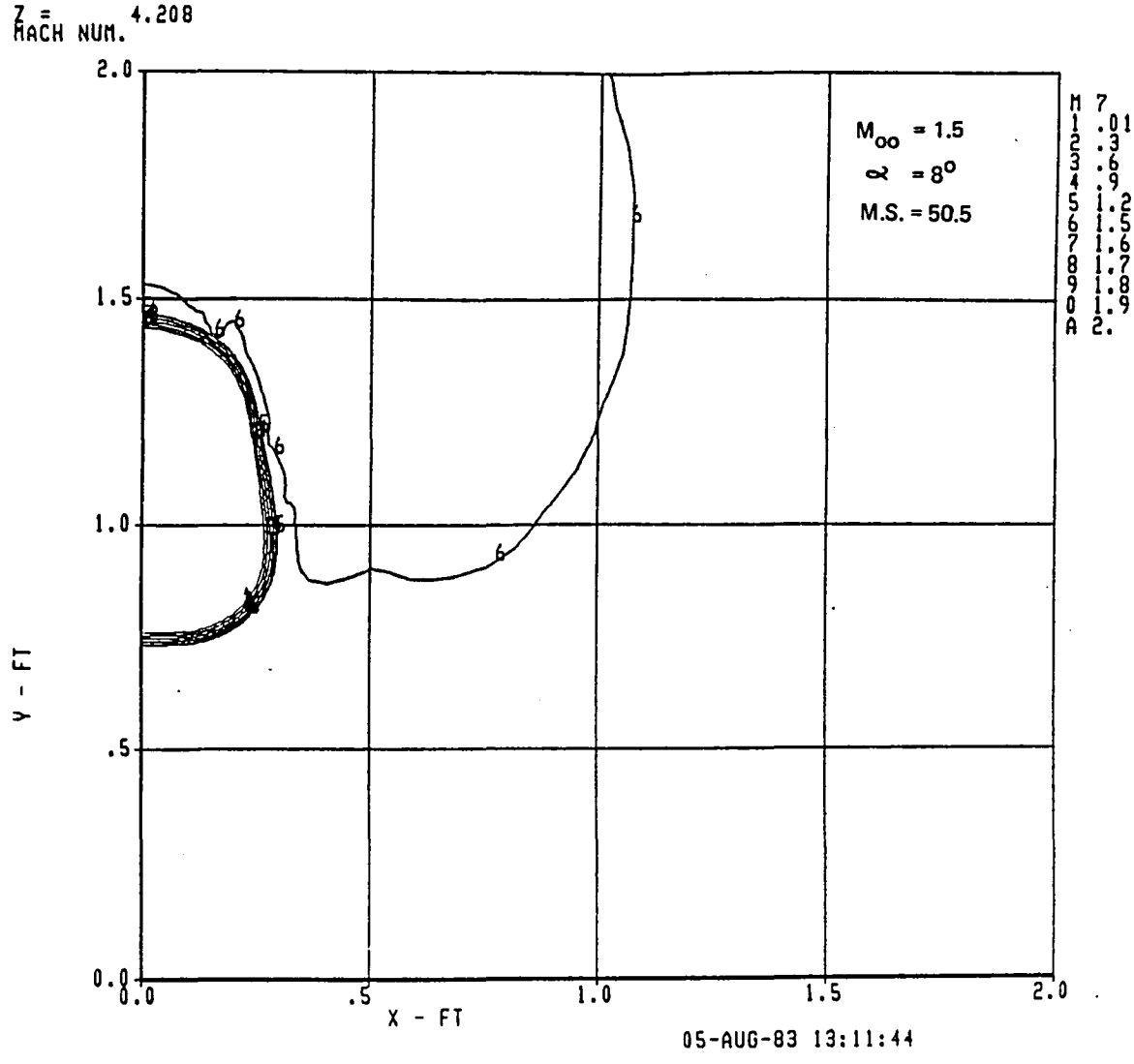

Figure 14(a). Mach Contours

Figure 14. Computed Results for Model Station 50.5, Mach 1.5, at 8-deg Angle of Attack

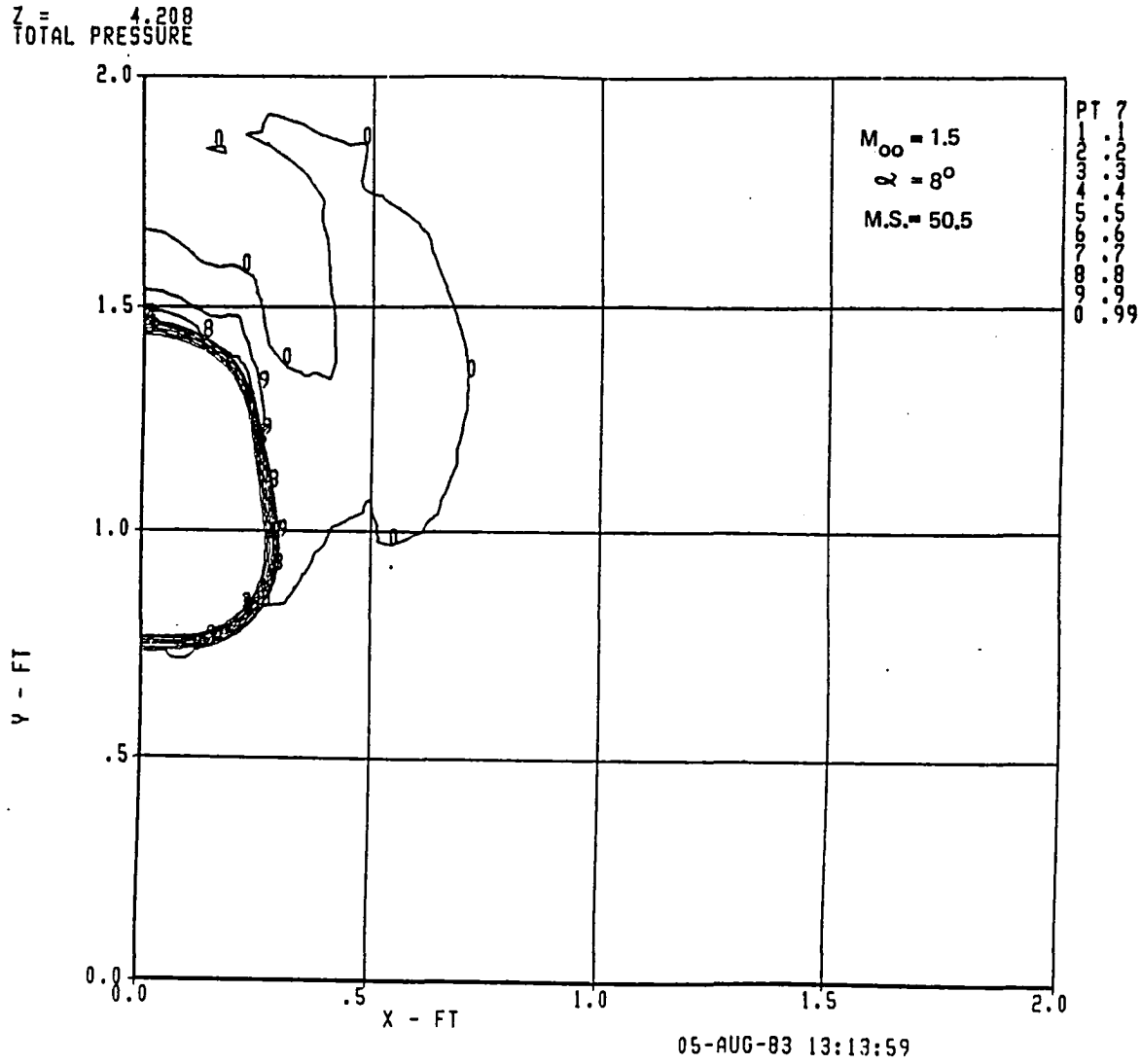

Figure 14(b). Total Pressure Contours

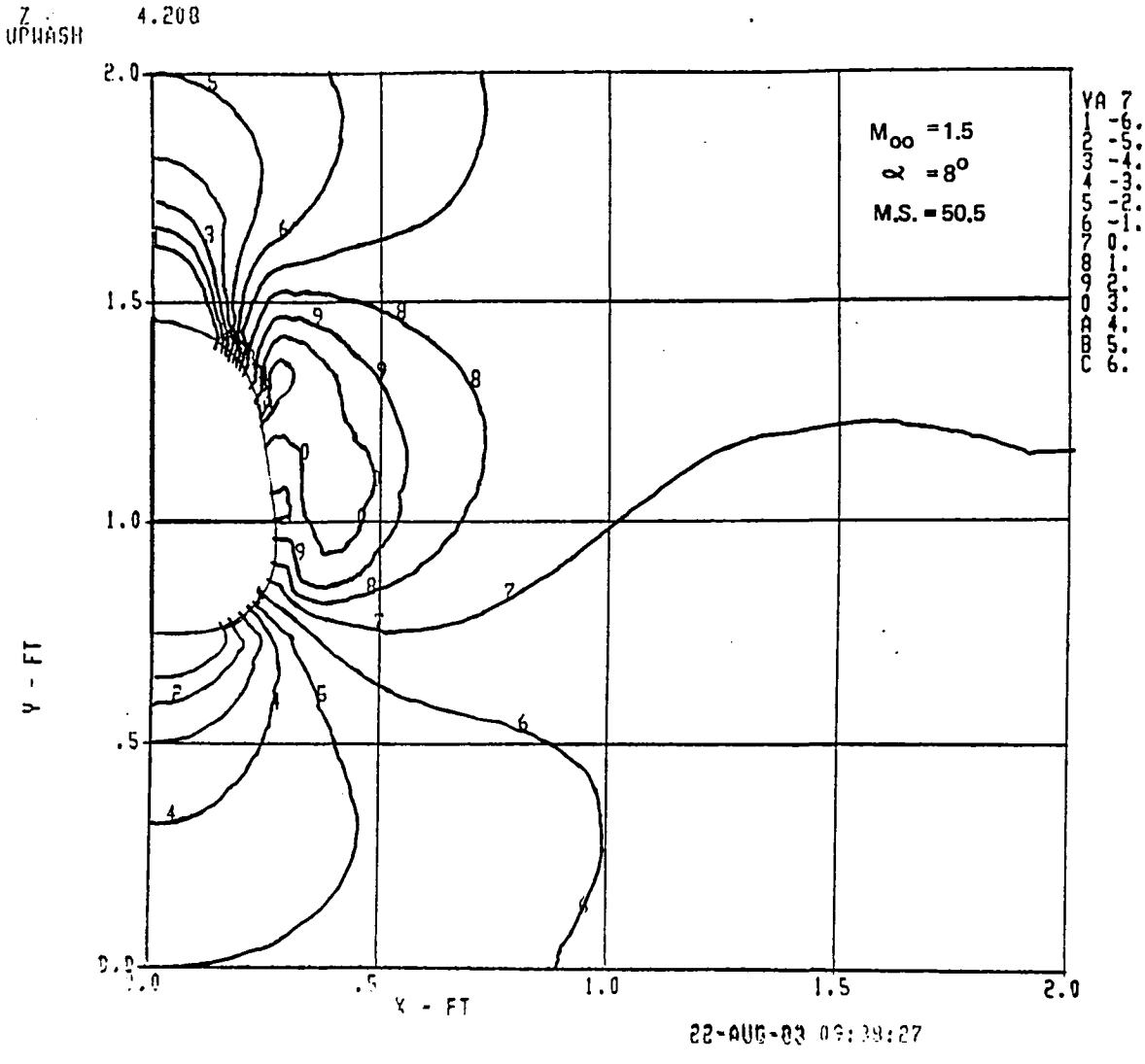

Figure 14(c). Upwash Angle Contours

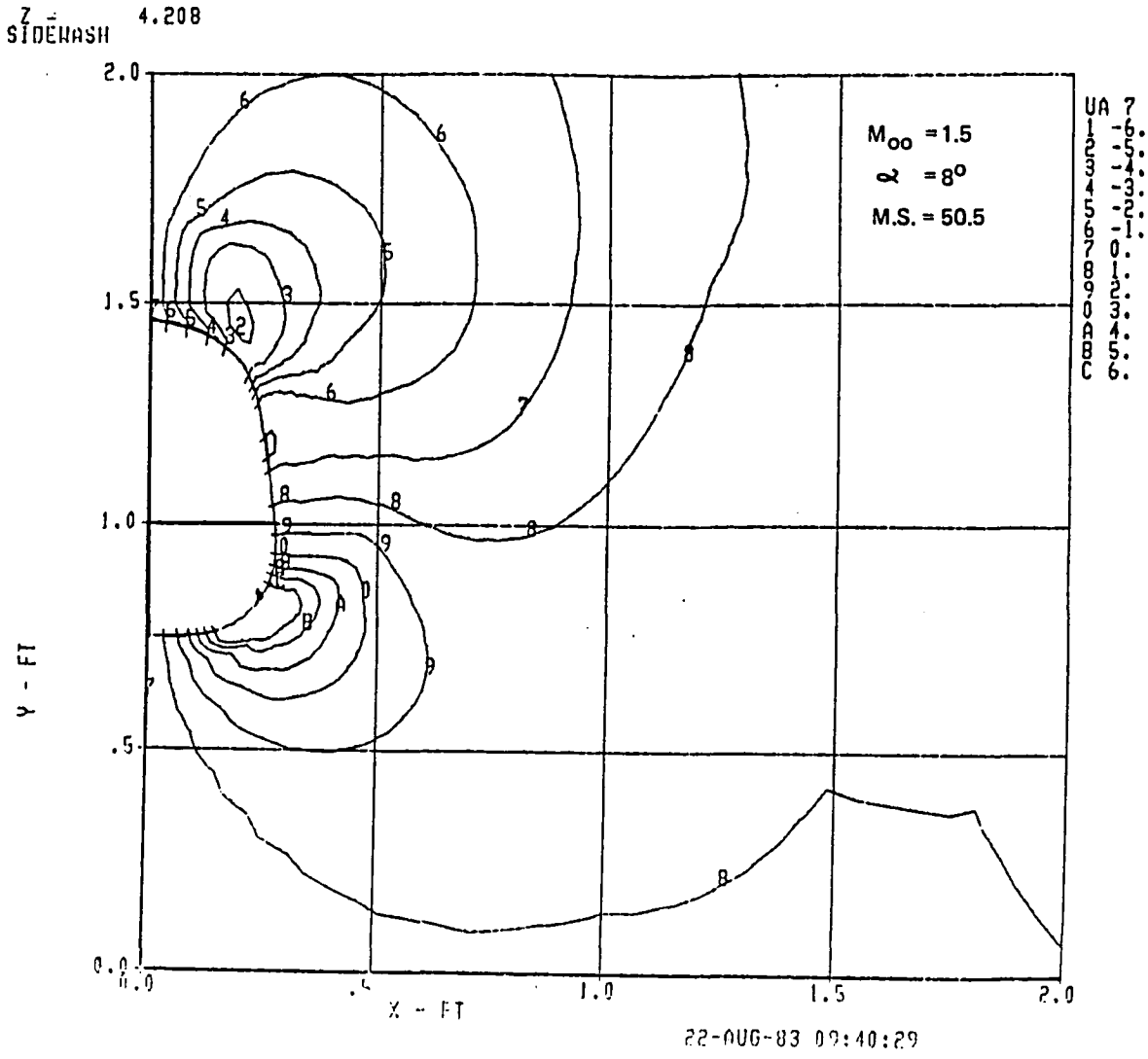

Figure 14(d). Sidewash Angle Contours

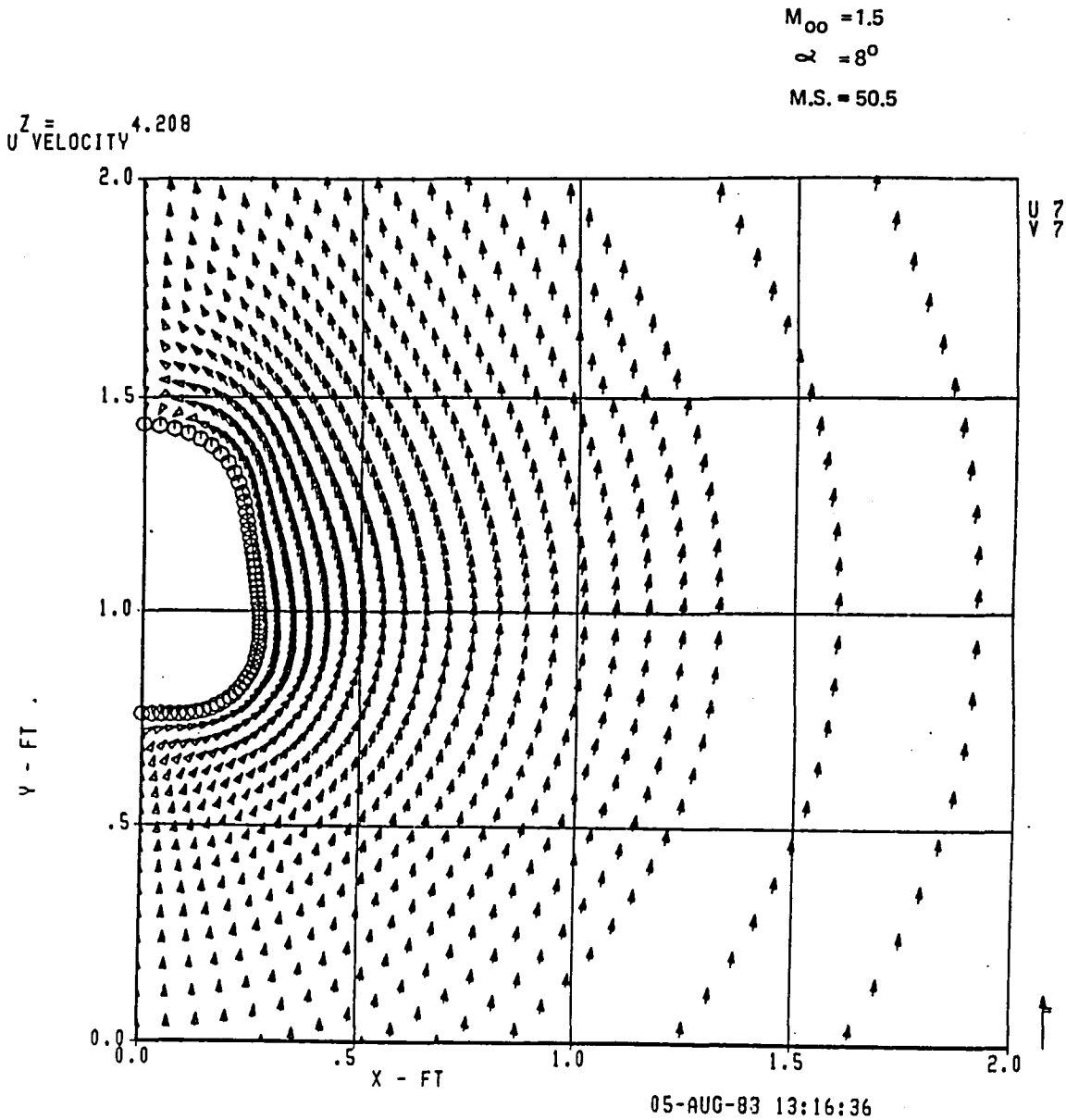

Figure 14(e). Cross-Plane Velocity

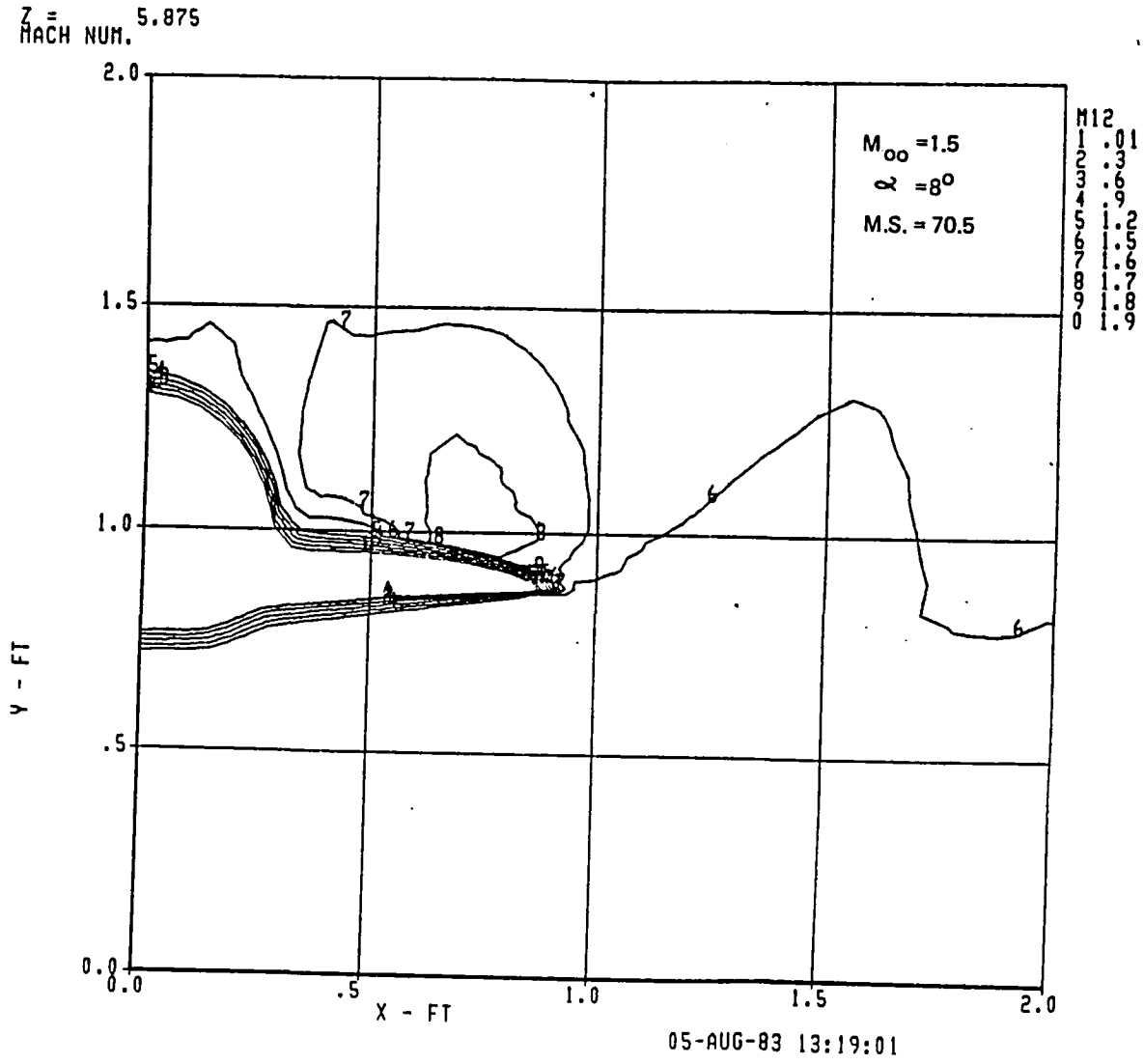

Figure 15(a). Mach Contours

Figure 15. Computed Results for Model Station 70.5, Mach 1.5, at 8-deg Angle of Attack

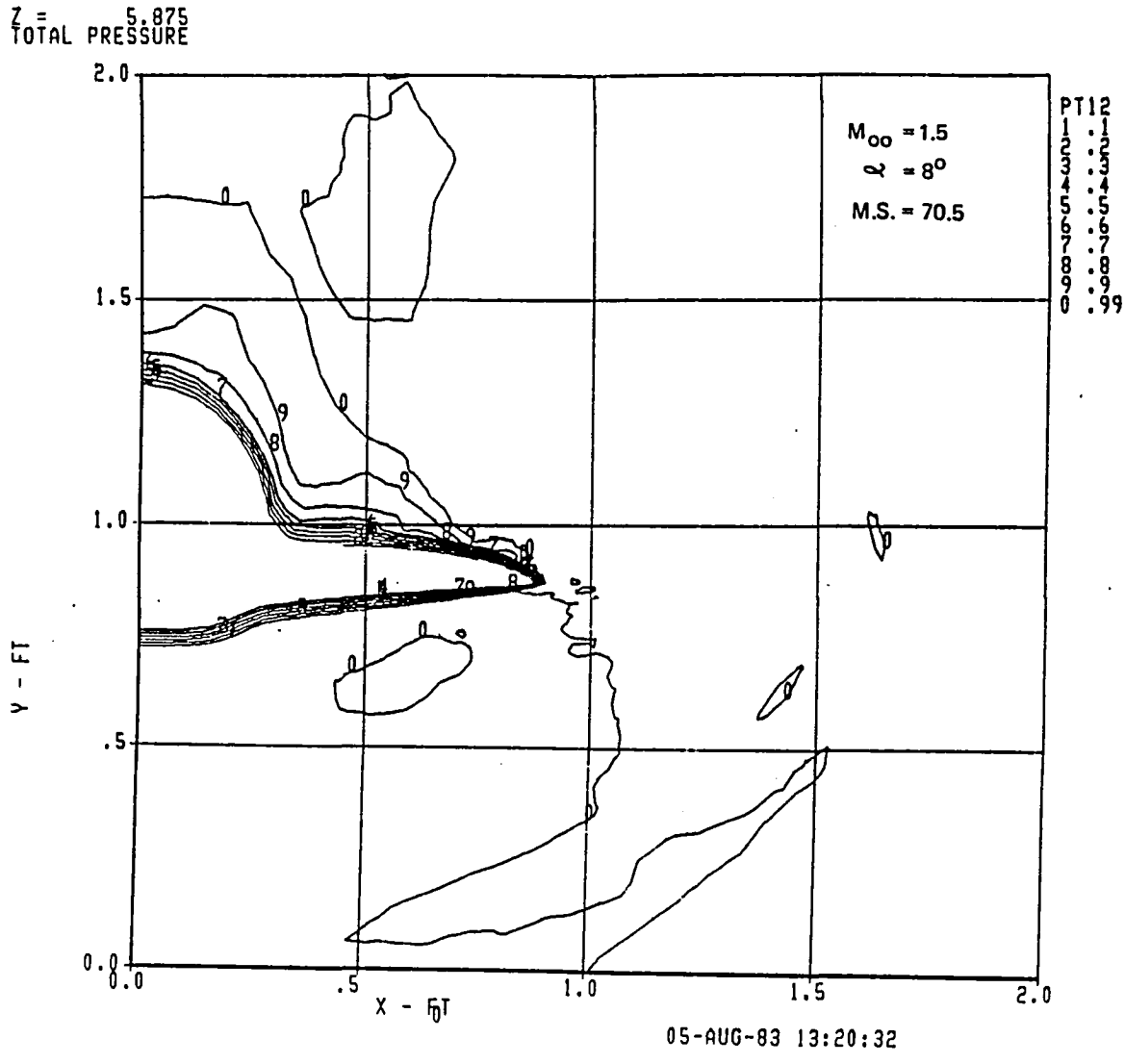

Figure 15(b). Total Pressure Contours

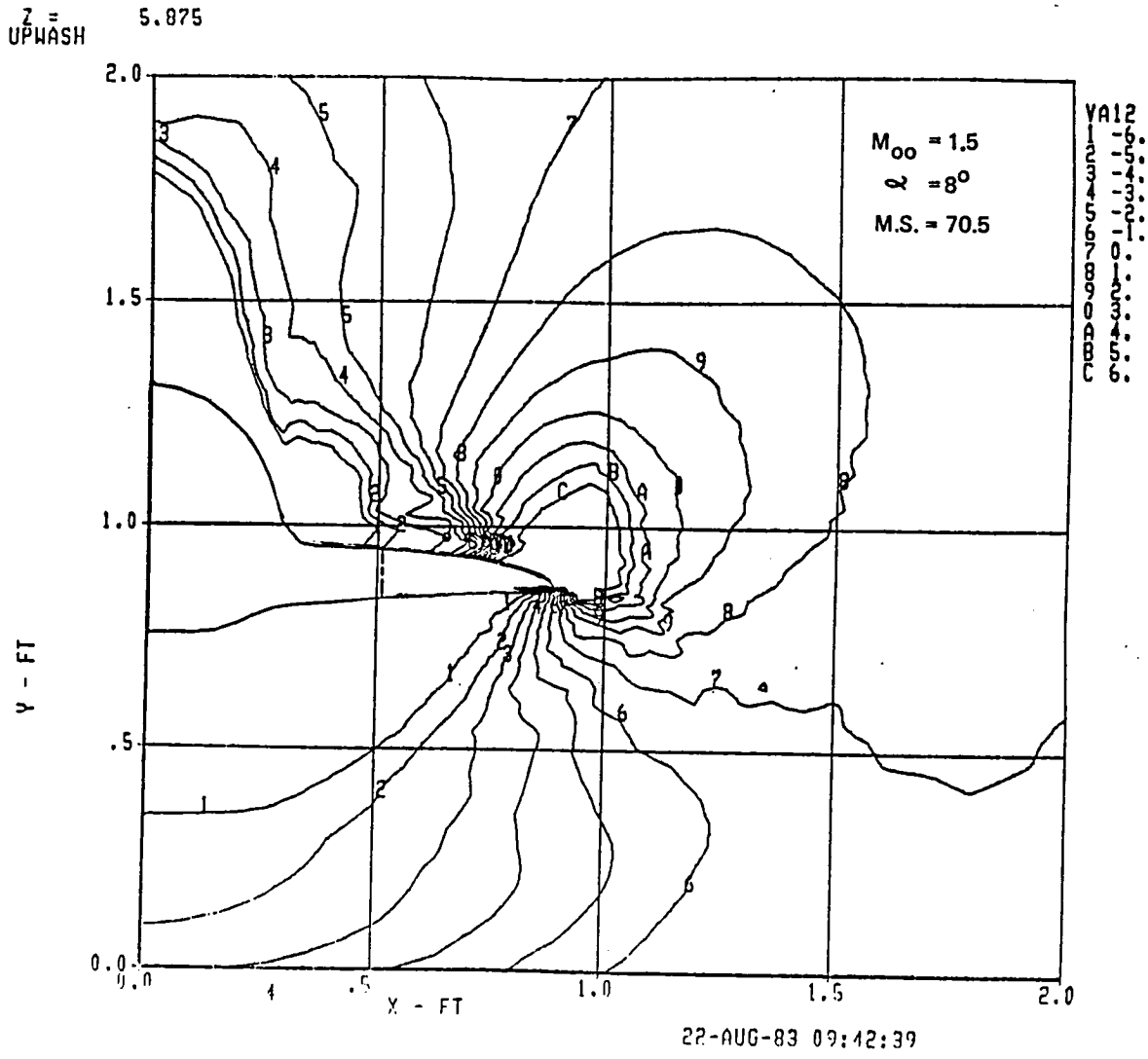

Figure 15(c). Upwash Angle Contours

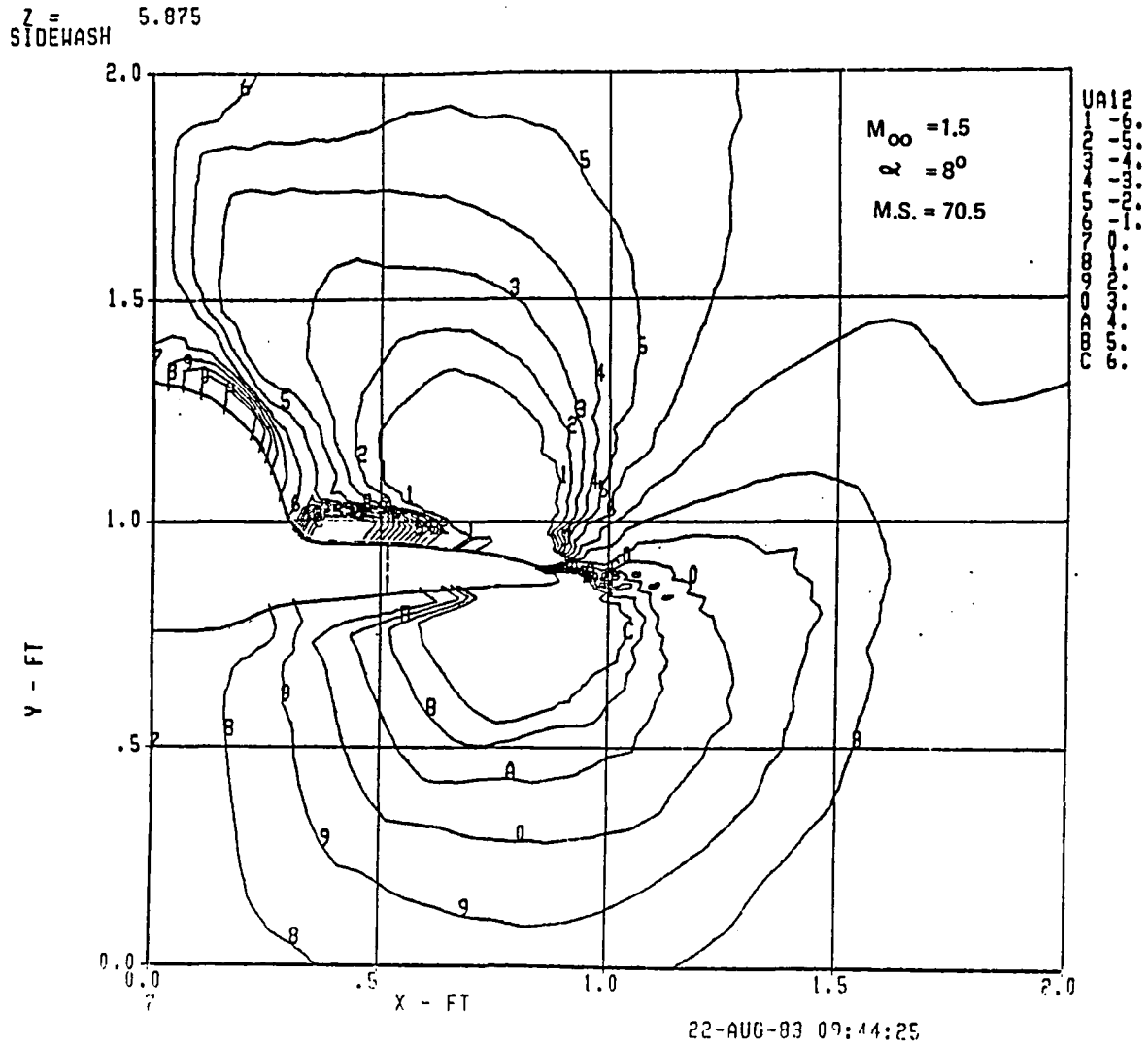

Figure 15(d). Sidewash Angle Contours

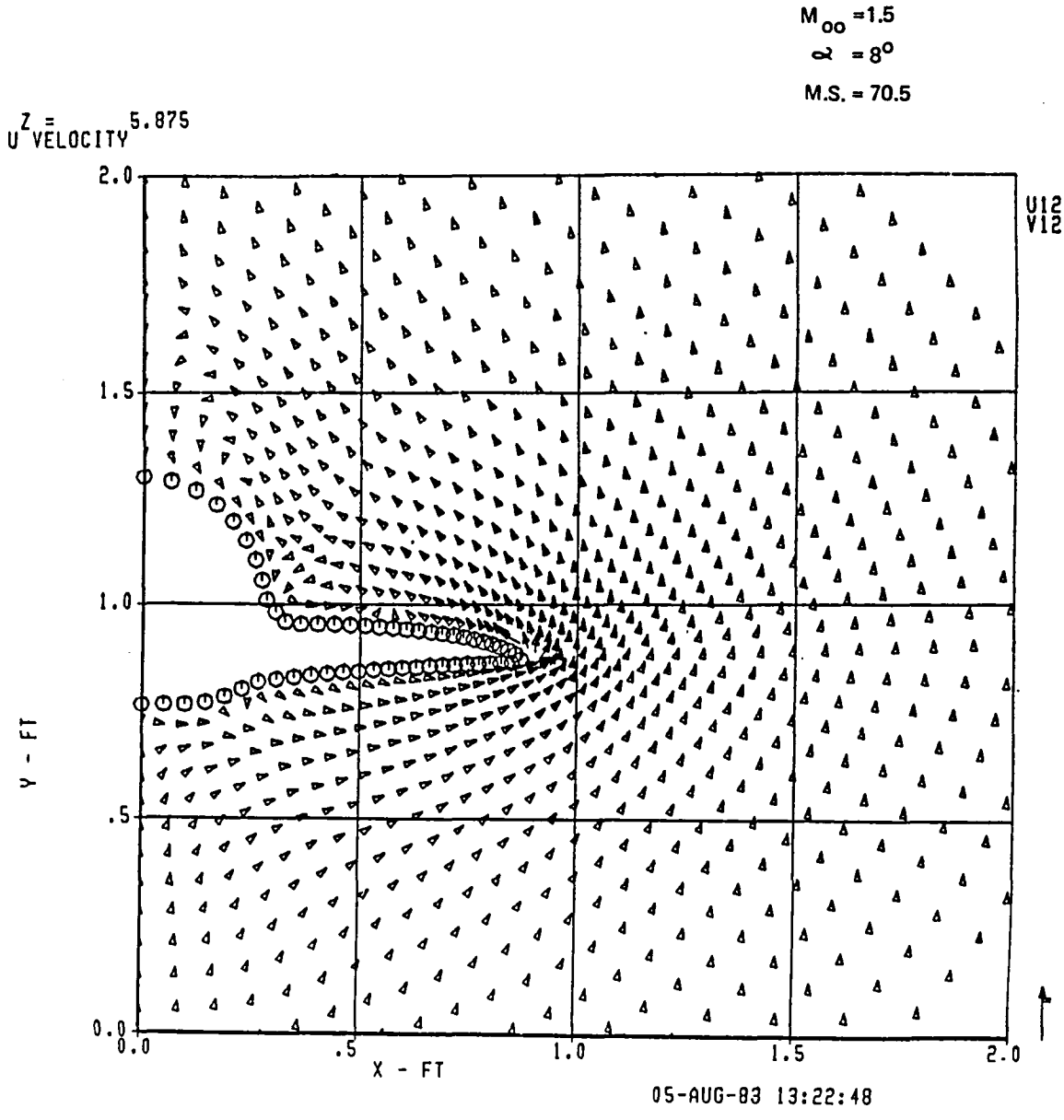

Figure 15(e). Cross-Plane Velocity

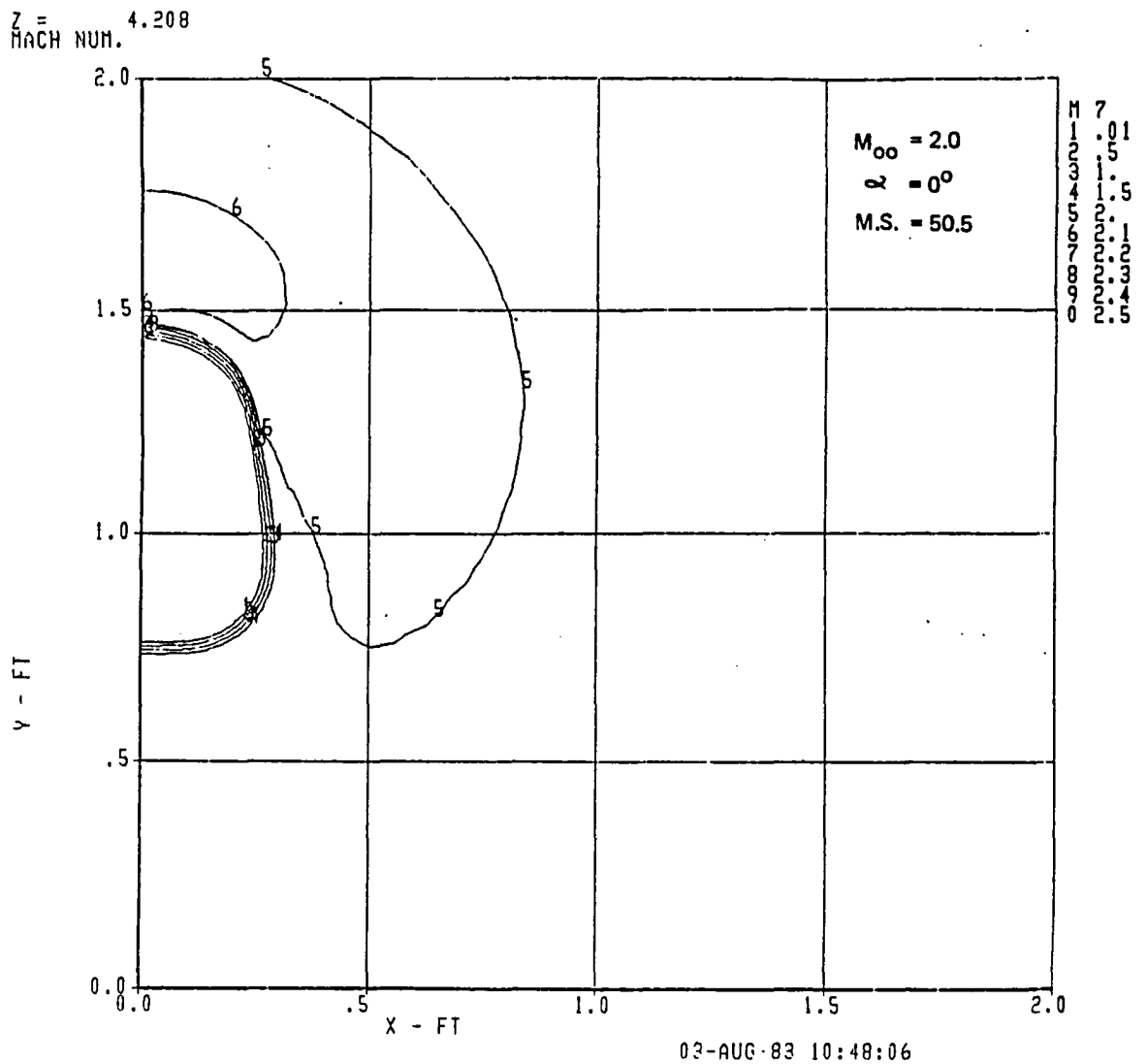

Figure 16(a). Mach Contours

Figure 16. Computed Results for Model Station 50.5, Mach 2.0, at 0-deg Angle of Attack

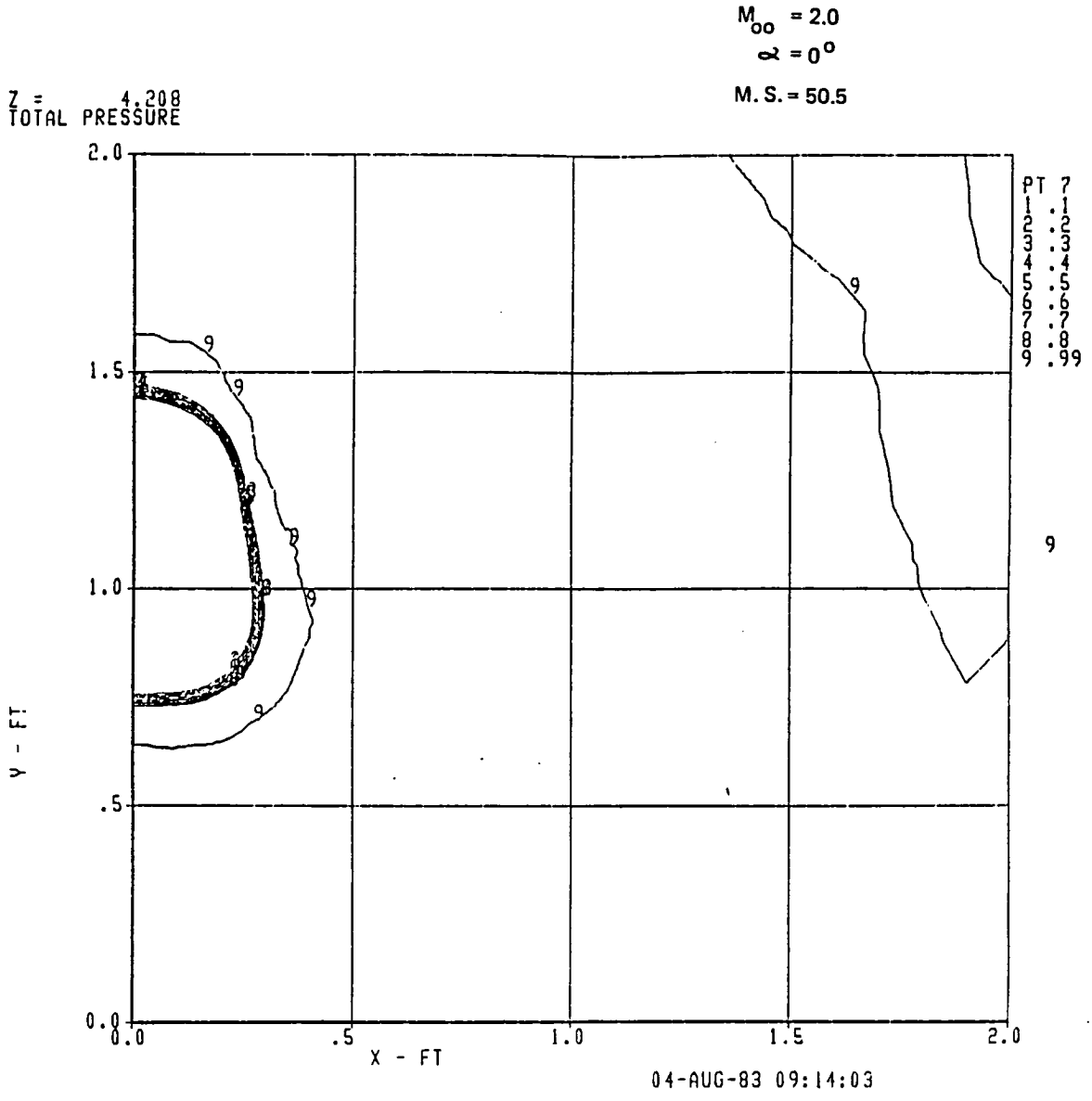

Figure 16(b). Total Pressure Contours

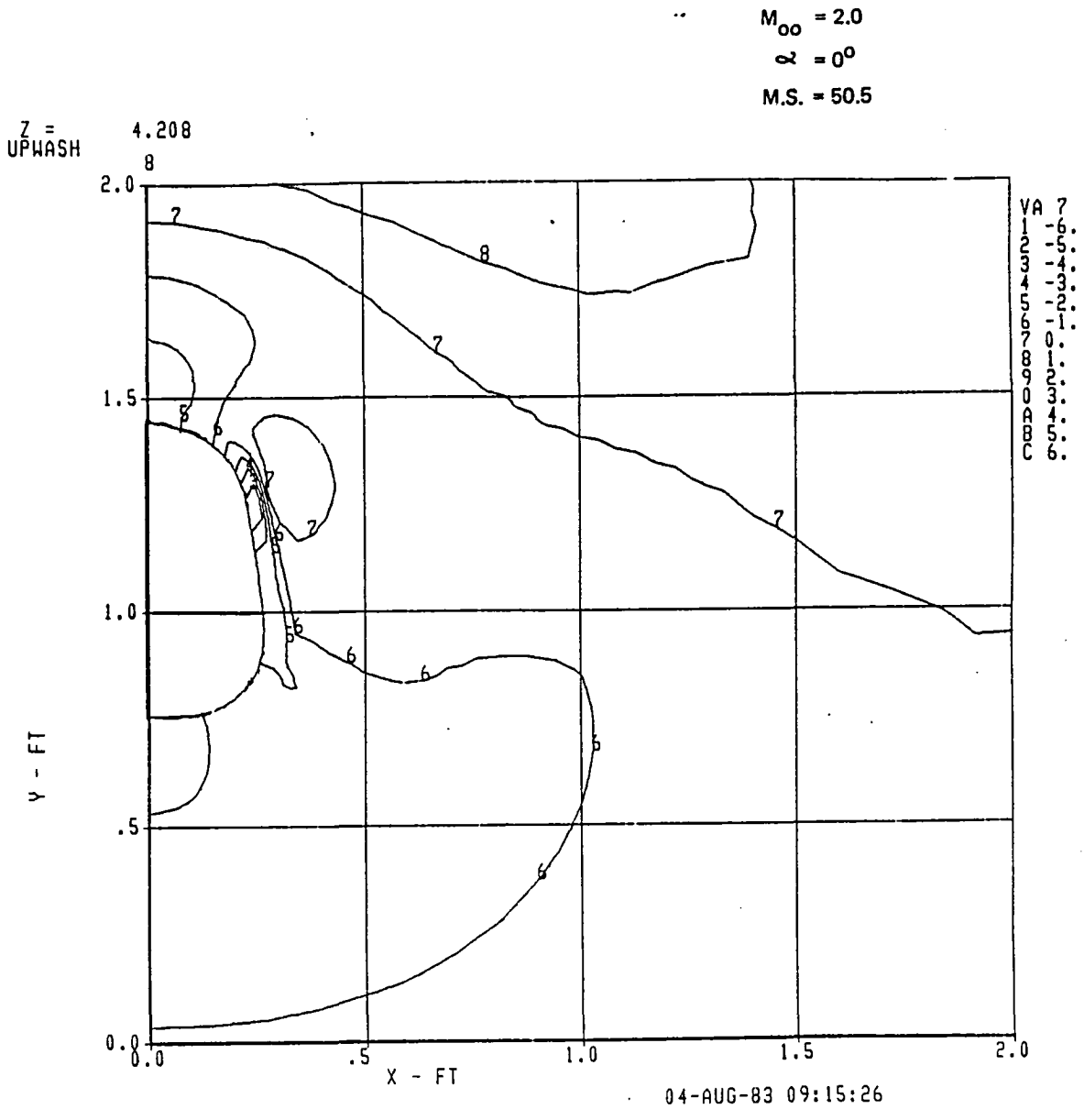

Figure 16(c). Upwash Angle Contours

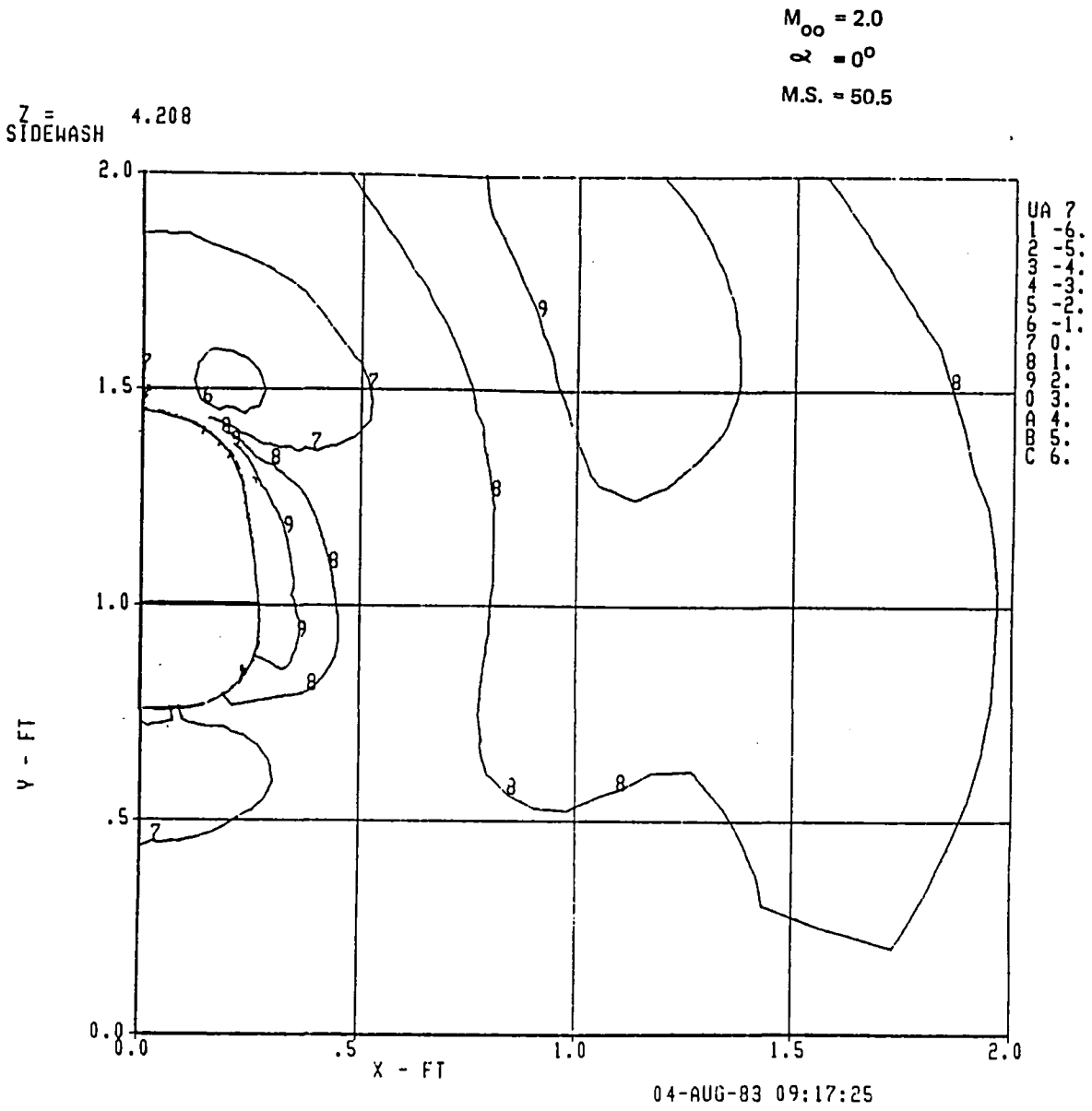

Figure 16(d). Sidewash Angle Contours

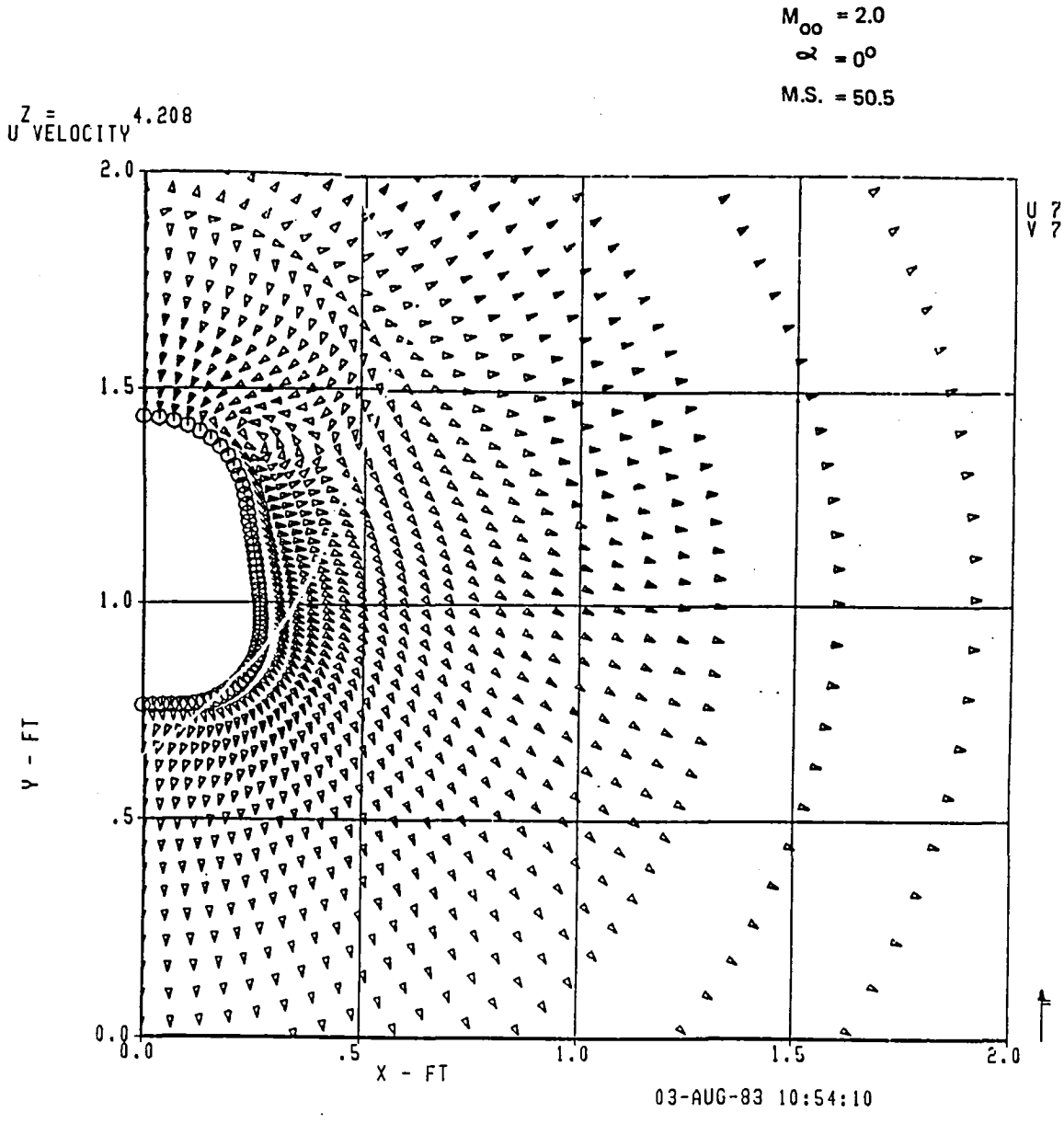

Figure 16(e). Cross-Plane Velocity

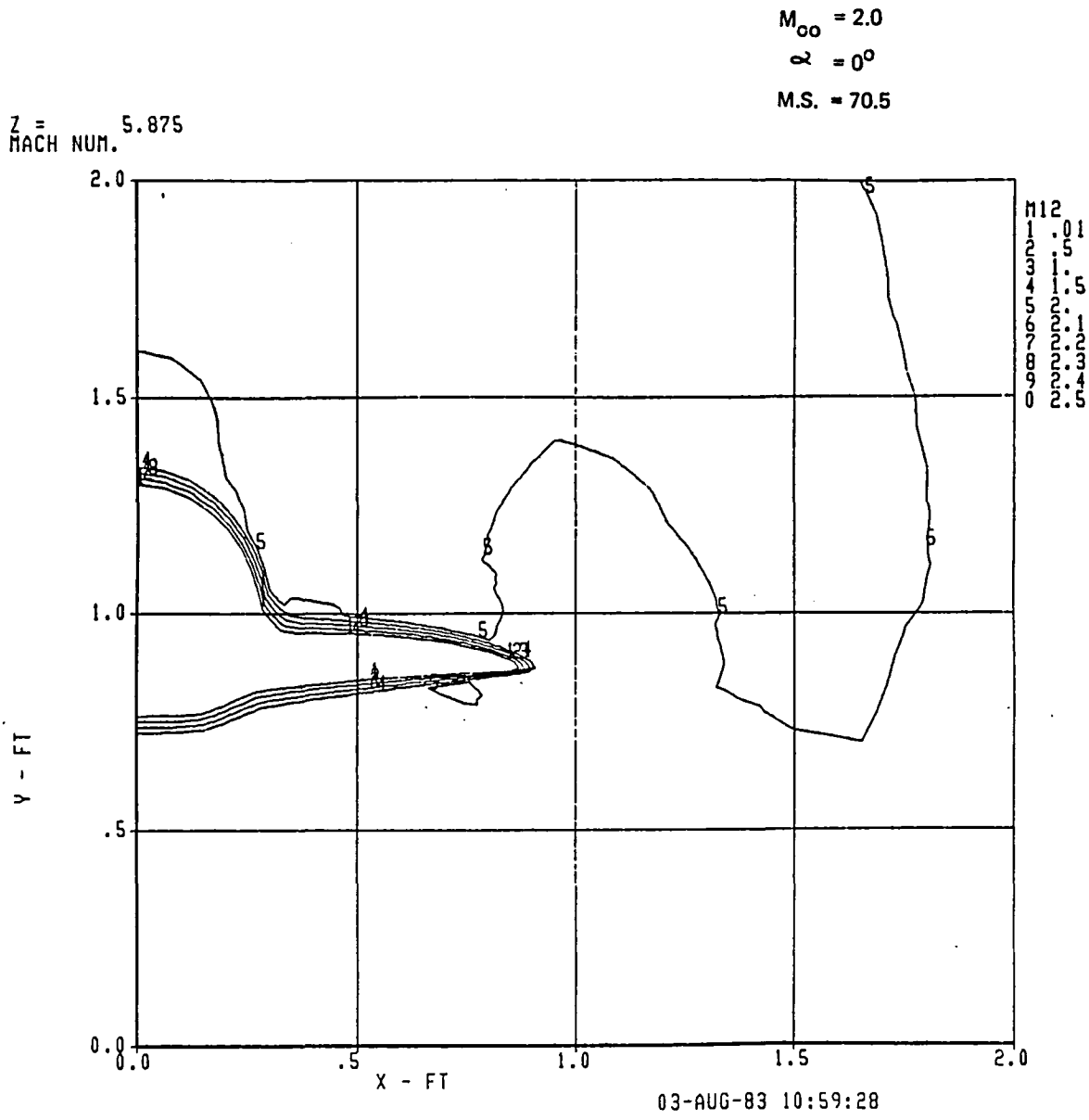

Figure 17(a). Mach Contours

Figure 17. Computed Results for Model Station 70.5, Mach 2.0, at 0-deg Angle of Attack

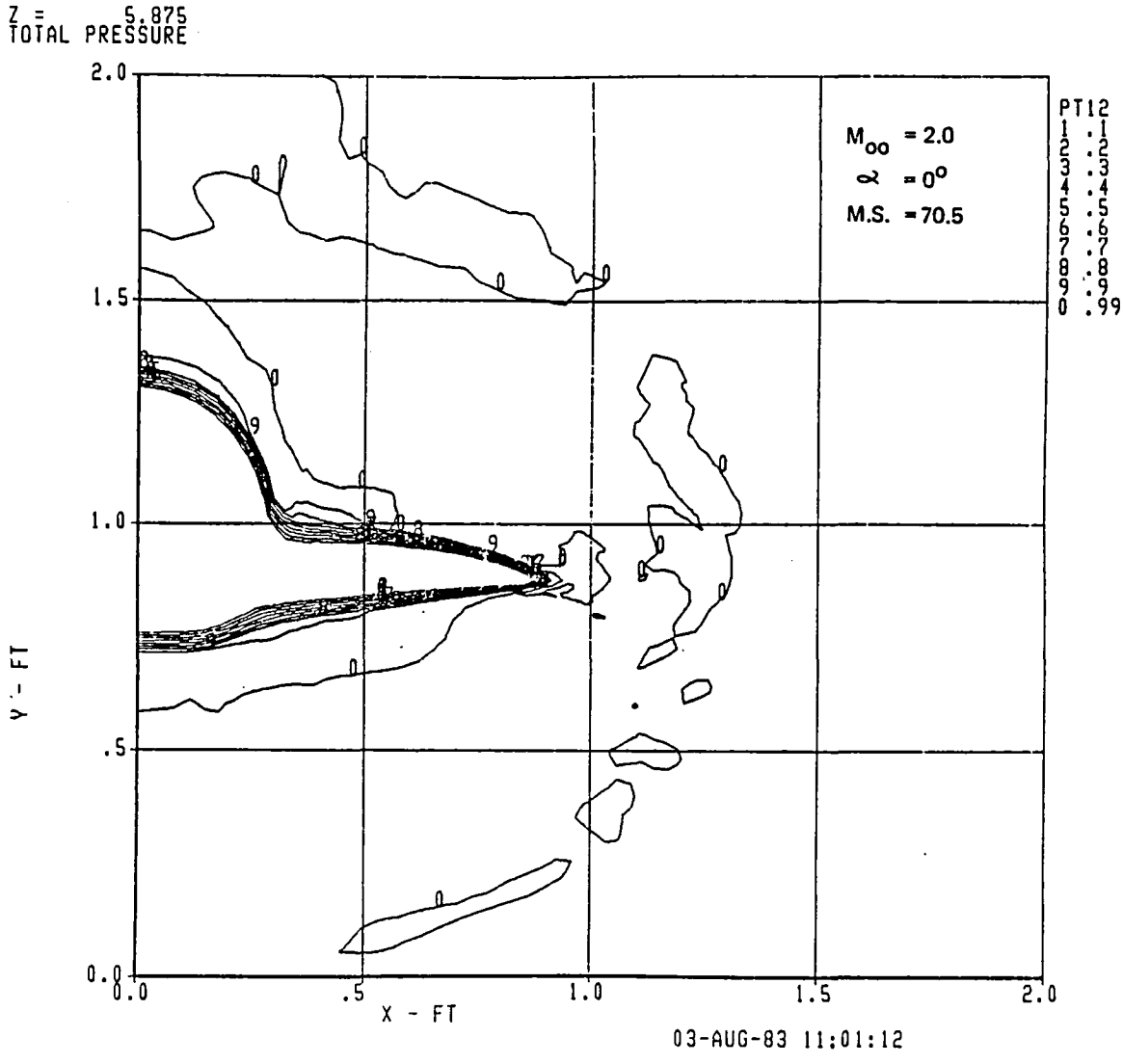

Figure 17(b). Total Pressure Contours

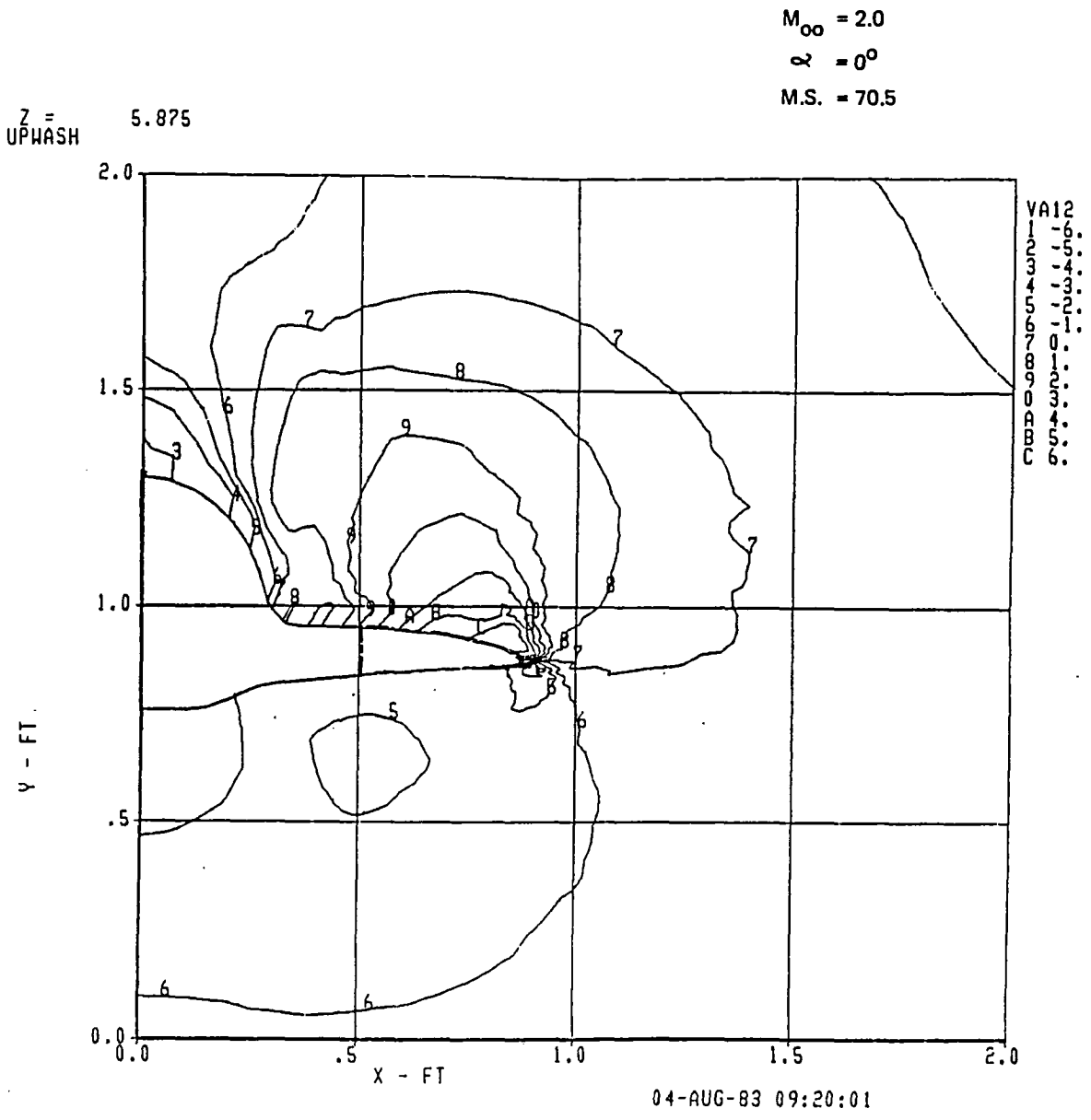

Figure 17(c). Upwash Angle Contours

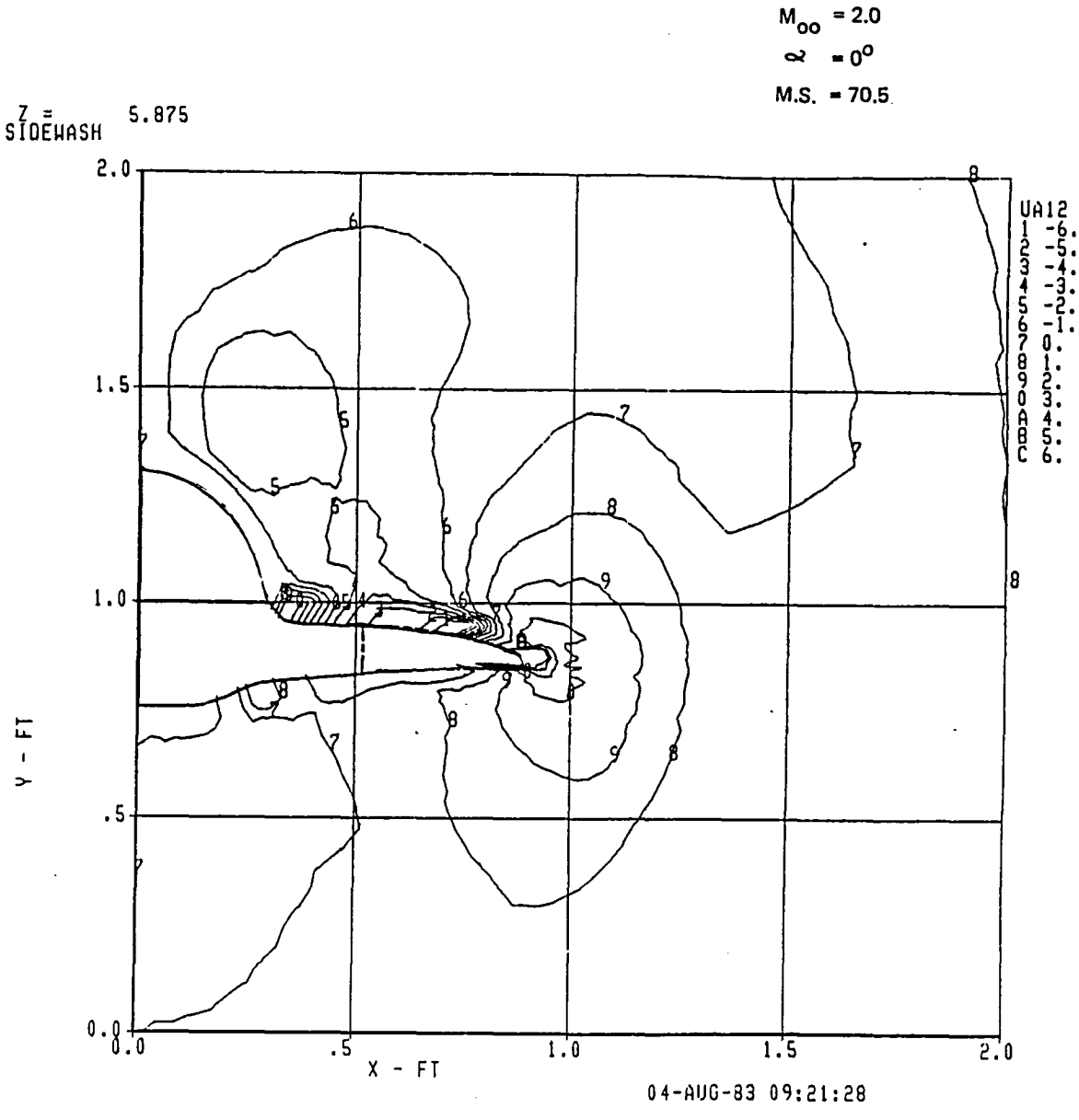

Figure 17(d). *Sidewash Angle Contours*

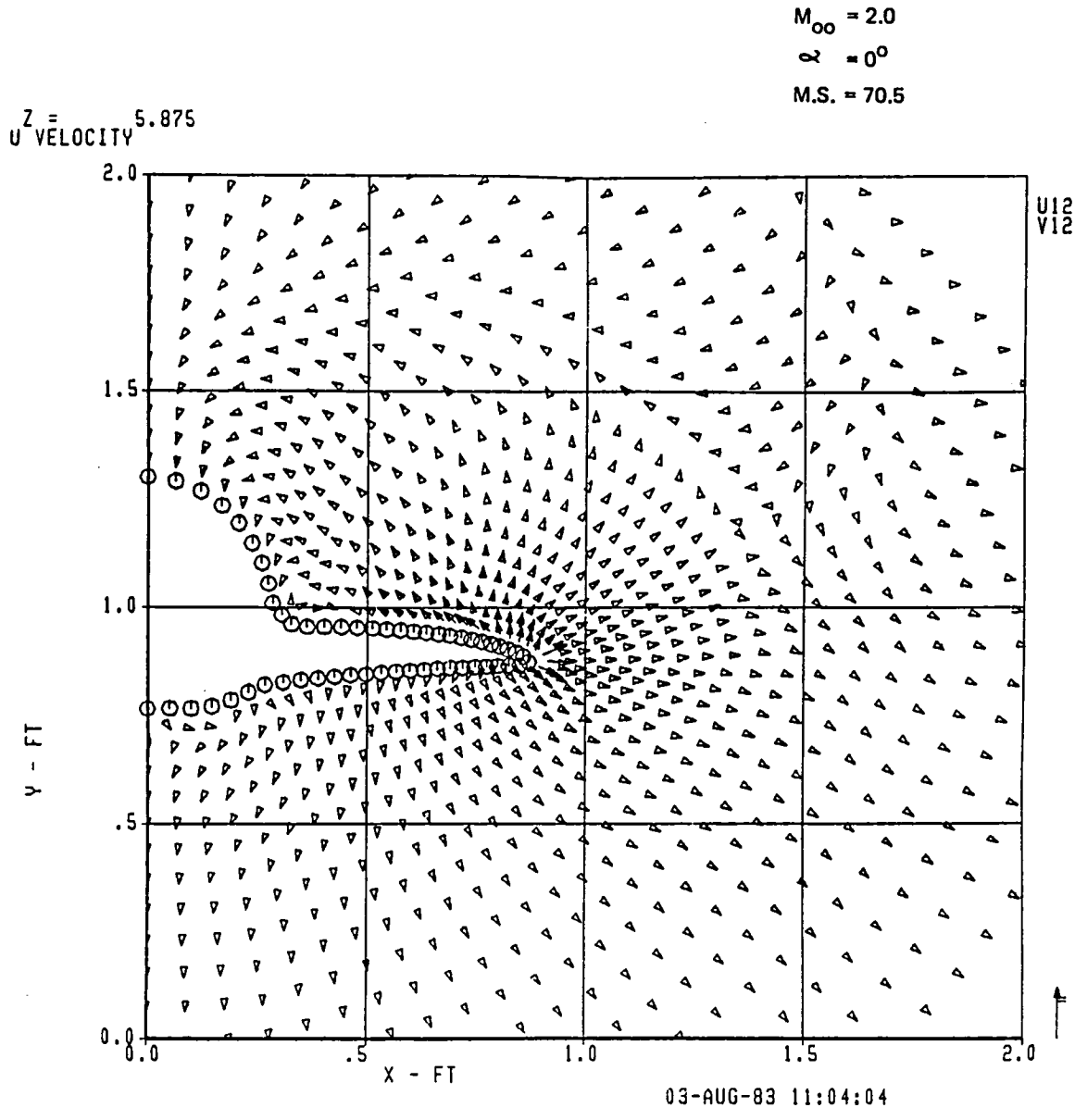

Figure 17(e). Cross-Plane Velocity

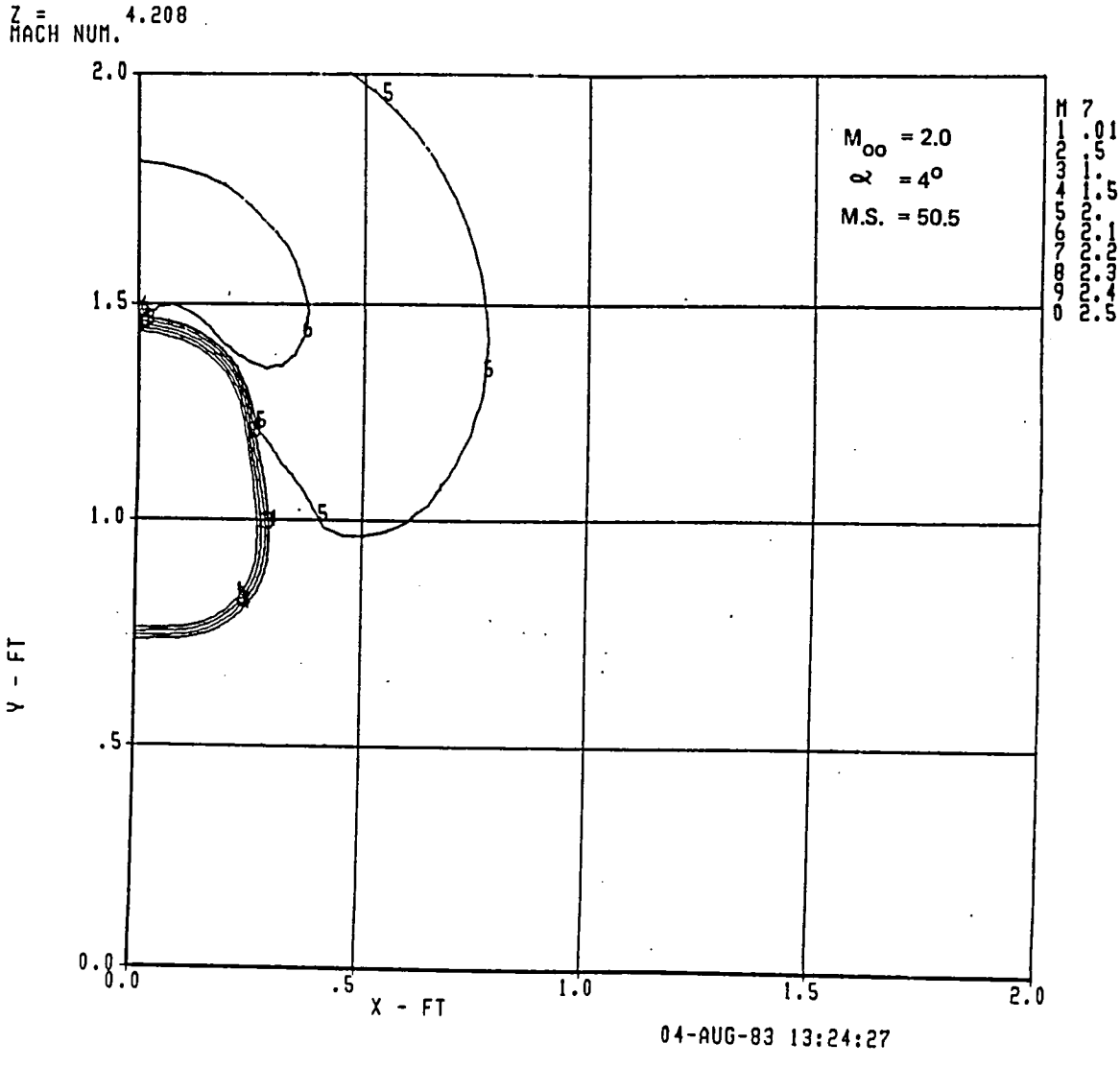

Figure 18(a). Mach Contours

Figure 18. Computed Results for Model Station 50.5, Mach 2.0, at 4-deg Angle of Attack

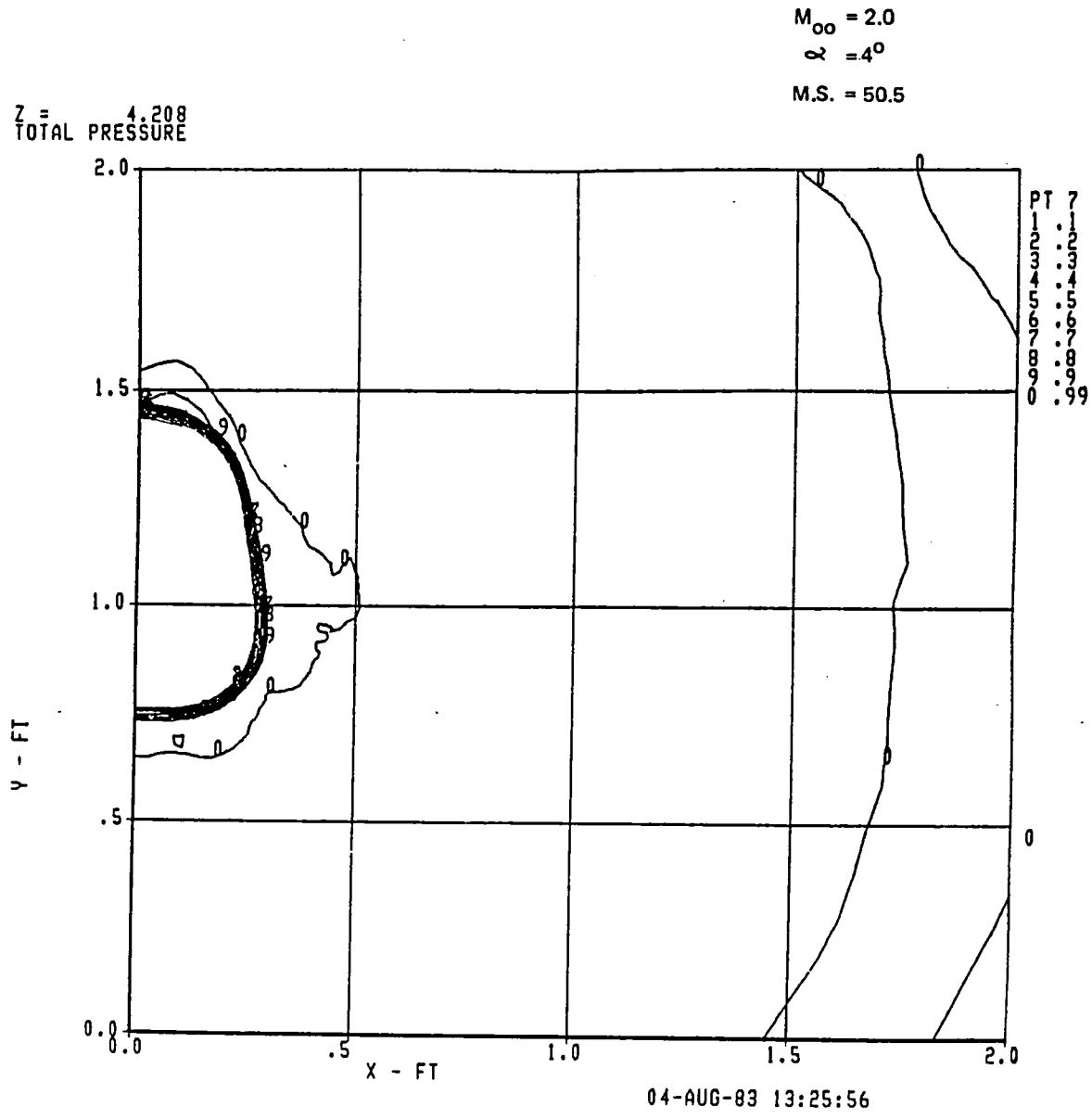

Figure 18(b). Total Pressure Contours

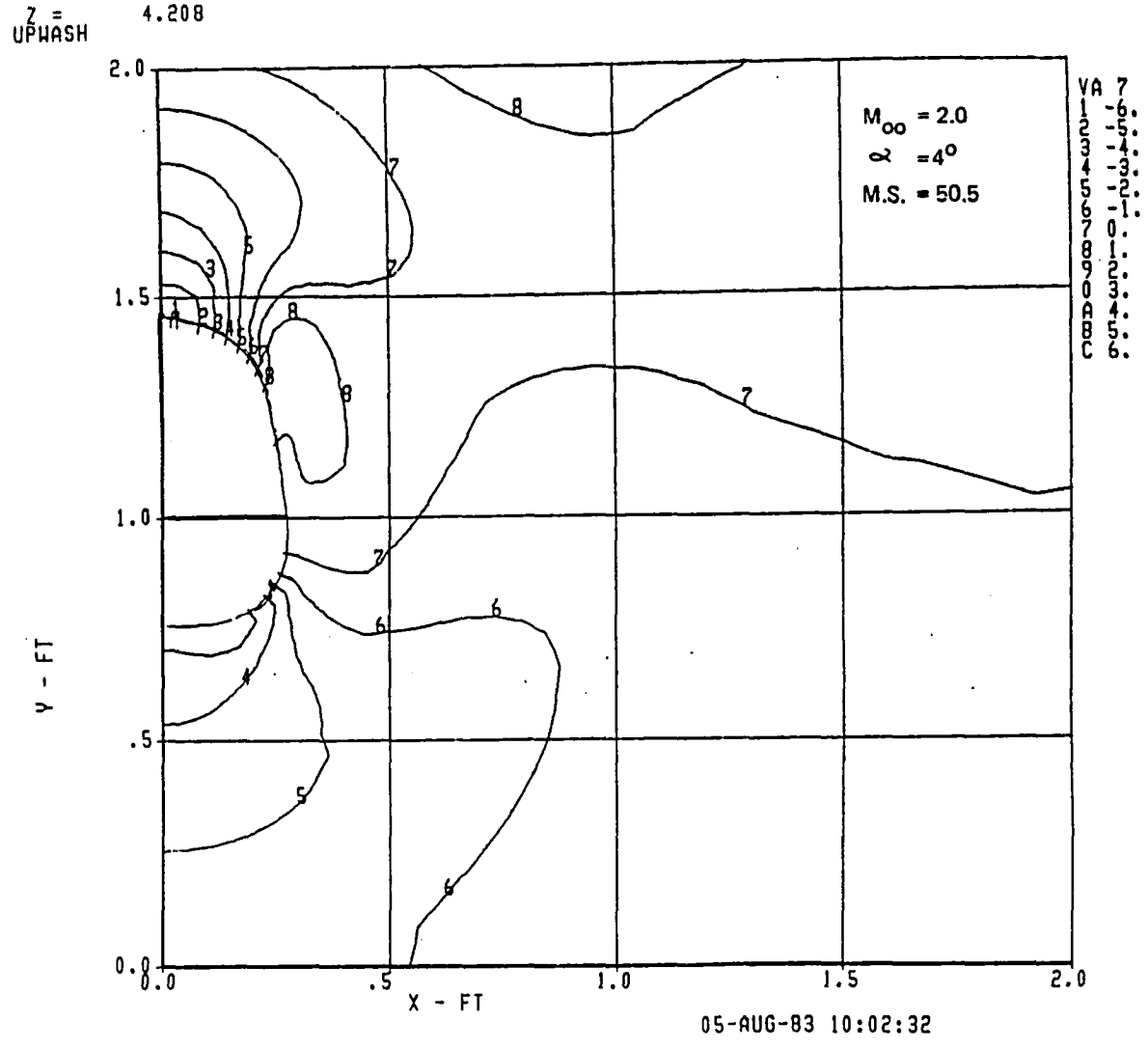

Figure 18(c). Upwash Angle Contours

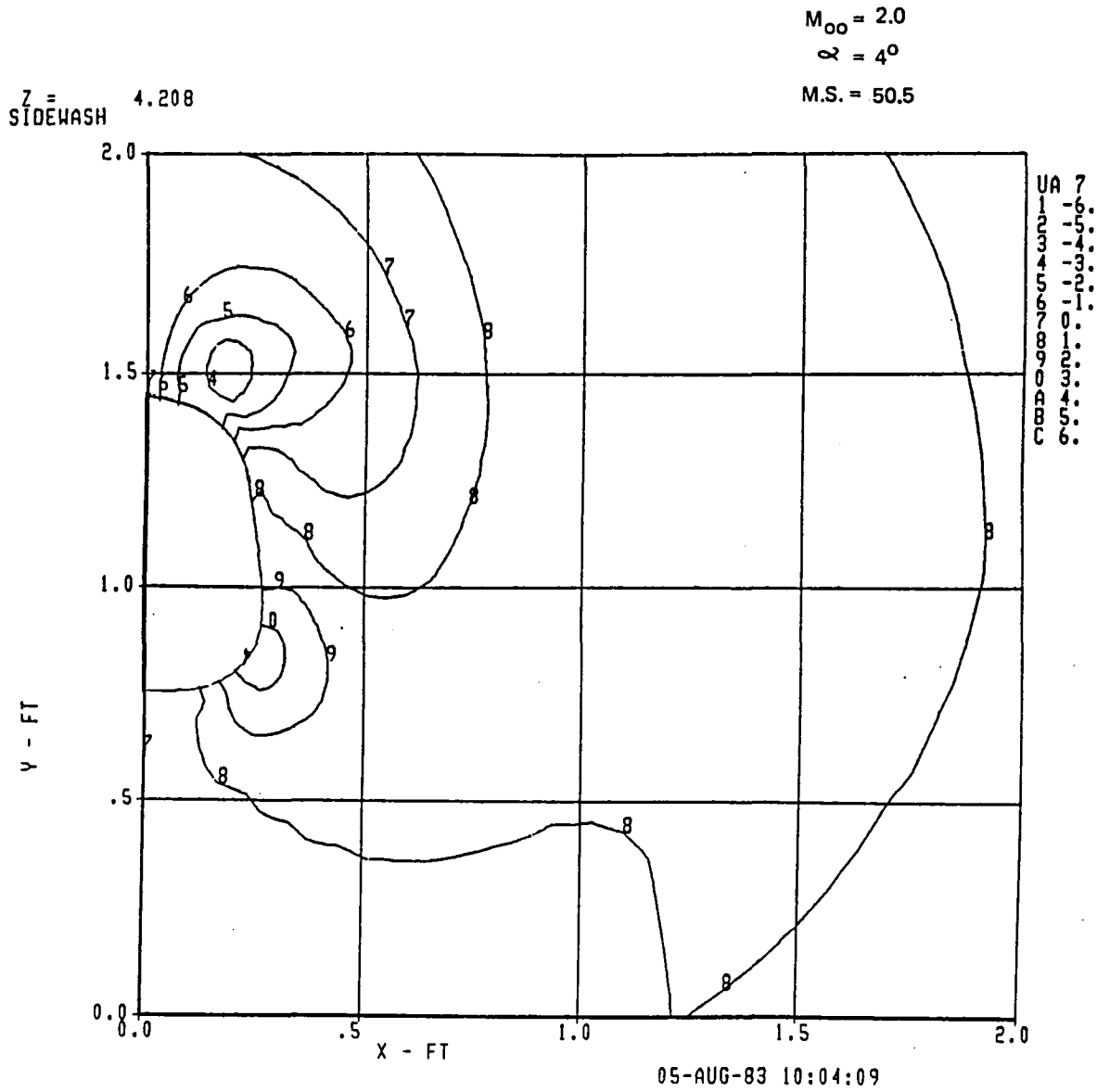

Figure 18(d). Sidewash Angle Contours

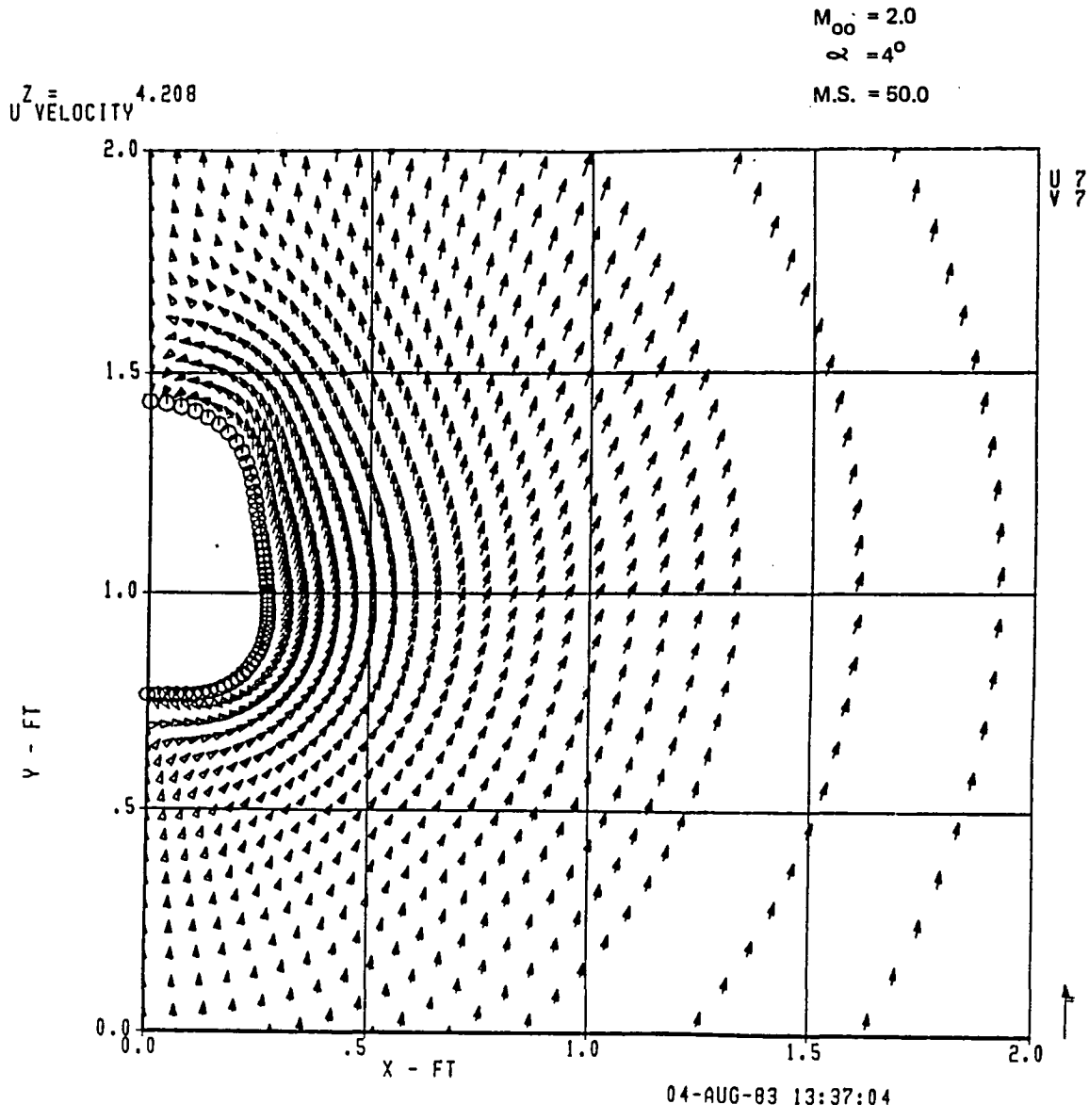

Figure 18(e). Cross-Plane Velocity

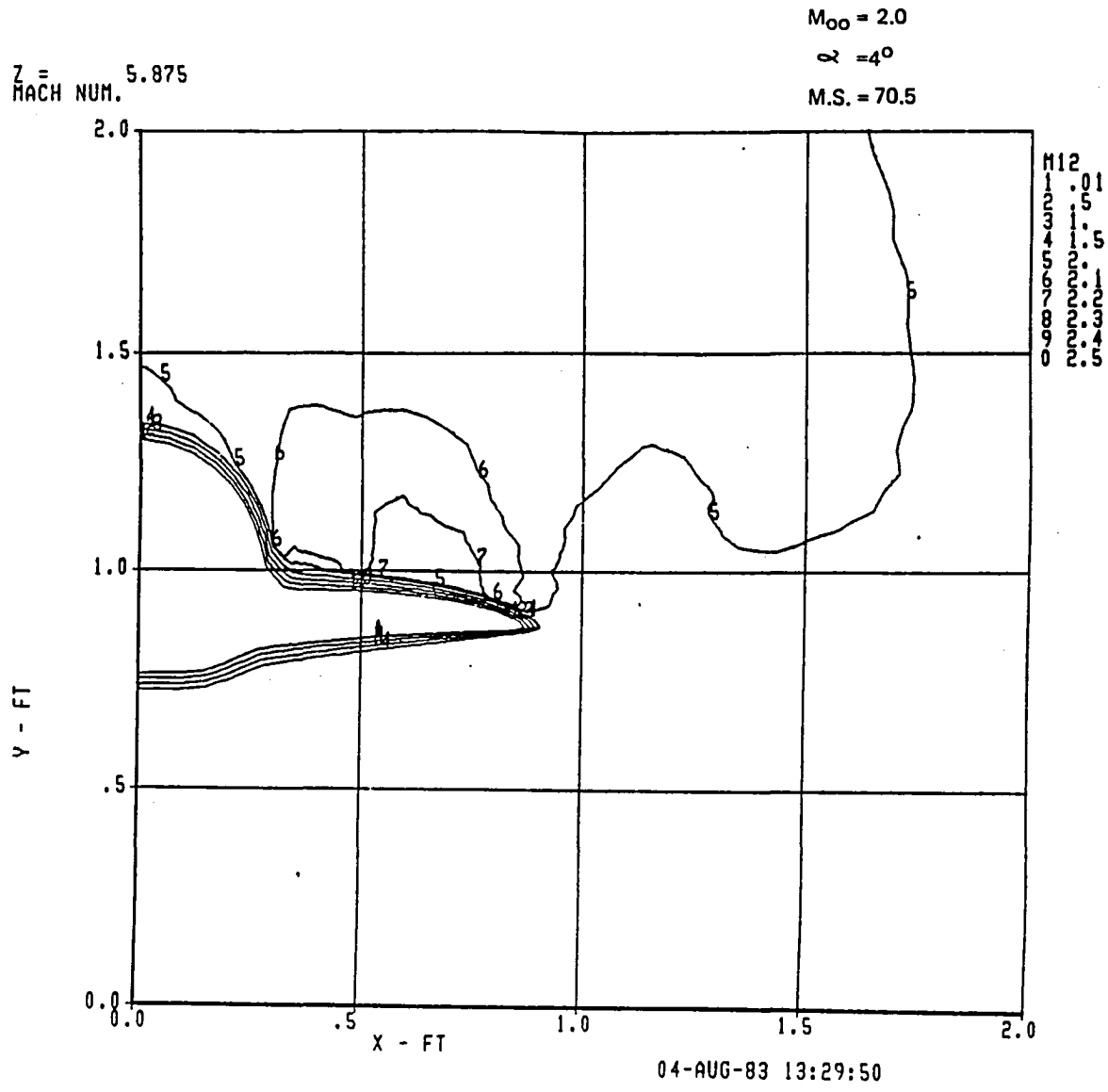

Figure 19(a). Mach Contours

Figure 19. Computed Results for Model Station 70.5, Mach 2.0, at 4-deg Angle of Attack

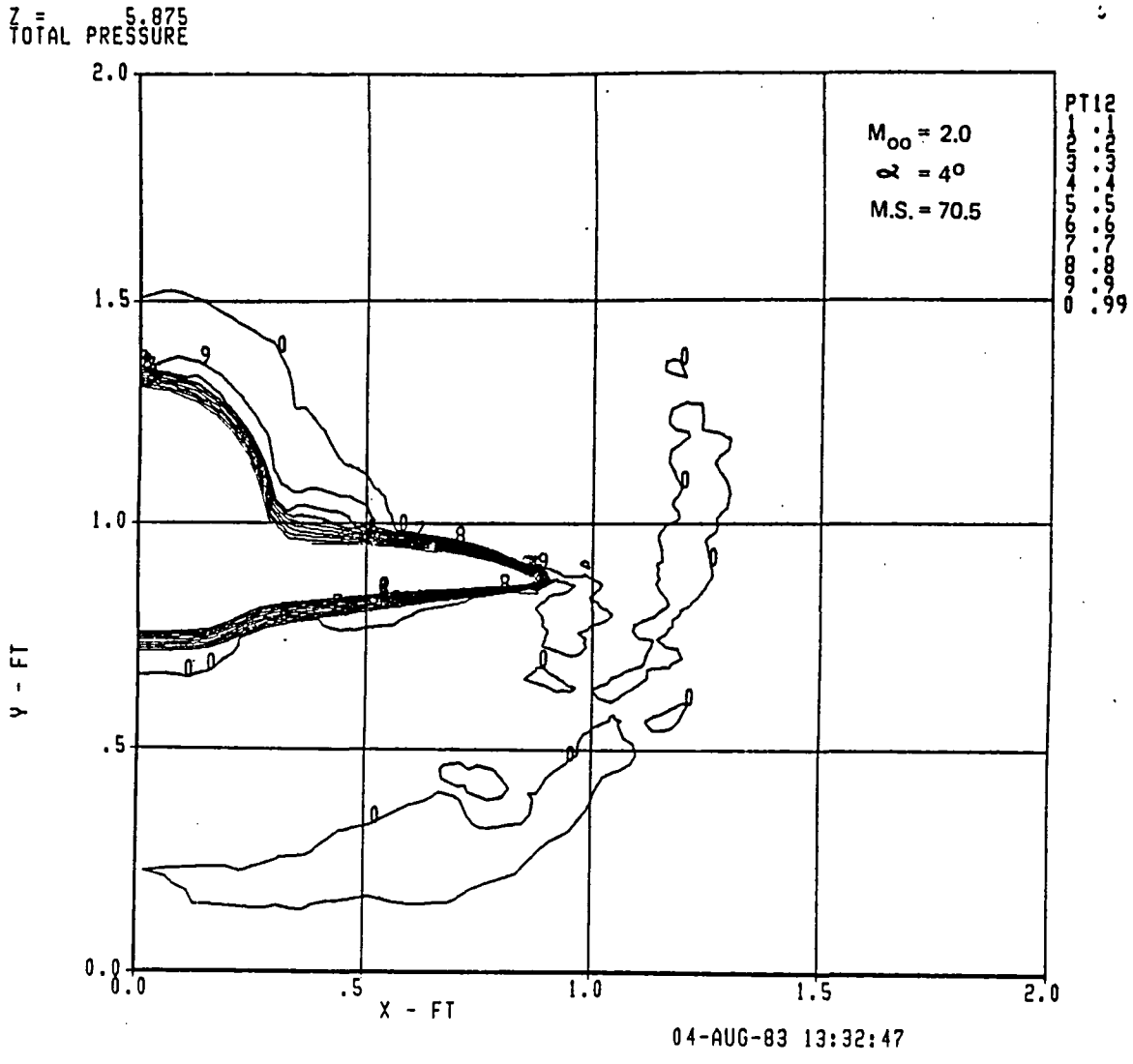

Figure 19(b). Total Pressure Contours

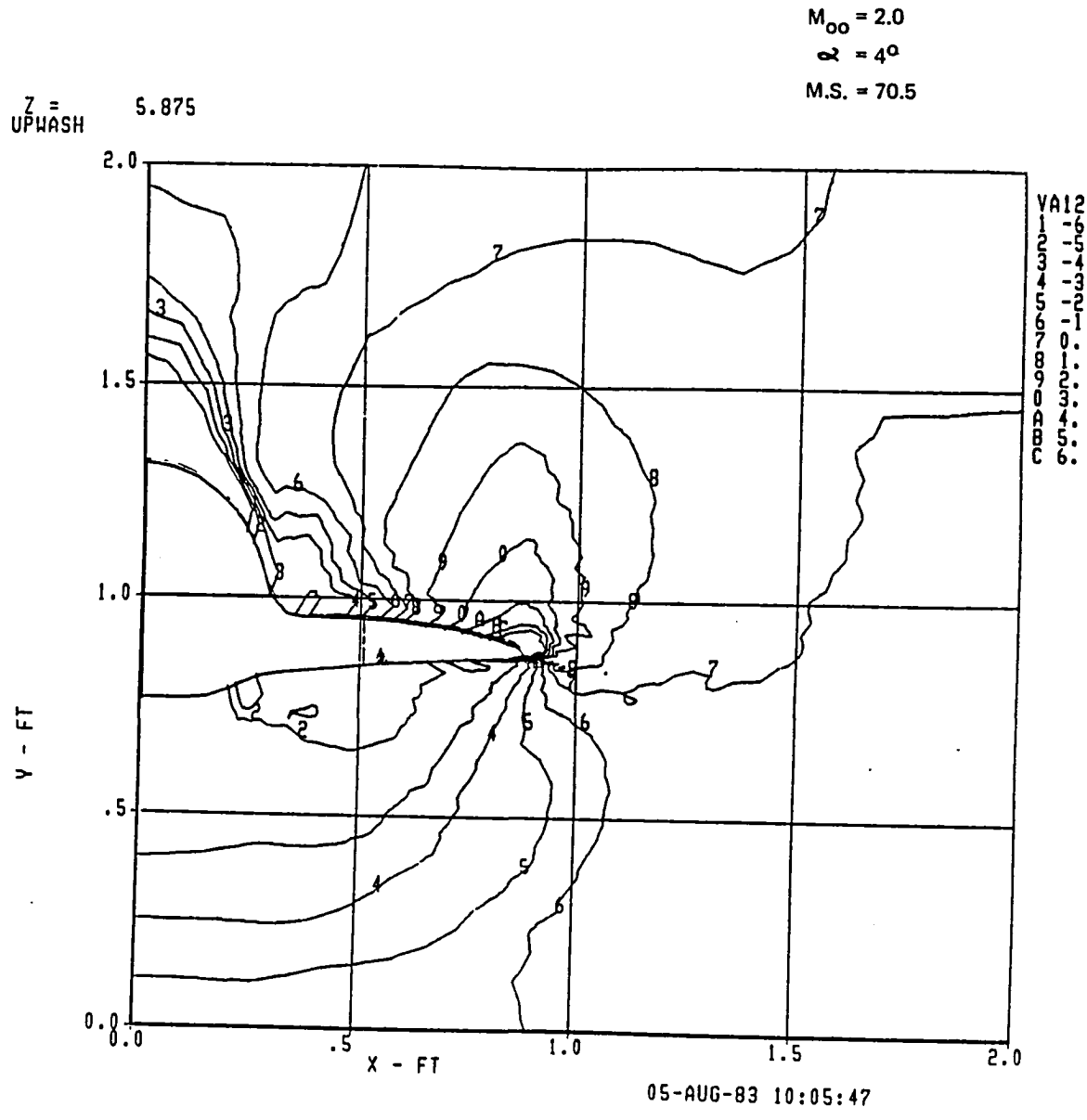

Figure 19(c). Upwash Angle Contours

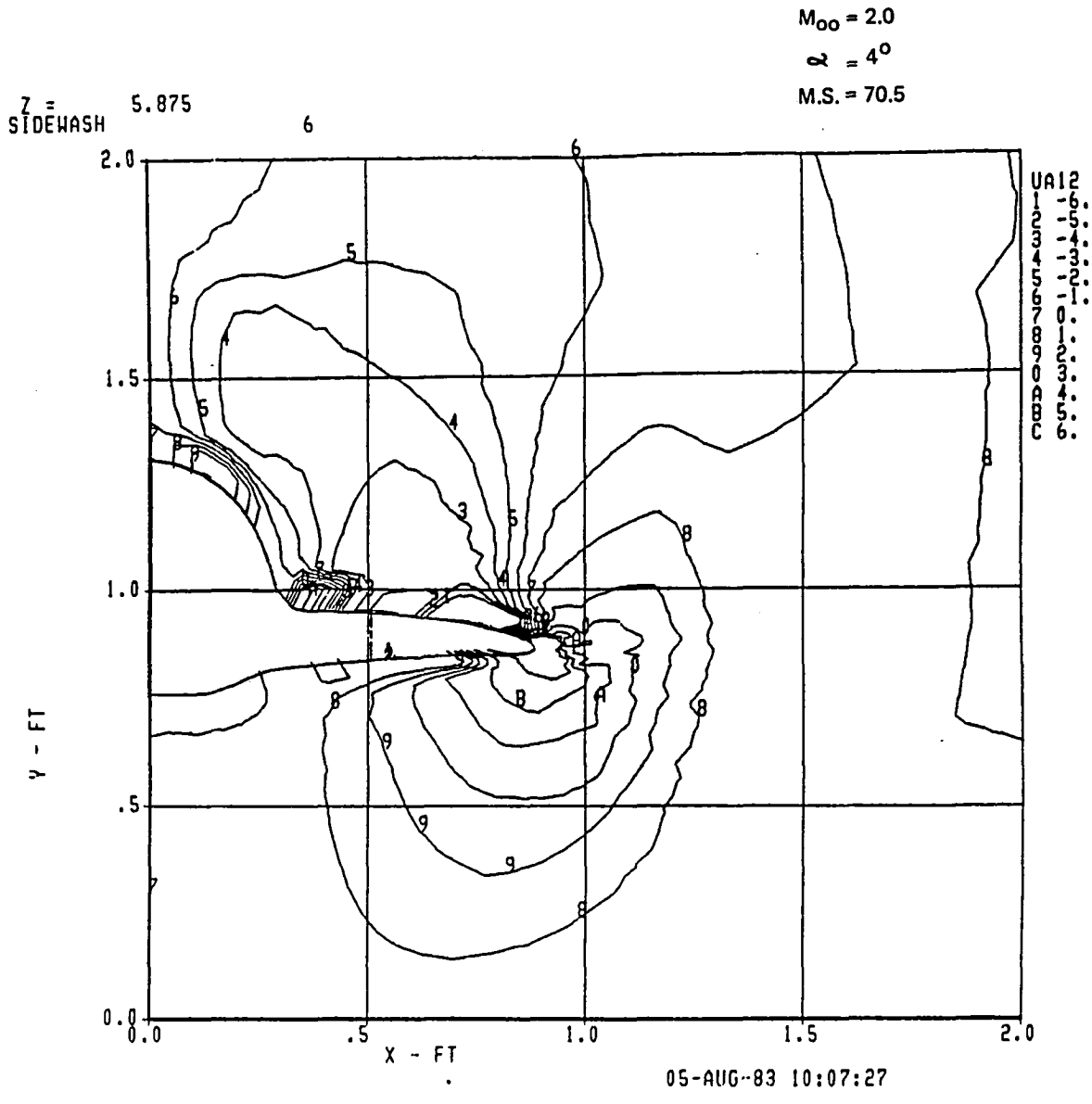

Figure 19(d). Sidewash Angle Contours

M_{oo} = 2.0

α = 4°

M. S. = 70.5

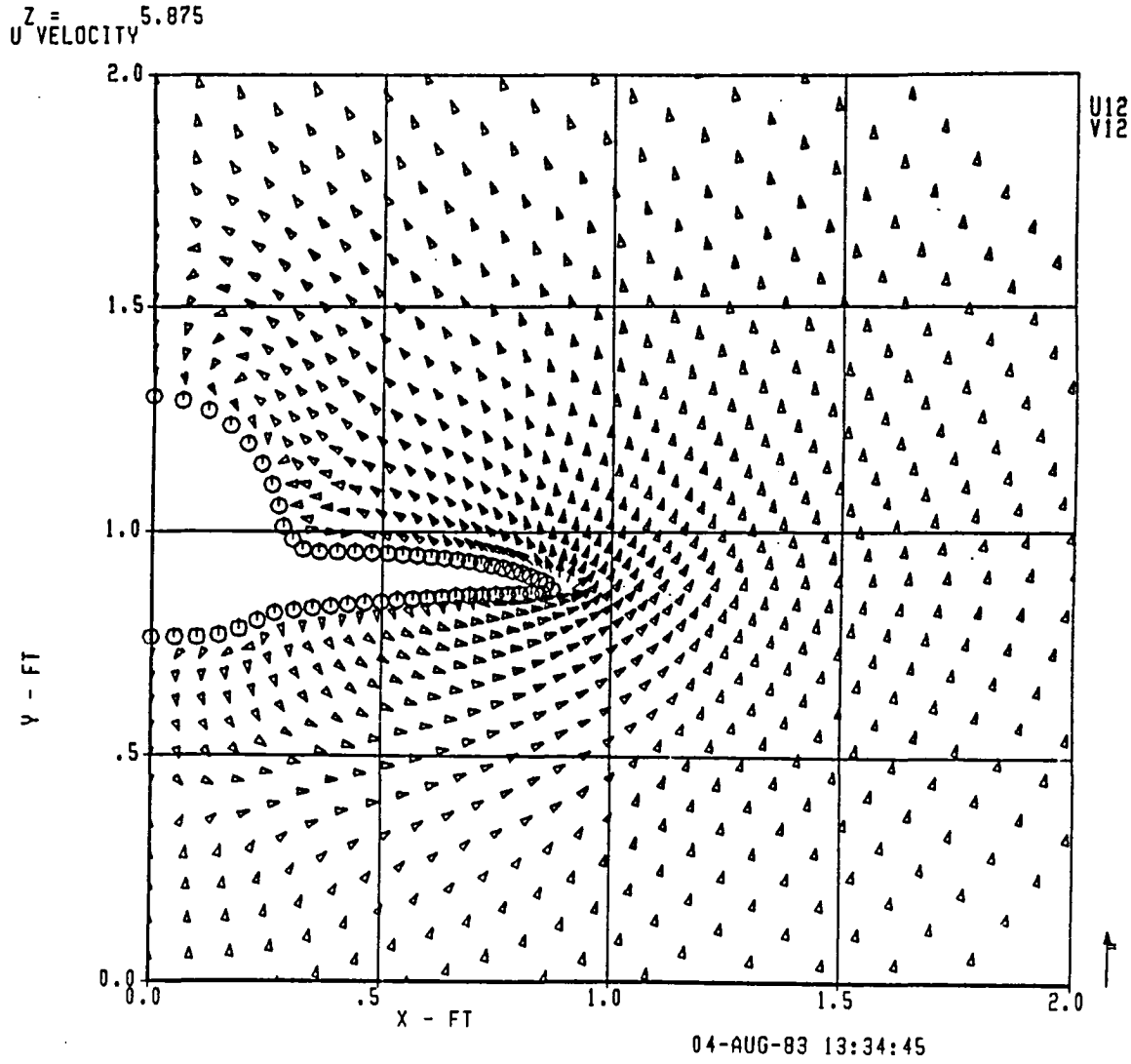

Figure 19(e). Cross-Plane Velocity

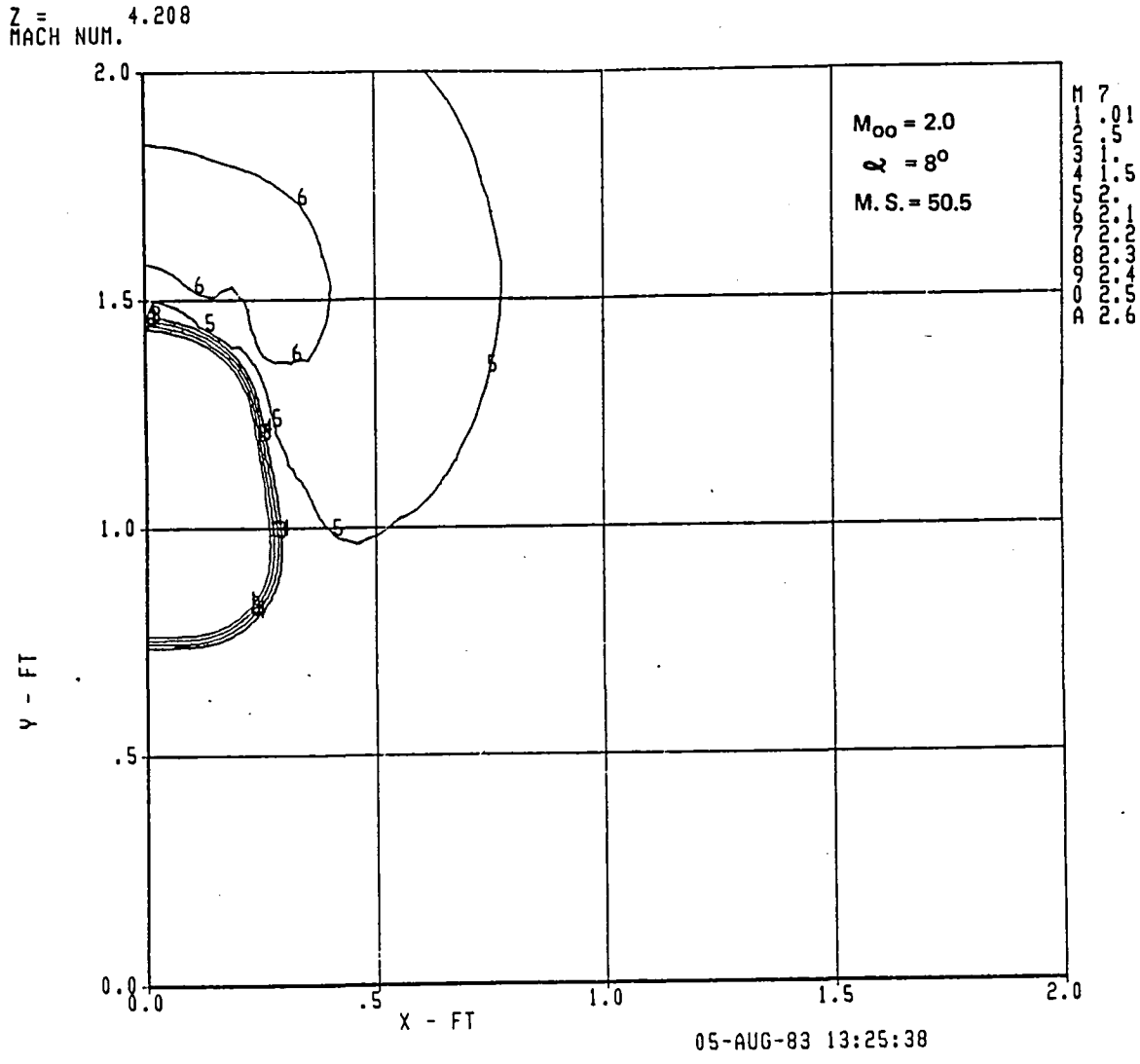

Figure 20(a). Mach Contours

Figure 20. Computed Results for Model Station 50.5, Mach 2.0, at 8-deg Angle of Attack

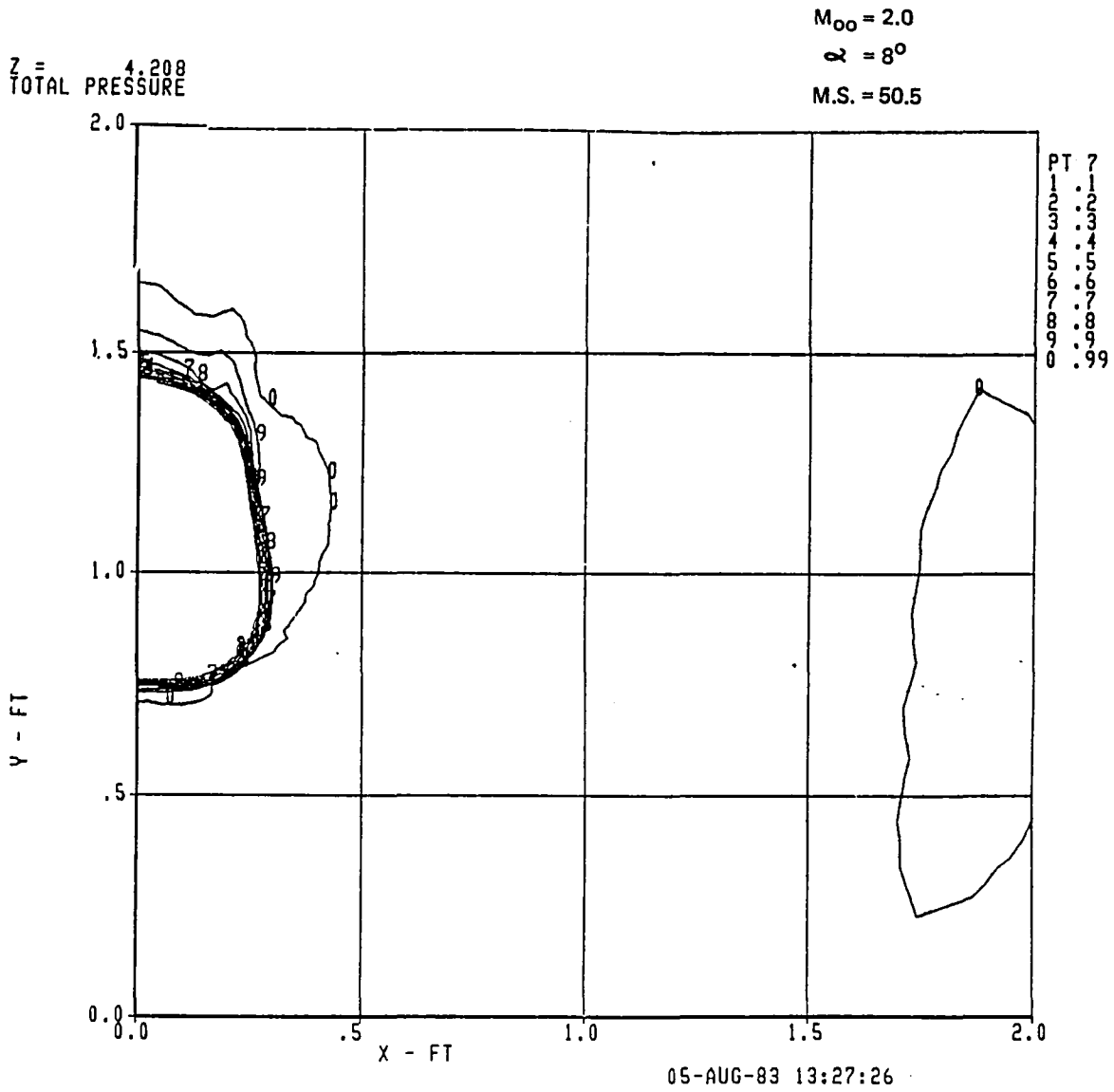

Figure 20(b). Total Pressure Contours

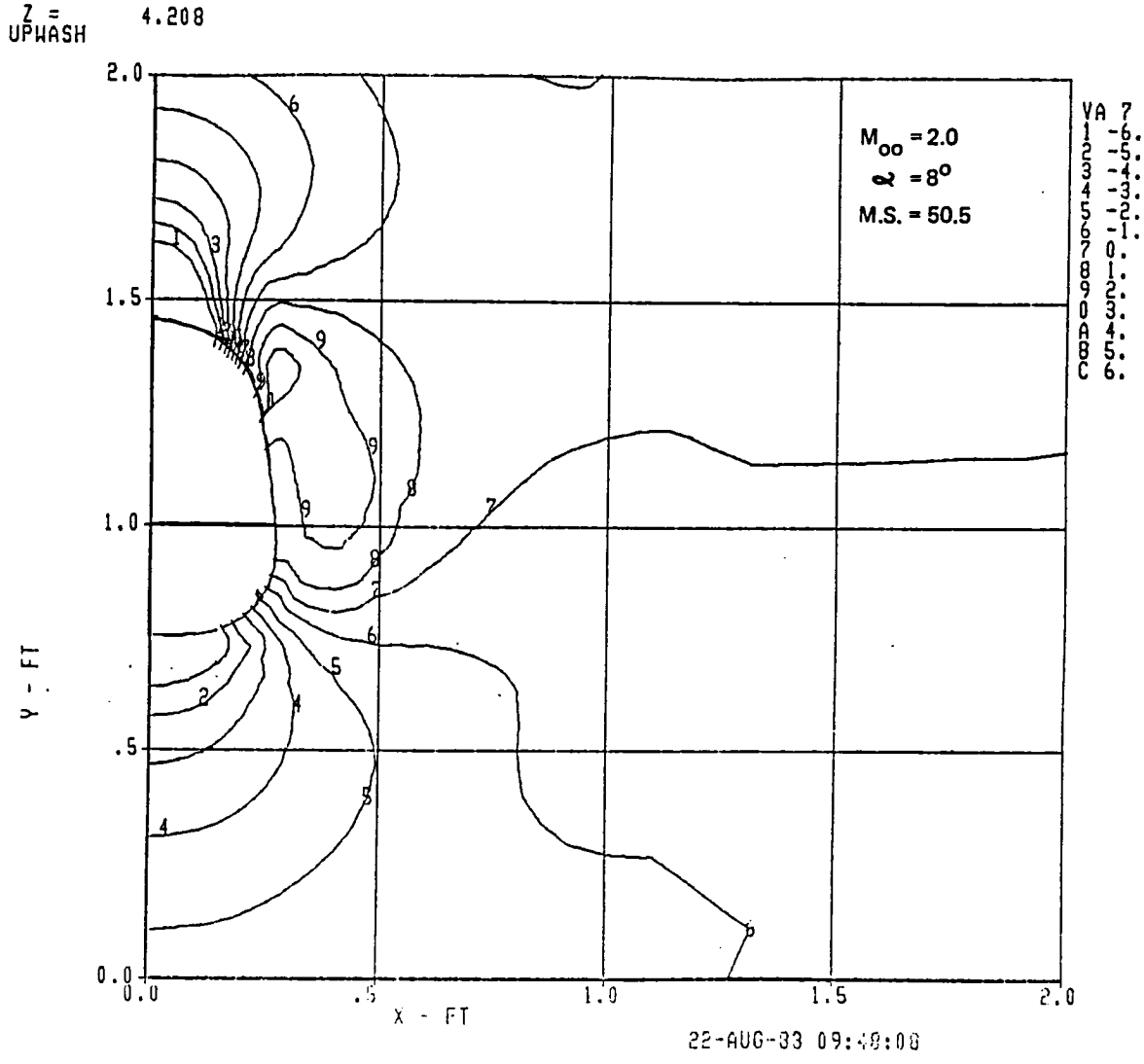

Figure 20(c). Upwash Angle Contours

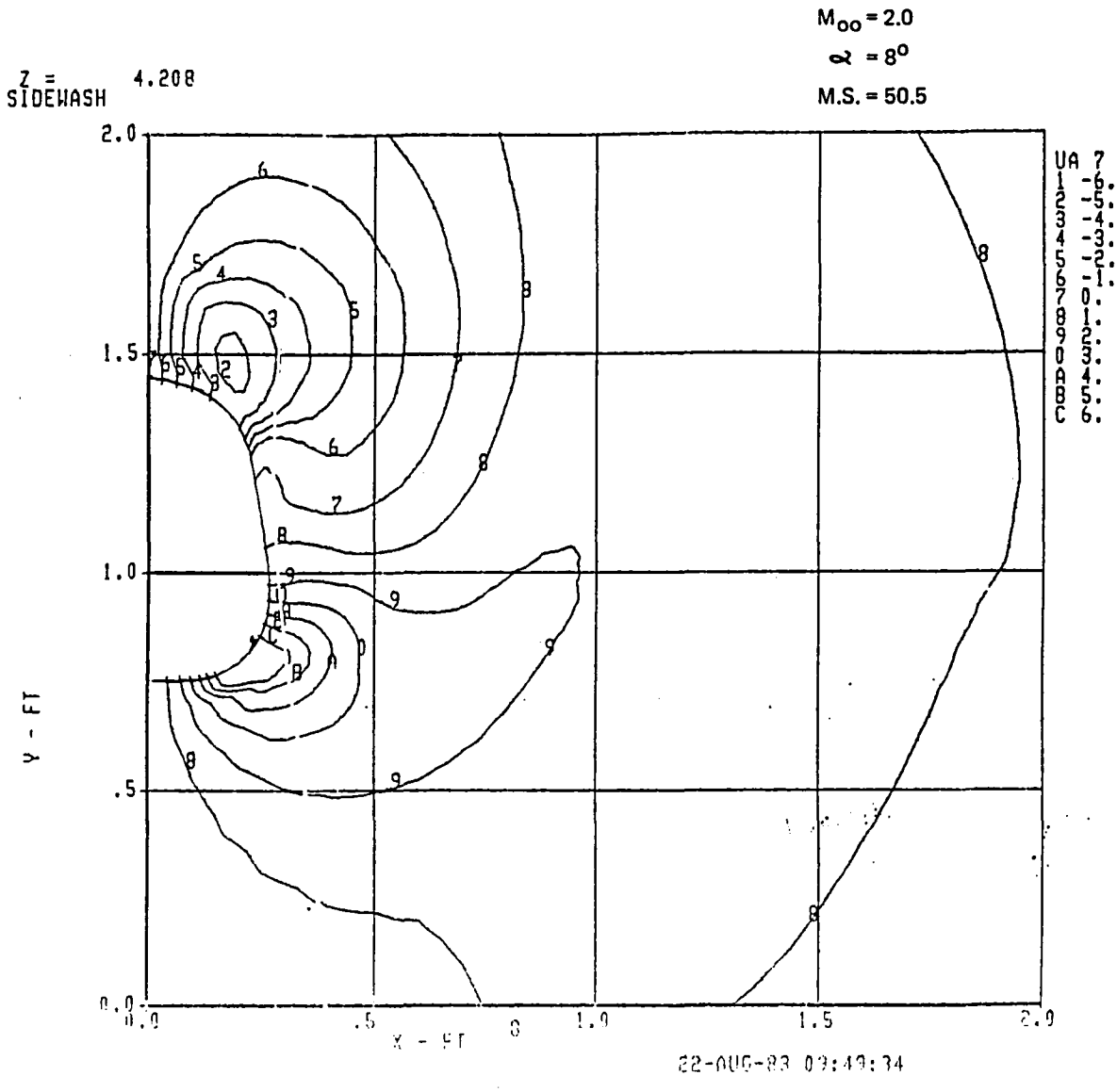

Figure 20(d). Sidewash Angle Contours

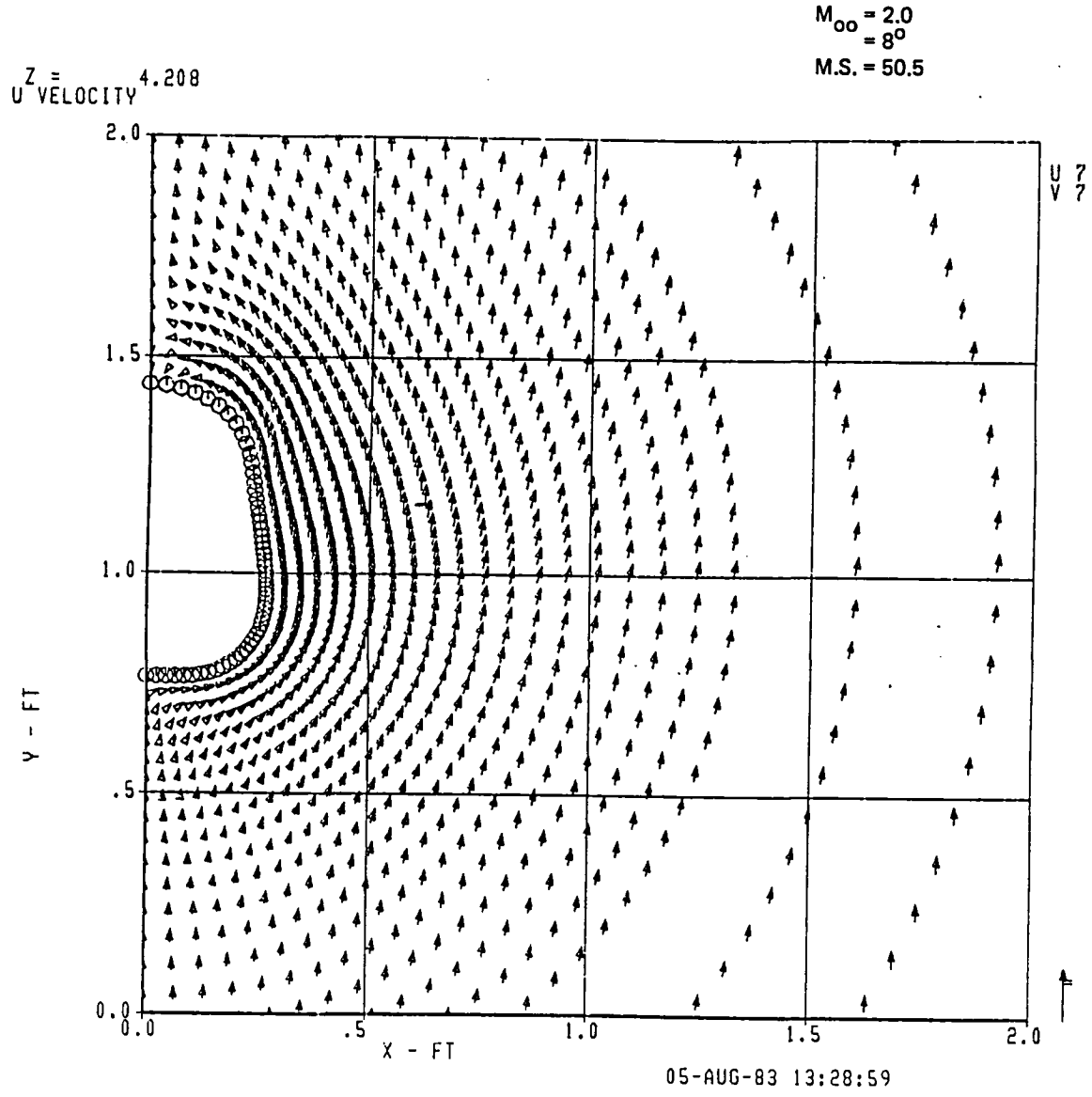

Figure 20(e). Cross-Plane Velocity

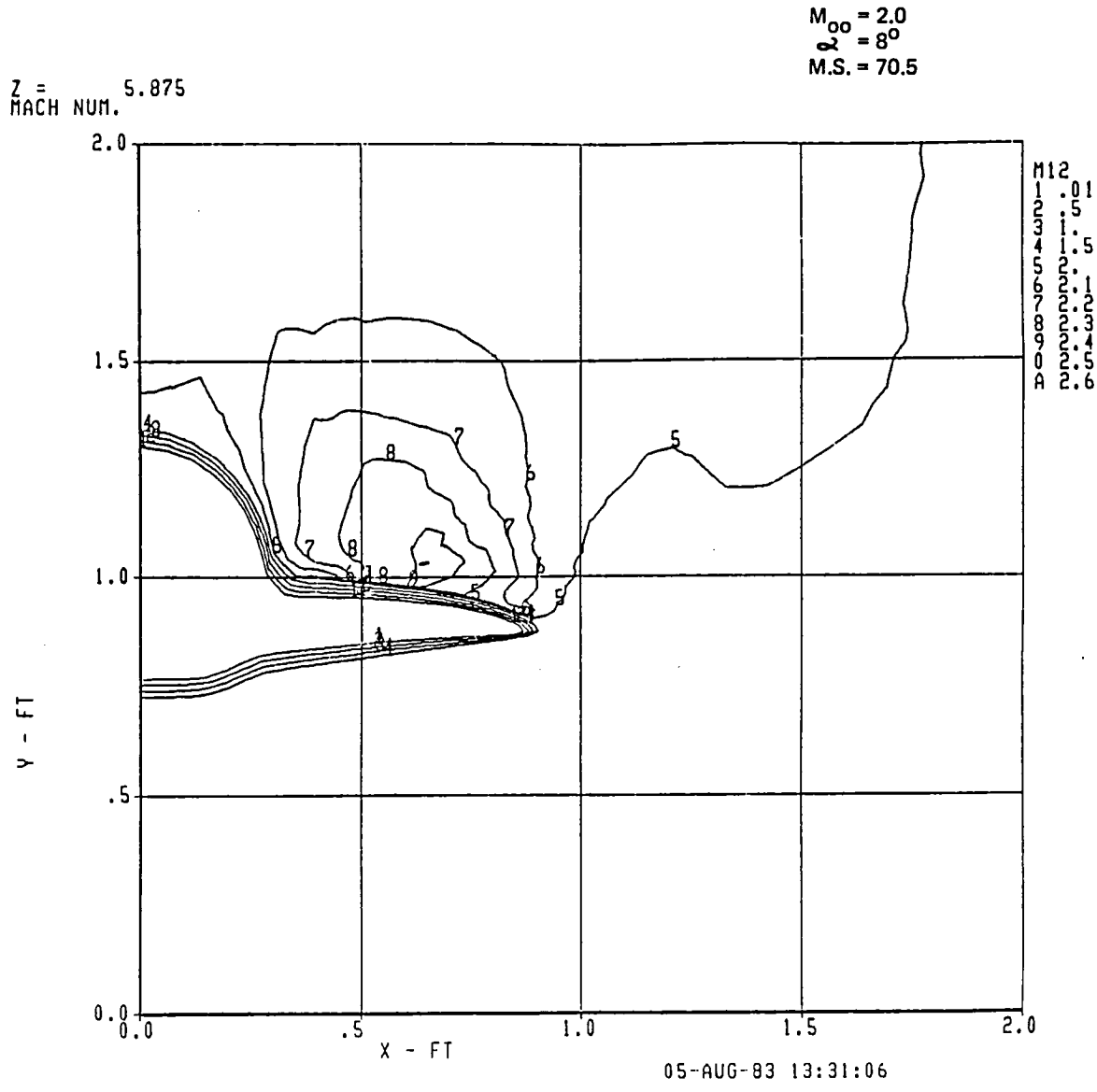

Figure 21(a). Mach Contours

Figure 21. Computed Results for Model Station 70.5, Mach 2.0, at 8-deg Angle of Attack

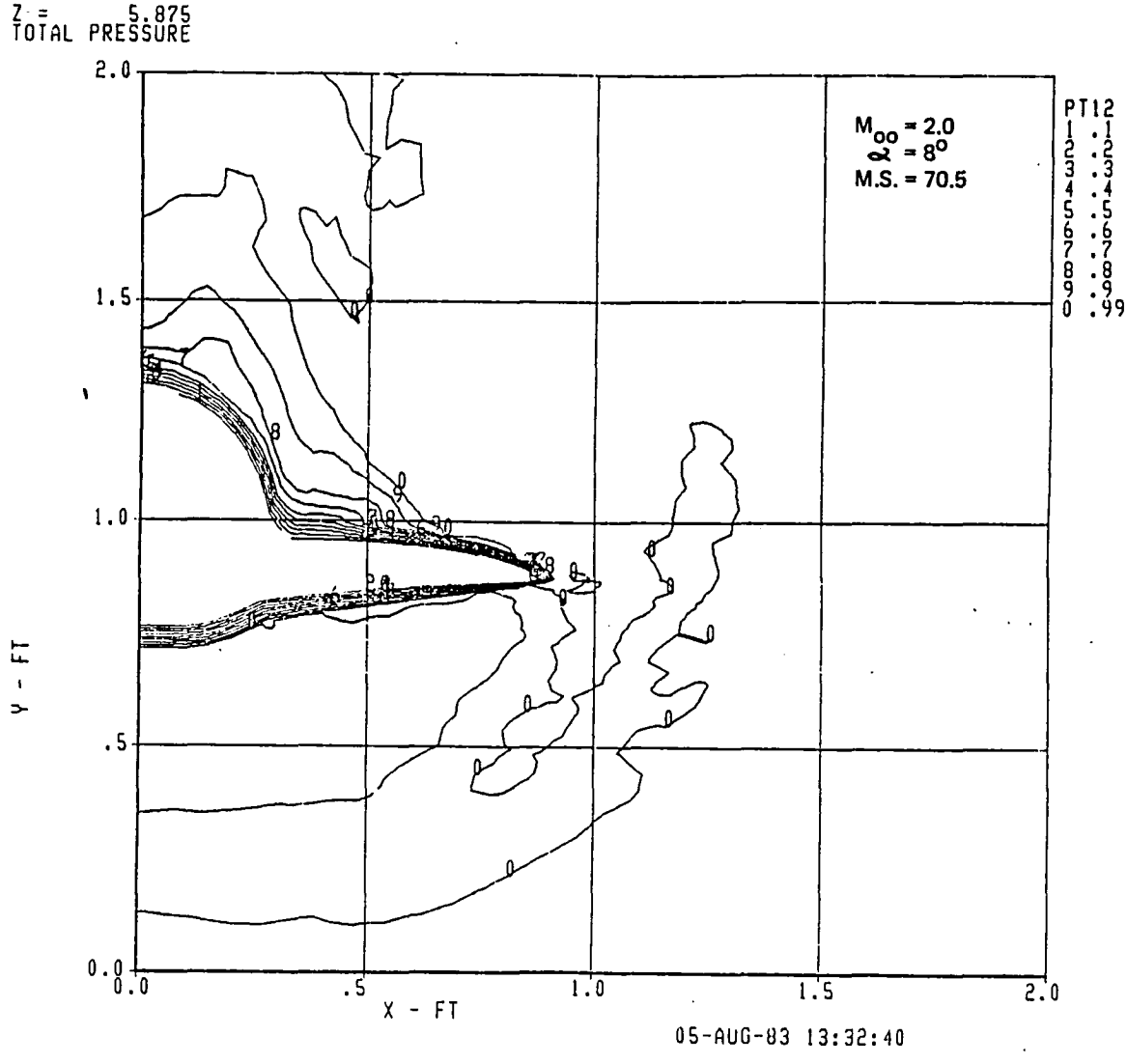

Figure 21(b). Total Pressure Contours

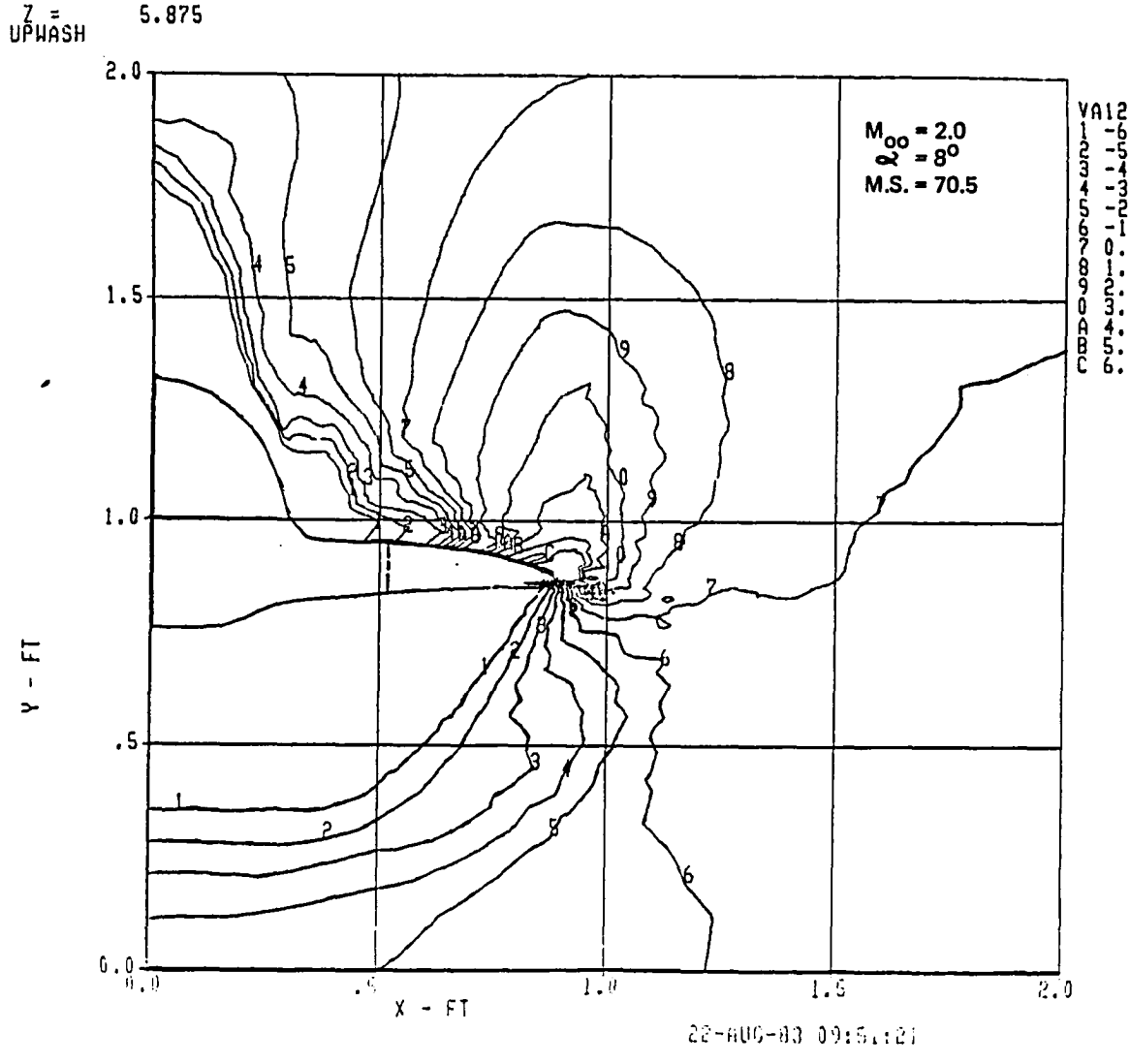

Figure 21(c). Upwash Angle Contours

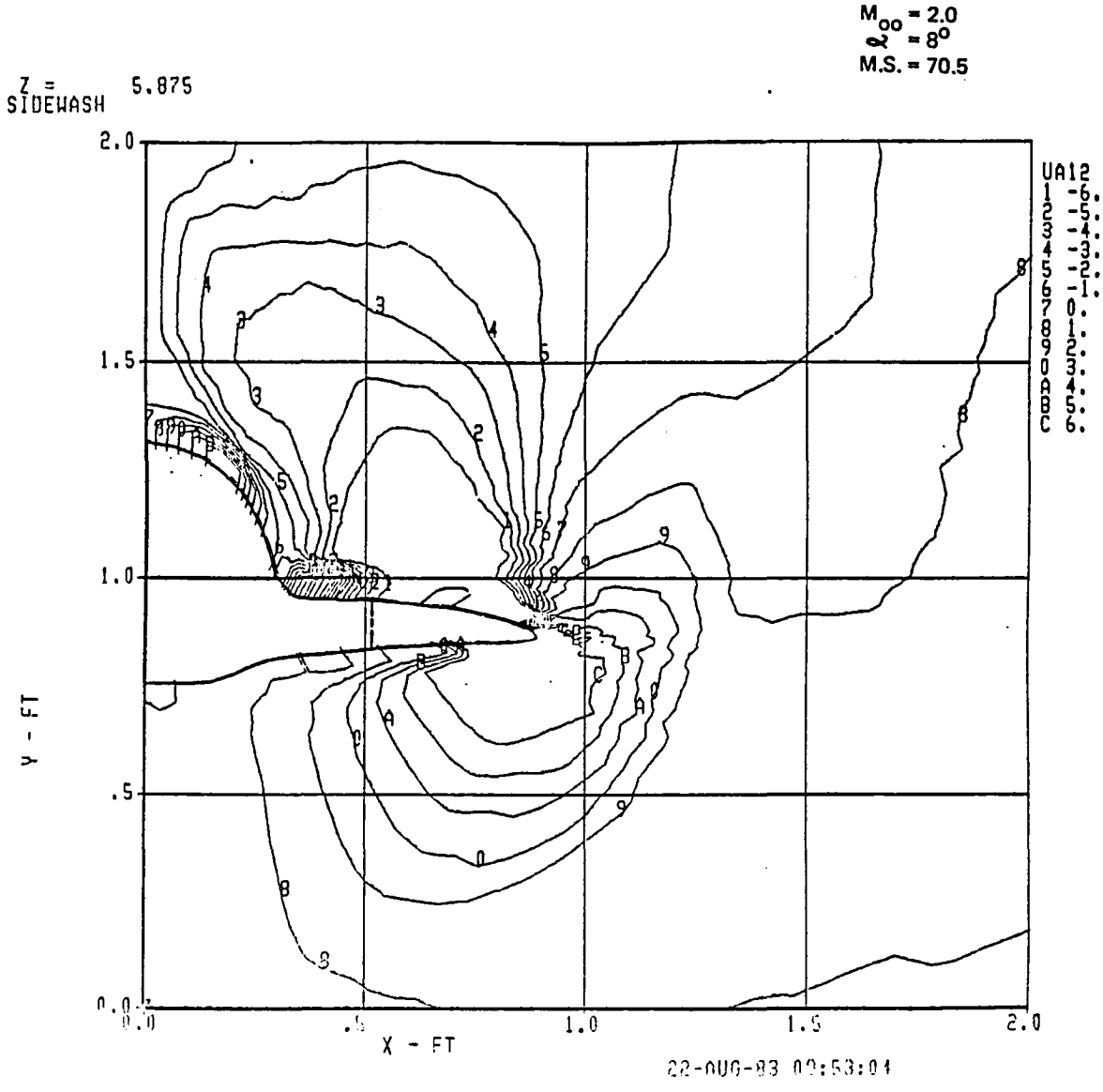

Figure 21(d). Sidewash Angle Contours

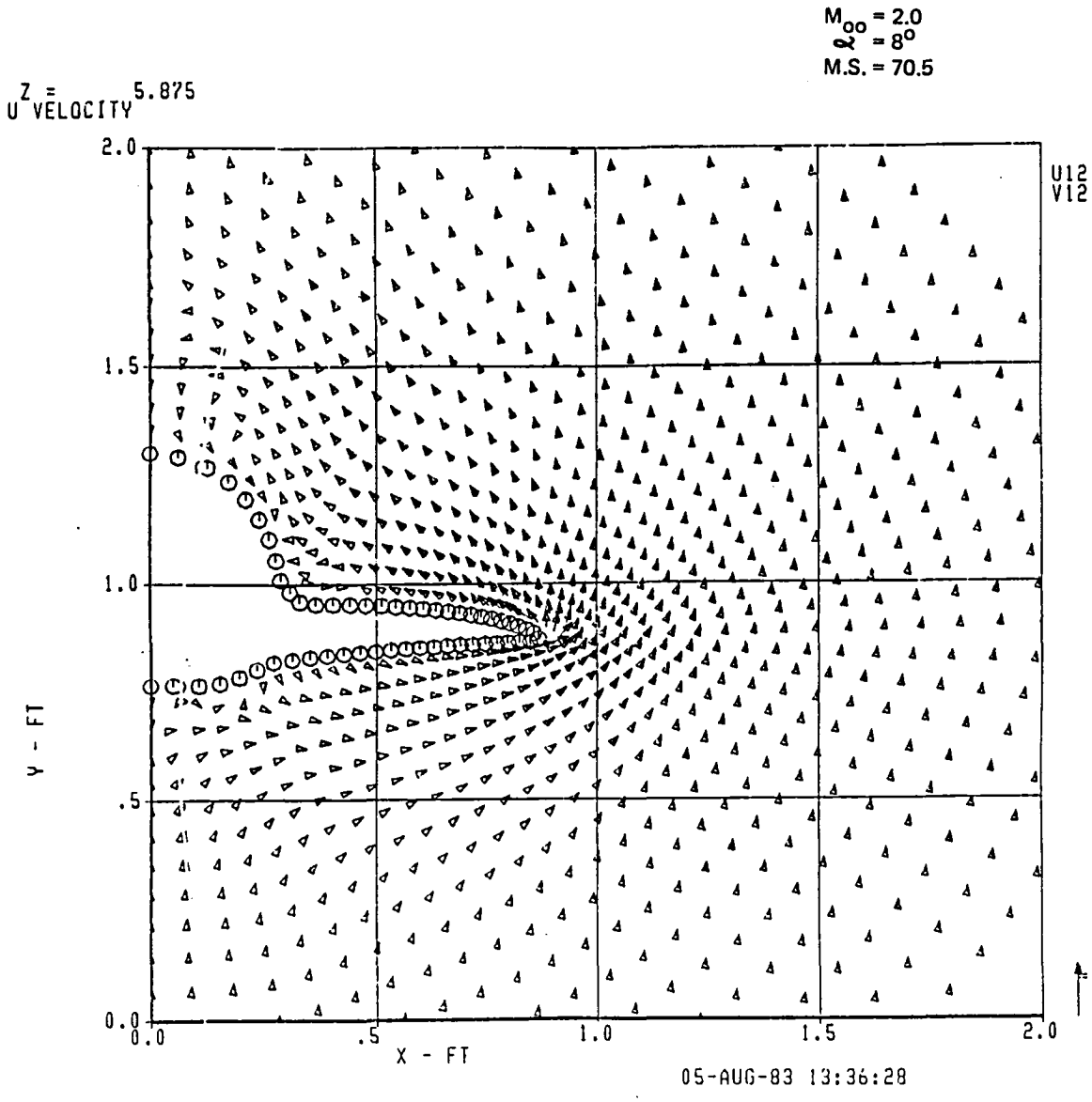

Figure 21(e). Cross-Plane Velocity

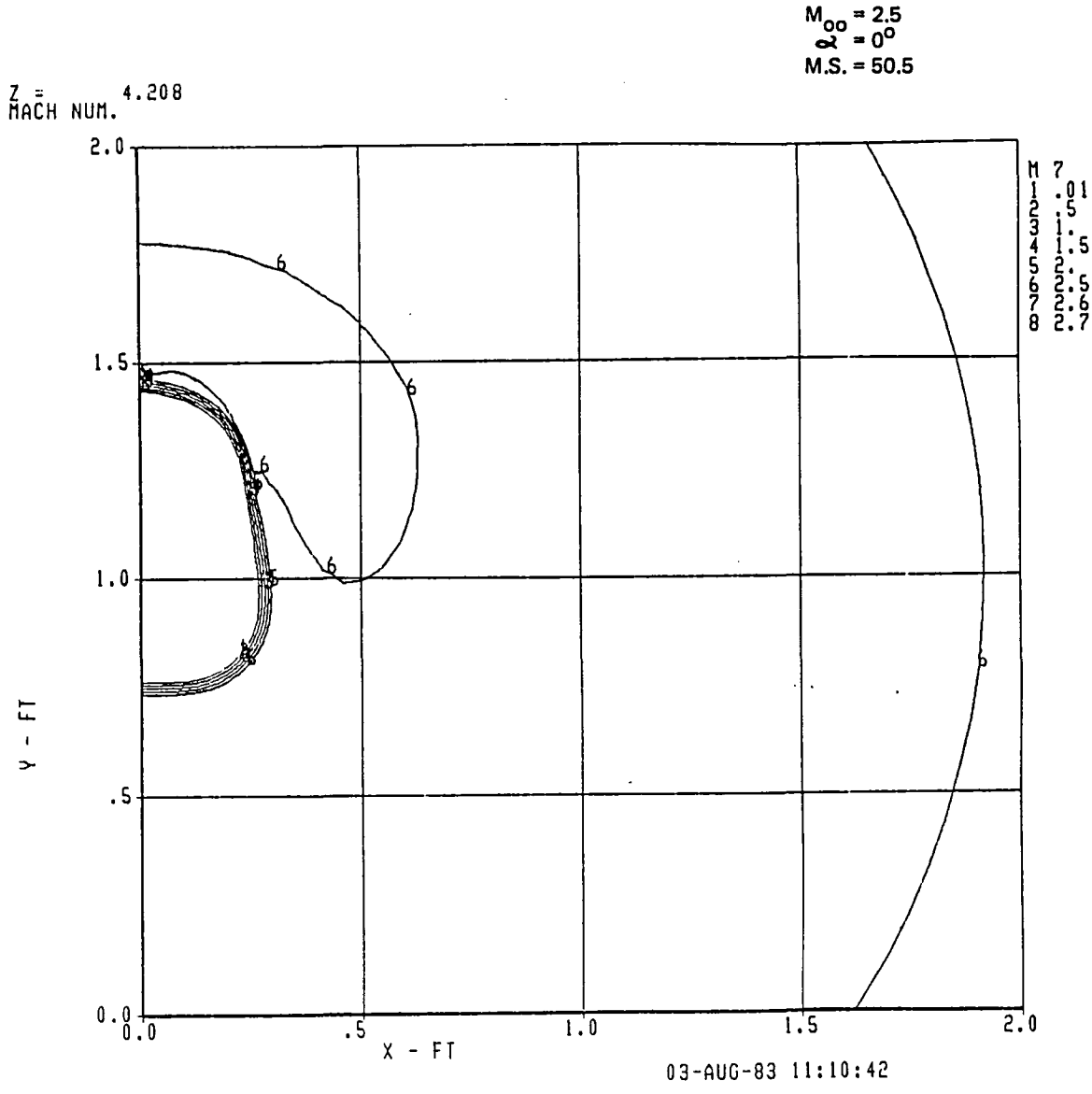

Figure 22(a). Mach Contours

Figure 22. Computed Results for Model Station 50.5, Mach 2.5, at 0-deg Angle of Attack

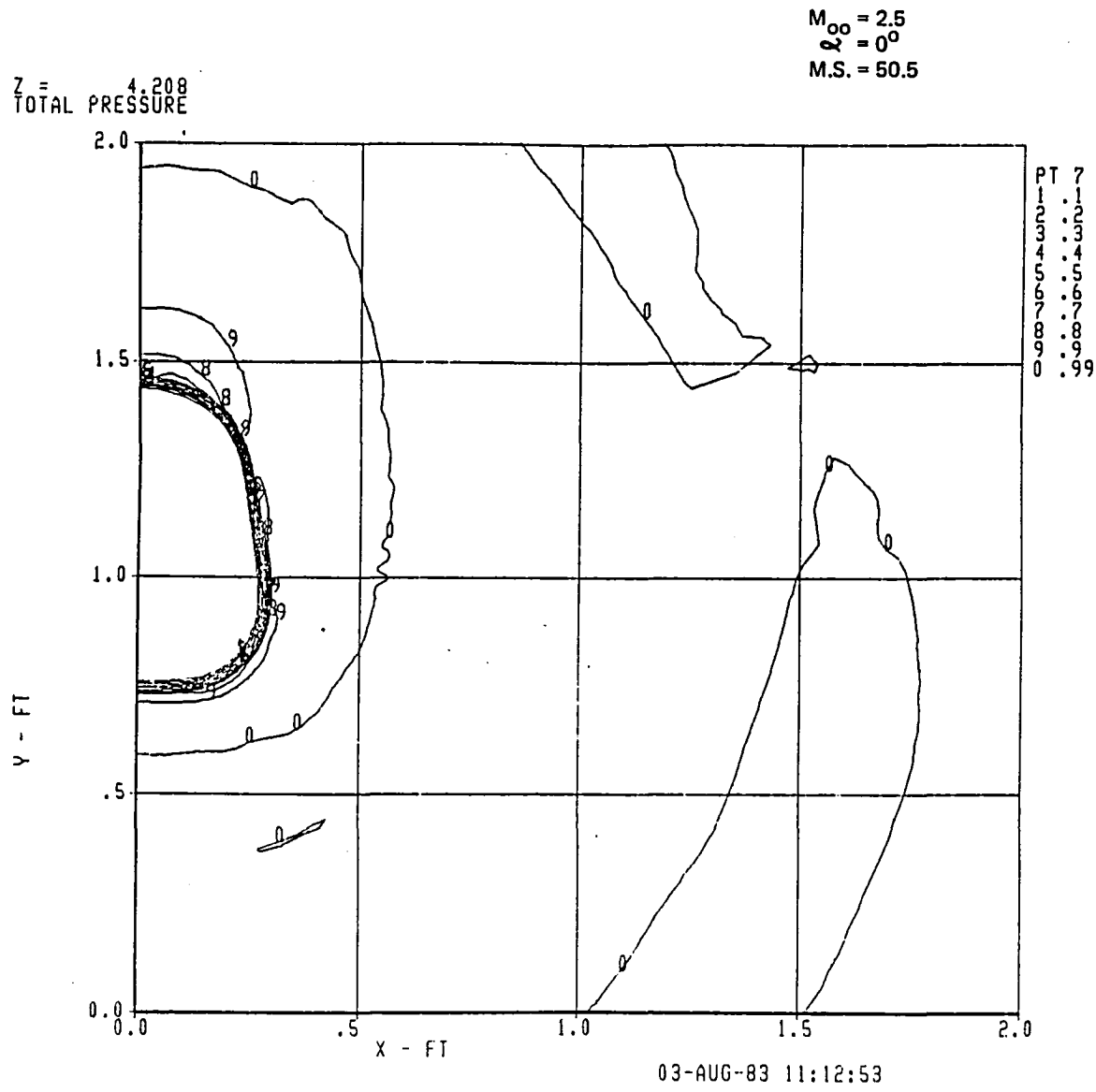

Figure 22(b). Total Pressure Contours

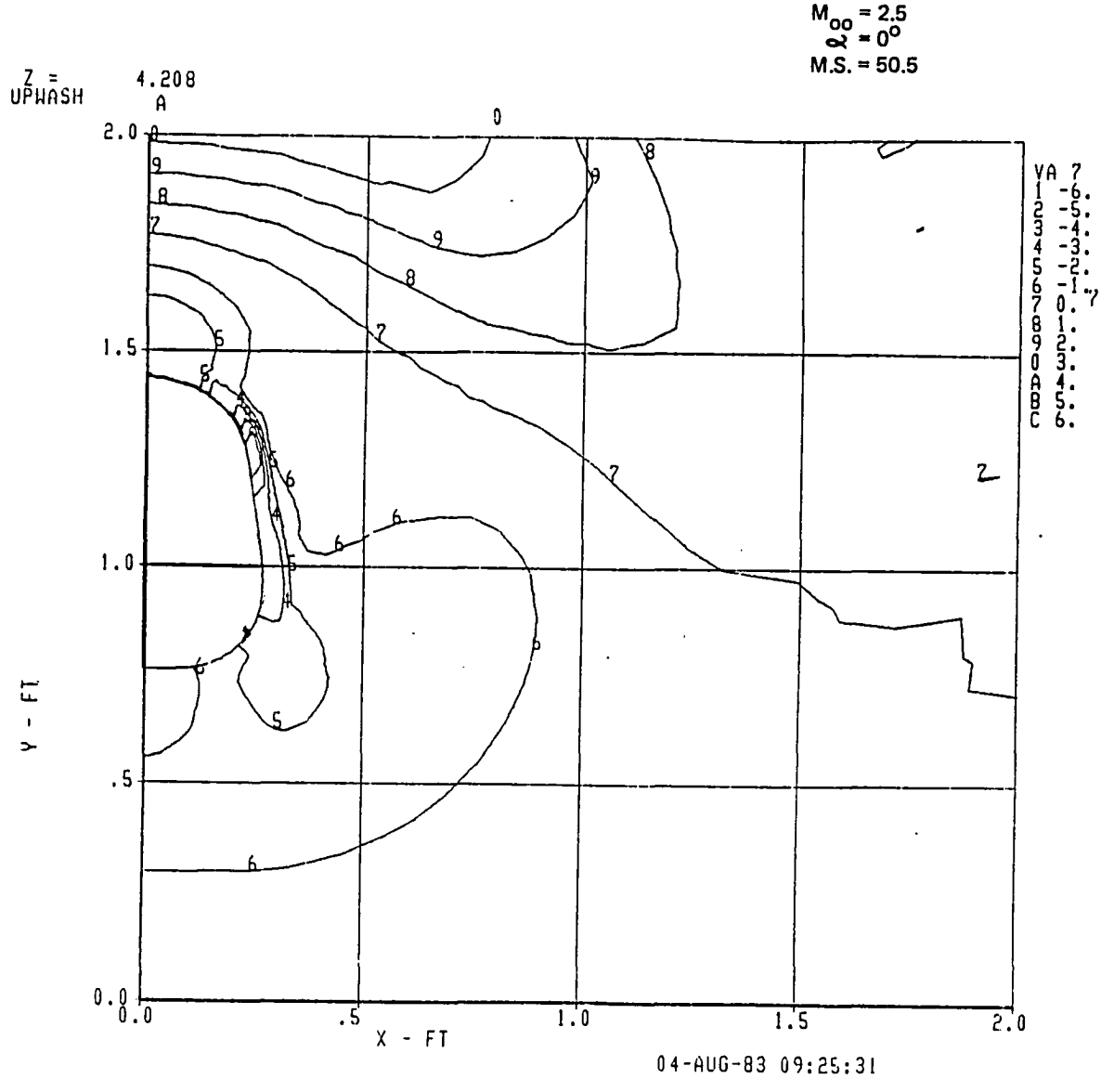

Figure 22(c). Upwash Angle Contours

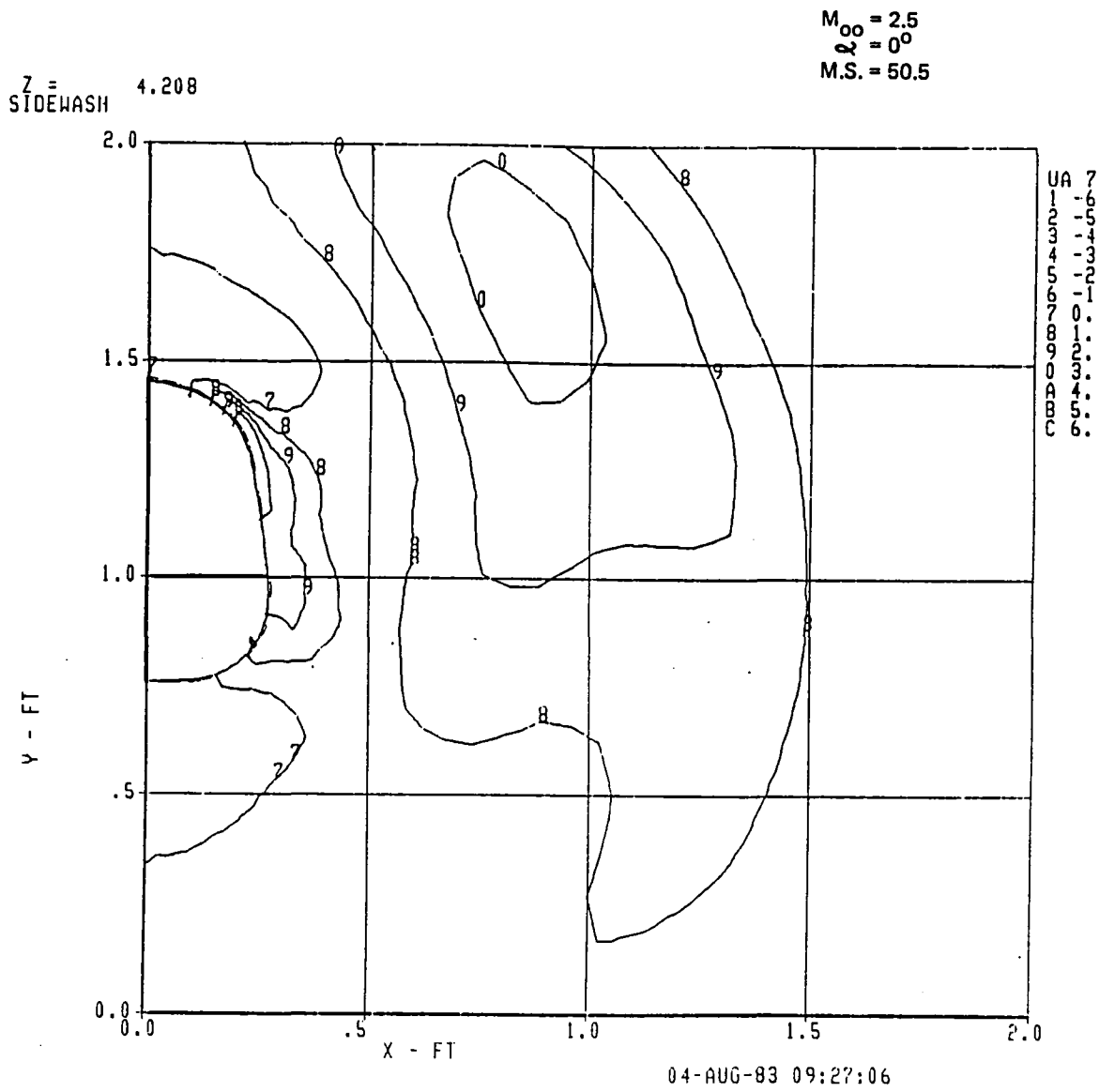

Figure 22(d). Sidewash Angle Contours

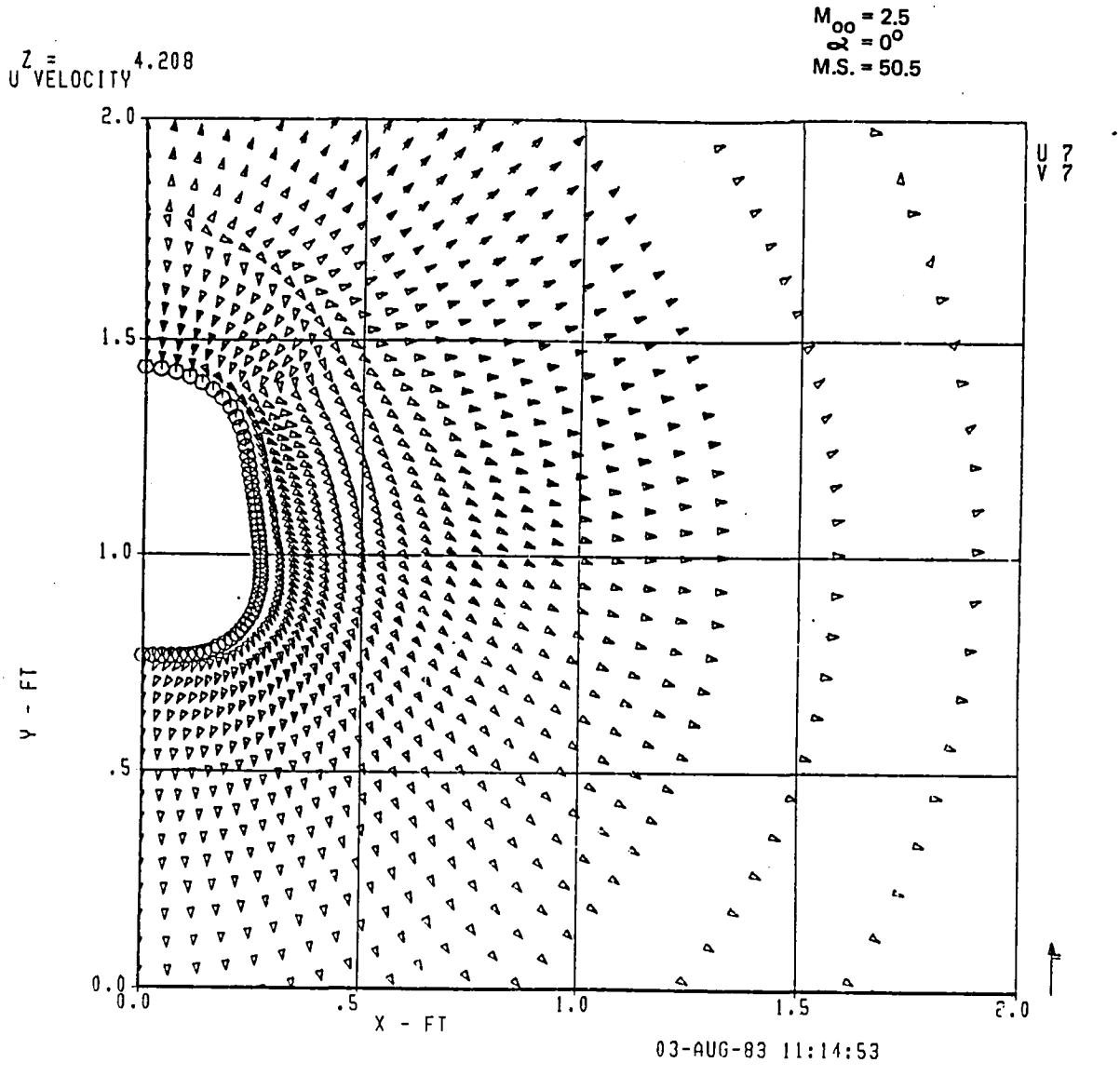

Figure 22(e). Cross-Plane Velocity

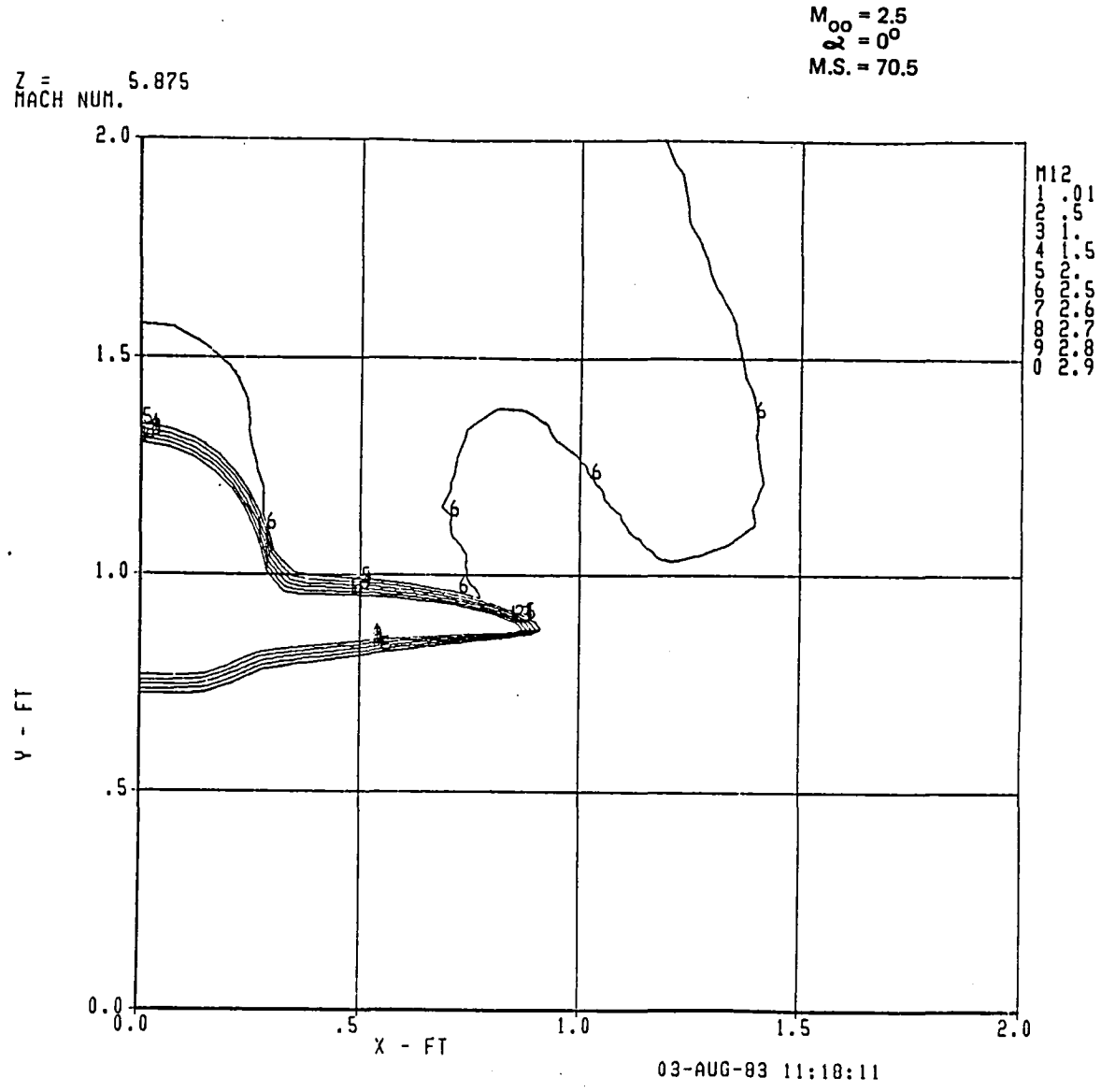

Figure 23(a). Mach Contours

Figure 23. Computed Results for Model Station 70.5, Mach 2.5, 0-deg at Angle of Attack

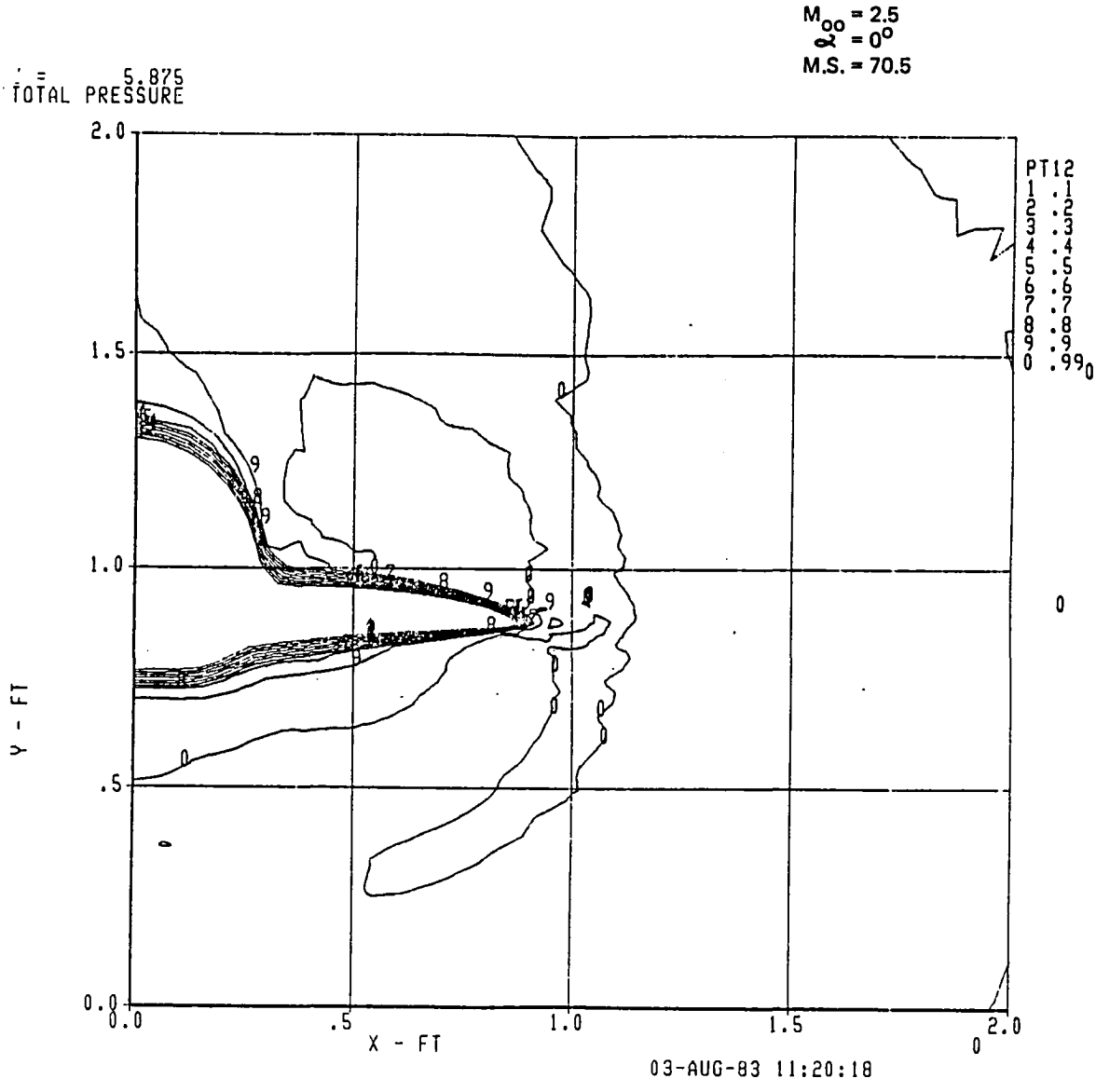

Figure 23(b). Total Pressure Contours

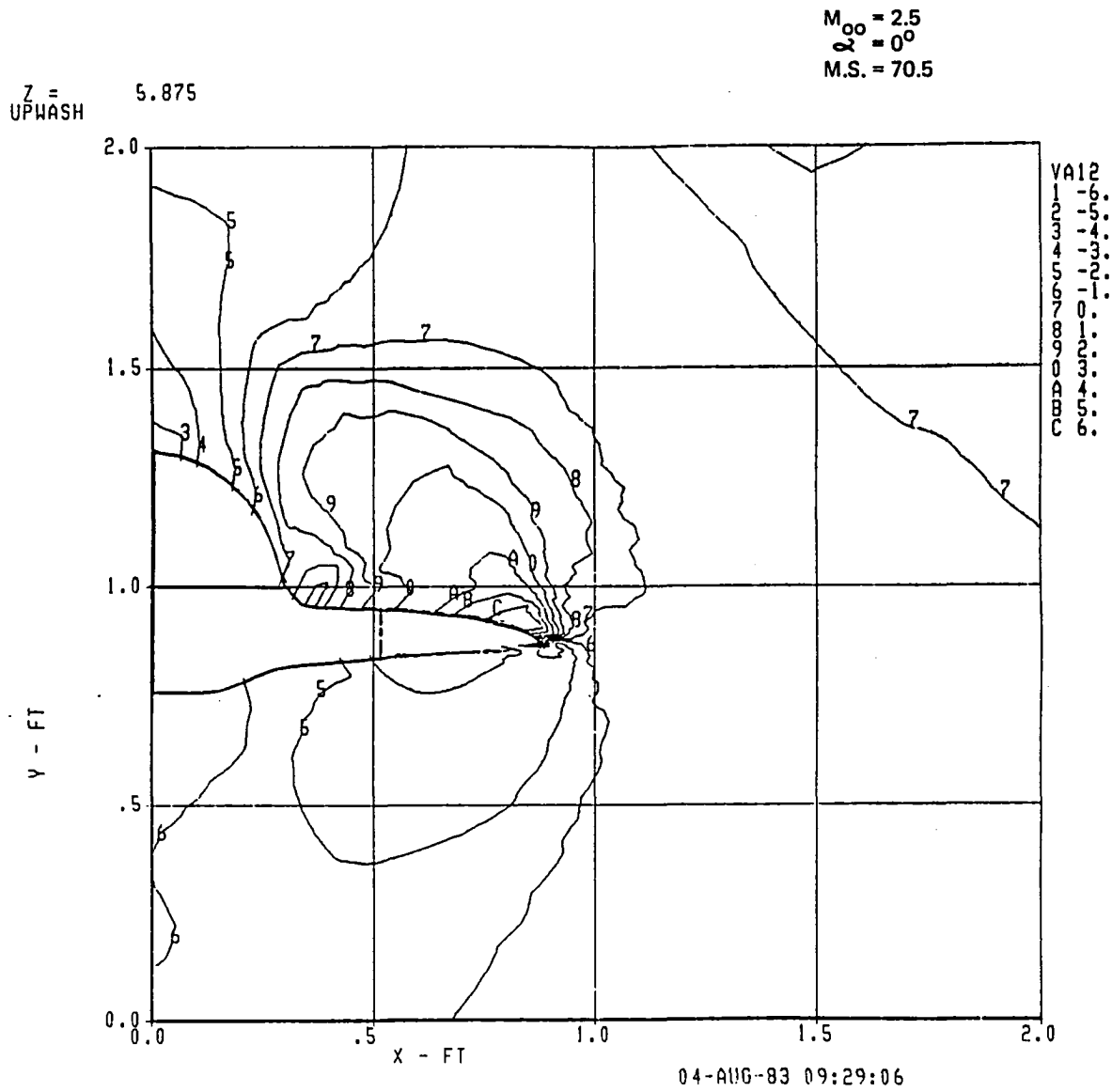

Figure 23(c). Upwash Angle Contours

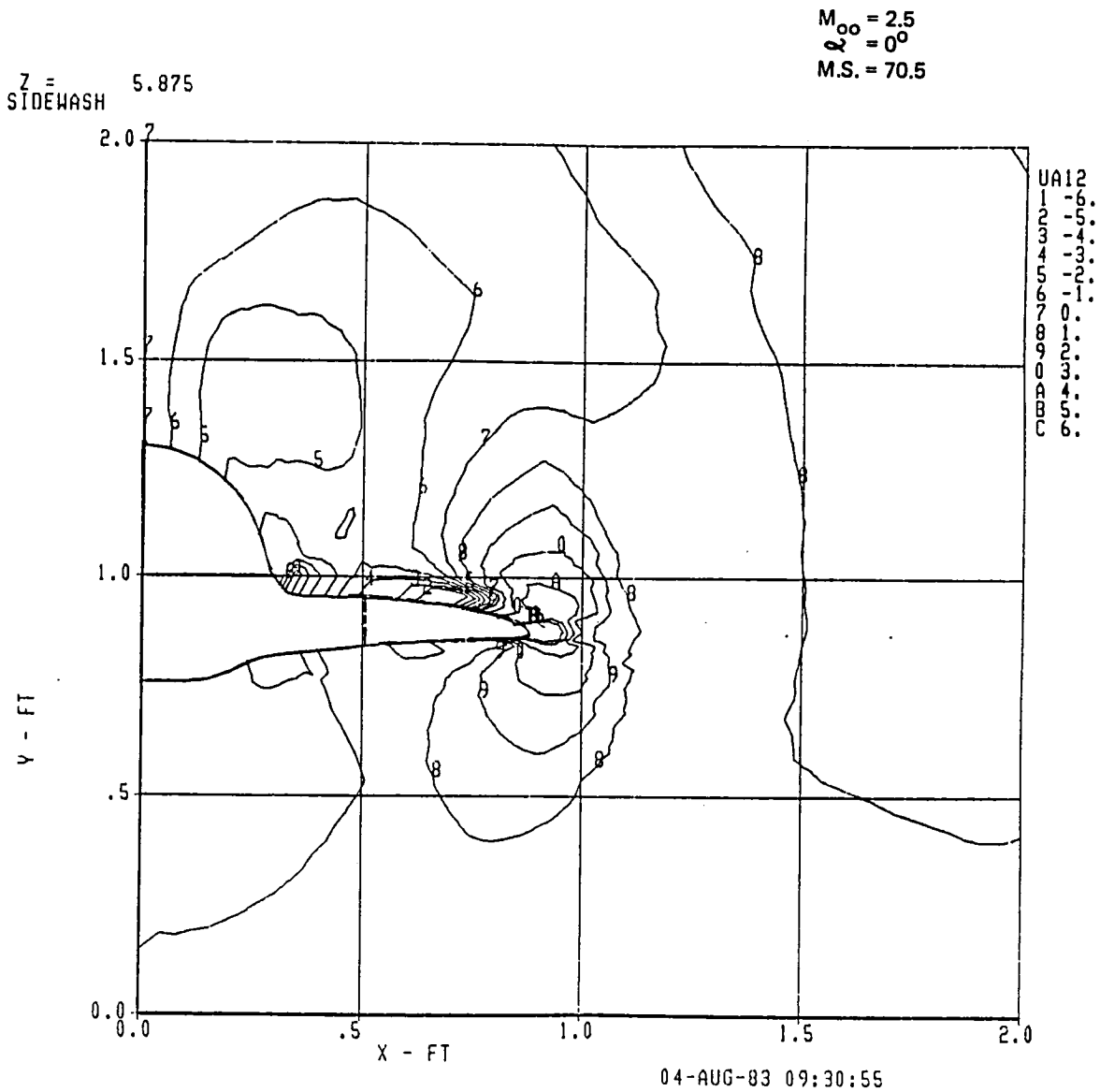

Figure 23(d). Sidewash Angle Contours

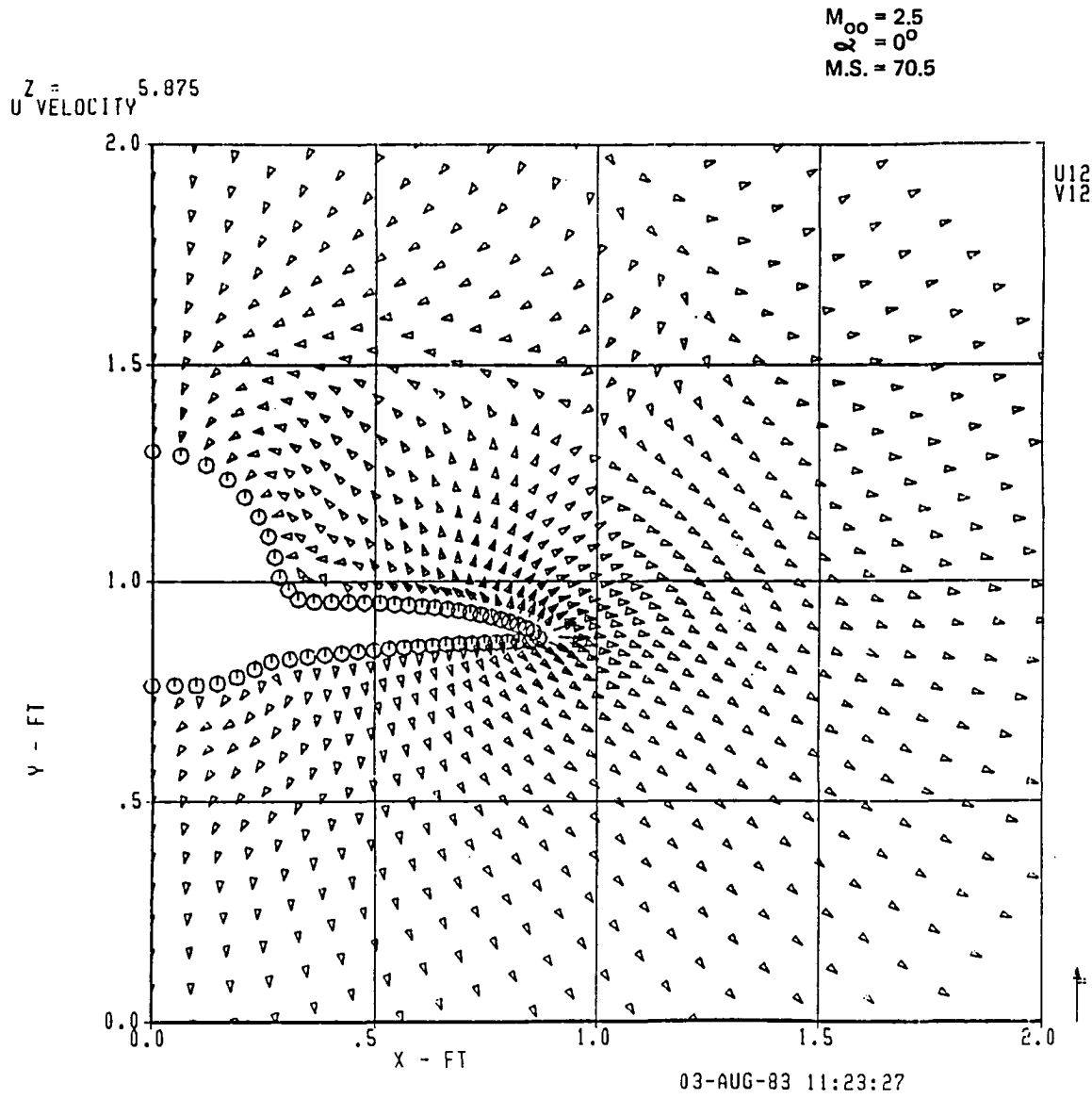

Figure 23(e). Cross-Plane Velocity

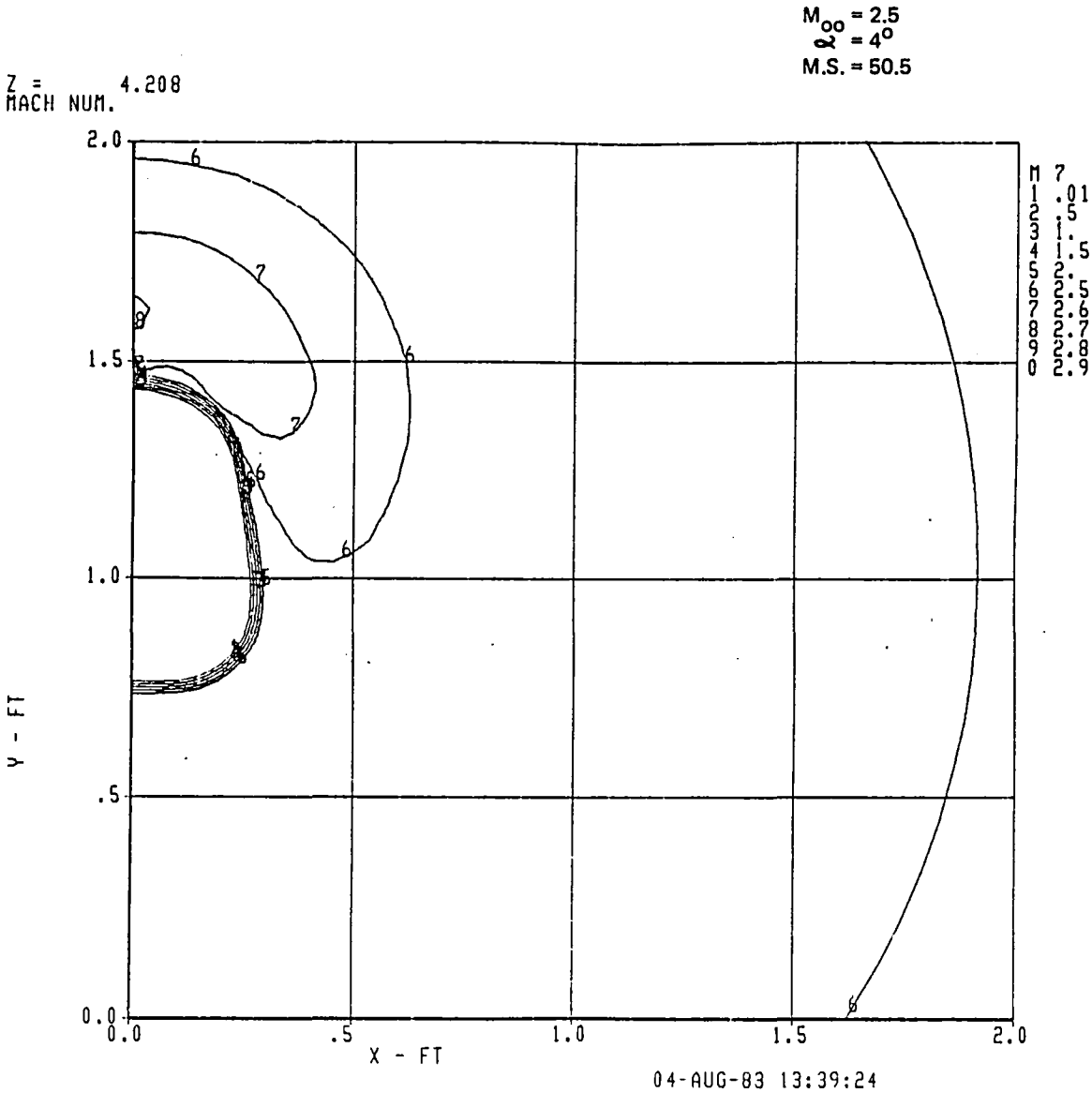

Figure 24(a). Mach Contours

Figure 24. Computed Results for Model Station 50.5, Mach 2.5, at 4-deg Angle of Attack

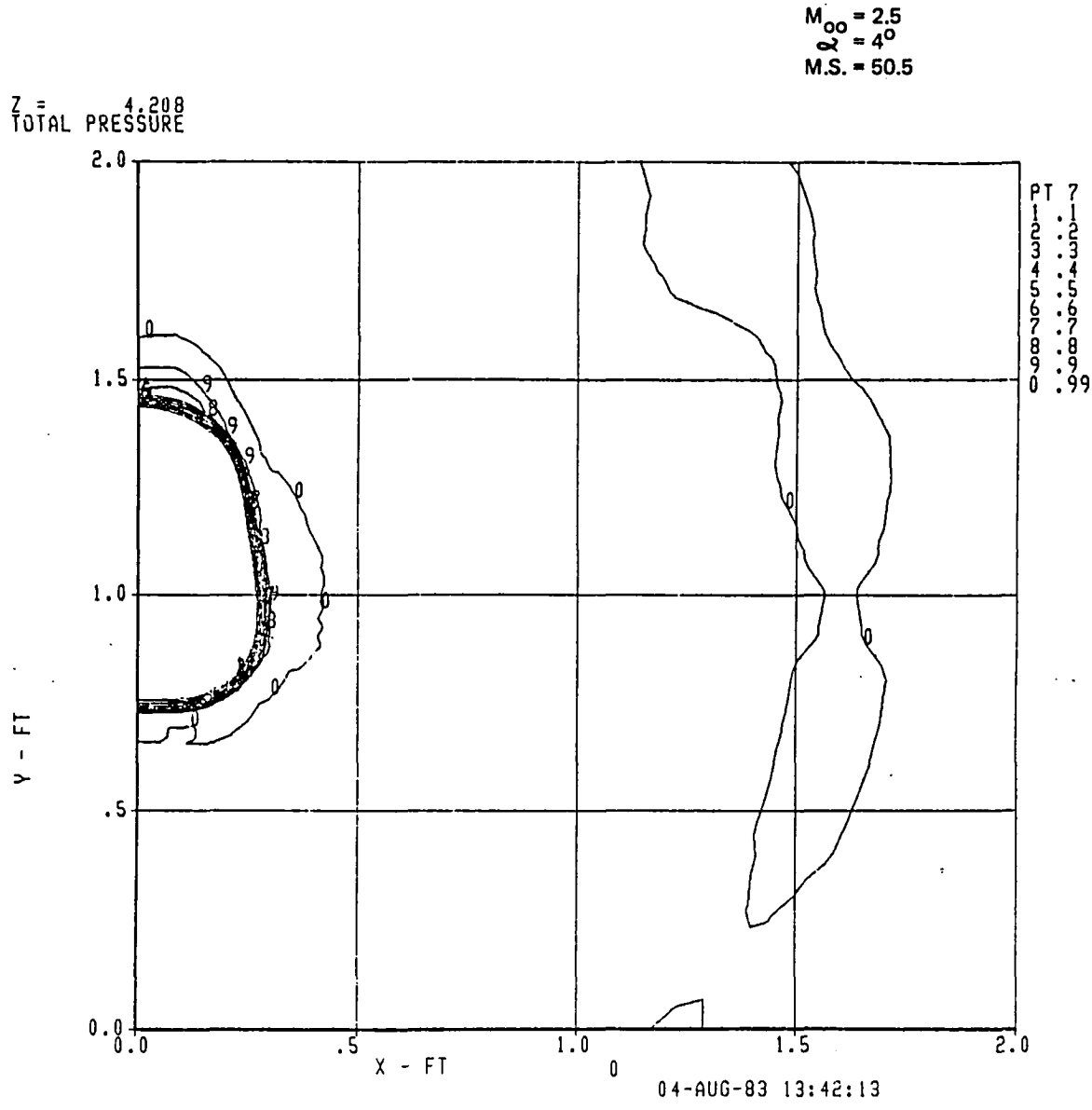

Figure 24(b). Total Pressure Contours

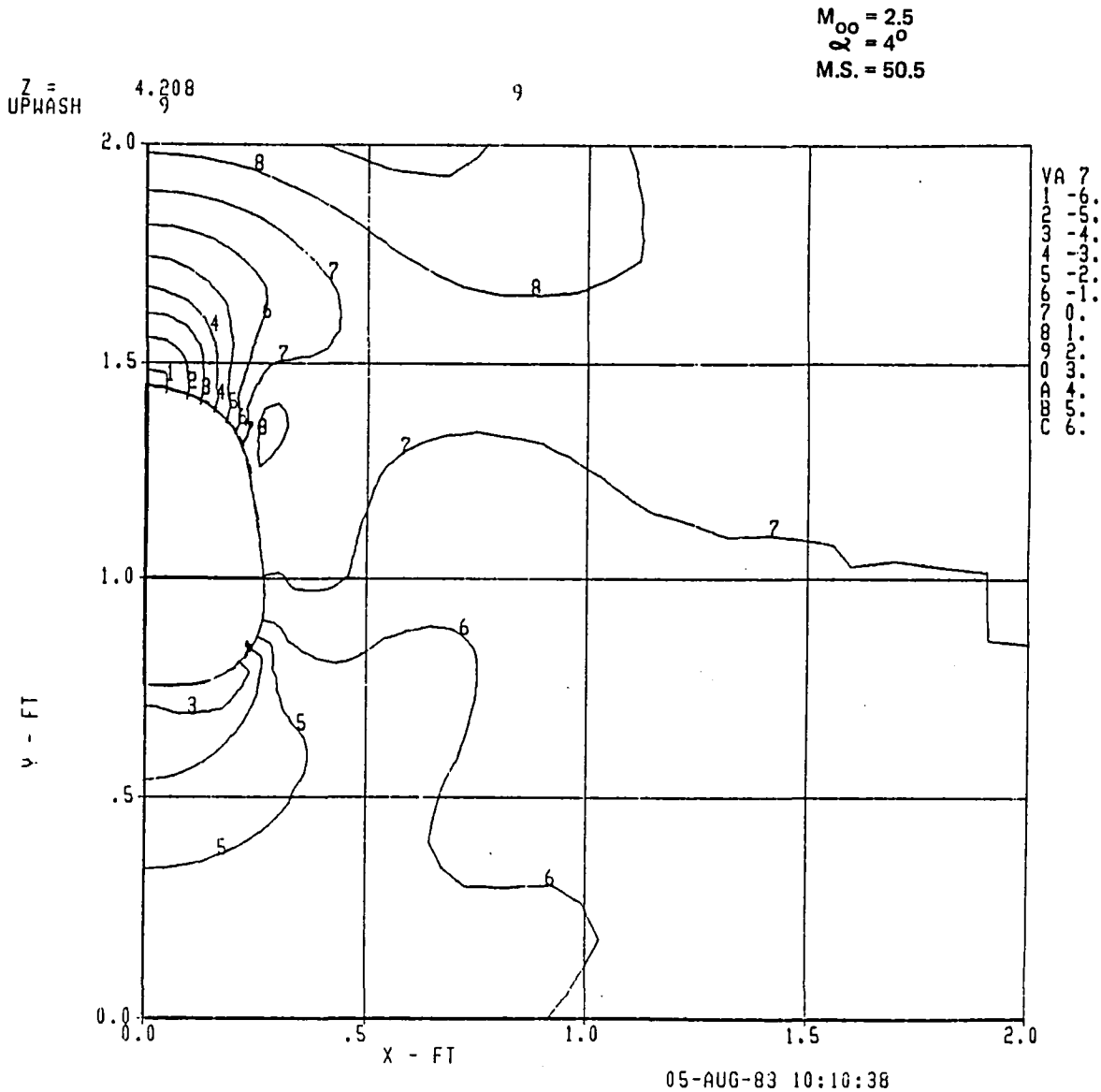

Figure 24(c). Upwash Angle Contours

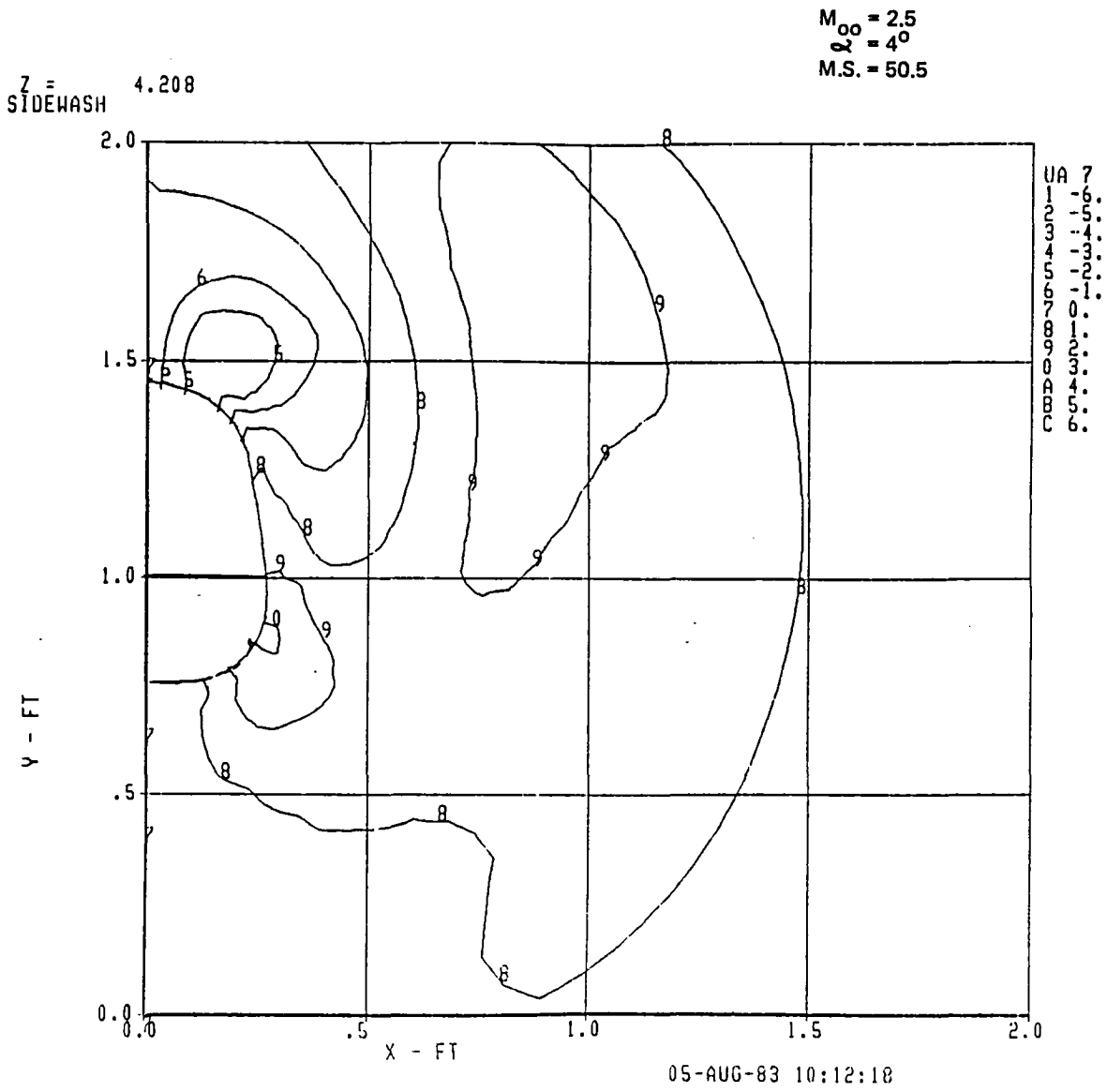

Figure 24(d). Sidewash Angle Contours

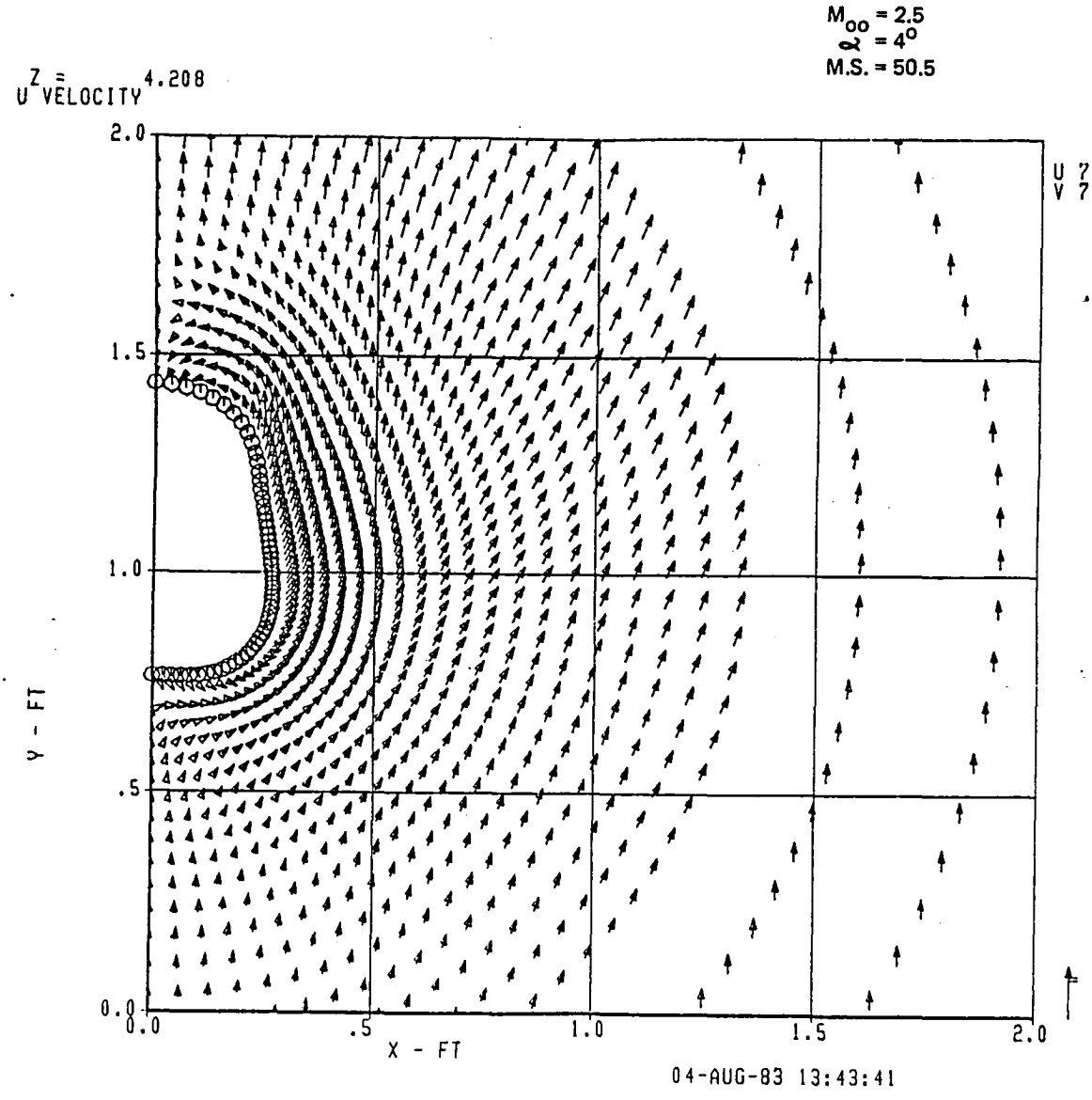

Figure 24(e). Cross-Plane Velocity

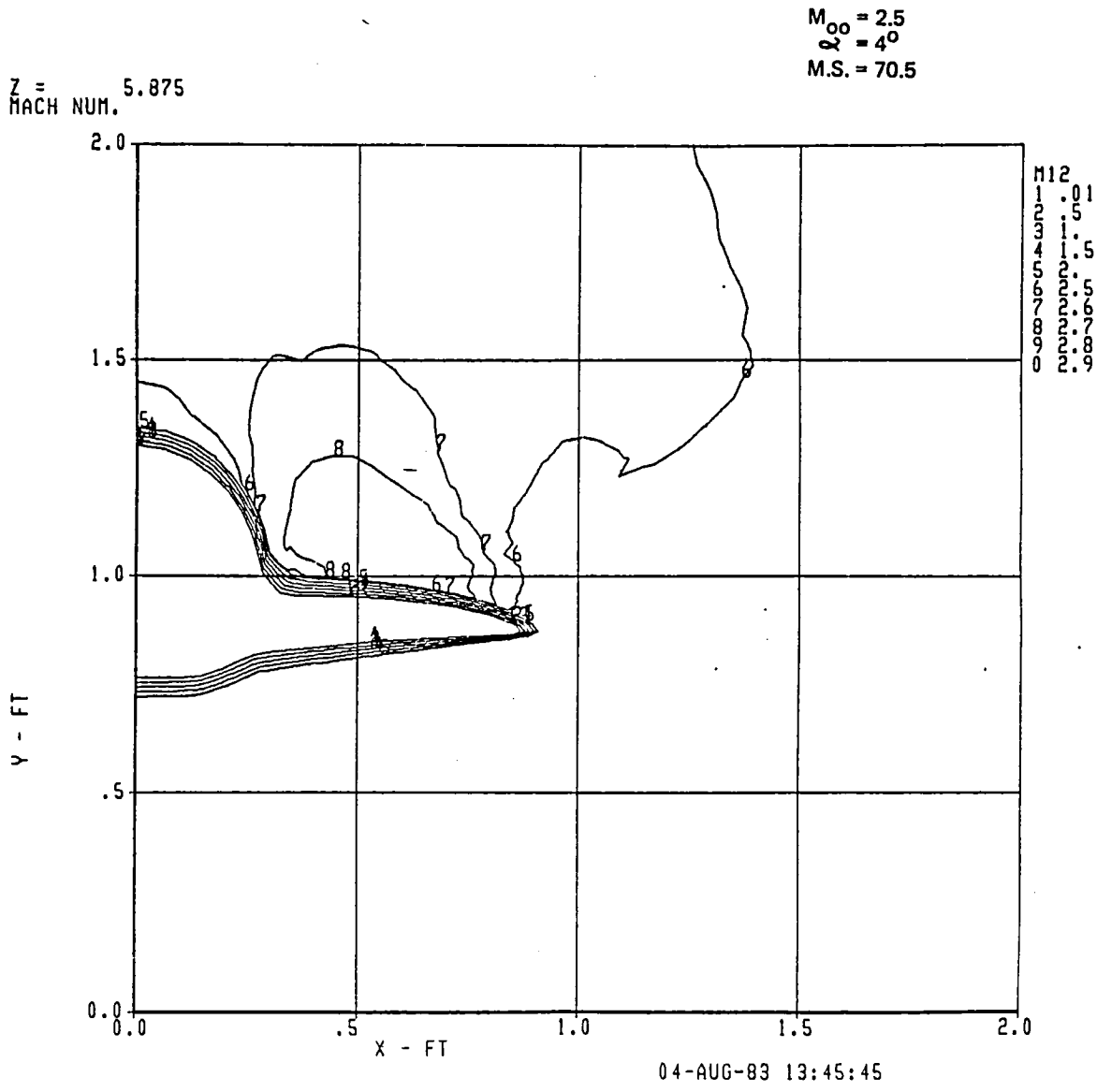

Figure 25(a). Mach Contours

Figure 25. Computed Results for Model Station 70.5, Mach 2.5, at 4-deg Angle of Attack

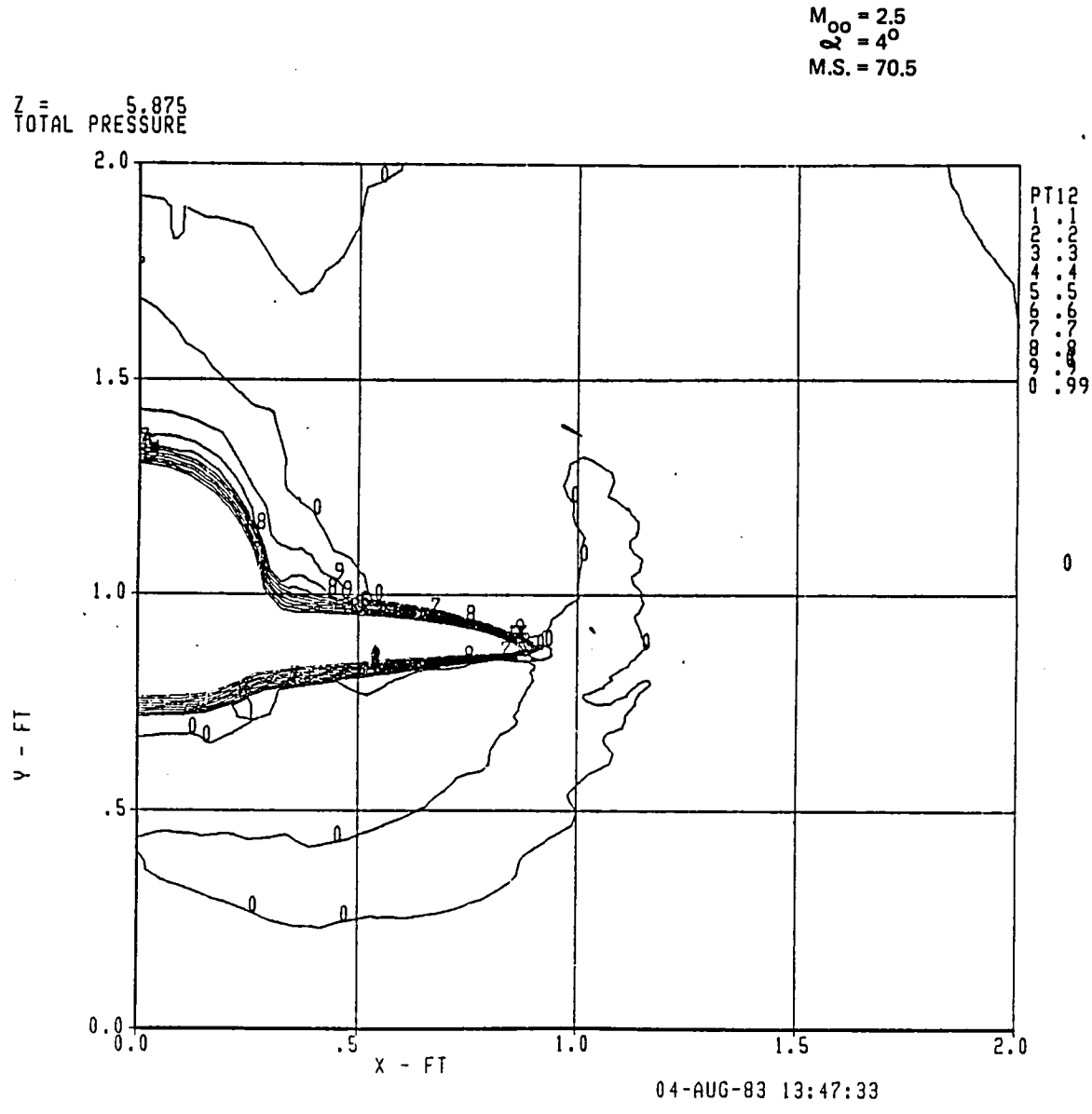

Figure 25(b). Total Pressure Contours

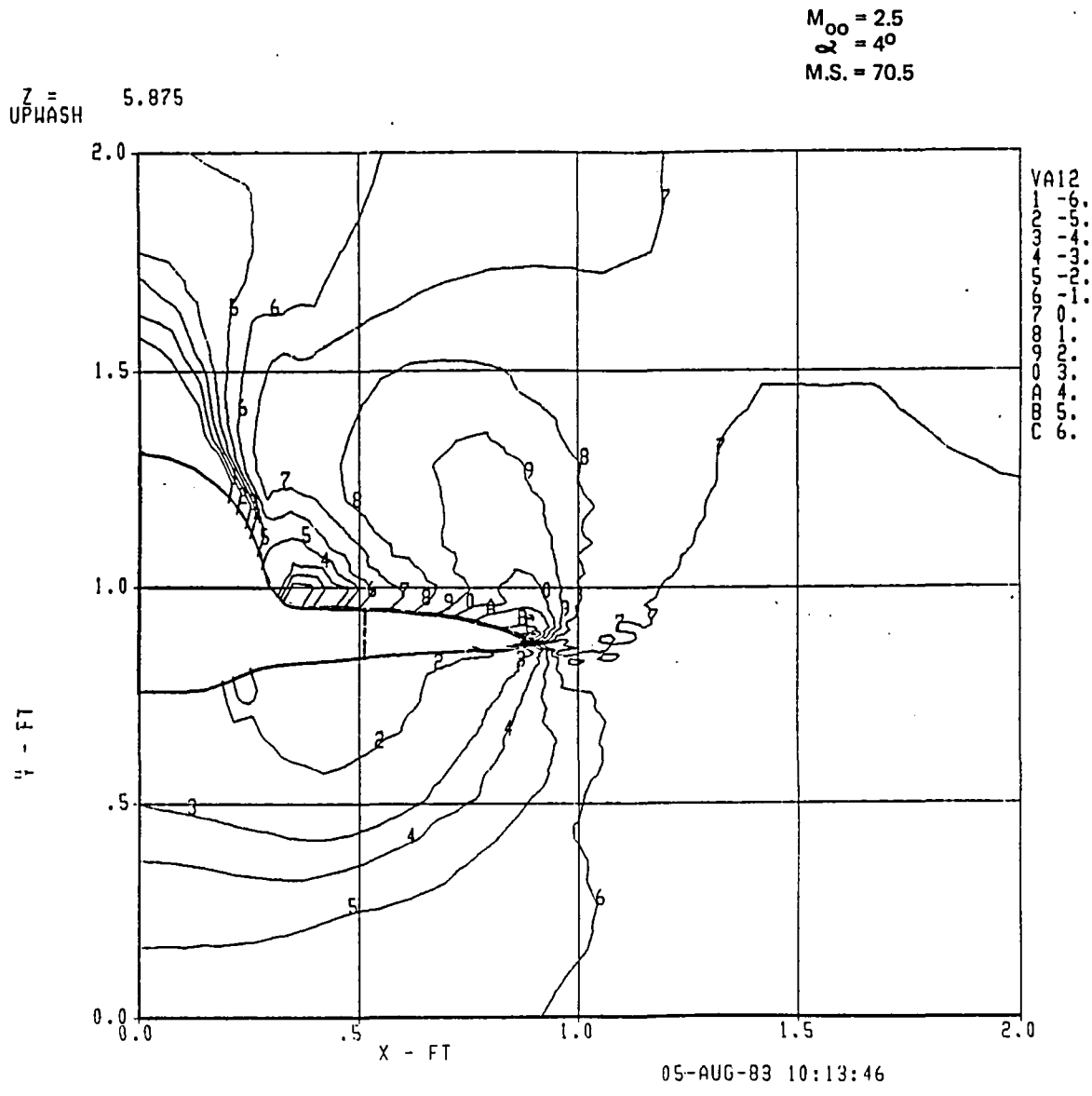

Figure 25(c). Upwash Angle Contours

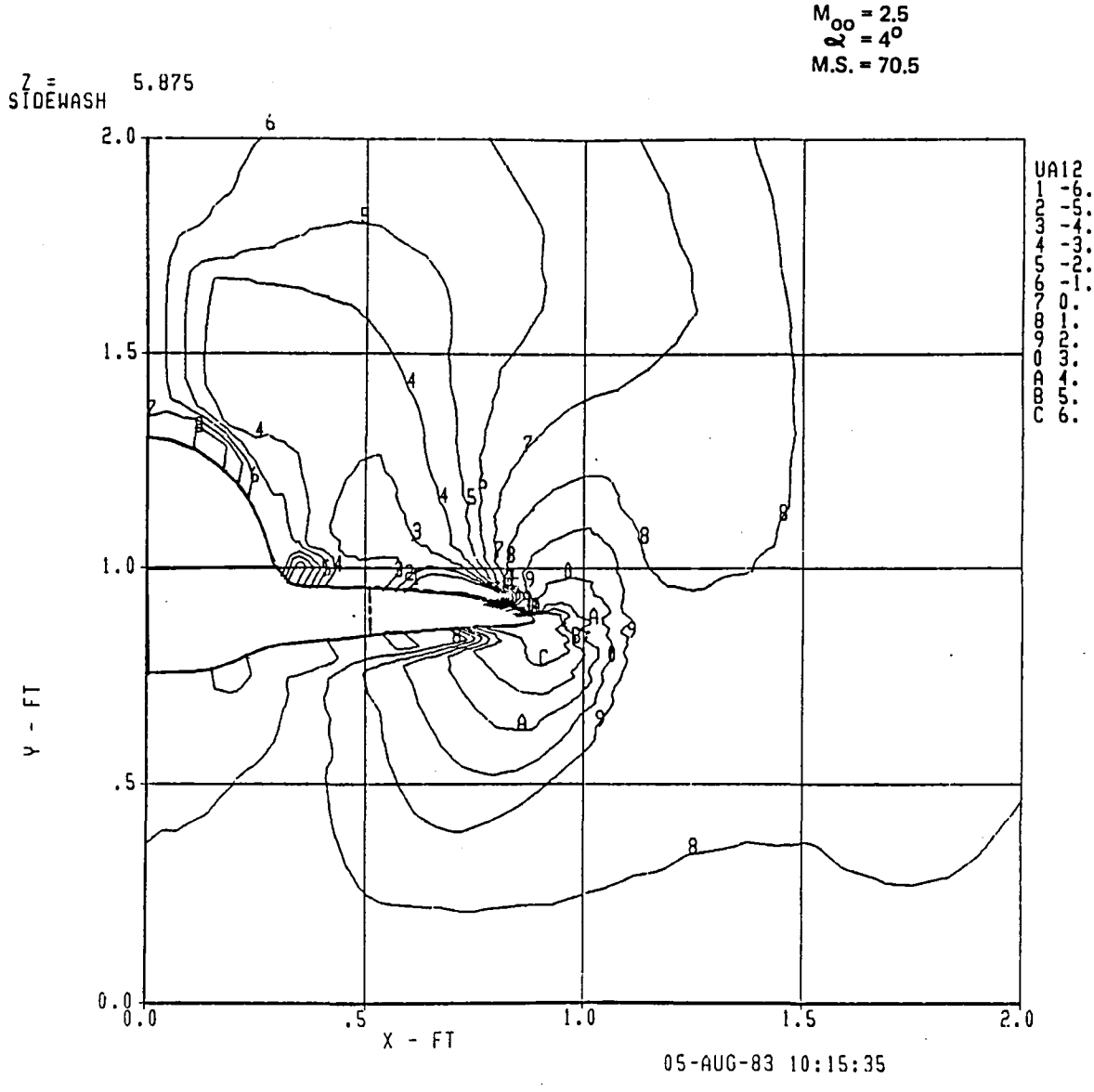

Figure 25(d). Sidewash Angle Contours

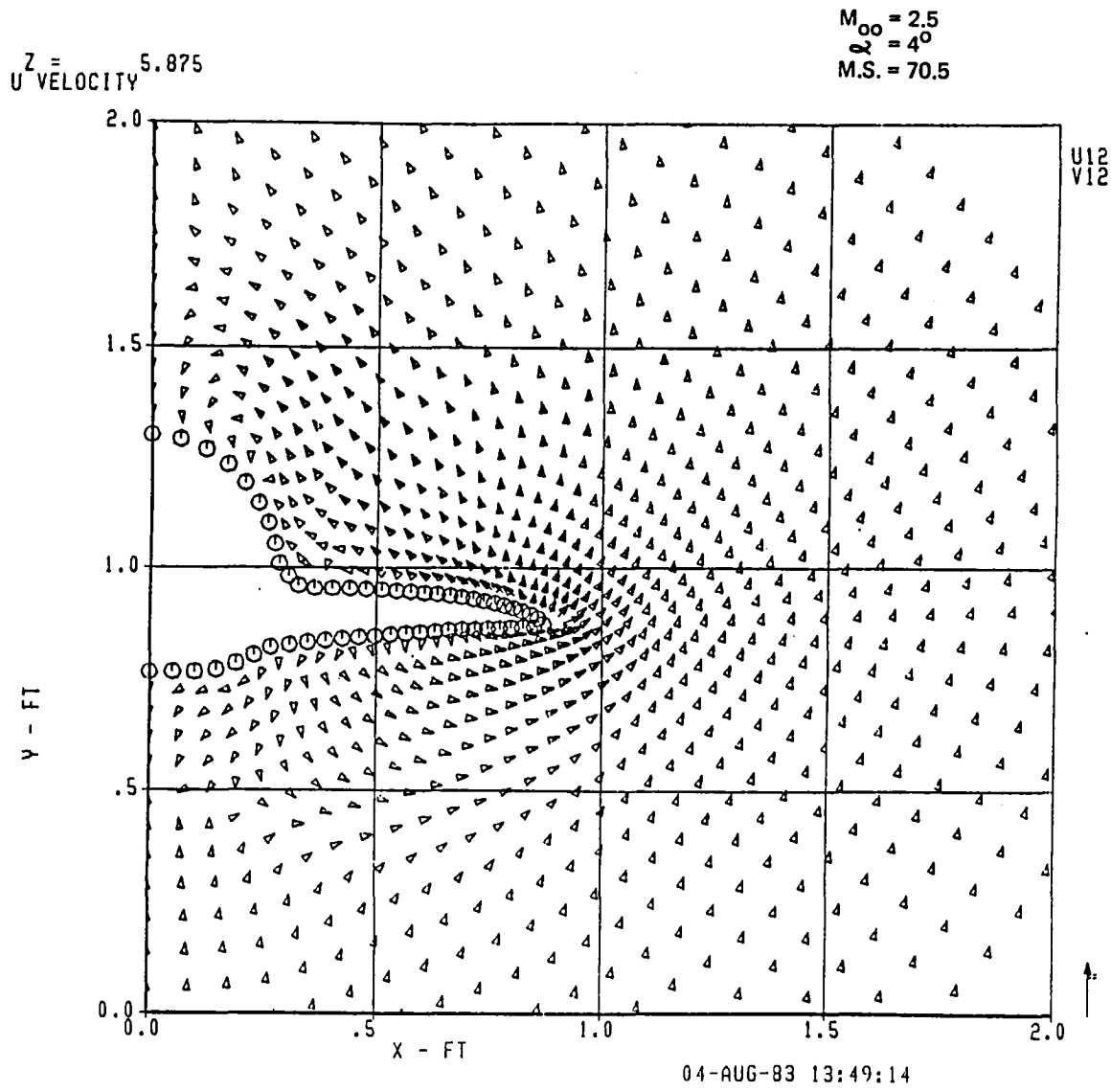

Figure 25(e). Cross-Plane Velocity

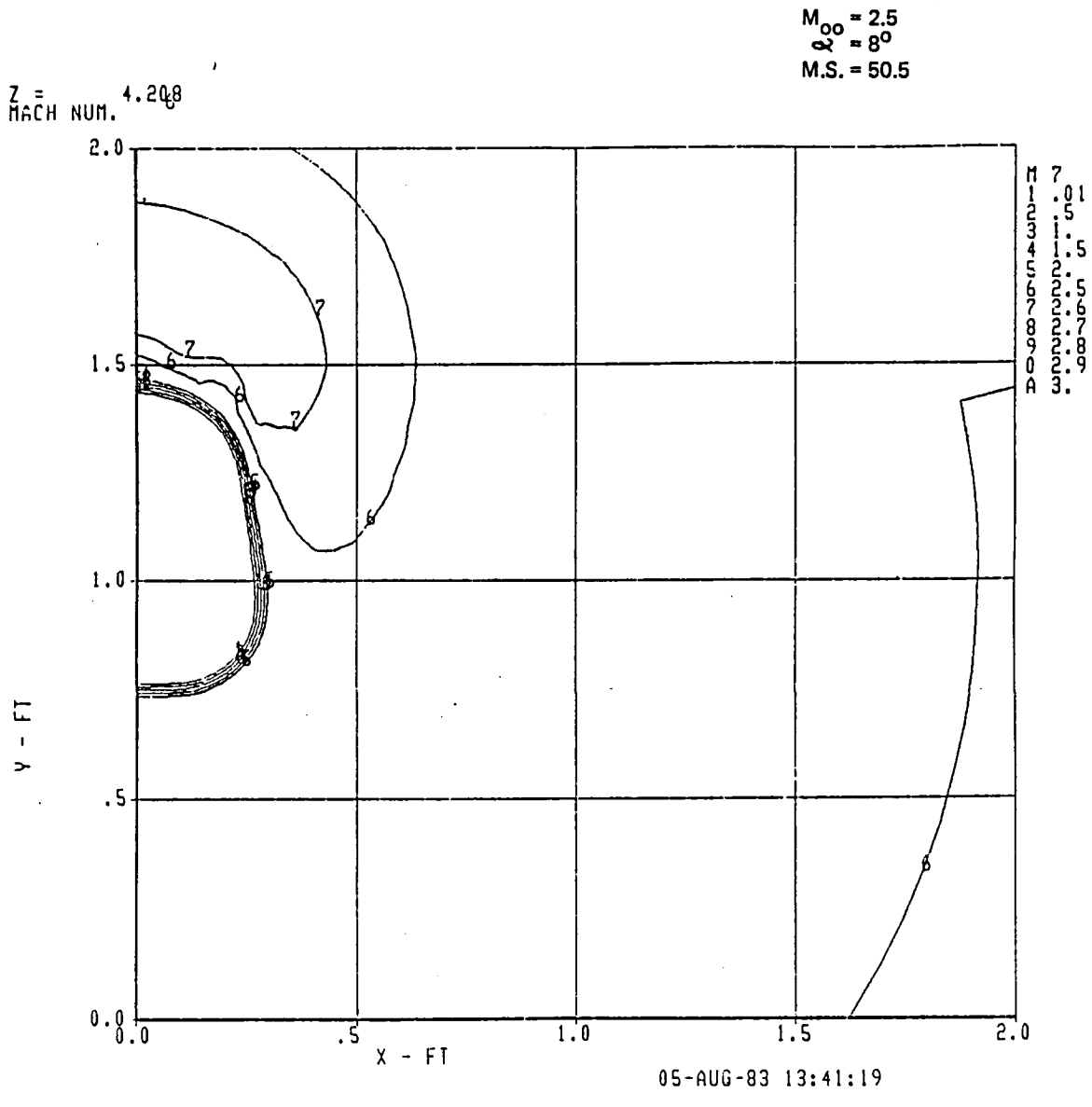

Figure 26(a). Mach Contours

Figure 26. Computed Results for Model Station 50.5, Mach 2.5, at 8-deg Angle of Attack

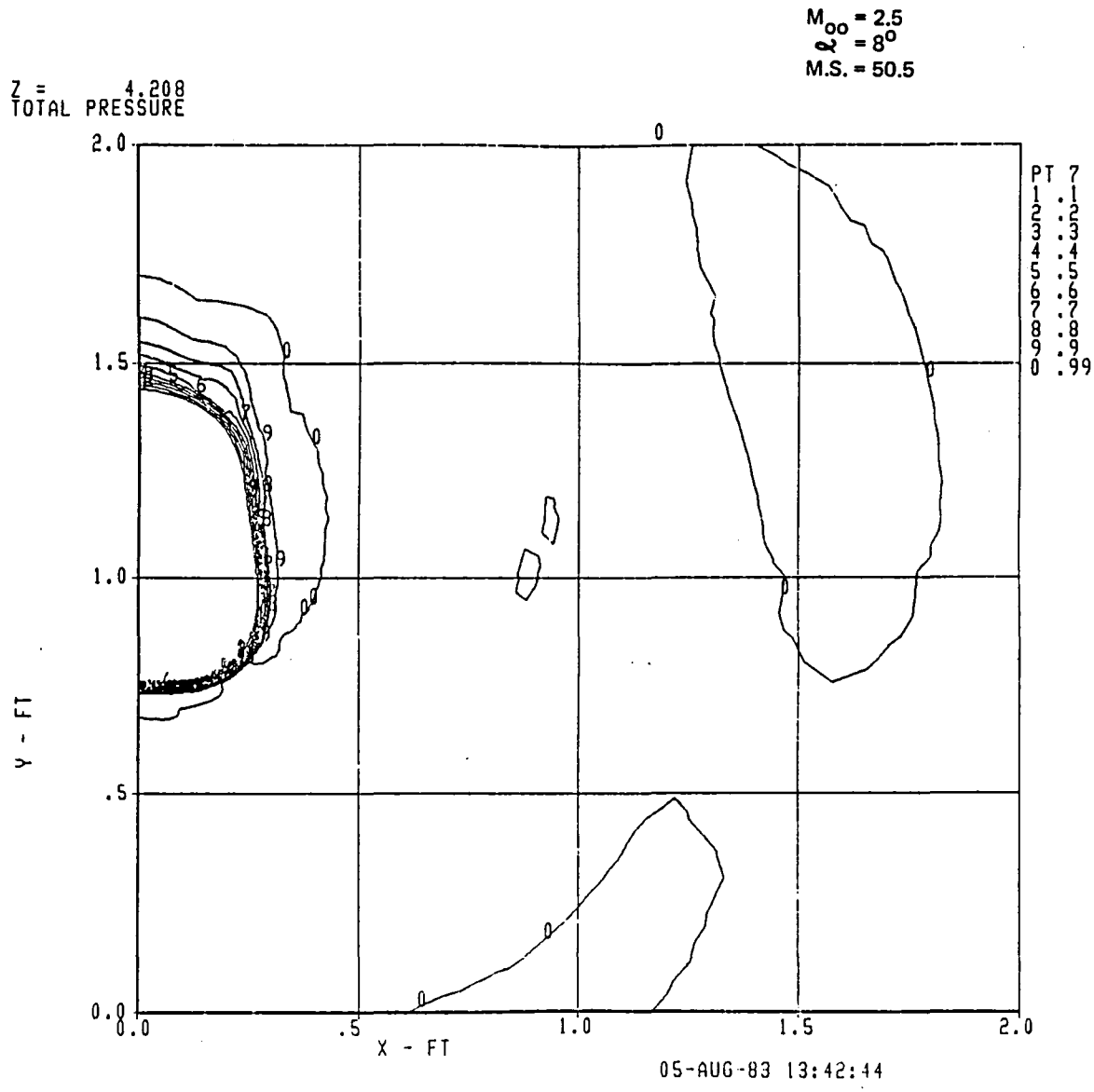

Figure 26(b). Total Pressure Contours

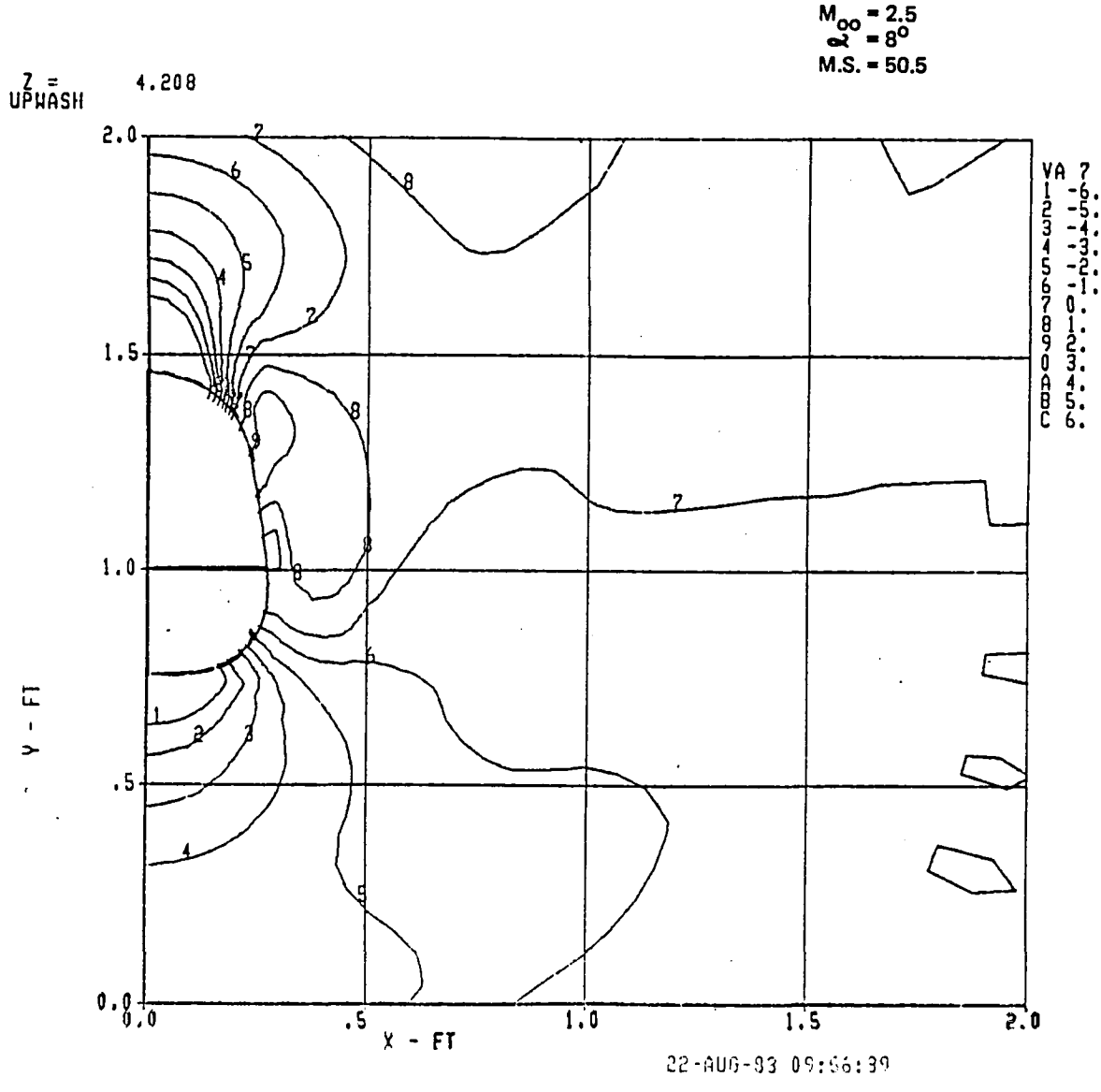

Figure 26(c). Upwash Angle Contours

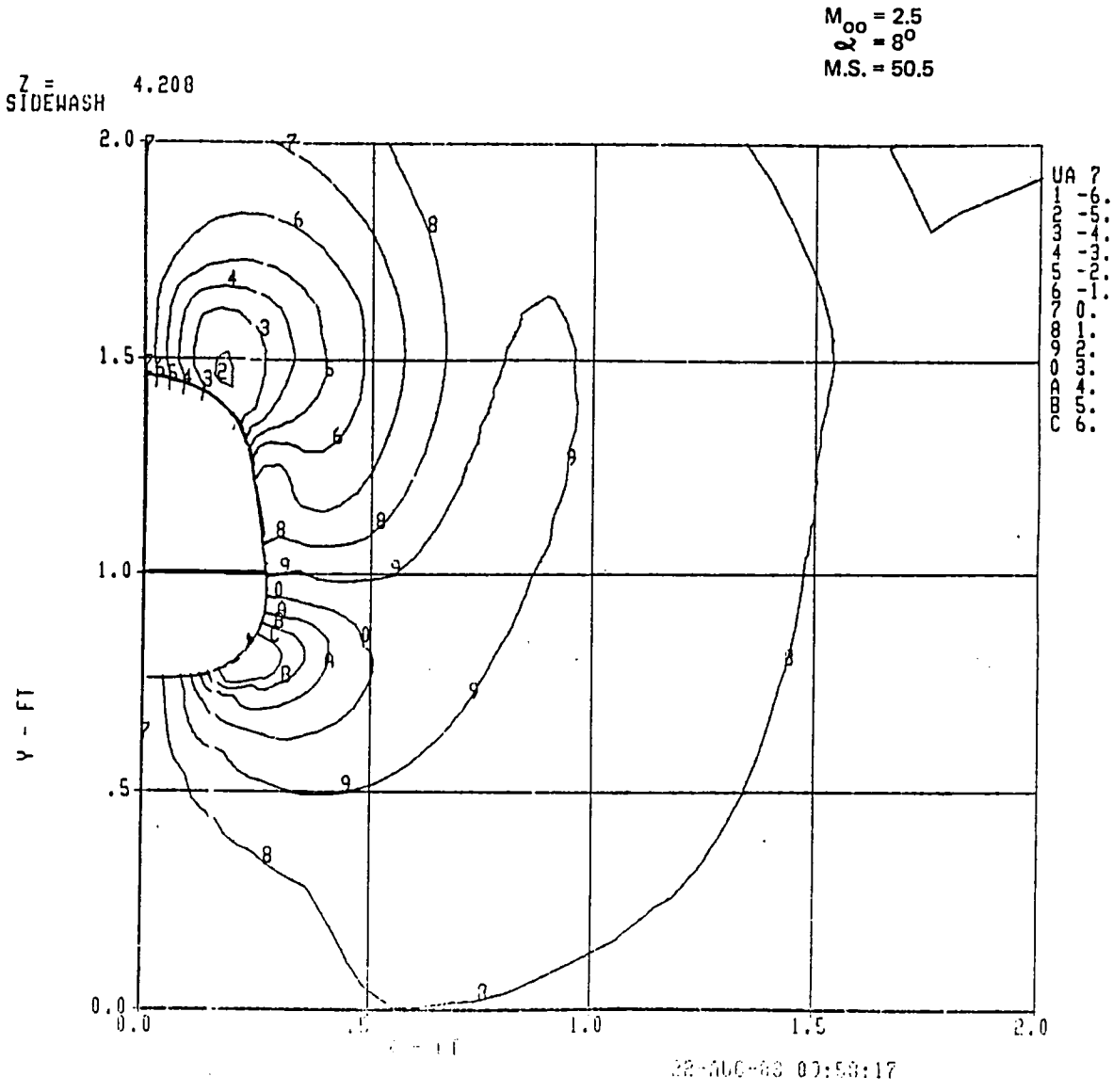

Figure 26(d). Sidewash Angle Contours

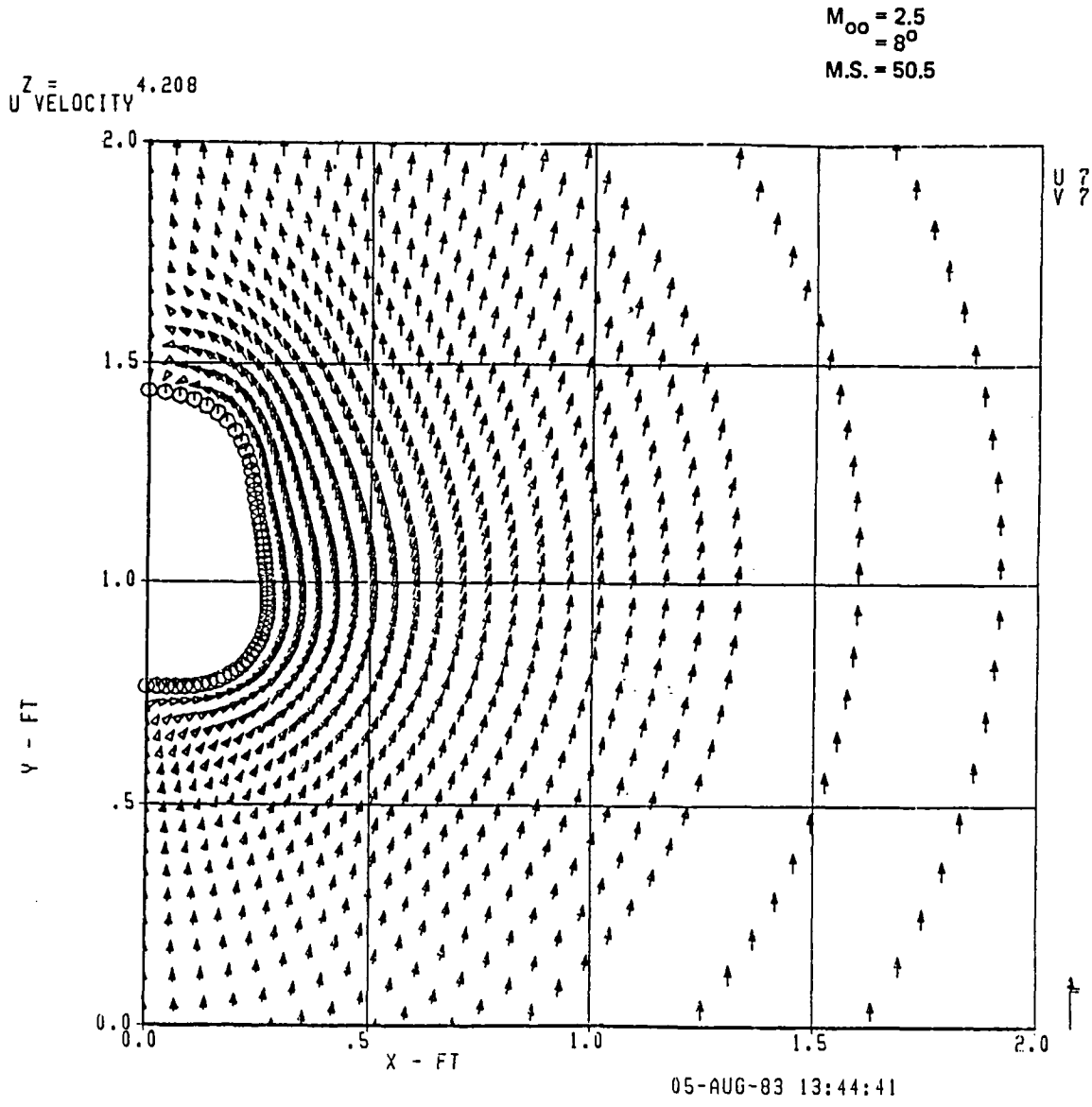

Figure 26(e). Cross-Plane Velocity

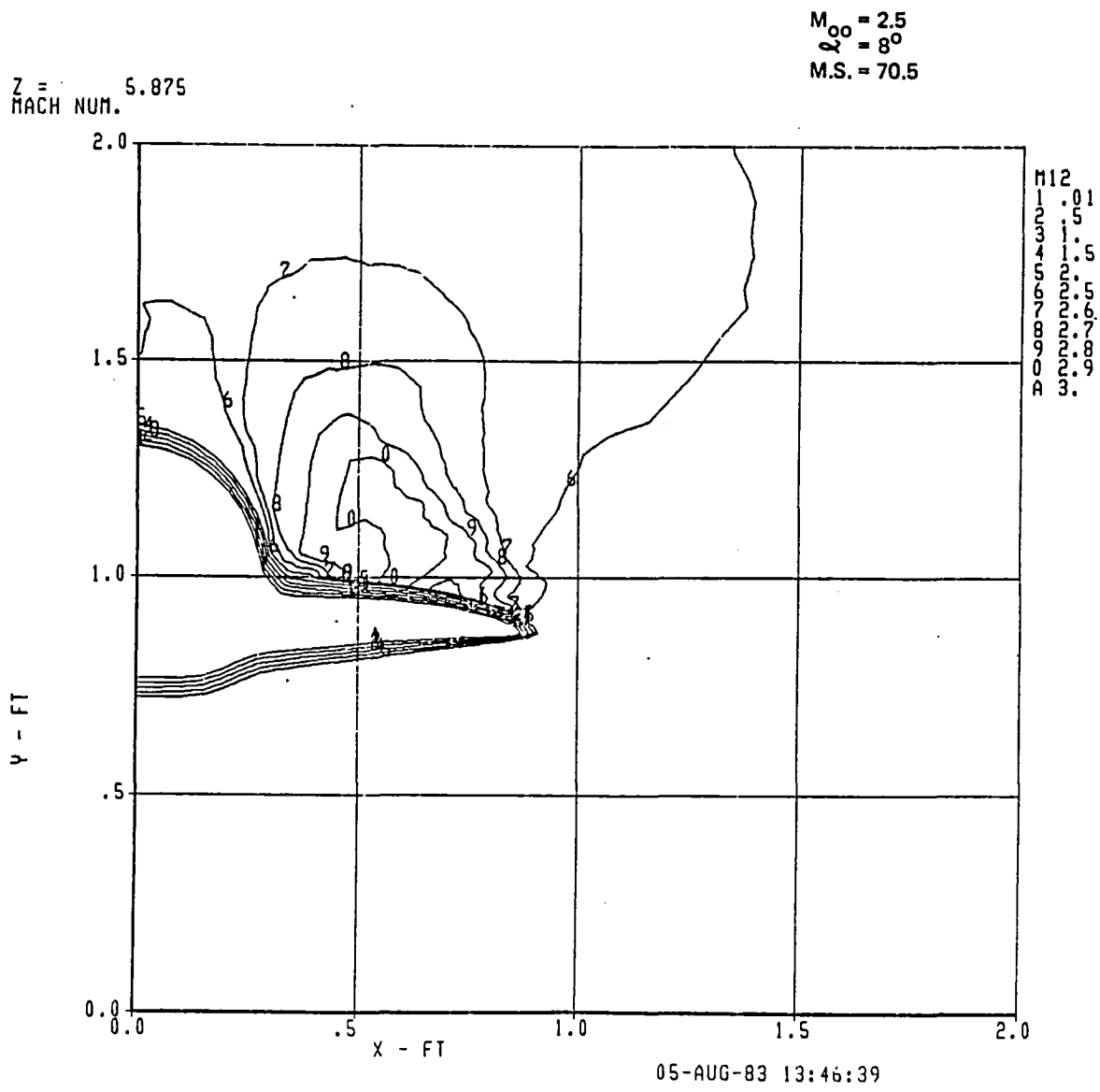

Figure 27(a). Mach Contours

Figure 27. Computed Results for Model Station 70.5, Mach 2.5, at 8-deg Angle of Attack

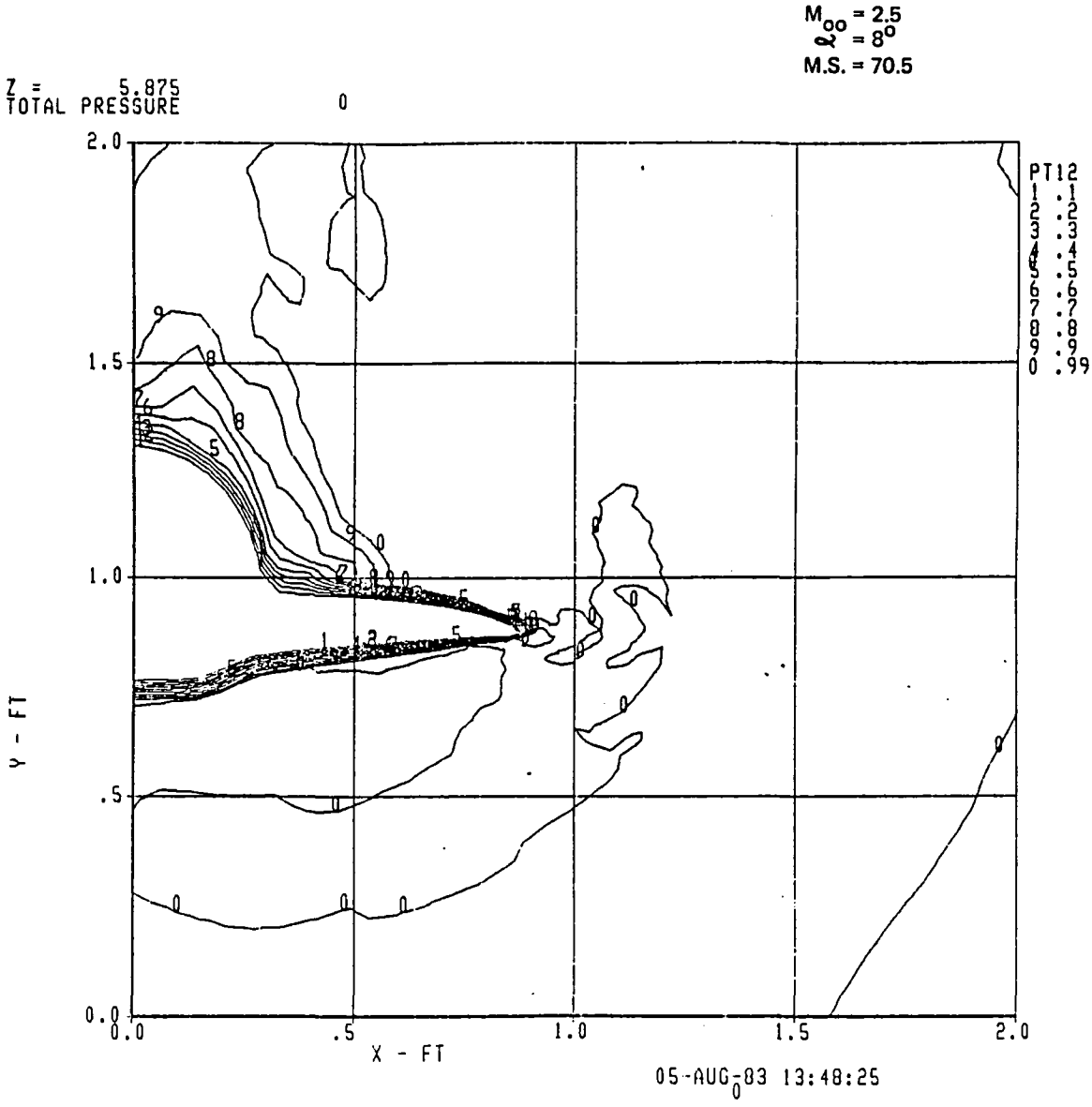

Figure 27(b). Total Pressure Contours

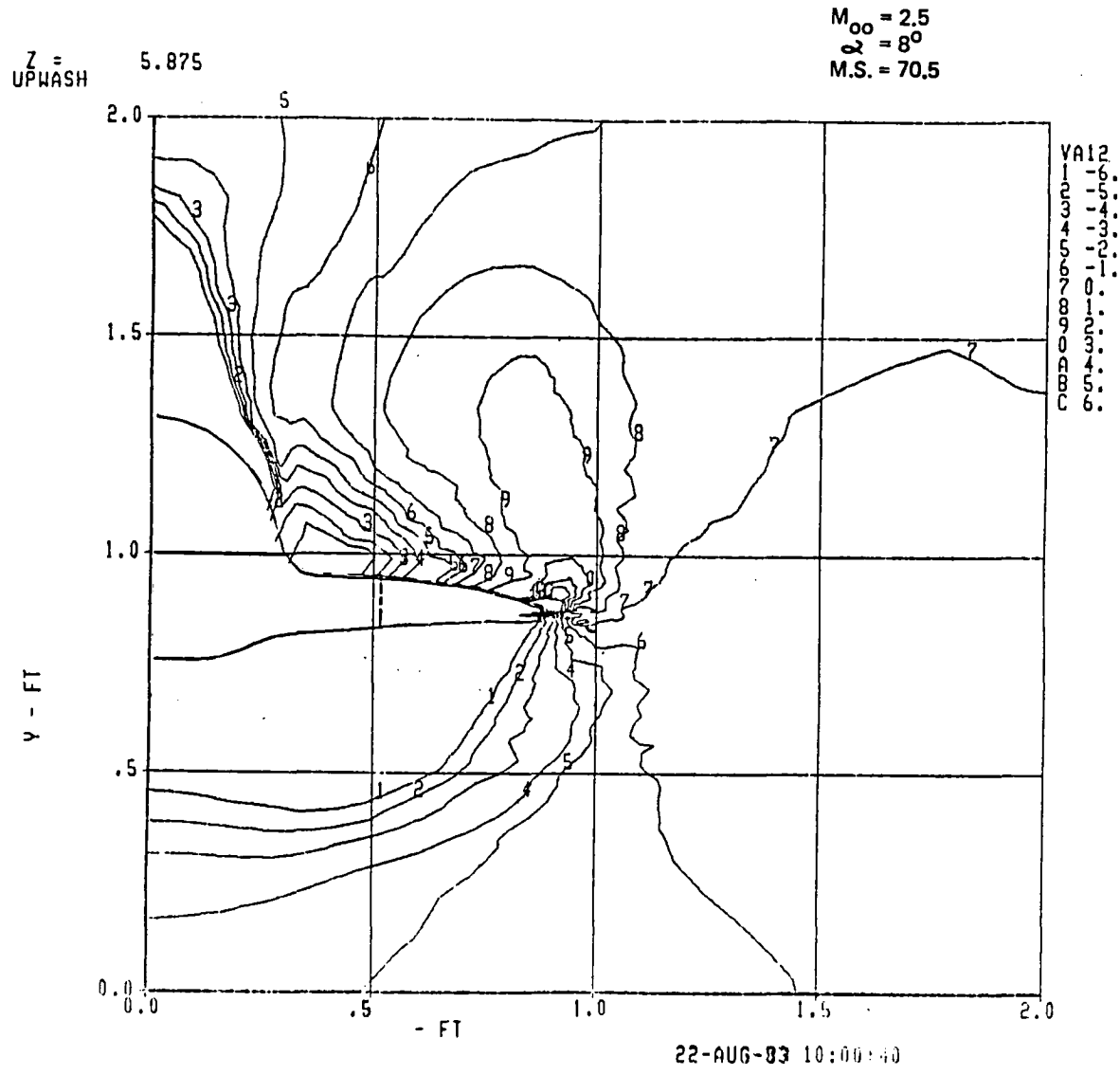

Figure 27(c). Upwash Angle Contours

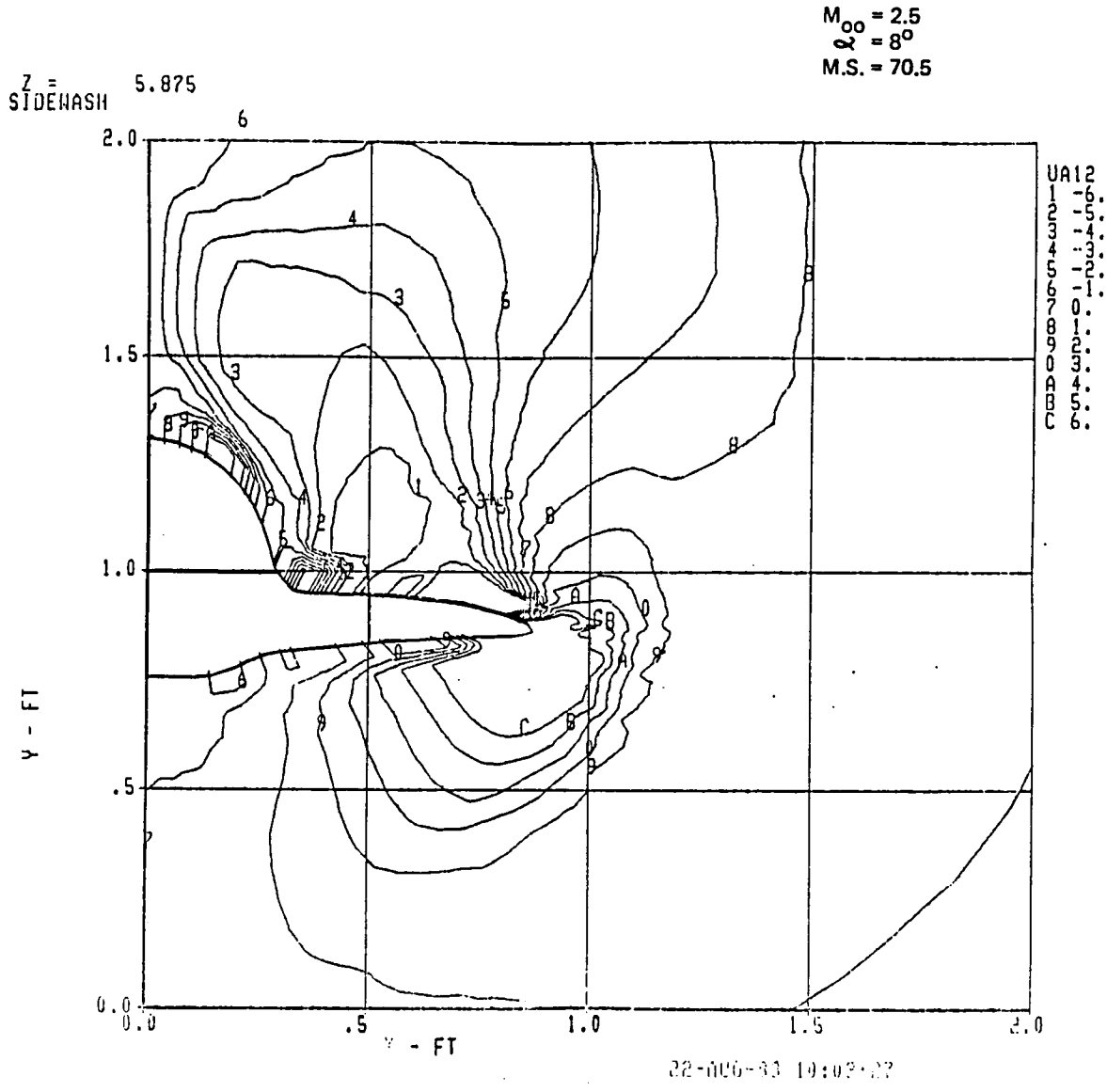

Figure 27(d). Sidewash Angle Contours

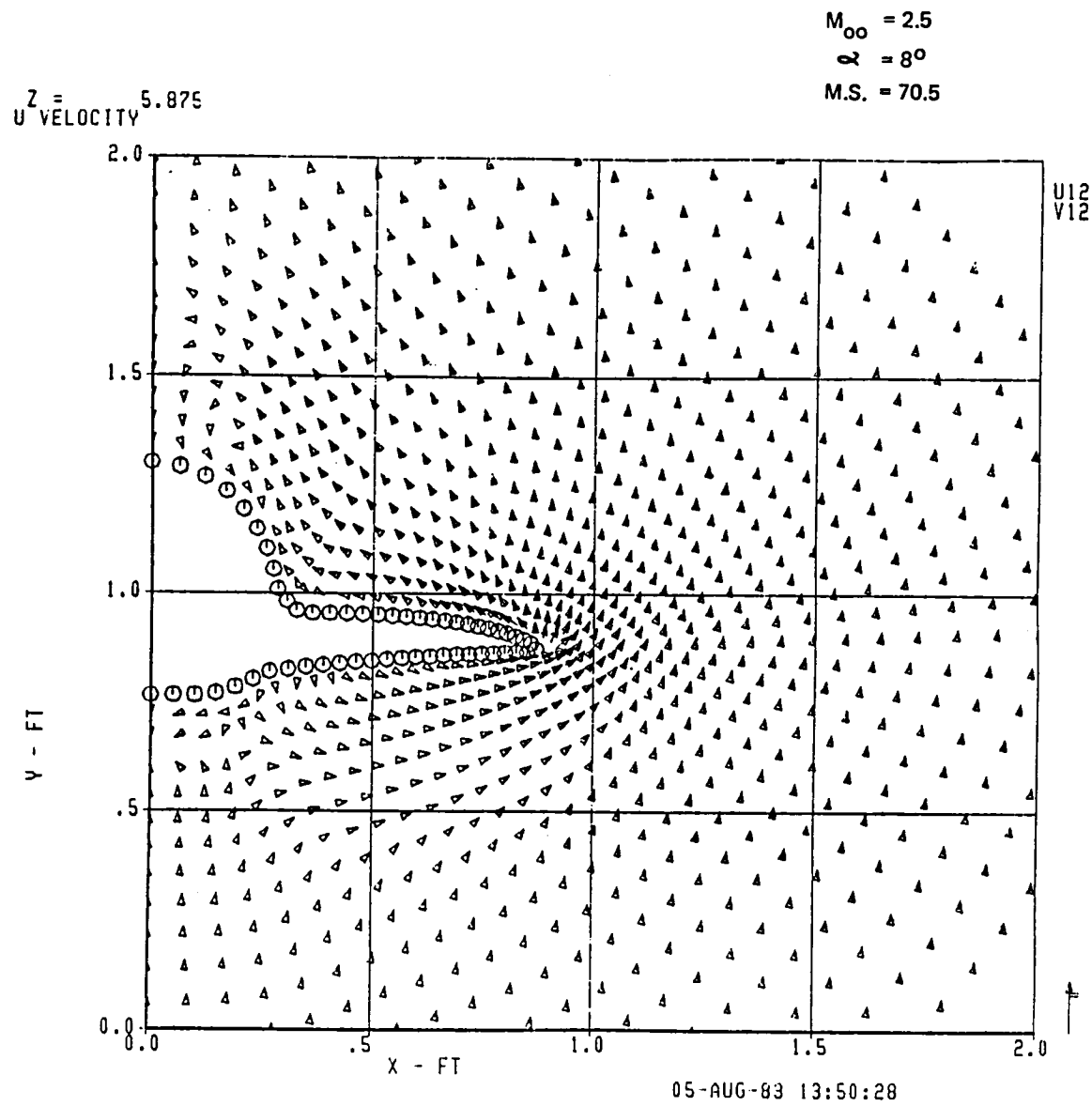

Figure 27(e). Cross-Plane Velocity

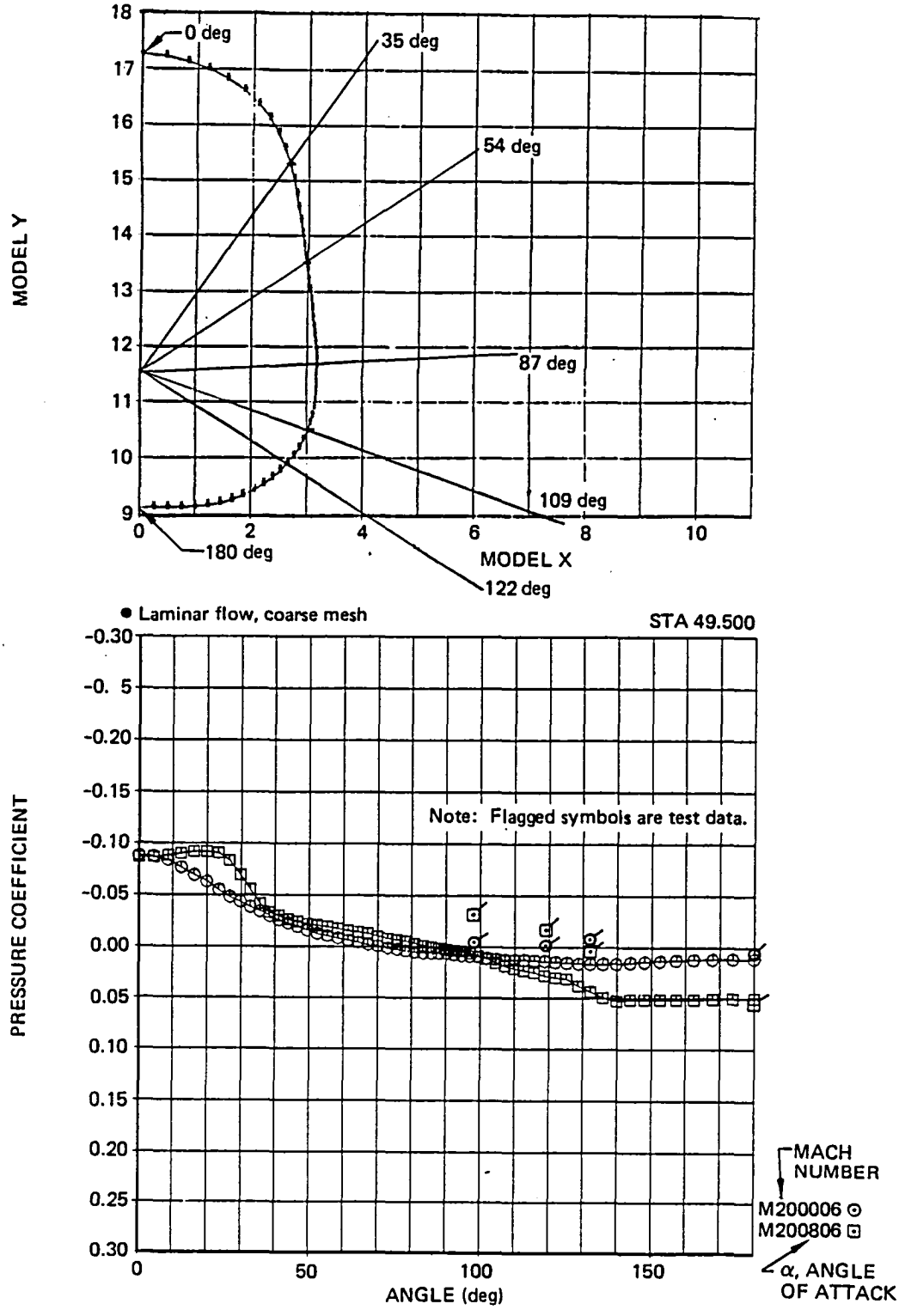

Figure 28. Comparison Between Computed and Measured Body Pressure Coefficients at the Forward Survey Station, Mach 2.0

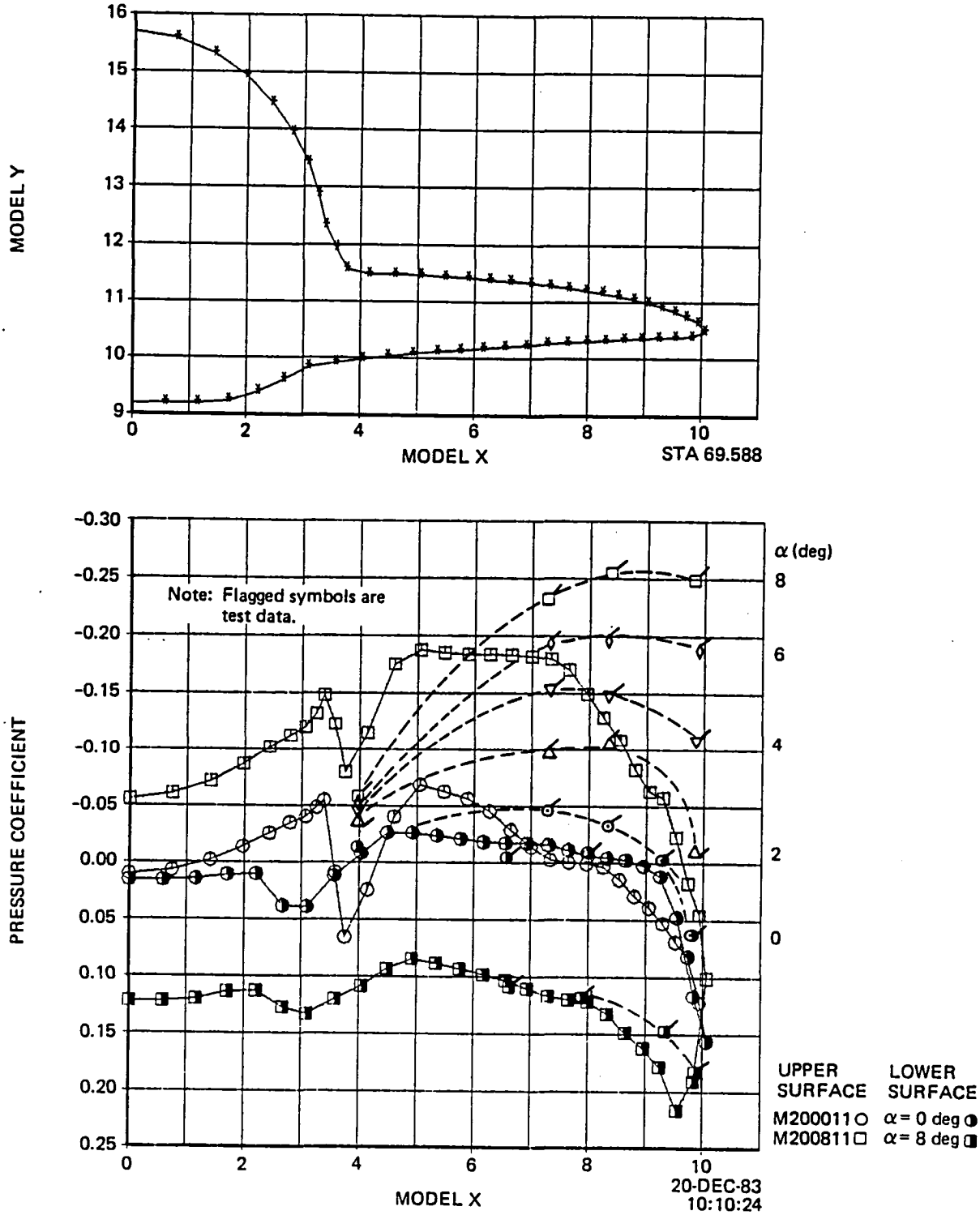

Figure 29. Comparison Between Computed and Measured Pressure Coefficients at the Aft Survey Station, Mach 2.0

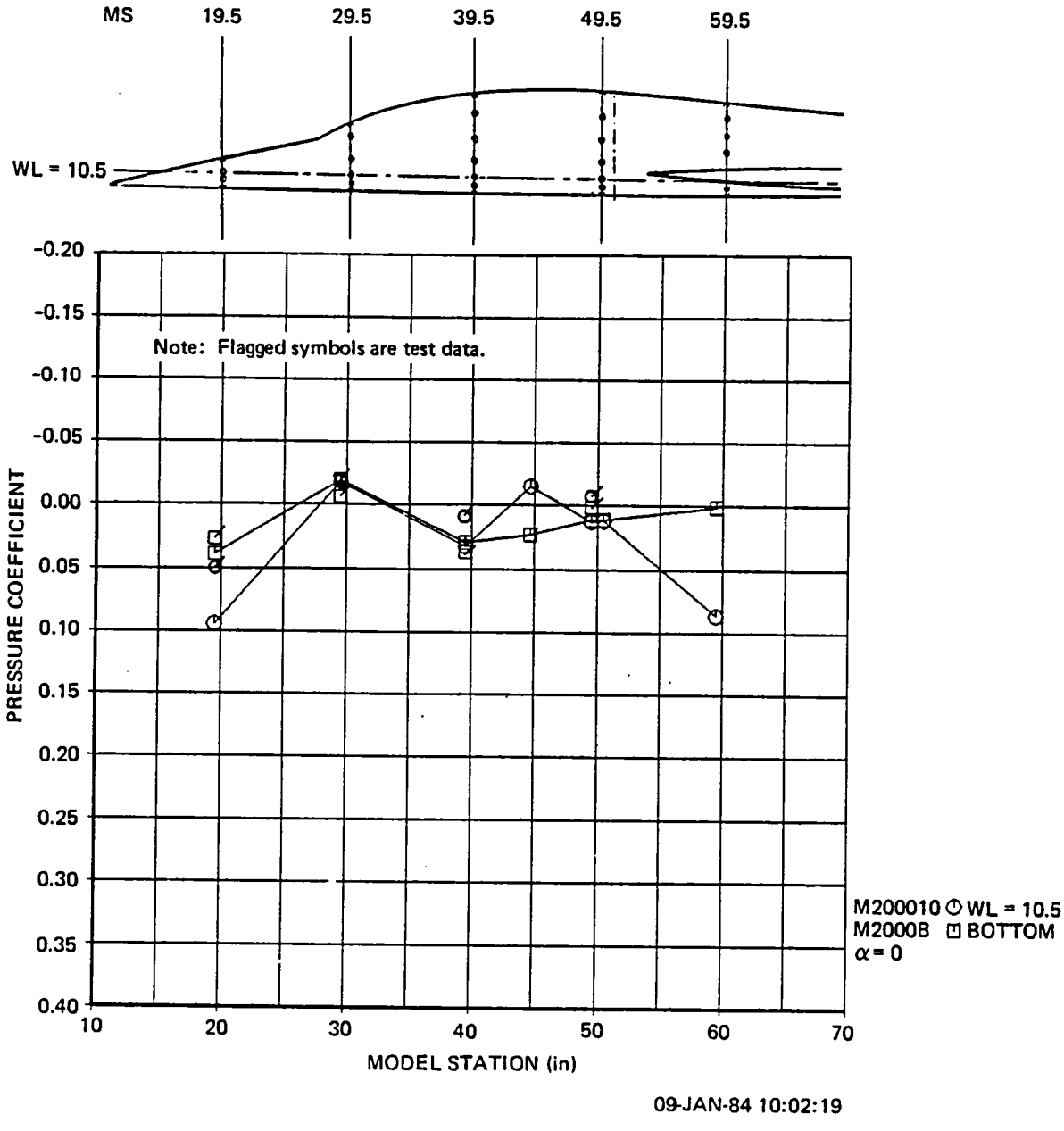

Figure 30a. Comparison Between Computed and Measured Pressure Coefficients Along the Body, Mach 2.0, $\alpha = 0$ deg

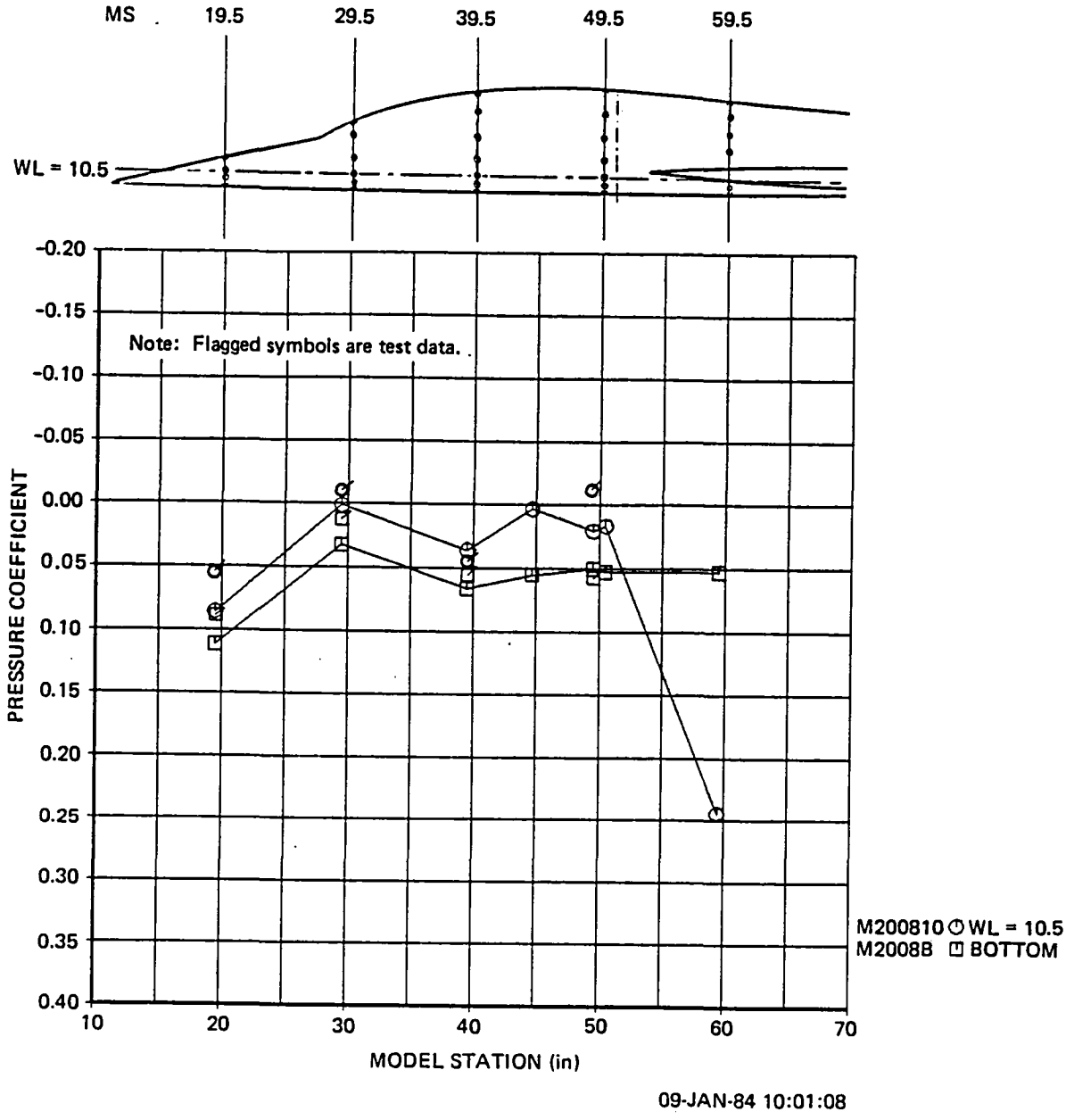

Figure 30b. Comparison Between Computed and Measured Pressure Coefficients Along the Body, Mach 2.0, $\alpha = 8$ deg

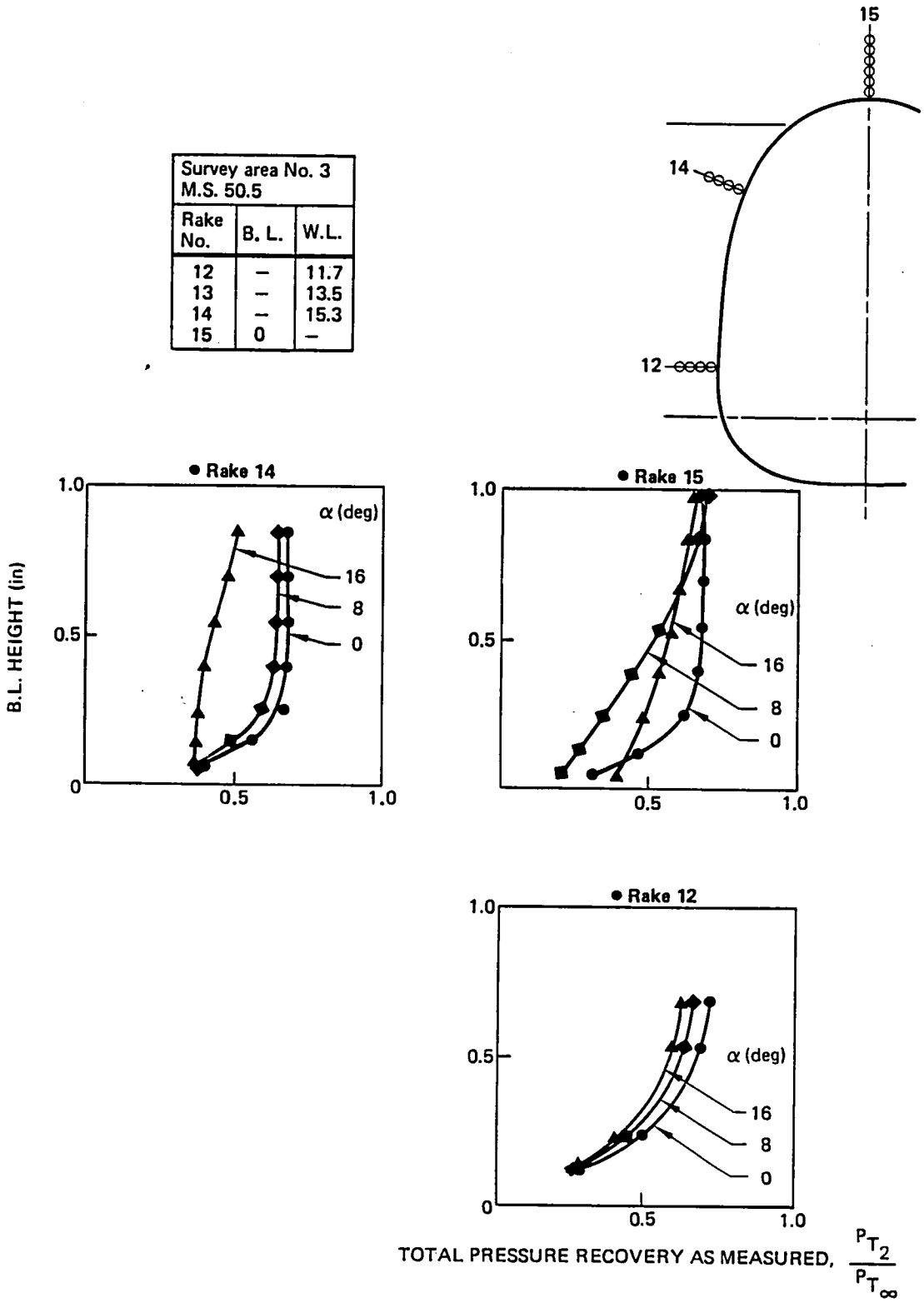

Figure 31. Boundary Layer Data at the Forward Survey Station, Mach 2.0

Survey area No. 3 M.S. 50.5		
Rake No.	B.L.	W.L.
12	–	11.7
13	–	13.5
14	–	15.3
15	0	–

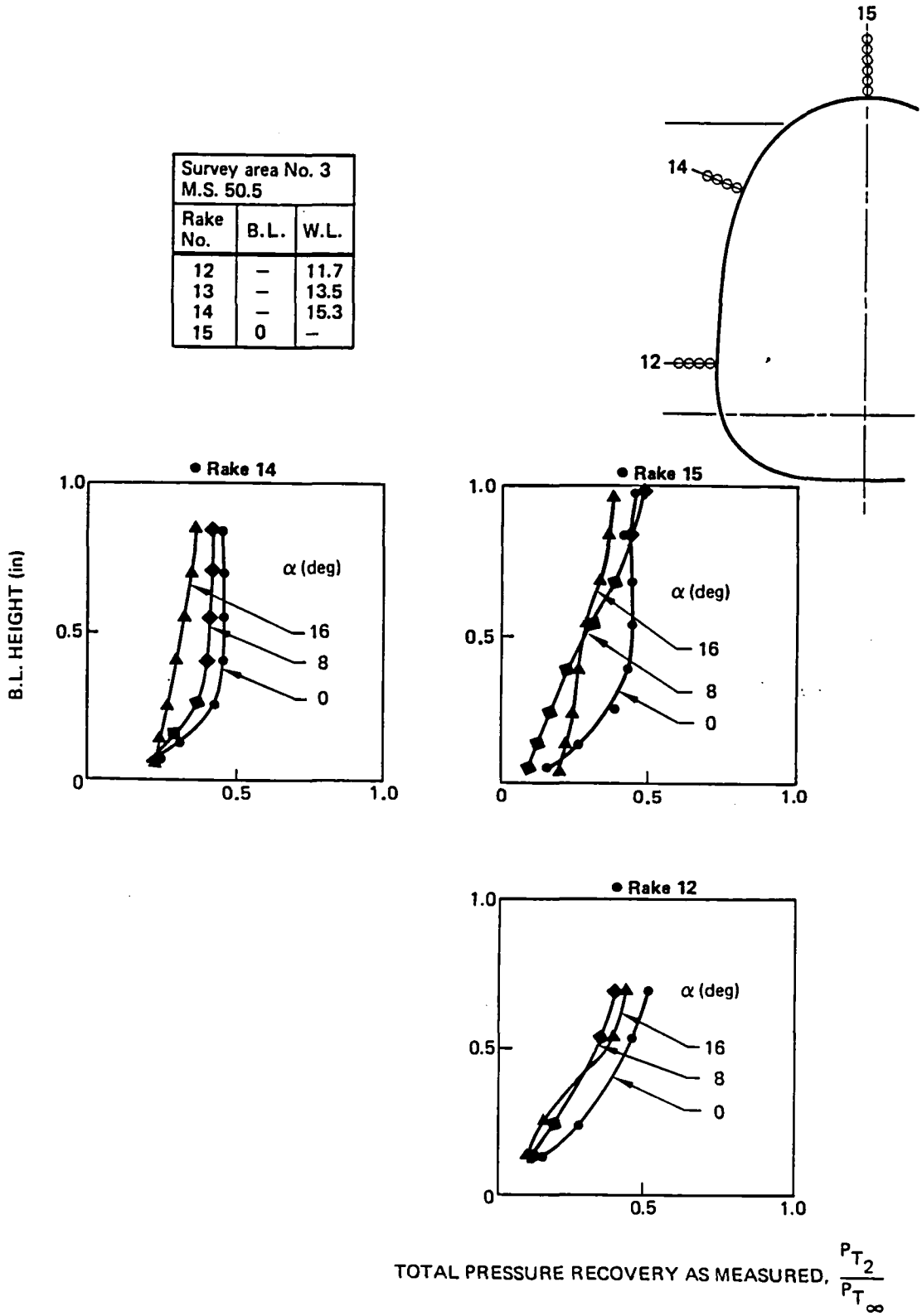

Figure 32. Boundary Layer Data at the Forward Survey Station, Mach 2.5

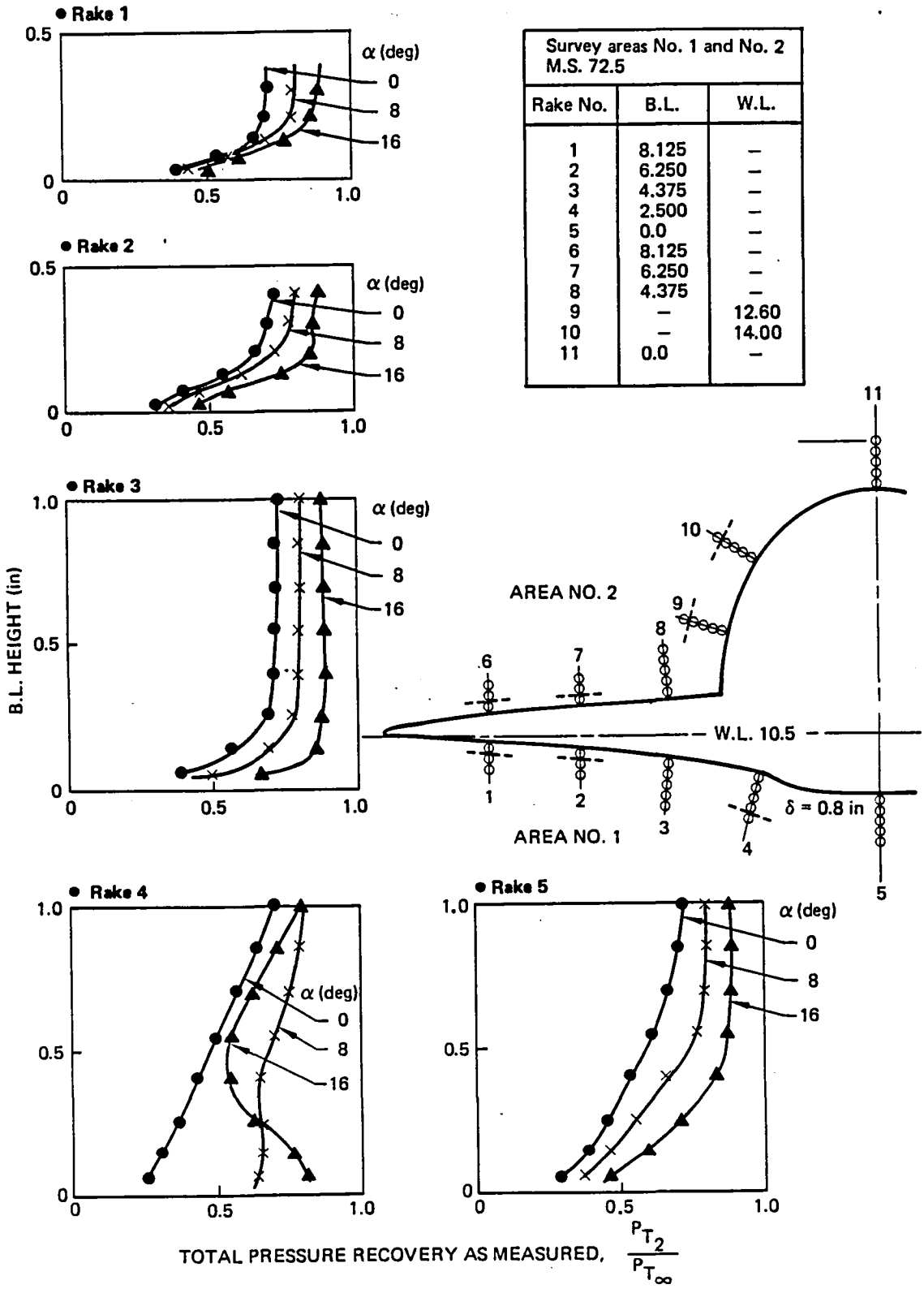

Survey areas No. 1 and No. 2 M.S. 72.5		
Rake No.	B.L.	W.L.
1	8.125	–
2	6.250	–
3	4.375	–
4	2.500	–
5	0.0	–
6	8.125	–
7	6.250	–
8	4.375	–
9	–	12.60
10	–	14.00
11	0.0	–

Figure 33(a). Boundary Layer Data at the Aft Survey Station, Mach 2.0

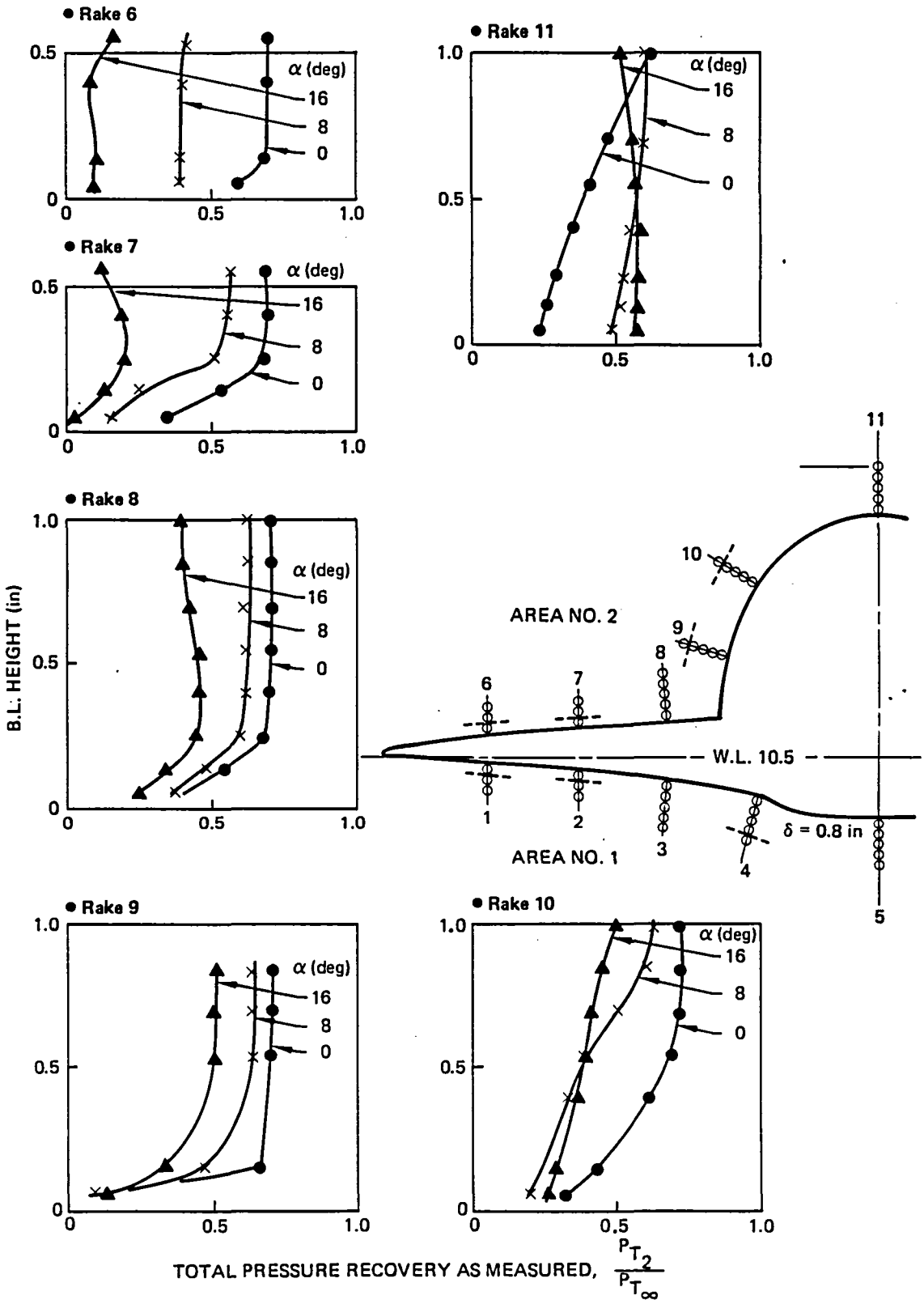

Figure 33(b). Boundary Layer Data at the Aft Survey Station, Mach 2.0

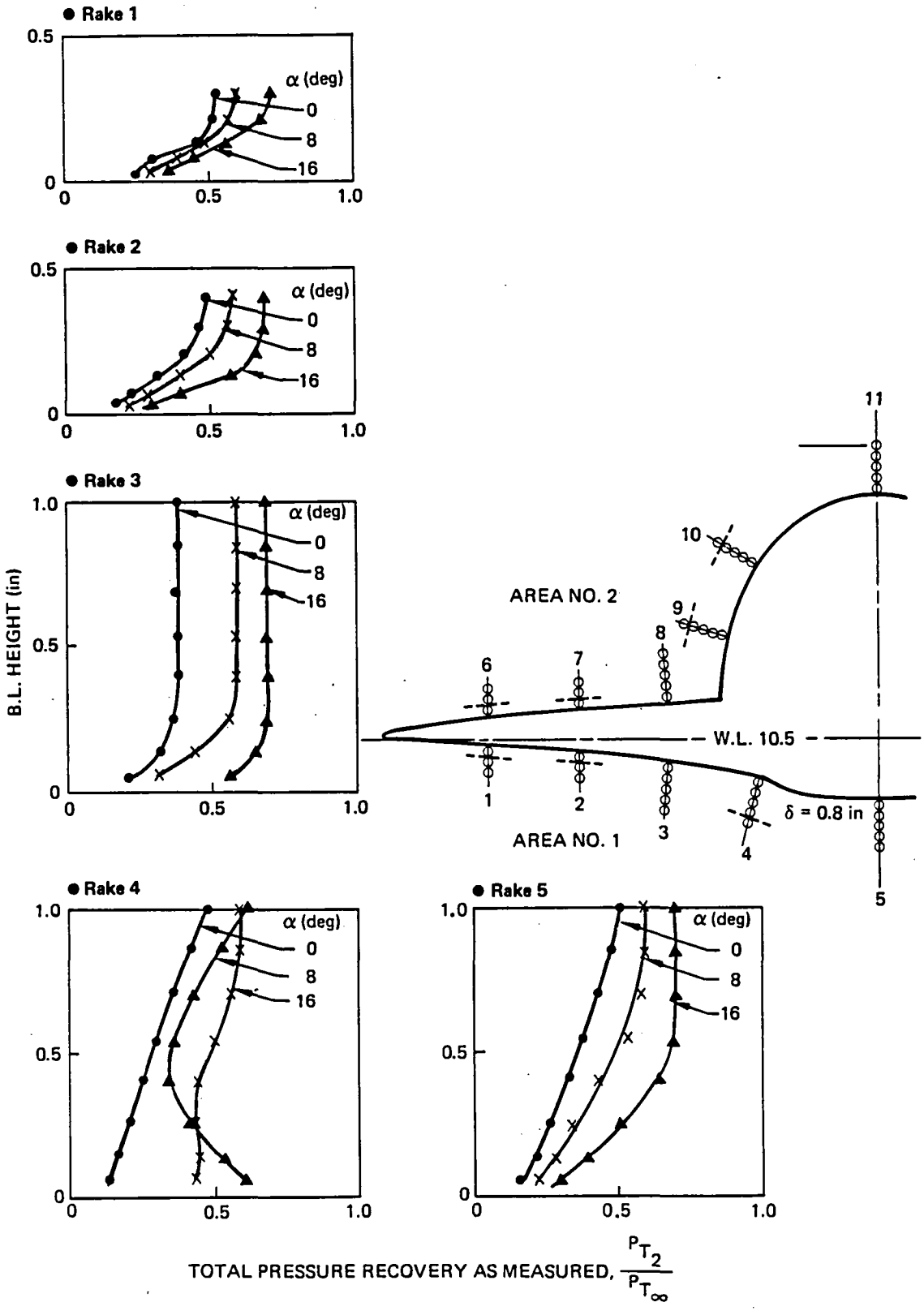

Figure 34(a). Boundary Layer Data at the Aft Survey Station, Mach 2.5

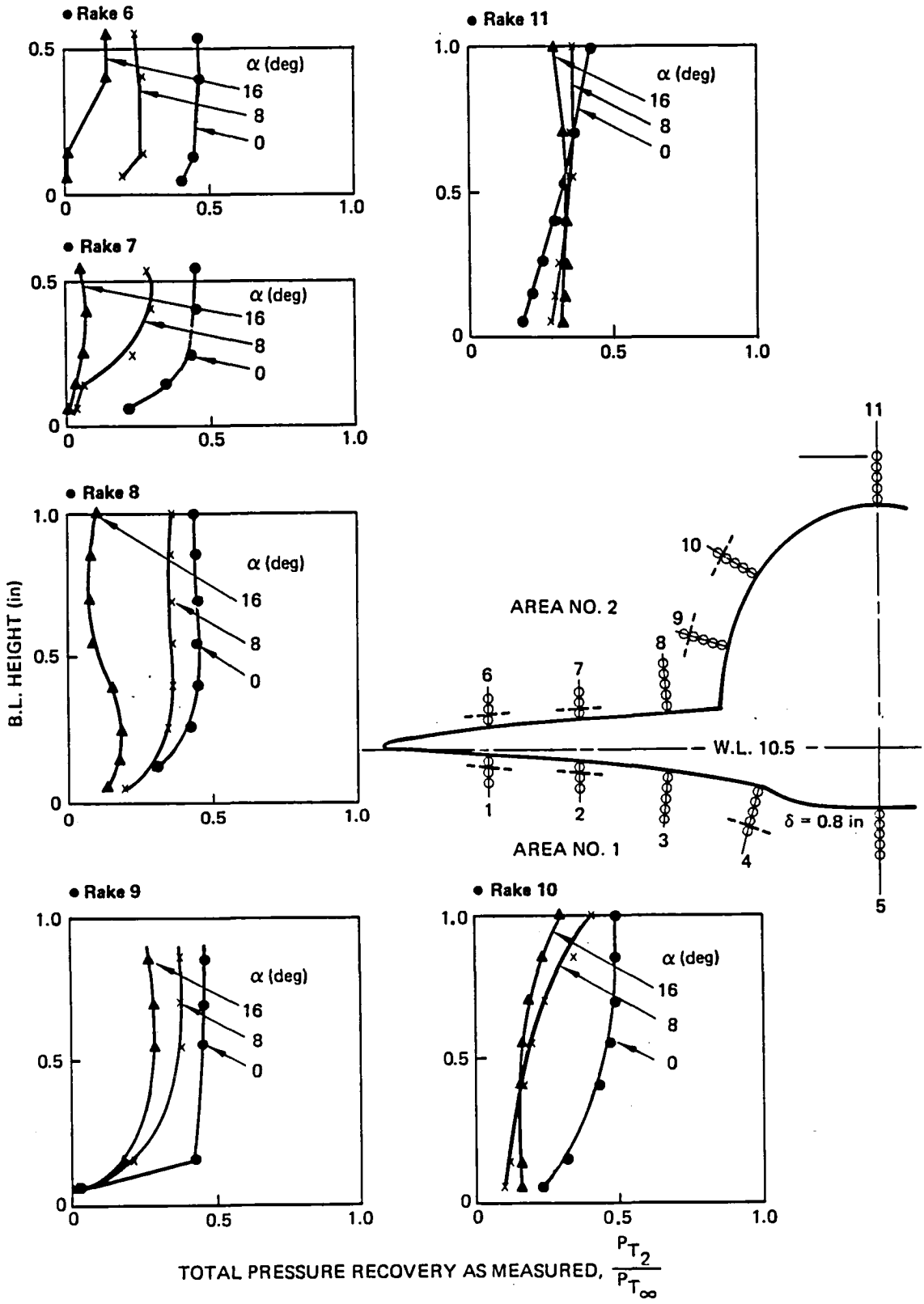

Figure 34(b). Boundary Layer Data at the Aft Survey Station, Mach 2.5

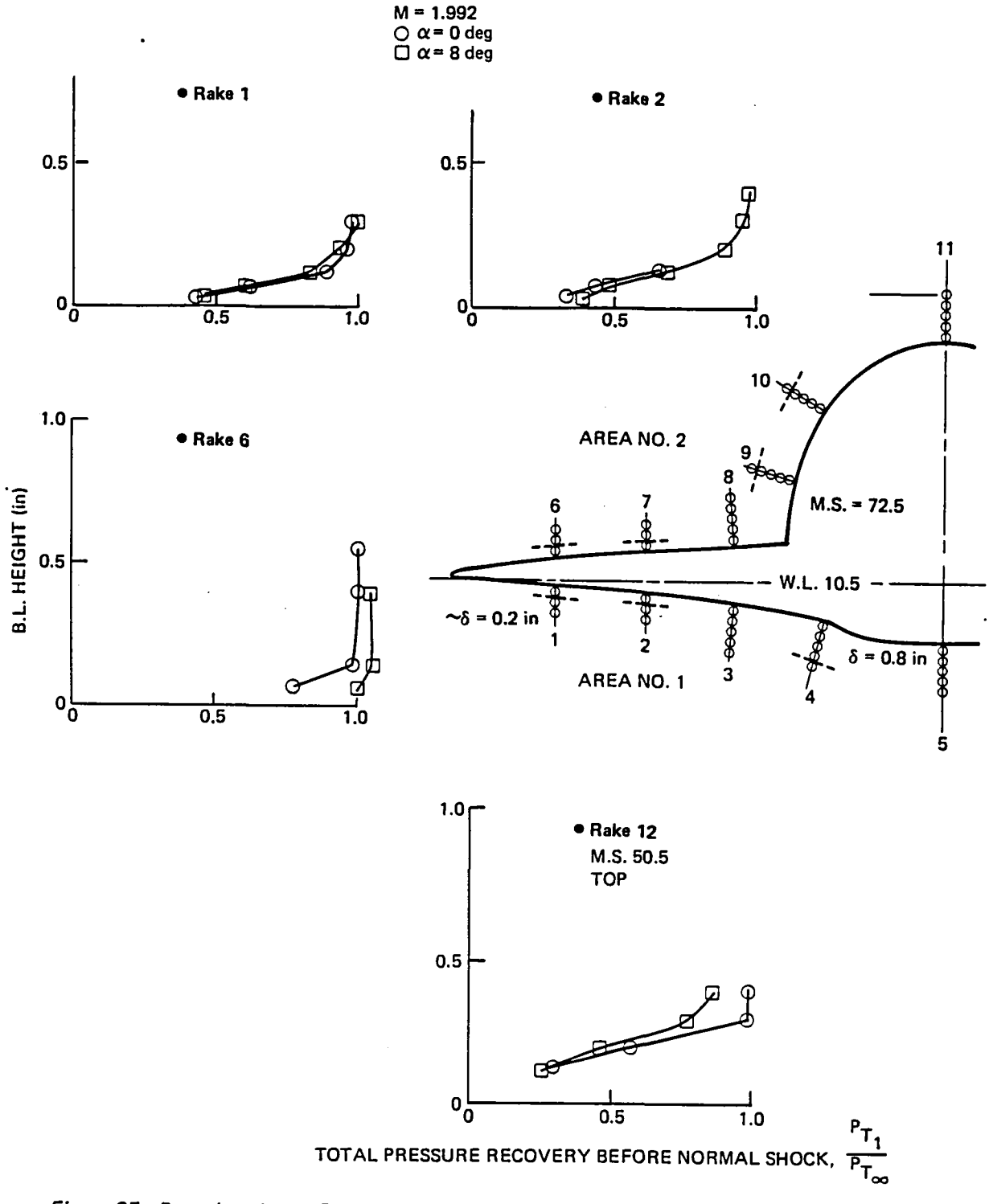

Figure 35. Boundary Layer Data Corrected for Normal Shock Probe Losses, Mach 2.0

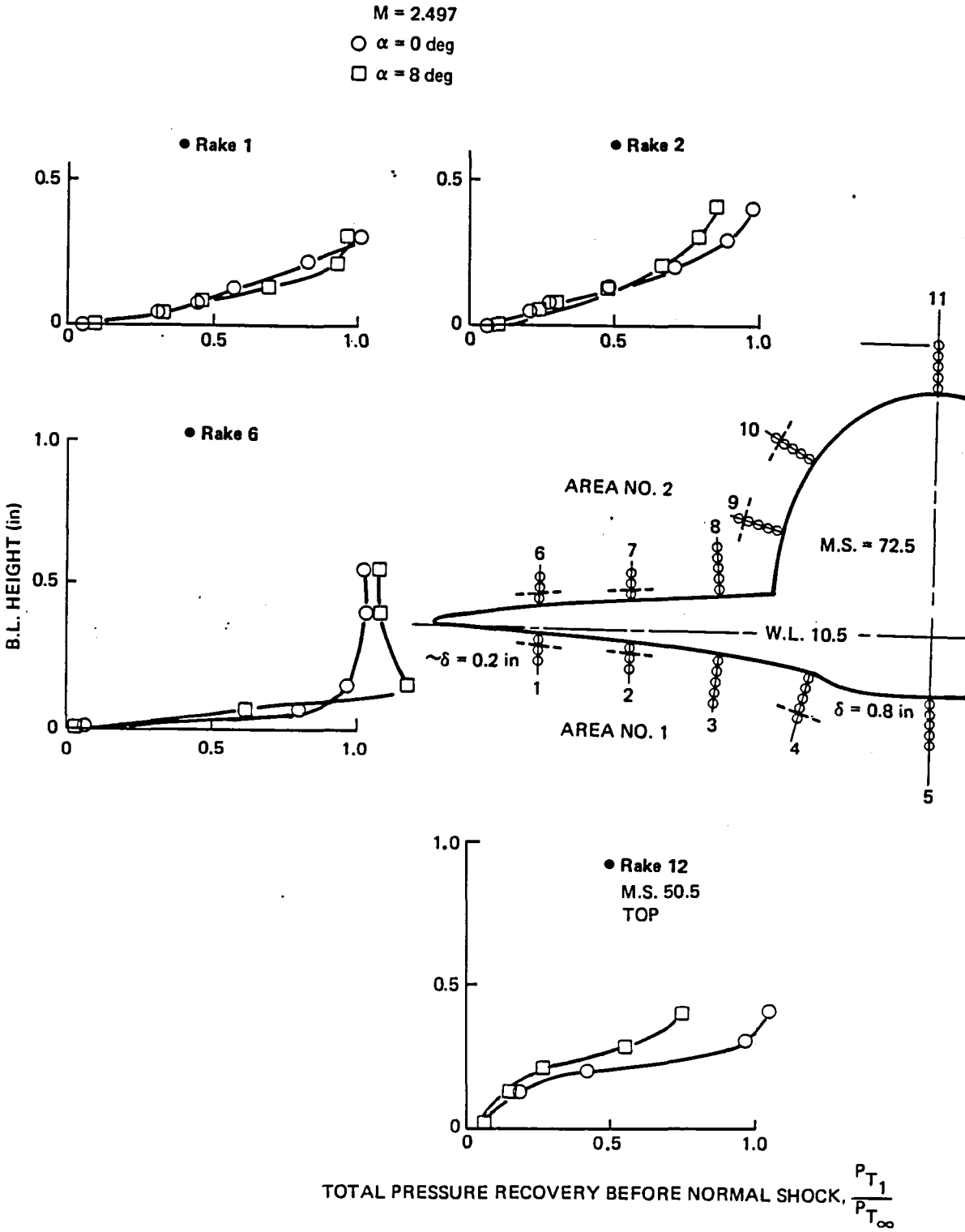

Figure 36. Boundary Layer Data Corrected for Normal Shock Probe Losses, Mach 2.5

1. Report No.	2. Government Accession No.	3. Recipient's Catalog No.
NASA CR-172315		

4. Title and Subtitle	5. Report Date
Inlet Flow Field Investigation - Part II Computation of the Flow about a Supercruise Forebody at Supersonic Speeds	April 1984
	6. Performing Organization Code
7. Author(s)	8. Performing Organization Report No.
E. E. I. Strom, G. C. Paynter, and V. Salemann	D180-27939-2
9. Performing Organization Name and Address Boeing Military Airplane Company Propulsion Technology P.O. Box 3707 Seattle, Washington 98124	10. Work Unit No.
	11. Contract or Grant No. NAS1-16612
12. Sponsoring Agency Name and Address Langley Technical Monitor; S. F. Yaros Final REport - Part II	13. Type of Report and Period Covered Contractor Report
	14. Sponsoring Agency Code

15. Supplementary Notes

16. Abstract

A numerical procedure which solves the parabolized Navier-Stokes (PNS) equations on a body fitted mesh was used to compute the flow about the forebody of an advanced tactical supercruise fighter configuration. The objective of this study was to explore the use of a PNS method for design of supersonic cruise forebody geometries. Forebody flow fields were computed at Mach numbers of 1.5, 2.0, and 2.5, and at angles-of-attack of 0^{o}, 4^{o}, and 8^{o} at each Mach number. Computed results are presented at several body stations and include contour plots of Mach number, total pressure, upwash angle, sidewash angle and the cross-plane velocity. The computational analysis procedure was found reliable for evaluating forebody flow fields of advanced aircraft configurations for flight conditions where the vortex shed from the wing leading edge is not a dominant flow phenomenon.

Static pressure distributions and boundary layer profiles on the forebody and wing were surveyed in a wind tunnel test, and the analytical results are compared to the data.

The current status of the parabolized flow field code is described along with desirable improvements in the code.

17. Key Words (Suggested by Author(s))	18. Distribution Statement
Inlet Flow Field Forebody Flow Field Supersonic Flow Parabolized Navier-Stokes	Unclassified - Unlimited Subject Category 02

19. Security Classif. (of this report)	20. Security Classif. (of this page)	21. No. of Pages	22. Price*
Unclassified	Unclassified	137	

* For sale by the National Technical Information Service, Springfield, Virginia 22161